AD-A186 634

(2)

DTIC FILE COPY

Bulletin 50
(Part 3 of 4 Parts)

THE SHOCK AND VIBRATION BULLETIN

Part 3
Dynamic Analysis, Design Techniques

DTIC
ELECTE
NOV 19 1987
S D
D

SEPTEMBER 1980

A Publication of
THE SHOCK AND VIBRATION
INFORMATION CENTER
Naval Research Laboratory, Washington, D.C.

DEPARTMENT OF DEFENSE
UNITED STATES OF AMERICA

Office of
The Under Secretary of Defense
for Research and Engineering

Approved for public release; distribution unlimited

87 10 28 003

BLANK PAGES
IN THIS
DOCUMENT
WERE NOT
FILMED

DISCLAIMER NOTICE

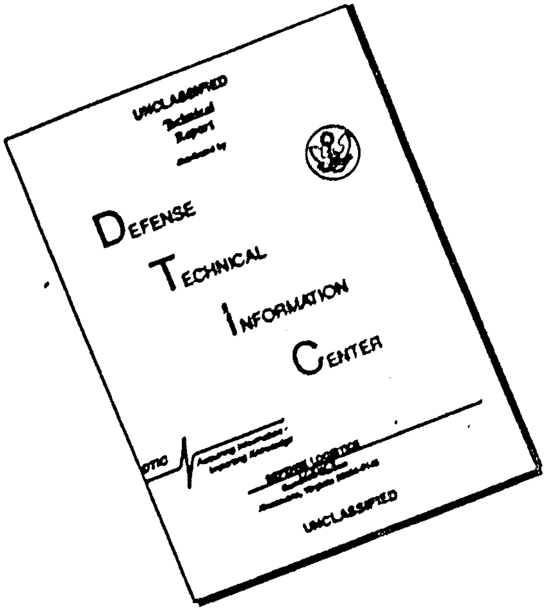

THIS DOCUMENT IS BEST QUALITY AVAILABLE. THE COPY FURNISHED TO DTIC CONTAINED A SIGNIFICANT NUMBER OF PAGES WHICH DO NOT REPRODUCE LEGIBLY.

SYMPOSIUM MANAGEMENT

THE SHOCK AND VIBRATION INFORMATION CENTER

Henry C. Pusey, Director
Rudolph H. Volin
J. Gordan Showalter
Carol Healey
Elizabeth A. McLaughlin

Bulletin Production

Publications Branch, Technical Information Division,
Naval Research Laboratory

Bulletin 50
(Part 3 of 4 Parts)

THE
SHOCK AND VIBRATION
BULLETIN

SEPTEMBER 1980

A Publication of
THE SHOCK AND VIBRATION
INFORMATION CENTER
Naval Research Laboratory, Washington, D.C.

The 50th Symposium on Shock and Vibration was held at the Antlers Plaza Hotel, Colorado Springs, CO on October 16-18, 1979. The U.S. Air Force Academy, Colorado Springs, CO, was host on behalf of the Air Force.

DTIC
COPY
INSPECTED
6

Accesion For
NTIS CRA&I ☒
DTIC TAB ☐
Unannounced ☐
Justification ....
By ....
Distribution /
Availability Codes
Dist | Avail and/or Special
A-1

Office of
The Under Secretary of Defense
for Research and Engineering

PAPERS APPEARING IN PART 3

DYNAMIC ANALYSIS

THE RELATIVE COMPLEXITIES OF PLATE AND SHELL VIBRATIONS 1
A. W. Leissa, Ohio State University, Columbus, OH

IN-FLUID CYLINDRICAL BEAM VIBRATION WITH MULTI-DEGREE OF FREEDOM ABSORBERS 11
B. E. Sandman and J. S. Griffin, Naval Underwater Systems Center, Newport, RI

DYNAMIC STABILITY OF FIBROUS COMPOSITE CYLINDERS UNDER PULSE LOADING 21
R. J. Stuart and S. Dharmarajan, San Diego State University, San Diego, CA

TRANSFER MATRIX ANALYSIS OF DYNAMIC RESPONSE OF COMPOSITE-MATERIAL STRUCTURAL ELEMENTS WITH MATERIAL DAMPING 27
M. M. Wallace and C. W. Bert, The University of Oklahoma, Norman, OK

CONTRIBUTIONS TO THE DYNAMIC ANALYSIS OF MAGLEV VEHICLES ON ELEVATED GUIDEWAYS 39
K. Popp, Technical University Munich, West Germany

DYNAMICS OF LONG VERTICAL CABLES 63
F. H. Wolff, Westinghouse R&D Center, Pittsburgh, PA

RESPONSE AND FAILURE OF UNDERGROUND REINFORCED CONCRETE PLATES SUBJECTED TO BLAST 71
C. A. Ross and C. C. Schauble, University of Florida Graduate Engineering Center, Eglin AFB, FL and P. T. Nash, USAF Armament Laboratory, Eglin AFB, FL

WHIPPING ANALYSIS TECHNIQUES FOR SHIPS AND SUBMARINES 83
K. A. Bannister, Naval Surface Weapons Center, White Oak, Silver Spring, MD

LIMITATIONS ON RANDOM INPUT FORCES IN RANDOMDEC COMPUTATION FOR MODAL IDENTIFICATION 99
S. R. Ibrahim, Old Dominion University, Norfolk, VA

STRUCTURAL-DYNAMIC CHARACTERIZATION OF AN EXPERIMENTAL 1200-KILOVOLT ELECTRICAL TRANSMISSION LINE SYSTEM 113
Leon Kempner, Jr., Bonneville Power Administration, Portland, OR and Strether Smith and Richard C. Stroud, Synergistic Technology Incorporated, Cupertino, CA

DESIGN TECHNIQUES

ANALYSIS AND DESIGN OF THE SHUTTLE REMOTE MANIPULATOR SYSTEM MECHANICAL ARM FOR LAUNCH DYNAMIC ENVIRONMENT 125
D. M. Gossain, E. Quittner and S. S. Sachdev, Spar Aerospace Limited, Toronto, Canada

STRUCTURAL DYNAMIC CHARACTERISTICS OF THE SPACE SHUTTLE REACTION CONTROL THRUSTERS 151
G. L. Schachne and J. H. Schmidt, The Marquardt Company, Van Nuys, CA

MODIFICATION OF FLIGHT VEHICLE VIBRATION MODES TO ACCOUNT FOR DESIGN CHANGES 163
C. W. Coale and M. R. White, Lockheed Missiles and Space Company, Sunnyvale, CA

EVALUATION OF AIRBORNE LASER BEAM JITTER USING STRUCTURAL DYNAMICS COMPUTER CODES AND CONTROL SYSTEM SIMULATIONS 179
C. L. Budde and P. H. Merritt, Air Force Weapons Laboratory, Kirtland AFB, NM and
C. D. Johnson, Anamet Laboratories, Inc., San Carlos, CA

FATIGUE LIFE PREDICTION FOR MULTILEVEL STEP-STRESS APPLICATIONS 189
R. G. Lambert, General Electric Company, Utica, NY

LATERAL INSTABILITY DURING SPIN TESTS OF A PENDULOUSLY SUPPORTED DISC 201
F. H. Wolff, A. J. Molnar, G. O. Sankey and J. H. Bitzer, Westinghouse R&D Center, Pittsburgh, PA

PAPERS APPEARING IN PART 1

WELCOME

WELCOME
Brigadier General William A. Orth, United State Air Force Academy

WELCOME
Colonel Ralph L. Kuster, Air Force Flight Dynamics Laboratory

KEYNOTE ADDRESS

U.S. ARMY KEYNOTE ADDRESS
Lieutenant General Robert J. Baer, U.S. Army Material Development and Readiness Command

U.S. NAVY KEYNOTE ADDRESS
Dr. T. T. G. Horwath, Naval Material Command

U.S. AIR FORCE KEYNOTE ADDRESS
Brigadier General Brien D. Ward, Air Force Systems Command

INVITED PAPERS

MEASUREMENT IN PERSPECTIVE
Professor Robert M. Mains, Washington University

DYNAMIC ANALYSIS AND DESIGN-CHALLENGE FOR THE FUTURE
Mr. Robert Hager, Boeing Company

MATERIALS IN DYNAMICS
Mr. Richard Shea and Mr. John Mescall, U.S. Army Materials and Mechanics Research Agency

DYNAMIC TESTING – HOW FAR WE'VE COME -- HOW MUCH FURTHER TO GO
Dr. Allen J. Curtis, Hughes Aircraft Company

PAPERS APPEARING IN PART 2

MEASUREMENT TECHNIQUES AND DATA ANALYSIS

A PRECISION INERTIAL ANGULAR VIBRATION MEASURING SYSTEM
H. D. Morris and R. B. Peters, Systron-Donner Corporation, Concord, CA and
P. H. Merritt, Air Force Weapons Laboratory, Kirtland AFB, NM

ANGULAR ACCELERATION MEASUREMENT ERRORS INDUCED BY LINEAR ACCELEROMETER CROSS-AXIS COUPLING
A. S. Hu, New Mexico State University, Las Cruces, NM

A METHOD FOR EXPERIMENTALLY DETERMINING ROTATIONAL MOBILITIES OF STRUCTURES
S. S. Sattinger, Westinghouse-Bettis Atomic Power Laboratory, Pittsburgh, PA

TRANSIENT EFFECTS IN ACOUSTIC SOUND REDUCTION MEASUREMENTS
A. J. Kalinowski, Naval Underwater Systems Center, New London, CT

SHOCK MEASUREMENT DURING BALLISTIC IMPACT INTO ARMORED VEHICLES
W. S. Walton, U.S. Army Aberdeen Proving Ground, Aberdeen Proving Ground, MD

AUTOMATIC DATA CHANNEL CALIBRATION AND NOISE IDENTIFICATION
E. E. Nesbit, Lawrence Livermore Laboratory, Livermore, CA

STATISTICAL ESTIMATION OF SIMULATED YIELD AND OVERPRESSURE
P. F. Mlakar and R. E. Walker, U.S. Army Engineer, Waterways Experiment Station, Vicksburg, MS

DYNAMIC MEASUREMENTS

AN ASSESSMENT OF THE COMMON CARRIER SHIPPING ENVIRONMENT
F. E. Ostrem, GARD, Inc., Niles, IL

SHOCK AND VIBRATION ENVIRONMENT IN A LIVESTOCK TRAILER
M. T. Turczyn, U.S. Department of Agriculture, Beltsville, MD, D. G. Stevens and T. H. Camp, U.S. Department of Agriculture, College Station, TX

SHOCK INDUCED IN MISSILES DURING TRUCK TRANSPORT
D. B. Meeker and J. A. Sears, Pacific Missile Test Center, Point Mugu, CA

DYNAMIC CHARACTERISTICS OF AN INDUCED-DRAFT FAN AND ITS FOUNDATION
S. P. Ying and E. E. Dennison, Gilbert/Commonwealth, Jackson, MI

VIBRATION AND ACOUSTICS

A METHOD TO DETERMINE REALISTIC RANDOM VIBRATION TEST LEVELS TAKING INTO ACCOUNT MECHANICAL IMPEDANCE DATA - PART 1: BASIC IDEAS AND THEORY
O. Sylwan, IFM Akustikbyran AB, Stockholm, Sweden

A METHOD TO DETERMINE REALISTIC RANDOM VIBRATION TEST LEVELS TAKING INTO ACCOUNT MECHANICAL IMPEDANCE DATA - PART 2: VERIFICATION TESTS
T. Hell, SAAB-SCANIA AB, Linkoping, Sweden

VIBRATION ANALYSIS OF A HELICOPTER PLUS AN EXTERNALLY-ATTACHED STRUCTURE
D. J. Ewins, Imperial College of Science and Technology, London, England, J. M. M. Silva, University of Lisbon, Portugal and G. Maleci, Nuovo Pignone, Florence, Italy

IMPROVING VIBRATION TECHNIQUES FOR DETECTING WORKMANSHIP DEFECTS IN ELECTRONIC EQUIPMENT
J. W. Burt and M. A. Condouris, U.S. Army Electronics Command, Fort Monmouth, NJ

SINGLE-POINT RANDOM AND MULTI-SHAKER SINE SPACECRAFT MODAL TESTING
M. Ferrante, C. V. Stahle and D. G. Breskman, General Electric Company, Space Division, King of Prussia, PA

BIAS ERRORS IN A RANDOM VIBRATION EXTREMAL CONTROL STRATEGY
D. O. Smallwood and D. L. Gregory, Sandia Laboratories, Albuquerque, NM

A NEW METHOD OF IMPROVING SPECTRA SHAPING IN REVERBERANT CHAMBERS
J. N. Scott, NASA Goddard Space Flight Center, Greenbelt, MD and R. L. Burkhardt, Northrop Services, Inc., NASA, Goddard Space Flight Center, Greenbelt, MD

THE VIBRATION TEST UNIT A UNIQUE RAIL VEHICLE VIBRATION TEST FACILITY
R. O. Coupland and A. J. Nintzel, Wyle Laboratories, Colorado Springs, CO

THE APPLICATION OF COMPUTERS TO DYNAMIC RAIL VEHICLE TESTING
B. Clark, Wyle Laboratories, Colorado Springs, CO

LOW FREQUENCY STRUCTURAL DYNAMICS OF THE SPACE SHUTTLE SOLID ROCKET BOOSTER MOTOR DURING STATIC TESTS
M. A. Behring and D. R. Mason, Thiokol Corporation/Wasatch Division, Brigham City, UT

VIBRATION ENVIRONMENT OF THE SPACE SHUTTLE SOLID ROCKET BOOSTER MOTOR DURING STATIC TESTS
D. R. Mason and M. A. Behring, Thiokol Corporation/Wasatch Division, Brigham City, UT

ELIMINATION OF A DISCRETE FREQUENCY ACOUSTICAL PHENOMENON ASSOCIATED WITH THE SPACE SHUTTLE MAIN ENGINE OXIDIZER VALVE-DUCT SYSTEM
L. A. Schutzenhofer, J. H. Jones, R. E. Jewell and R. S. Ryan, NASA, George C. Marshall Space Flight Center, Marshall Space Flight Center, AL

PAPERS APPEARING IN PART 4

DYNAMIC PROPERTIES OF MATERIALS

MATERIAL DAMPING AS A MEANS OF QUANTIFYING FATIGUE DAMAGE IN COMPOSITES
P. J. Torvik, Air Force Institute of Technology, Wright-Patterson AFB, OH and C. J. Bourne,
Air Force Flight Test Center, Edwards AFB, CA

SONIC FATIGUE TESTING OF THE NASA L-1011 COMPOSITE AILERON
J. Soovere, Lockheed-California Company, Burbank, CA

MODELING A TEMPERATURE SENSITIVE CONFINED CUSHIONING SYSTEM
V. P. Kobler, U.S. Army Missile Command, Huntsville, AL, R. M. Wyskida and J. D. Johannes,
The University of Alabama in Huntsville, Huntsville, AL

APPLICATIONS OF MATERIALS

PRELIMINARY HARDNESS EVALUATION PROCEDURE FOR IDENTIFYING SHOCK ISOLATION REQUIREMENTS
R. J. Bradshaw, Jr., U.S. Army Engineer Division, Huntsville, Huntsville, AL and P. N. Sonnenburg,
U. S. Army Construction Engineering Research Laboratory, Champaign, IL

AN APPLICATION OF TUNED MASS DAMPERS TO THE SUPPRESSION OF SEVERE VIBRATION IN THE ROOF OF AN AIRCRAFT ENGINE TEST CELL
J. L. Goldberg, N. H. Clark and B. H. Meldrum, CSIRO Division of Applied Physics, Sydney, Australia

COMPARISON OF ANALYTICAL AND EXPERIMENTAL RESULTS FOR A SEMI-ACTIVE VIBRATION ISOLATOR
E. J. Krasnicki, Lord Kinematics, Erie, PA

AN EXPERIMENTAL INVESTIGATION OF NOISE ATTENUATING TECHNIQUES FOR SPACE-SHUTTLE CANISTERS
L. Mirandy, General Electric Company, Philadelphia, PA, F. On and J. Scott, NASA Goddard
Space Flight Center, Greenbelt, Md

DYNAMIC INTEGRITY METHODS INCLUDING DAMPING FOR ELECTRONIC PACKAGES IN RANDOM VIBRATION
J. M. Medaglia, General Electric Company, Philadelphia, PA

AN OVERVIEW OF SHOCK ANALYSIS AND TESTING IN THE FEDERAL REPUBLIC OF GERMANY
K. -E. Meier-Dornberg, Institut fur Mechanik, Technische Hochschule Darmstadt,
Federal Republic of Germany

CONSERVATISM IN SHOCK ANALYSIS AND TESTING
T. L. Paez, The University of New Mexico, Albuquerque, NM

MEASUREMENT OF DYNAMIC STRUCTURAL CHARACTERISTICS OF MASSIVE BUILDINGS BY HIGH-LEVEL MULTIPULSE TECHNIQUES
D. G. Yates and F. B. Safford, Agbabian Associates, El Segundo, CA

CONSIDERATION OF AN OPTIMAL PROCEDURE FOR TESTING THE OPERABILITY OF EQUIPMENT UNDER SEISMIC DISTURBANCES
C. W. de Silva, Carnegie-Mellon University, Pittsburgh, PA, F. Loceff and K. M. Vashi,
Westinghouse Nuclear Energy Systems, Pittsburgh, PA

DYNAMIC LOADING OF METAL RIVETED JOINTS
R. L. Sierakowski, C. A. Ross, J. Hoover, University of Florida, Gainesville, FL and
W. S. Strickland, USAF Armament Lab, AFATL/DLYV Eglin AFB, FL

GENERALIZED GRAPHICAL SOLUTION FOR ESTIMATING RECOILLESS RIFLE BREECH BLAST OVERPRESSURES AND IMPULSES
P. S. Westine, G. J. Friesenhahn and J. P. Riegel, III, Southwest Research Institute, San Antonio, TX

PREDICTING THE MOTION OF FLYER PLATES DRIVEN BY LIGHT-INITIATED EXPLOSIVE FOR IMPULSE LOADING EXPERIMENTS
R. A. Benham, Sandia Laboratories, Albuquerque, NM

FRAGMENTS

SCALING OF INITIATION OF EXPLOSIVES BY FRAGMENT IMPACT
W. E. Baker, M. G. Whitney and V. B. Parr, Southwest Research Institute, San Antonio, TX

EQUATIONS FOR DETERMINING FRAGMENT PENETRATION AND PERFORATION AGAINST METALS
I. M. Gyllenspetz, National Defense Research Institute (FOA), Stockholm, Sweden

BREACHING OF STRUCTURAL STEEL PLATES USING EXPLOSIVE DISKS
D. L. Shirey, Sandia Laboratories, Albuquerque, NM

TITLES AND AUTHORS OF PAPERS PRESENTED IN THE SHORT DISCUSSION TOPICS SESSION

NOTE: These papers were only presented at the Symposium. They are not published in the Bulletin and are only listed here as a convenience.

DAMAGE EQUIVALENCE BETWEEN DISCRETELY APPLIED AND COMPLEX HARMONICS
J. J. Richardson, USAMICOM, Huntsville, AL

ON A UNIFIED THEORY OF VIBRATION CONTROL AND ISOLATION
P. W. Whaley, Air Force Institute of Technology, Wright-Patterson AFB, OH

THE VIBRATION OF WELDED PLATES
S. M. Dickinson and M. M. Kaldas, The University of Western Ontario, London, Ontario, Canada

SENSIBLE DISPLAY OF PSD INFORMATION
W. D. Everett, Pacific, Missile Test Center, Point Mugu, CA

RAIL SHIPMENT SHOCK SIMULATION ON A PEACEFUL NUCLEAR EXPLOSION INSTRUMENT VAN
R. O. Brooks, Sandia Laboratories, Albuquerque, NM

FREE FALL TESTING OF ARRESTMENT DEVICES FOR MAN CONVEYANCES IN MINE SHAFTS
F. A. Penning, Colorado School of Mines, Golden, CO, and E. H. Skinner, Spokane Mining Research Center, Spokane, WA

REVERSAL IN TIME DOMAIN EQUALS COMPLEX CONJUGATE IN FREQUENCY DOMAIN
A. J. Curtis, Hughes Aircraft Co., Culver City, CA

ELIMINATION OF INTERFERING ACOUSTIC STANDING WAVES IN A SONIC FATIGUE FACILITY
H. N. Bolton, McDonnel Douglas Corporation, Long Beach, CA

TEST VEHICLE CONFIGURATION EFFECTS ON VIBRO-ACOUSTIC TESTING
C. J. Beck, Jr., Boeing Aerospace Company, Seattle, WA

RANDOM VIBRATION CONCEPTS CLARIFIED
W. Tustin, Tustin Institute of Technology, Inc., Santa Barbara, CA

TRANSMISSION-LINE WIND-LOADING RESEARCH
R. C. Stroud, Synergistic Technology Inc., Cupertino, CA

A METHOD FOR MEASURING END LOAD IN A HOLLOW ROD USING STRAIN GAGE ORIENTATION TO CONCEL UNWANTED STRAIN OUTPUTS
J. Favour, Boeing Aerospace Company, Seattle, WA

CRITICAL ASPECTS OF FIXTURE DESIGN AND FABRICATION FOR 781C
D. V. Kimball, Kimball Industries, Inc., Monrovia, CA

DYNAMIC ANALYSIS

THE RELATIVE COMPLEXITIES OF PLATE AND SHELL VIBRATIONS

A.W. Leissa
Department of Engineering Mechanics
Ohio State University
Columbus, Ohio

The vibrations of plates and shells is a vast and complicated field. The main purpose of the present paper is to separate out the various complexities which can arise, and to identify those which typically exist in shell vibration problems that are not usually found in plates.

INTRODUCTION

Plates and shells are frequently occuring elements in structural applications. They typically exist in two forms:

1. As components of larger structures.
2. As representations of complete structures.

For dynamic loading situations it is important to know the results of free vibration studies in order to:

1. Avoid the resonant, natural frequencies.
2. Know the shapes (and associated stresses) of the modes excited in a forced vibration.
3. Have the normal modes (eigenfunctions) needed for a general, dynamic analysis.

A plate or shell is a structural element having an infinite number of degrees of freedom; that is, it is a continuous, rather than discrete, system having an infinite number of free vibration frequencies and mode shapes. However, in most applications it is usually sufficient to know the first (i.e., lowest) several frequencies and mode shapes.

A beam is also a continuous system having an infinite number of vibration frequencies and mode shapes. However, the problem is mathematically only one-dimensional, whereas plates ahd shells are two-dimensional. A thin membrane requires a two-dimensional model, but the order of the differential equations of motion (and the number of edge conditions) is only half as great as for the plate or shell having bending stiffness.

A vast literature exists for the field of plate and shell vibrations. Two monographs, sponsored by NASA [1,2], were written by the author a decade ago and were published by the U.S. Government Printing Office. The one dealing with plate vibrations included approximately 500 references; the second one had about 1000. Recent surveys [3,4] indicate that the literature of plate vibrations has more than doubled since then, while a few hundred more published papers, reports, theses, etc. have recently appeared involving free vibrations of shells.

For these reasons the subject of vibrations of plates and shells is a rather complex and confusing one. The purposes of the present paper are to:

1. Point out the types of complexities that arise.
2. Emphasize the complexities which typically exist in shell vibration problems that are usually not found for plates.

CLASSICAL PLATE VIBRATIONS

By a "plate" we mean a flat element having a thickness (h) which is much smaller than its length or width. Figure 1 shows a plate of arbitrary, curvilinear shape. The classical theory of thin plates is applicable for $h/a \leq 1/20$, where "a" is the smallest length dimension. If the plate is not flat, but has curvature, no matter how small, we will call it a "shell". Indeed, as we shall see later, a very small amount of curvature can cause significant changes

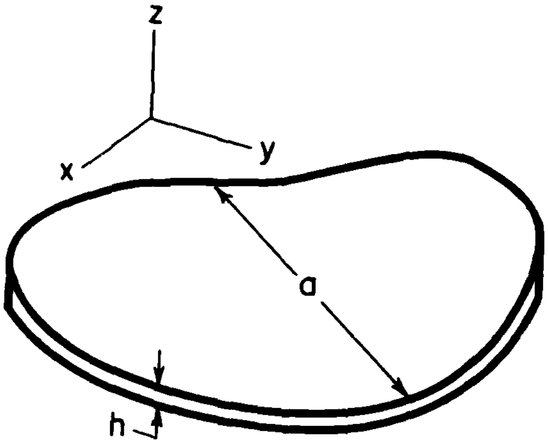

Figure 1. Plate of arbitrary shape

in the free vibration frequencies. We will consider only the transverse (z-direction) motions: that is, the bending vibration modes. The in-plane vibrations are at much higher frequencies for a thin plate. Only free, undamped vibrations will be taken up, and the plate material will be assumed to be isotropic, homogeneous, and linearly elastic. Finally, to avoid the endless complications of complex structures, stiffeners such as edge beams will not be included. These are the restrictions for problems addressed in the first 8 chapters of [1], for which hundreds of references exist, and will be called the "classical theory".

The classical theory of plate vibration is governed by the well-known differential equation of motion

$$D\nabla^4 w + \rho \frac{\partial^2 w}{\partial t^2} = 0 \qquad (1)$$

where $w = w(x,y,t)$ is the transverse displacement ρ is mass density per unit surface area of the plate, t is time, D is the flexural rigidity given by

$$D = \frac{Eh^3}{12(1-\nu^2)} \qquad (2)$$

E is the modulus of elasticity, h is again the thickness, ν is Poisson's ratio, and ∇^4 is the biharmonic differential operator given by

$$\nabla^4 = \nabla^2\nabla^2 = \left(\frac{\partial^2 w}{\partial x^2} + \frac{\partial^2 w}{\partial y^2}\right)^2 \qquad (3)$$

in rectangular coordinates. Alternately, the problem may be stated in terms of an energy formulation.

In addition, to completely determine the problem, the boundary (or edge) conditions must be given. There are three classical boundary conditions:

1. Clamped - zero deflection and zero normal slope.
2. Simply supported - zero deflection and zero normal bending moment.
3. Free - zero normal bending moment and zero normal shear (the Kirchhoff shear).

In this descriptive paper we will not bother with the well-known (cf. [1]) mathematical statements of the above boundary conditions. Suffice it to say that they involve w and derivatives of up to the third order in x and y. Elastic edge restraints (i.e., distributed translational and/or rotational springs) result in linear combinations of the deflections, slopes, moments and shears. Laura (cf., [5-6]) has solved a great variety of the latter problems.

Solutions to Eq.(1) are available in rectangular, polar and elliptical coordinates (cf., [1], Chapter 1), which permit some exact results for free vibration frequencies and mode shapes of plates of rectangular, circular and elliptical shape. Specifically, the following shapes have exact solutions:

1. Rectangular - solid, having two opposite sides simply supported (6 cases out of 21 possible ones).
2. Circular - solid and annular, all boundary conditions.
3. Elliptical - solid and annular, all boundary conditions.

Taking exact solutions to Eq. (1) and substituting them into the boundary conditions yields a frequency determinant, the roots of which are the nondimensional frequency parameters (eigenvalues). For an exact solution the determinant will be of finite size (indeed, no larger than fourth order). Substituting the eigenvalues back into the boundary condition equations yields the corresponding mode shapes (eigenfunctions).

Because the antisymmetric modes of the

above problems yield straight nodal lines (lines of zero deflection) of antisymmetry which duplicate simply supported boundary conditions, there are a few additional shapes having exact solutions, contained within those above. Examples are semicircles and semi-ellipses and other sectors of solid and annular circular and elliptical plates, and the isosceles right triangle.

But most classical plate vibration problems have no exact solutions. This is generally true for the great variety of other possible boundary shapes (e.g., parallelogram, trapezoidal, triangular, etc.) as well as the 15 other cases of rectangular plates not having two opposite sides simply supported. Other complications which generally prohibit obtaining exact solutions include:

1. Discontinuous boundary conditions (e.g., a straight edge which is clamped along one portion and either simply supported or free along the remainder).
2. Point supports - in the corners, along the edge, or internal.
3. Added mass (e.g., point masses representing accelerometers, equipment mounting).
4. Cutouts (and cracks) - internal or external (e.g., square plate with a round hole, saw cut).

Thus for most free vibration problems, even for classical theory, approximate solution methods must be used. By far, the most useful and popular methods are the Rayleigh-Ritz-Galerkin methods. The Rayleigh method [7,8] uses an assumed mode shape and calculates the corresponding natural frequency by setting the maximum potential energy in the vibration cycle equal to the maximum kinetic energy. The resultant frequency is too high, (i.e., an upper bound to the true frequency) due to the modal constraints introduced by the non-exact assumed mode shape. The Ritz method [9,10] improves upon the Rayleigh procedure by allowing more than a single deflection function, and choosing the best "mix" of the deflection functions by a minimizing process. The Galerkin method [11] appears to be quite different than the other two - indeed, it is a weighted residual rather than a stationary functional method - but, a transformation shows that it is completely equivalent to the other two for the free vibration eigenvalue problem if used correctly. Other approximate methods used frequently on plate vibration problems include: Point matching, finite elements, finite differences and various rather difficult methods for obtaining lower bounds to frequencies.

But in spite of the complexities mentioned above, and the lack of exact solutions, the solution of classical plate vibration problems is relatively straightforward. Typical solutions yield nondimensional frequency parameters of the form

$$\lambda = \omega a^2 \sqrt{\rho / D} \qquad (4)$$

where a is some characteristic length of the plate. It is found that λ depends upon at most only two types of parameters. One is Poisson's ratio (ν). This enters the problem explicitly through the boundary conditions, in cases having one or more free straight edges or one or more simply supported or free curvilinear edges. Thus, for a clamped circular plate or a simply supported rectangular plate, λ does not depend upon ν. But, inasmuch as D depends upon ν (viz., Eq. (2)), ω itself always depends upon ν.

The other parameters of the problem are those needed to define the boundary shape. For a rectangular or annular circular plate, for example, a single a/b ratio is sufficient, where for the first case it represents the length-to-width ratio and for the second case it is inner radius to outer radius. Less regular shapes require more nondimensional geometric parameters. For example, the cantilevered triangle in Figure 2 requires a/b and the skew ratio c/b.

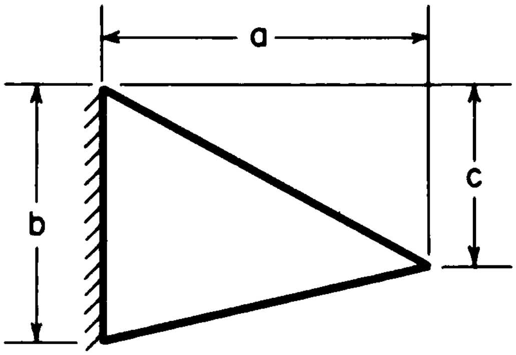

Figure 2. Skew cantilevered plate.

COMPLEXITIES IN PLATE THEORY

Anisotropic plates require more elastic constants to be defined. In the most general case the flexural regidity constant given by Eq. (2) is replaced by five independent rigidity constants, and Eq. (1) must be expanded to

$$D_1 \frac{\partial^4 w}{\partial x^4} + D_2 \frac{\partial^4 w}{\partial x^3 \partial y} + D_3 \frac{\partial^4 w}{\partial x^2 \partial y^2} + D_4 \frac{\partial^4 w}{\partial x \partial y^3} + D_5 \frac{\partial^4 w}{\partial y^4} + \rho \frac{\partial^2 w}{\partial t^2} = 0 \qquad (5)$$

in rectangular coordinates. For an orthotropic plate a more simple form is sufficient:

$$D_x \frac{\partial^4 w}{\partial x^4} + 2 D_{xy} \frac{\partial^4 w}{\partial x^2 \partial y^2} + D_y \frac{\partial^4 w}{\partial y^4} + \rho \frac{\partial^2 w}{\partial t^2} = 0 \qquad (6)$$

Similar equations can be written for plates made of materials having curvilinear orthotropy (e.g., polar orthotropy).

Equation (5) has, in general, no exact solution. However, Eq. (6) can be solved in the same manner as Eq. (1), and yields exact solutions to the same six problems as for an isotropic plate (i.e., two opposite edges simply supported).

Consider next a plate subjected to inplane forces. In general, the boundary of the plate can be subjected to inplane, distributed tensile or compressive forces N_x and N_y per unit length, and an inplane shearing force, N_{xy}, per unit length in, for example, rectangular coordinates. A simply supported rectangular plate having uniform (i.e., constant) inplane forces is shown in Figure 3. Or inplane forces can be caused by internal body or residual stresses. These initially applied forces are all assumed to be static. The effect of inplane forces upon the mathematical problem is to replace zero on the right-hand-sides of Eqs. (1), (5) and (6) by

$$N_x \frac{\partial^2 w}{\partial x^2} + 2 N_{xy} \frac{\partial^2 w}{\partial x \partial y} + N_y \frac{\partial^2 w}{\partial y^2} \qquad (7)$$

where N_x, N_y and N_{xy} denote the positive (tensile) inplane forces per unit length observed at a typical point (x, y) within the plate and, generally, are functions of x and y.

In the special case when N_x and N_y are constant everywhere within the plate, and $N_{xy} = 0$, Eq. (7) has an exact solution which, again, corresponds to the rectangular plate having two opposite sides simply supported. But many important practical cases arise where the above assumptions can be made as, for example, the transverse vibrations of a missile fin subjected to large acceleration in its plane [12].

For variable thickness plates the flexural rigidity, D, is no longer a constant and, consequently, neither is h. Thus, for example Eq. (1) generalizes to

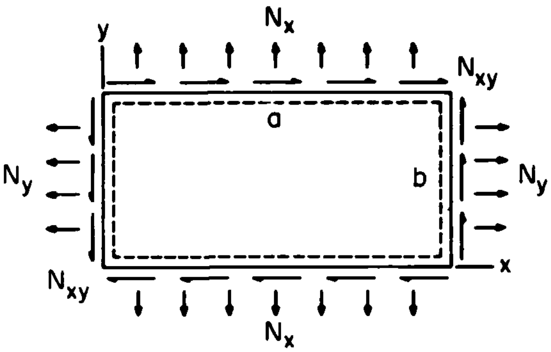

Figure 3. Simply supported rectangular plate having uniform inplane forces.

$$\nabla^2 (D \nabla^2 w) - (1-\nu)\left(\frac{\partial^2 D}{\partial y^2} \frac{\partial^2 w}{\partial x^2} - 2 \frac{\partial^2 D}{\partial x \partial y} \frac{\partial^2 w}{\partial x \partial y} + \frac{\partial^2 D}{\partial x^2} \frac{\partial^2 w}{\partial y^2} \right) + \rho \frac{\partial^2 w}{\partial t^2} = 0 \qquad (8)$$

where $\rho = \rho(x, y)$. This equation has variable coefficients and has no exact solution, although the Rayleigh-Ritz-Galerkin methods are essentially no more difficult to apply. An amazing number of publications have been recently devoted to this problem - at least 24 in the last three years [4].

The effects of surrounding media are significant in two very important ways:

1. Almost all theoretical results are for plates vibrating in a vacuum, whereas almost all experimental results are in air.
2. Surrounding liquids, such as water, cause drastic decreases from the natural frequencies calculated in a vacuum.

The decrease in frequency is, of course, mainly due to the necessity of moving additional mass, and not due to damping. Even the presence of air at atmospheric pressure will often reduce the frequencies by 5-10 percent (see [1], p. 302). Investigators are sometimes unaware of this and attempt to give unwarranted justification for the differences between their relatively close theoretical and experimental results.

Large deflections change the plate vibration problem to be a nonlinear one. This can take place in at least three ways:

1. Sufficiently large strains to require nonlinear stress-strain equations.

2. Large slopes in the deflected surfaces, so that the usual assumptions of replacing $\sin\theta$ by $\tan\theta$ and $\cos\theta$ by unity are no longer valid.

3. Inplane membrane forces generated by the transverse motion of the plate.

The latter phenomenon can easily occur to significant degree in plate vibrations and is a "hard spring" type of nonlinearity: that is, the frequency increases with the amplitude of vibration. Indeed, an amplitude on the order of the plate thickness will typically increase the frequency by about 30 percent if the edges are restrained against inplane motion. This phenomenon is therefore easily the source of much experimental error. Analytical results are often obtained by the Galerkin method, using an assumed mode shape. Reflecting the current interest in solving nonlinear problems, at least 72 references can be found in the last seven years dealing with this type of problem [3,4].

In 1877 Lord Rayleigh [7] showed how the addition of "rotatory" (in the language of his day) inertia effects to those of classical translational inertia affected the flexural vibration frequencies of beams. Timoshenko [13] in 1921 showed that the effects of shear deformation, previously disregarded, are at least equally important. The effects of including either rotary inertia or shear deformation are to decrease the frequencies from those calculated by classical theory, and are especially significant for relatively thick ($h/a > 1/20$) plates, as well as beams. The first consistent, dynamic, thick plate theories were presented by Uflyand [14] and Mindlin [15] and the latter is widely used today. The resulting plate theories are sixth order systems of differential equations, requiring the specification of three boundary conditions per edge.

Examples of nonhomogeneous plates include the following:

1. Material heterogeneity varying concontinuously (e.g., $E = E(x,y,z)$) due to varying density (e.g., styrofoam, rubber) or large temperature gradients.

2. Layered (or sandwich) plates.

Of particular importance today in the latter category are laminated plates made of composite materials. The equations of motion for such plates do not always permit uncoupling of the inplane and transverse vibration modes, and the resulting vibration frequencies can be significantly lower than those predicted by an "equivalent orthotropic theory" [16].

SHELL VIBRATIONS

A shell, like a plate, is also a three-dimensional body which, for the sake of reducing the formidable complexity of the problem, is replaced by a two-dimensional problem. All deformations are then characterized by displacements of the middle surface, as contrasted with the midplane for a plate. A typical, open shell, having thickness h, is shown in Figure 4. Radii of curvature, R_1 and R_2 in two orthogonal directions are also shown. It should be noted that R_1 and R_2 are generally not equal, not constant, and not even sufficient to define the middle surface, unless they are principal curvatures.

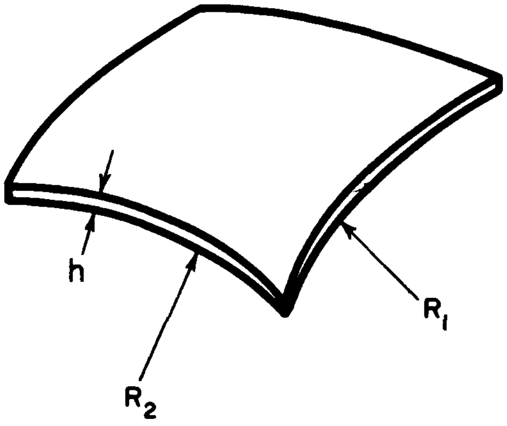

Figure 4. A shell having arbitrary curvatures.

Conversely, a plate is a special case of a shell when $R_1 = R_2 = \infty$ at all points, in all directions. Therefore, all of the complexities which exist for plates and are discussed on the previous pages also exist for shells. That is, for example, shells can have irregular shaped boundaries, discontinuous boundary conditions, point supports, cutouts, orthotropic material, variable thickness, shear deformation and rotary inertia, and so on, for all types of curvatures. But shell vibration analysis (and experiment) is considerably more complex than for plates for the following reasons:

1. Curvature specification.

2. Bending and stretching of the middle surface are coupled.

3. An eighth order system of differential equations of motion (without shear deformation).

4. Four boundary conditions required per edge.

5. Three times as many shell frequencies as plate frequencies.

6. No universally accepted set of equations which comprises the classical theory.

7. Additional geometric parameters to be specified.

8. The nondimensional frequency parameters are always functions of Poisson's ratio.

9. Mode shapes of the lowest natural frequencies are seldom obvious.

10. Test specimens are more difficult to fabricate.

11. Experimental fixtures and measurement methods are more complex.

Curvature specification is by itself a minor complexity. It is merely a matter of defining the shell in question. The added complexity arises from the vast number of important curvatures which are of interest. A practical list must necessarily include:

1. Circular cylindrical.
2. Elliptical, oval and other noncircular cylindrical.
3. Conical.
4. Spherical.
5. Ellipsoidal (or spheroidal).
6. Toroidal.
7. Paraboloidal, hyperboloidal, ogival and other shells of revolution.
8. Hyperbolic-paraboloidal
9. Others.

The last category is inevitable, no matter how long the list.

That the bending and stretching of the middle surface of a shell are (almost always) coupled is no doubt the most significant difference between a typical shell and a flat plate. Indeed, in the usual case, the membrane forces caused by the stretching result in considerable stiffening and, hence, increased frequencies. The enormous increase in the fundamental vibration frequency of a simply supported square panel due to the presence of a small amount of curvature was demonstrated in [17] (see Table 2, p. 182).

The coupling between bending and stretching also requires that the equations of motion, when shear deformation is neglected, are of the eighth order. That is, the transverse and tangential motions do not uncouple as they do for a typical plate. Consider, for example, a circular cylindrical shell, as shown in Figure 5. The three independent components of displacement are u, v (tangential) and w (transverse). The two-dimensional problem is stated in terms of the x (axial) and θ (circumferential) coordinates. The widely-used Donnell-Mushtari equations of motion can be written in matrix form as

$$\begin{bmatrix} \mathcal{L}_{11} & \mathcal{L}_{12} & \mathcal{L}_{13} \\ \mathcal{L}_{21} & \mathcal{L}_{22} & \mathcal{L}_{23} \\ \mathcal{L}_{31} & \mathcal{L}_{32} & \mathcal{L}_{33} \end{bmatrix} \begin{bmatrix} u \\ v \\ w \end{bmatrix} = \begin{bmatrix} 0 \\ 0 \\ 0 \end{bmatrix} \tag{9}$$

where the $\mathcal{L}_{ij}$ are differential operators given by

$$\begin{aligned}
\mathcal{L}_{11} &= \frac{\partial^2}{\partial s^2} + \frac{(1-\nu)}{2}\frac{\partial^2}{\partial\theta^2} - \rho\frac{(1-\nu^2)R^2}{E}\frac{\partial^2}{\partial t^2} \\
\mathcal{L}_{22} &= \frac{(1-\nu)}{2}\frac{\partial^2}{\partial s^2} + \frac{\partial^2}{\partial\theta^2} - \rho\frac{(1-\nu^2)R^2}{E}\frac{\partial^2}{\partial t^2} \\
\mathcal{L}_{33} &= 1 + k\nabla^4 w + \rho\frac{(1-\nu^2)R^2}{E}\frac{\partial^2}{\partial t^2} \\
\mathcal{L}_{12} &= \mathcal{L}_{21} = \frac{(1+\nu)}{2}\frac{\partial^2}{\partial s\,\partial\theta} \\
\mathcal{L}_{13} &= \mathcal{L}_{31} = \nu\frac{\partial}{\partial s} \\
\mathcal{L}_{23} &= \mathcal{L}_{32} = \frac{\partial}{\partial\theta}
\end{aligned} \tag{10}$$

where $s = x/R$ and $k = h^2/12R^2$. Just how much more complex these equations are than the one for a plate, Eq. (1), can be seen by looking at the operator $\mathcal{L}_{33}$ in Eqs. (10), which contains Eq. (1) in its last two terms. And these particular equations of motion are often used because they are the most simple form available including both bending and stretching effects. Consideration of shear deformation results in a 10th order system of equations, an order not frequently found in the broad scope of mathematical physics.

An eighth order system of equations requires the statement of four boundary conditions along each edge. Two of these are associated with the transverse constraints (as in plate bending) and two with the tangential constraints (as in plate stretching). The statements of these conditions is not particularly difficult. Complexity arises, rather, from the large number of possible combinations of them. For example, a closed circular cylindrical shell, as shown in Figure 5, has 136 pos-

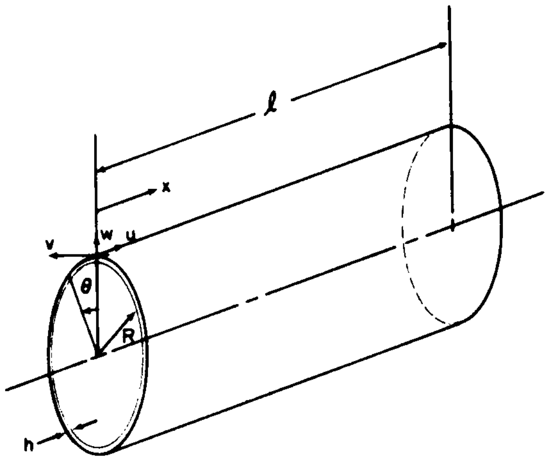

Figure 5. Closed circular cylindrical shell and coordinate system.

sible combinations of "simple" boundary conditions along its two boundaries, $x = 0$ and $x = \ell$!

Because of the aforementioned coupling, the transverse displacement w remains coupled with the tangential displacements, u and v. Free vibration eigenvalue problems therefore result in, typically, cubic equations in a nondimensional frequency parameter (λ), rather than linear frequency equations as for plates. The cubic equations yield three real roots for λ. For a thin, circular cylindrical shell the smallest (lowest frequency) root will usually correspond to a predominantly (but not purely) flexural mode, while the other two frequencies will correspond to predominantly stretching modes of vibration.

Equation (1) is universally accepted as the governing, classical equation of motion for a thin plate. Unfortunately, a similar statement cannot be made for thin shells. A study of this situation (see [2], Ch. 1 and 2) turned up at least 20 independent works by academicians, yielding equations of motion. Careful comparison showed that about half of them were completely equivalent to those of others. For circular cylindrical shells, for example, it was shown that ([2], pp. 32-34) each independent set of equations of motion can be written as

$$[\mathcal{L}]\{u_i\} = \{0\} \qquad (11)$$

where $\{u_i\}$ is the vector displacement components, u, v and w, as in the format of Eq. (9). Furthermore, $[\mathcal{L}]$ can be written for each "theory" as

$$[\mathcal{L}] = [\mathcal{L}_{D\text{-}M}] + k[\mathcal{L}_{MOD}] \qquad (12)$$

where $[\mathcal{L}_{D\text{-}M}]$ is the differential operator according to the Donnell-Mushtari theory, the elements of which were given in Eqs. (10), and $[\mathcal{L}_{MOD}]$ is a "modifying" operator to be added for the appropriate theory. What is interesting is that each element of $[\mathcal{L}_{MOD}]$ is multiplied by the thickness parameter, $k = h^2/12R^2$, a term which appeared in only $\mathcal{L}_{3j}$ (see Eqs. (10)) of $[\mathcal{L}_{D\text{-}M}]$, and that k is an extremely small number for ordinary, thin shells.

The latter fact has led some authors to believe that frequencies obtained from all thin shell theories are, for practical purposes, the same. A careful study performed in [1], pp. 44-61, shows that this is far from the case. Indeed, the widely-used Donnell-Mushtari theory itself is highly inaccurate in determining frequencies of some modes of shell vibration. Similar demonstration was provided earlier in the excellent work of Forsberg [18,19].

The complexity of the equations of motion has led to further simplications, in the attempt to obtain more tractable solutions. Among these are:

1. Membrane theory - a fourth order theory neglecting bending stiffness.
2. Inextensional theory - a fourth order theory neglecting stretching stiffness.
3. Neglecting tangential inertia terms.
4. Neglecting terms containing k^2 and k^3 in the characteristic equations.

and many others of a nature similar to the last one. Unfortunately, each type of simplification can result in very large errors in some types of problems.

For a flat rectangular panel (i.e., a plate) simply supported along all four edges, the frequency parameters depend upon only the aspect ratio, a/b. For a cylindrically curved panel they depend upon two additional geometric parameters (say h/R and a/R) as well as Poisson's ratio, explicitly. Thus, a careful, parametric study for the shell panel is considerably more involved.

Again, as a relatively simple problem, consider the closed, circular cylindrical shell shown in Figure 5. Let the ends be supported by shear diaphragms (also called "freely supported" or "simply supported" elsewhere in the literature), which is a generalization of simply supported edge conditions for a plate. For this problem, a simple exact solution for the frequencies and mode shapes can be found (cf., [1], ch. 2). It is found that the displacements take the form

$$
\begin{aligned}
u &= A \cos \alpha_m x \cos n\theta \cos \omega t \\
v &= B \sin \alpha_m x \sin n\theta \cos \omega t \qquad (13) \\
w &= C \sin \alpha_m x \cos n\theta \cos \omega t
\end{aligned}
$$

where $\alpha_m = m\pi/\ell$ and m and n are integers. The resultant mode shapes can be identified by the number of axial half-waves (m) and the number of circumferential waves (n). Typical nodal patterns (meaning, lines of $w = 0$) are depicted in Figure 6.

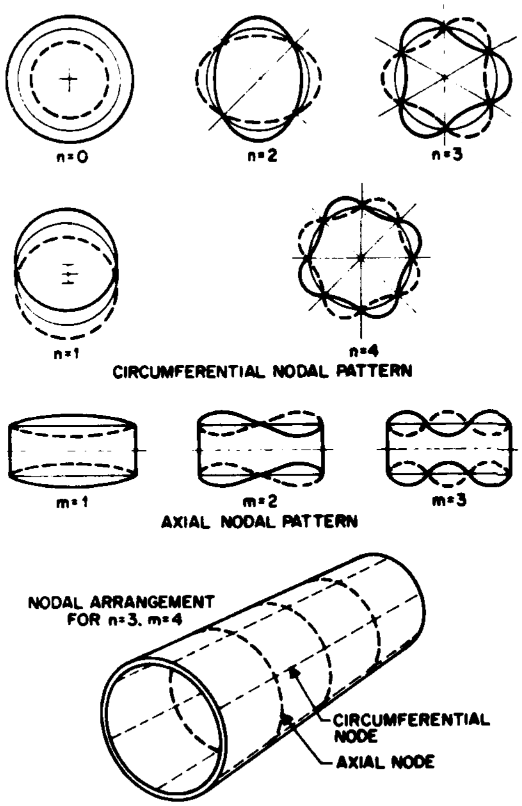

Figure 6. Nodal patterns for circular cylindrical shells supported at both ends by shear diaphragms.

One important question is: " Of all the possible combinations of m and n, which gives the lowest frequency?" For m, the answer is simple: $m = 1$. Suppose we say further that the shell has parameters $h/R = 1/50$ and $\ell/R = 5$, a shell of moderate thickness and length. The exact solution from above yields a lowest frequency parameter $\omega R\sqrt{\rho(1-\nu^2)/E}$ of about 0.6 , for $n = 3$ (see [2], Figure 2.15). That is, the fundamental mode has three circumferential waves. The first eight frequencies, and their associated m and n, are listed below, in order:

1. $m = 1, n = 3$
2. $m = 1, n = 2$
3. $m = 1, n = 4$
4. $m = 2, n = 4$
5. $m = 2, n = 3$
6. $m = 1, n = 5$
7. $m = 1, n = 1$
8. $m = 1, n = 6$

with the eighth frequency being only about three times as high as the first. We note that the "beam binding mode" ($n = 1$) has only the seventh lowest frequency, and that two of the lower ones have even two axial half-waves in their mode shapes. There are literally dozens of frequencies lower than that of the first "breathing mode" ($n = 0$). Thus, the prediction of the mode shape for the lowest, or any other, mode is not at all obvious.

Finally, anyone can cut out a flat plate specimen from a piece of sheet metal. However, fabricating most types of shells accurately is a much more difficult task. And finding the resonances experimentally requires more complicated equipment; for example, how does one keep sand patterns on a shell?!

REFERENCES

1. A.W. Leissa, Vibration of Plates, NASA SP-160, U.S. Govt. Printing Office (1969).

2. A.W. Leissa, Vibration of Shells, NASA SP-288, U.S. Govt. Printing Office (1973).

3. A.W. Leissa, "Recent Research in Plate Vibrations. 1973-1976", Shock and Vib. Digest.
   Part 1. "Classical Theory", vol. 9, No. 10, pp. 13-24, October, 1977.
   Part 2. "Complicating Effects", vol. 10, No. 12, pp. 21-35, December, 1978.

4. Class notes; Short course in "Vibrations of Beams, Plates and Shells", Ohio State University, Dept. of Engineering Mechanics, Sept. 10-14, 1979.

5. P.A.A. Laura, L.E. Luisoni and G. Ficcadenti, "On the Effect of Different Edge Flexibility Coefficients on Transverse Vibrations of Thin, Rectangular Plates", J. Sound Vib., vol. 57, No. 3, pp. 333-340, 1978.

6. P.A.A. Laura and R. Grossi, "Transverse

Vibration of a Rectangular Plate Elastically Restrained Against Rotation Along Three Edges and Free on the Fourth Edge", J. Sound Vib., vol. 59, no. 3, pp. 355-368, 1978.

7. Lord Rayleigh, Theory of Sound, vol. 1. Dover Pub., 1945 (originally published in 1877).

8. G.B. Warburton, "The Vibration of Rectangular Plates", Proc. Inst. Mech. Eng., Ser. A., vol. 168, no. 12, pp. 371-384, 1954.

9. W. Ritz, "Theorie der Transversalschwingungen, einer quadratische Platte mit freien Rändern", Ann. Physik, Bd. 28, pp. 737-786, 1909.

10. D. Young, "Vibration of Rectangular Plates by the Ritz Method", J. Appl. Mech., vol. 17, no. 4, pp. 448-453, 1950.

11. B.G. Galerkin, Vestnik Inzhenerov, pp. 897-908, 1915.

12. D.A. Simons and A.W. Leissa, "Vibrations of Rectangular Plates Subjected to In-Plane Acceleration Loads", J. Sound Vib., vol. 17, no. 3, pp. 407-422 (1971).

13. S. Timoshenko, "On the Correction for Shear of the Differential Equations for Transverse Vibrations of Prismatic Bars", Phil. Mag., Ser. 6, vol. 41, p. 742, 1921.

14. Y.S. Uflyand, " The Propagation of Waves in the Transverse Vibrations of Bars and Plates" (in Russian), Akad. Nauk. SSSR, Prik. Mat. Mech., vol. 12, pp. 287-300, 1948.

15. R.D. Mindlin, "Influence of Rotatory Inertia and Shear on Flexural Motions of Isotropic, Elastic Plates", J. Appl. Mech., vol. 18, no. 1, pp. 31-38, 1951.

16. J.M. Whitney and A.W. Leissa, "Analysis of Heterogeneous Anisotropic Plates", J. Appl. Mech., vol. 36, no. 2, pp. 261-267, 1969.

17. A.W. Leissa and A.S. Kadi, "Curvature Effects on Shallow Shell Vibrations", J. Sound Vib., vol. 16, no. 2, pp. 173-187, 1971.

18. K. Forsberg, "A Review of Analytical Methods Used to Determine the Modal Characteristics of Cylindrical Shells", NASA CR-613, 1966.

19. K. Forsberg, "Influence of Boundary Conditions on the Modal Characteristics of Thin Cylindrical Shells", AIAA J., vol 2, no. 12, pp. 2150-2157, 1964.

IN-FLUID CYLINDRICAL BEAM VIBRATION WITH MULTI-DEGREE OF FREEDOM ABSORBERS

B. E. SANDMAN AND J. S. GRIFFIN
NAVAL UNDERWATER SYSTEMS CENTER
NEWPORT, RI 02840

The title investigation considers the theoretical study of the effects of vibration absorbers with two-point attachments and possessing both translation and rotational degrees of freedom. In particular, the analysis considers and demonstrates the dual tuning of rocking and translating absorber resonances to produce attenuation of two low-order beam mode resonances. Cantilevered and free-free hollow Timoshenko beam configurations are utilized as the basis for the presentation of results. The location of attachment points and the effect of fluid loading induced by the motion of the beam in a heavy fluid medium such as water are shown to be significant factors in terms of absorber optimization. The method of analysis can be directly applied to consider all types of boundary conditions for the beam. The immediate extension to the study of cylindrical shells containing numerous attachments of internal components and arbitrary boundary conditions can be achieved without severe modifications of the procedures.

INTRODUCTION

Vibration control of fluid-loaded structures is an area of considerable importance in marine, submarine, and reactor engineering. The ability to describe, analyze, and predict the dynamic characteristics of submerged structures is essential to determine the mechanisms for optimum vibration control. A generalized method for the analysis of fluid-loaded structural vibration is presented and documented in Ref. [1]. The theoretical approach utilizes a complete set of orthogonal functions as the basis for representation of both fluid and structure frequency response characteristics. Thus, the mobilities and impedances are established in terms of the elements of complex matrices. Subsequently, the solution for the coupled response of fluid and structure is obtained by methods of matrix algebra. The current investigation considers the modification and extension of this methodology to the study of the performance of multi-degree of freedom absorbers when attached to a submerged hollow cylindrical beam with contilevered and free-free boundary conditions. Examples of approximate multi-mode absorber tuning are presented.

Numerous authors [2-7] have considered the effects of attached masses and single degree of freedom absorbers upon the in-vacuo vibration of structures. The effects of a single rigidly attached mass upon the in-fluid vibration and sound radiation of a flat plate was studied in Ref. [8]. This paper exemplifies the feasibility of tuning a two-point attached absorber system with rocking and translational degrees of freedom to produce attenuation of two in-fluid resonant beam modes. Cantilevered and free-free hollow cylindrical beams are utilized as the basic configurations for the investigation. The numerical results presented show a marked dependence of tuning upon the induced fluid loading and the locations of absorber attachment points. The illustrated findings have direct application to the design of mounts for internal components in slender submerged bodies where vibration control is a fundamental objective. In the following, a theoretical discussion of the fluid-structure interaction problem is given and the mathematical considerations required for the attachment of the absorber system is discussed.

I. FLUID-BEAM INTERACTION AND DYNAMIC ABSORPTION

For the formulation of the title problem consider a *finite* length hollow cylindrical beam submerged in-fluid and supporting in an evacuated interior a dimensional mass with a two-point spring absorber attachment system as shown in Fig. 1. For the purpose of characterizing the system the temporal input and response is assumed to be steady state and harmonic. For the analytical approach the spatial characteristics of the complex frequency response for each component of the fluid, beam, and absorber system are defined on a common basis of orthogonal functions with the Fourier coefficients representing the generalized coordinates. The coupling of the components of the system and the solution for the combined response is then obtained by the methods of matrix analysis.

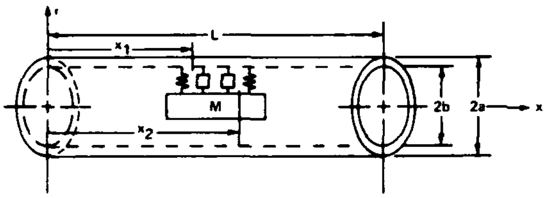

Figure 1. Submerged Configuration of Beam and Attached Mass

a. Fluid Impedance - For the flexural vibration of a slender beam it may be assumed that the axial interaction of the beam with the fluid is a negligible effect. Thus, for the purpose of simplification the beam is considered to be embodied by two semi-infinite rigid cylinders for $x \epsilon (-\infty, 0)$ and $x \epsilon (L, +\infty)$. The fluid field surrounding the cylindrical beam and baffles of radius $r = a$ is described by the cylindrical wave equation in terms of the velocity potential $\tilde{\phi}$

$$\nabla^2\tilde{\phi} + k^2\tilde{\phi} = 0 \; ; \; r > a \qquad (1)$$

where $k = \omega/c_f$ and c_f is the speed of sound in the fluid. The corresponding acoustic pressure is given by $\tilde{P}_f = -(i\omega)\rho_f\tilde{\phi}$. For the motion of a beam between $x = o$ and $x = L$ the normal velocity on the surface $r = a$ may be described by

$$\left(\frac{\partial\tilde{\phi}}{\partial r}\right)_{r=a} = \begin{cases} \sum_{m=o}^{\infty} \tilde{v}_m \cos k_m x \cos\theta & ; \; o \leq x \leq L \\ 0 & ; \; x < o, x > L \end{cases} \qquad (2)$$

with $k_m = m\pi/L$. It is noted that the functions $\cos k_m x$ are orthogonal over the length of the beam and the expression in equation (2) represents the beam motion in terms of the generalized velocities, $\tilde{v}_m$. Utilizing the methods of Fourier integral transforms the solution

$$\tilde{\phi} = \frac{1}{2\pi} \left\{ \sum_{m=o}^{\infty} \tilde{v}_m \int_{-\infty}^{\infty} \frac{H_1(ur)}{uH_1'(ua)} \Psi_m(\alpha)\exp(-i\alpha x)d\alpha \right\} \cos\theta \qquad (3)$$

is established [9] where H_1 is the first-order Hankel function of the second kind and $u^2 = k^2-\alpha^2$. The function

$$\Psi_m(\alpha) = \frac{(i\alpha)\left[(-1)^m\exp(i\alpha L)-1\right]}{k_m^2-\alpha^2}$$

arises from the Fourier integral transform of $\cos k_m x$; $o \leq x \leq L$ with α being the Kernel variable. The net force acting on the beam per unit length is given by the integral of the pressure at $r = a$

$$\tilde{f}(x) = -(i\omega)\rho_f a \int_o^{2\pi} (\tilde{\phi})_{r=a} \cos\theta d\theta \qquad (4)$$

By implementing the series

$$\tilde{f}(x) = \tilde{f}_o/2 + \sum_{n=1}^{\infty} \tilde{f}_n \cos k_n x$$
$$\tilde{f}_n = \frac{2}{L}\int_o^L \tilde{f}(x)\cos k_n x dx \qquad (5)$$

as a generalized representation of this force, it is determined that

$$\{\tilde{f}_n\} = \rho_f c_f a (Z_{nm}^f)\{\tilde{v}_m\} \qquad (6)$$

represents the relationship between the generalized forces and velocities for the fluid. The integral

$$Z_{nm}^f = -\frac{(ik)}{L}\int_o^{\infty}\left[\bar{\Psi}_n\Psi_m + \Psi_n\bar{\Psi}_m\right]\frac{H_1(ua)}{uH_1'(ua)}\,d\alpha \qquad (7)$$

provides the definition for the elements of the fluid impedance matrix. A detailed discussion of the numerical evaluation of equation (7) is presented in Ref. [9].

b. Two-Point Mass Coupling Impedance - For a mass having a two-point attachment configuration as shown in Figure 2 it is determined that

$$\tilde{g}_1 + \tilde{g}_2 = M\omega^2\tilde{y}_G \qquad (8a)$$

$$\tilde{g}_1 - \tilde{g}_2 = \frac{I_G\omega^2}{d}\tilde{\theta} \qquad (8b)$$

are the equations governing steady state dynamic equilibrium at the frequency ω of harmonic oscillation where $\tilde{g}_1$ and $\tilde{g}_2$ are the forces acting at the attachment points x_1 and x_2, respectively.

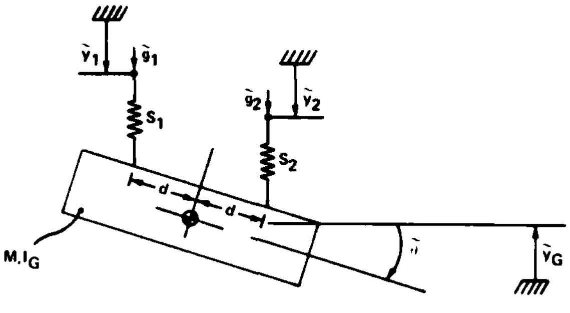

Figure 2. Displaced Configuration of Mass Attachment

From kinematics and the force-displacement relations for the linear springs the relationships

$$\tilde{g}_1 = S_1(\tilde{y}_1 + \tilde{y}_G + d\Theta) \quad (9a)$$

$$\tilde{g}_2 = S_2(\tilde{y}_2 + \tilde{y}_G - d\tilde{\Theta}) \quad (9b)$$

are established with $\tilde{y}_1$ and $\tilde{y}_2$ denoting the attachment point displacements. The simultaneous solution of equations (8) and (9) for the mass displacement $\tilde{y}_G$ and mass rotation $d\tilde{\Theta}$ yields the result

$$\begin{aligned}\tilde{y}_G = \ & [(\beta^2\omega^2 - \omega_2^2)\omega_1^2\tilde{y}_1 \\ & + (\beta^2\omega^2 - \omega_1^2)\omega_2^2\tilde{y}_2]/D(\omega)\end{aligned} \quad (10a)$$

$$\begin{aligned}d\tilde{\Theta} = \ & [(\omega^2 - \omega_2^2)\omega_1^2\tilde{y}_1 \\ & - (\omega^2 - \omega_1^2)\omega_2^2\tilde{y}_2]/D(\omega)\end{aligned} \quad (10b)$$

where

$$\begin{aligned}D(\omega) = \ & (\omega^2 - \omega_1^2)(\beta^2\omega^2 - \omega_2^2) \\ & + (\omega^2 - \omega_2^2)(\beta^2\omega^2 - \omega_1^2\end{aligned}$$

$$\beta^2 = I_G/Md^2 \ ; \ \omega_1^2 = 2S_1/M \ ; \ \omega_2^2 = 2S_2/M$$

The load distribution imparted to the beam by attachment of the spring-mass system at x = x_1 and x = x_2 may be written in the form

$$\begin{aligned}\tilde{G}(x) = \ & \frac{\tilde{g}_1+\tilde{g}_2}{2}[\delta(x - x_1) + \delta(x - x_2)] \\ & + \frac{\tilde{g}_1-\tilde{g}_2}{2}[\delta(x - x_1) - \delta(x - x_2)]\end{aligned} \quad (11)$$

where $\delta(x)$ denotes the Dirac delta function. The Fourier components of this load are obtained from the integral

$$\tilde{G}_n = \frac{2}{L}\int_o^L \tilde{G}(x)\cos k_n x dx \quad (12a)$$

where

$$\tilde{G}(x) = \tilde{G}_o/2 + \sum_{n=1}^{\infty}\tilde{G}_n \cos k_n x \quad (12b)$$

provides the series representation of the distribution function. The substitution of equations (8) and (11) into equation (12a) yields

$$\begin{aligned}\tilde{G}_n = \frac{M\omega^2}{L}\{ & [\cos k_n x_1 + \cos k_n x_2]\tilde{y}_G \\ & + \beta^2[\cos k_n x_1 - \cos k_n x_2]d\tilde{\Theta}\}\end{aligned} \quad (13a)$$

Since, we chose to write

$$\tilde{y}(x) = \sum_{m=o}^{\infty}\tilde{w}_m \cos k_m x \ ; \ o \le x \le L \quad (13b)$$

and $\tilde{y}_1 = \tilde{y}(x_1)$, $\tilde{y}_2 = \tilde{y}(x_2)$ equation (13) is equivalent to the matrix equation

$$\{\tilde{G}_n\} = \frac{M\omega^2}{L}(Z_{nm}^A)\{\tilde{w}_m\} \quad (14)$$

with the elements of the infinite dimensional impedance matrix defined by

$$\begin{aligned}Z_{nm}^A = \{ & [\cos k_n x_1 + \cos k_n x_2](\hat{y}_G)_m \\ & + \beta^2[\cos k_n x_1 - \cos k_n x_2](d\hat{\Theta})_m\}\end{aligned} \quad (15)$$

where

$$\begin{aligned}(\hat{y}_G)_m = \ & [(\beta^2\omega^2 - \omega_2^2)\omega_1^2\cos k_m x_1 \\ & + (\beta^2\omega^2 - \omega_1^2)\omega_2^2\cos k_m x_2]/D(\omega)\end{aligned} \quad (16a)$$

$$\begin{aligned}(d\hat{\Theta})_m = \ & [(\omega^2 - \omega_2^2)\omega_1^2\cos k_m x_1 \\ & - (\omega^2 - \omega_1^2)\omega_2^2\cos k_m x_2]/D(\omega)\end{aligned} \quad (16b)$$

Thus, equation (14) specifies the relationship that exists between the generalized forces, $\tilde{G}_n$ and generalized displacements, $\tilde{w}_m$ for the attachment points of the two degree of freedom spring-mass system. Damping or dissipation of dashpots in parallel with the springs is included by merely considering the spring constants to be complex. The appropriate modifications of equations (16) are achieved by introducing replacement relations

$$\omega_1^2 \longrightarrow \omega_1^2(1 + i\eta_1)$$

$$\omega_2^2 \longrightarrow \omega_2^2(1 + i\eta_2)$$

where η_1 and η_2 are the frequency independent loss factors that accompany the two springs S_1 and S_2, respectively. Thus, equations (14) - (16) characterize the absorber system in terms of the impedance matrix (Z^A_{nm}) as established for the attachment points x_1 and x_2. The generalized forces $\tilde{g}_n$ and displacements $\tilde{w}_m$ represent distributions on the interval $o \le x \le L$ in terms of the spanning set of orthogonal functions, $\cos k_n x$; $n = 0,1,2,$---.

c. Cylindrical Beam Mobility - Consider the steady state harmonic motion of a cylindrical beam with an arbitrary cross-sectional inertia. With shear deformation of the cross-section the motion is governed by Timoshenko beam theory [10] and the equations

$$E_s \frac{d}{dx}\left(I \frac{d\tilde{\psi}}{dx}\right) + K^1 A G_s \left(\frac{d\tilde{y}}{dx} - \tilde{\psi}\right) + \rho_s I \omega^2 \tilde{\psi} = o \tag{17a}$$

$$K^1 G_s \frac{d}{dx}\left[A\left(\frac{d\tilde{y}}{dx} - \tilde{\psi}\right)\right] + \rho_s A \omega^2 \tilde{y} = - \tilde{F} + \tilde{f} + \tilde{G} \tag{17b}$$

where $\tilde{y}(x)$ is the transverse displacement and $\tilde{\psi}(x)$ is the bending angle. $\tilde{F}$ is the applied forcing function acting at the frequency ω, and $\tilde{f}$, $\tilde{G}$ denote the loadings induced by the presence of the fluid and the attachment of the absorber system, respectively. For a normalized input distribution function described by the form

$$\tilde{F}(x) = \frac{\epsilon_n}{2} \cos k_n x \; ; \; o \le x \le L \tag{18}$$

with a fixed integer n, $\epsilon_o = 1$; $\epsilon_n = 2$ for $n \neq o$, and $\tilde{f}, \tilde{G} \equiv o$, a corresponding solution for the transverse displacement, say $\tilde{\Gamma}_n(x)$, may be obtained that satisfies a set of prescribed boundary conditions at the ends $x = o$ and $x = L$. Thus, for a sequence of generalized force amplitudes $\tilde{F}_n$ that correspond to the distributions of equation (18) the complete superposed solution may be written for the steady state displacement as

$$\tilde{y}(x) = \sum_{n = o}^{\infty} \tilde{\Gamma}_n(x) \tilde{F}_n \; ; \; o \le x \le L \tag{19}$$

utilizing the representation of equation (13b) where

$$\tilde{w}_m = \frac{\epsilon_m}{L} \int_o^L \tilde{y}(x) \cos k_m x dx \tag{20}$$

it is determined that

$$\{\tilde{w}_m\} = (Y^s_{mn})\{\tilde{F}_n\} \tag{21}$$

with the elements of the beam mobility matrix defined by the equation

$$Y^s_{mn} = \frac{\epsilon_m}{L} \int_o^L \tilde{\Gamma}_n(x) \cos k_m x dx \tag{22}$$

Thus, equations (21) and (22) establish the relationship between the generalized forces and displacements for the beam as it oscillates in steady state motion. For a given force distribution the components $\tilde{F}_n$ are determined by the integral

$$\tilde{F}_n = \frac{2}{L} \int_o^L \tilde{F}(x) \cos k_n x dx \tag{23}$$

and the corresponding response may be obtained from equation (21). Thus, the characteristics of the fluid, absorber system, and beam are established on a common independent basis of orthogonal functions.

d. Solution for Coupled Interactive Response - With the established forms of impedance and mobility matrices of equations (6), (14), and (21) the solution for the coupled response can be obtained by performing the algebraic matrix manipulations. By introducing the nondimensional expressions

$$\hat{F}_n = \tilde{F}_n L^3 / E_s I_o, \; \hat{w}_m = \tilde{w}_m / L, \text{ and } \hat{Y}^s_{mn} = E_s I_o \, Y^s_{mn} / L^4$$

equation (21) may be written in the expanded form

$$\{\hat{w}_m\} = (\hat{Y}^s_{mn})\{\hat{F}_n\} - (\hat{Y}^s_{mn})\{\hat{f}_n + \hat{G}_n\} \tag{24}$$

which represents the interactive response of the beam under the combined influence of the applied load and induced loadings of the fluid and attached absorber. The corresponding matrix relationships are

$$\{\hat{f}_n\} = (\hat{Z}^f_{nm})\{\hat{w}_m\} \tag{25}$$

for the characteristics of the fluid with $\tilde{v}_m = i\omega L \hat{w}_m$ and

$$\{\hat{G}_n\} = (\hat{Z}^A_{nm})\{\hat{w}_m\} \tag{26}$$

for the response of the absorber where

$$\hat{Z}^f_{nm} = 4i\kappa \frac{\rho_f c_f^2}{\rho_s c_s^2} \left(\frac{L}{a}\right)^4 Z^f_{nm}$$

and

$$\hat{Z}^A_{nm} = 4\gamma \left(\frac{c_f}{c_s}\right)^2 \left(\frac{L}{a}\right)^4 \kappa^2 Z^A_{nm}$$

are the respective impedances and $c_s^2 = E_s/\rho_s$, $\gamma = M/\rho_s \pi a^2 L$, $\kappa = \omega a/c_f$. The substitution of equations (25) and (26) into equation (24) yields

$$\left[I + (\hat{Y}^s_{mn})(\hat{Z}^f_{nm} + \hat{Z}^A_{nm})\right]\{\hat{w}_m\} = (\hat{Y}^s_{mn})\{\hat{F}_n\} \qquad (27)$$

as the matrix equation whose solution provides the interactive beam response in terms of the generalized displacements. The actual displacement distribution function is then obtained from the summation

$$\tilde{y}(x) = L\sum_{m=o}^{\infty} \hat{w}_m \cos k_m x \qquad (28)$$

It is noted that the above equations represent infinite dimensional arrays that are continuous functions of frequency. To obtain a numerical solution a truncated finite dimensional approximation must be utilized at a fixed discrete frequency. For the results presented in this paper the numerical values of $\hat{Z}^f_{nm}$ are established by the methods of Ref. [9] and the values of $\hat{Z}^A_{nm}$ are computed directly. In order to provide the elements of the beam mobility matrix equations (17) are written as a system of four first-order differential equations and integrated numerically with a Runge-Kutta-Gill method from $x/L = 0.0$ to $x/L = 1.0$. In this manner two homogeneous solutions that satisfy the prescribed boundary conditions at $x/L = 0.0$ and a particular solution for each force input of the form shown in equation (18) that satisfies homogeneous boundary conditions at $x/L = 0.0$ are established. The two arbitrary constants that accompany the homogeneous solutions are then determined by Gauss-Jordon reduction of the equations obtained from the prescribed boundary conditions at $x/L = 1.0$. Thus, the set of solutions denoted by $\tilde{\Gamma}_n(x)$ in equation (19) are generated for $n = 0,1,2,---,N-1$. Concurrent to the generation of the solution of the beam equations the integrals of equation (22) are constructed for $m = 0,1,2,---,N-1$ and simultaneous numerical quadrature is performed to establish a N x N mobility matrix $(\hat{Y}^s_{mn})$. Subsequently, an N x N system of equations (27) is formed and solved using a Gauss-Jordon reduction method.

II. NUMERICAL RESULTS AND DISCUSSION

In order to provide a demonstration of the current methods and present illustrative numerical results cantilevered and free-free beam configurations under point excitation are considered as the basis for study. For the purpose of considering point excitation of the beam the generalized forces are determined by

$$\hat{F}_n = \frac{2\tilde{Q}_o L^2}{E_s I_o}\int_o^L \delta(x - x_o)\cos k_n x\,dx = \frac{2\tilde{Q}_o L^2}{E_s I_o}\cos k_n x_o$$

where $\tilde{Q}_o$ is the magnitude of the force acting at the location x_o. In addition, the cross-sectional shear factor is held fixed by the condition $K^1 Gs/E_s = 1/3$ in all cases. The characteristics of the attached absorber system are limited to the consideration of $\beta^2 = 1.0$ which implies that $D(\omega)=o$ for absorber resonances at $\kappa_1 = \omega_1 a/c_f$ and $\kappa_2 = \omega_2 a/c_f$. The loss factors of the absorber system are set at $\eta_1 = \eta_2 = 0.4$ for all cases of analysis. Other relevant parameters that are held fixed include

$$\rho_f/\rho_s = 0.37 \;;\; c_f/c_s = 0.3$$

which represent aluminum emersed in water.

a. Cantilevered Beam Vibration - The cylindrical beam considered for vibration with cantilevered boundary conditions has an aspect ratio of $a/L = 0.1$ and a radii ratio of $b/a = 0.95$. It is excited by the point force acting at the tip, $x_o/L = 1.0$. The magnitude of the mass considered for the study of absorber attachment is fixed by the ratio $\gamma = 0.25$. By successive trials for various cases, the numerical sensitivity of the solutions to the dimensionality N was examined and it was determined that ten generalized degrees of freedom ($N = 10$) provided a numerically stable and convergent solution for the considered frequency range. In addition, it was found that the omission of the fluid cross-coupling coefficients, the off-diagonal elements of $(\hat{Z}^f_{nm})$, had little effect on the amplitude response of the beam and therefore the $\hat{Z}^f_{nm}$ for $m \neq n$ were neglected. Figure 3 illustrates the effects of various types of absorber attachment upon the in-vacuo $(\hat{Z}^f_{nm} \equiv 0)$ tip amplitude response of the cantilever beam. The case where $x_1/L = x_2/L = 0.9$ and $\kappa_1 = \kappa_2 = 0.035$ demonstrates the effect of a single degree-of-freedom absorber. It is seen that the predominant influence occurs relative to the first resonant beam mode where "splitting" and attenuation of the resonance is induced by the action of the absorber. The case where $x_1/L = 0.9$, $x_2/L = 1.0$ and $\kappa_1 = \kappa_2 = 0.035$ shows the effect of supporting the mass with a two-point mount configuration having equivalent spring/dashpot characteristics. It is seen the two-point attached absorber with a single resonance acts nearly the same as single mount system. Finally, with $x_1/L = 0.9$, $x_2/L = 1.0$ and $\kappa_1 = 0.035$, $\kappa_2 = 0.40$ it is shown that attenuation of both the first and second resonant beam modes is achieved. The effect of introducing the secondary absorber resonance is most notable for the second beam mode resonance. Although true absorber optimization [7] was not attempted the current results illustrate the marked effects that can be achieved by proper choice of the absorber mounting characteristics. Figure 4 exemplifies the additional influence of emersing the cantilever beam and absorber system in water. It is seen that the effect of the "virtual" mass loading of the surrounding fluid tends to de-tune the absorber in relation to its in-vacuo performance. In particular, a change of the secondary absorber resonance from $\kappa_2 = 0.4$ to $\kappa_2 = 0.2$ is required to reproduce the attenuation of the second resonant beam demonstrated for the in-vacuo vibration in Figure 3.

B. Free-Free Beam Vibration - The cylindrical beam considered for the analysis with free-free boundary conditions was chosen to have an aspect ratio of $a/L = 0.044$ and a radii ratio of $b/a = 0.97$. The excitation force is located at $x_o/L = 0.7$. The dimensionality of $N = 10$ was found to be sufficient for numerical stability and convergence within the frequency range of analysis for the free-free configuration. Figure 5 illustrates the effect of two-point absorber attachment upon the tip response at $x/L = 1.0$ and the driving point response $x/L = 0.7$ of the in-vacuo free-free beam. With $\kappa_2 = 0.035$ the secondary absorber resonance is approximately tuned to produce attenuation of the fundamental beam resonance. It is noted that at the resonance of $\kappa = \kappa_2$ the principle force transmitted by the absorber occurs at the x_2/L position and at $\kappa = \kappa_1$ the transmitted force occurs largely at x_1/L. For the case with $x_1/L = 0.9$ and $x_2/L = 1.0$ it was not possible to induce any significant attenuation by tuning of the κ_1 absorber resonance to the second free-free beam because of the location of a node in the neighborhood of $x/L = 0.9$ for the second beam mode resonance. Thus, the marked effect of moving the mount position from $x_1/L = 0.9$ to $x_1/L = 0.75$ is demonstrated in relationship to the tuning of the absorber at the second beam mode resonance. The modifications of the absorber characteristics required to produce in-water attenuation of the first and second resonant free-free beam modes are illustrated in Figure 6. In particular, the effect of changing the absorber resonance from $\kappa_1 = 0.075$ to $\kappa_1 = 0.095$ is illustrated. At the later absorber resonant frequency tuned absorbtion of the second resonant free-free in-water beam mode is achieved as noted by the low amplitude double peak in the neighborhood of $\kappa = 0.1$. In summary, in-water tuned attentuation of the first and second resonant free-free beam modes is produced by $\kappa_1 = 0.095$, $\kappa_2 = 0.025$. Thus, the environment for beam vibration is seen to be an important factor in regard to characterizing the performance of an attached absorber or spring-mass system.

III. CONCLUSIONS

The methods applied in this paper to solve the title problem are demonstrated and the versatility to consider various cases of parametric study is evident. The illustrated results show that by proper choice of the mount characteristics a component or mass can be attached to a cylindrical beam at two points to produce vibration attenuation of two resonant beam modes. The ability to produce tuned vibration absorbtion is found to be strongly dependent upon the locations of attachment. In addition, the results presented for both in-vacuo and in-water vibration exemplify the effects of fluid loading upon the performance of the attached dynamic absorber system. Generally, it may be concluded that in-vacuo optimum absorber tuning does not remain optimum upon submergence of the beam. The analysis performed in this study is directly applicable to vibration and noise control. Realizing that beam vibration is merely one form of cylindrical shell vibration the current approach and considerations may be extended to shell vibration analyses.

REFERENCES

1. Sandman, B. E., "Spacial Fourier Decomposition: Analysis of Fluid-Loaded Structural Vibration," to be presented at and published by the 16th Midwestern Mechanics Conference, 1979.

2. Hoppmann, W. H., "Forced Lateral Vibration of Beam Carrying a Concentrated Mass," Journal of Applied Mechanics, Vol. 19, pp. 303-307, 1952.

3. Pan, H. H., "Transverse Vibration of an Euler Beam Carrying a System of Heavy Bodies," Journal of Applied Mechanics, Vol. 32, pp. 434-437, 1959.

4. Amba-Rao, C. L., "On the Vibration of a Rectangular Plate Carrying a Concentrated Mass," Journal of Applied Mechanics, Vol. 31, pp. 550-551, 1964.

5. Magrab, E. B., "Vibration of a Rectangular Plate Carrying a Concentrated Mass," Journal of Applied Mechanics, Vol. 35, pp. 411-412, 1968.

6. Das, Y. C. and Navaratna, D. R., "Vibrations of a Rectangular Plate with Concentrated Mass, Spring, and Dashpot," Journal of Applied Mechanics, Vol. 30, pp. 31-36, 1963.

7. Snowdon, J. C., "Vibration of Simply Supported Rectangular and Square Plates

to which Lumped Masses and Dynamic Vibration Absorbers are Attached," Journal of the Acoustical Society of America, Vol. 57, pp. 646-654, 1975.

8. Sandman, B. E., "Fluid-Loaded Vibration of an Elastic Plate Carrying a Concentrated Mass," Journal of the Acoustical Society of America, Vol. 61, pp. 1503-1510, 1977.

9. Sandman, B. E., "Numerical Fluid Loading Coefficients for the Modal Velocities of a Cylindrical Shell," Journal of Computers and Structures, Vol. 6, pp. 467-473, 1976.

10. Timoshenko, S. and Young, D. H., Vibration Problems in Engineering, D. Van Nostrand Co., pp. 329-331, 1955.

NOMENCLATURE

L	length of beam
a, b	external and interior beam radii
x_1, x_2	absorber attachment points
$\tilde{\phi}$	fluid velocity potential
c_f, ρ_f	sound speed and mass density of fluid
$\tilde{y}_1$, $\tilde{y}_2$	time separated displacements at attachment points
$\tilde{g}_1$, $\tilde{g}_2$	time separated forces at attachment points
η_1, η_2	absorber loss factors
β	absorber rotational to translational inertia ratio
d	distance between absorber mounts and mass center
γ	absorber mass to beam mass ratio
E_s, G_s	extensional and shearing moduli of beam
K^1	cross-sectional shear shape factor
c_s, ρ_s	sound speed and mass density of beam
Ψ_m, $\bar{\Psi}_m$	Fourier transform of velocity distribution and complex conjugate

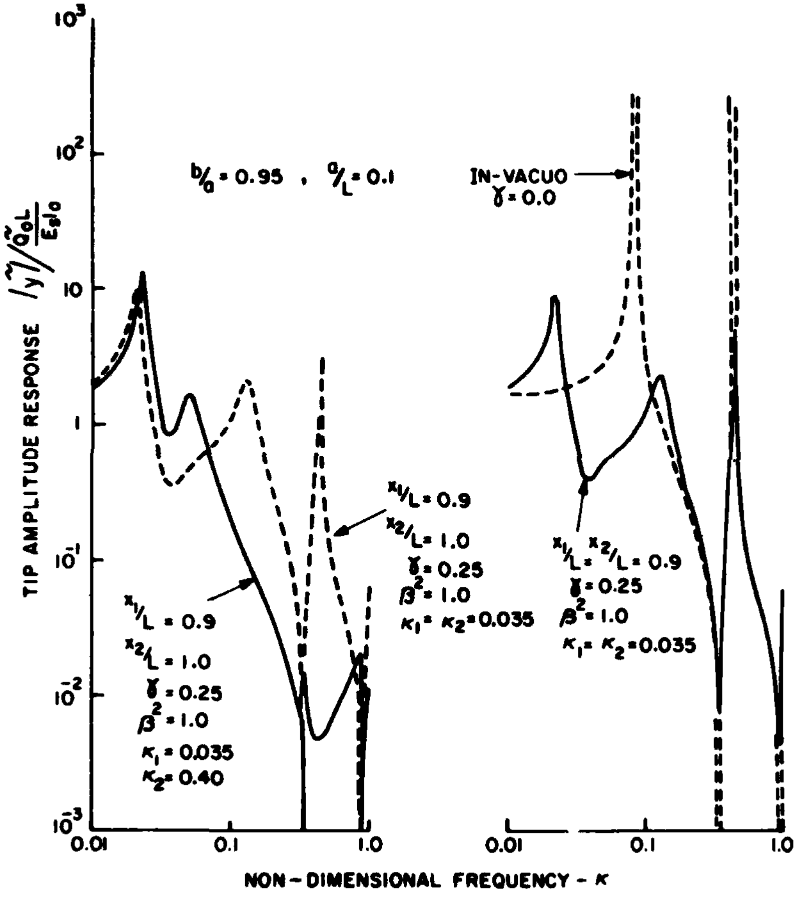

N5983-2

Figure 3. Tip Amplitude Response of Cantilever Beam Carrying an Attached Absorber/In-Vacuo Effect Multi-Degree of Freedom Resonant Tuning and Attachment

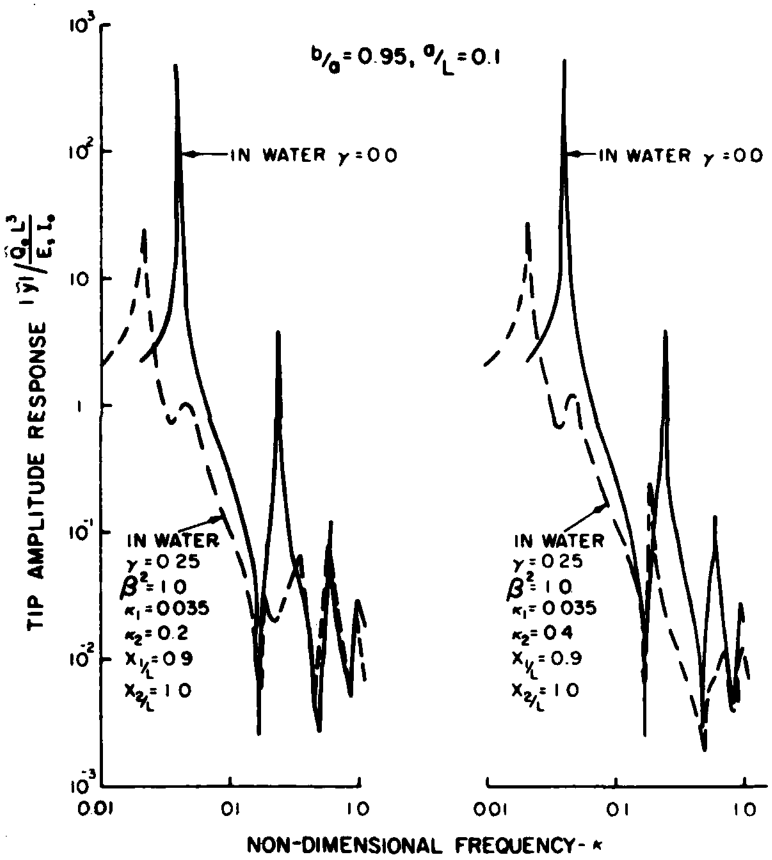

N5983-1

Figure 4. Tip Amplitude Response of Cantilever Beam Carrying an Attached Absorber/In-Water Effect of Secondary Resonant Tuning

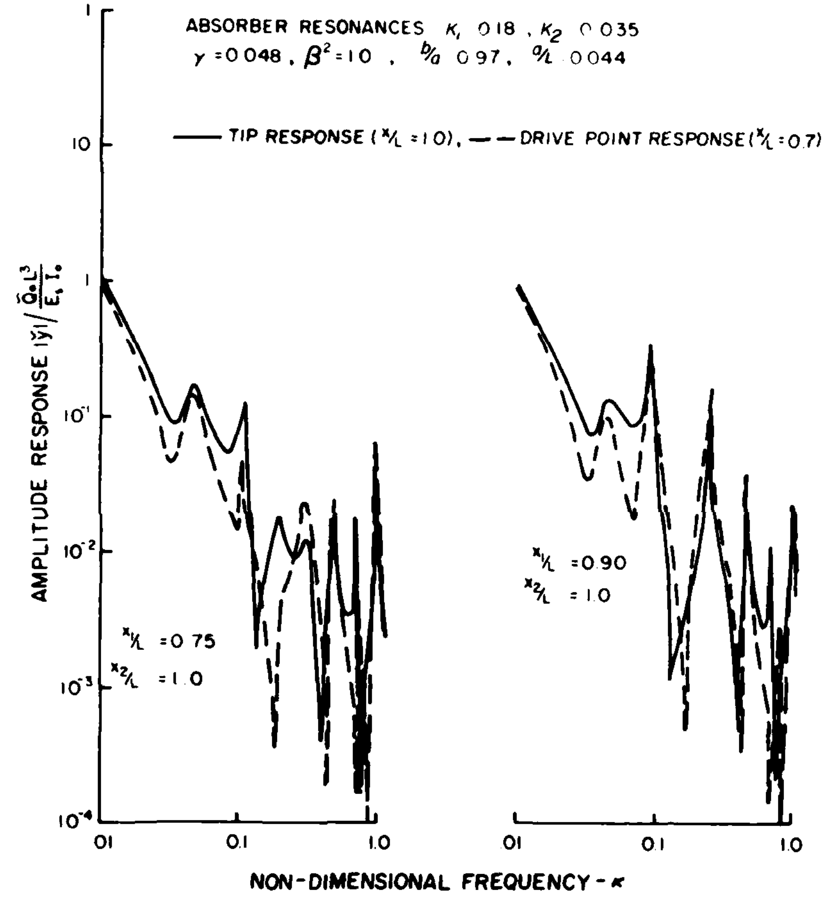

N5983-3

Figure 5. Amplitude Response of Free-Free Beam Carrying an Attached Absorber/In-Vacuo Effect of Attachment Location Upon Secondary Tuning

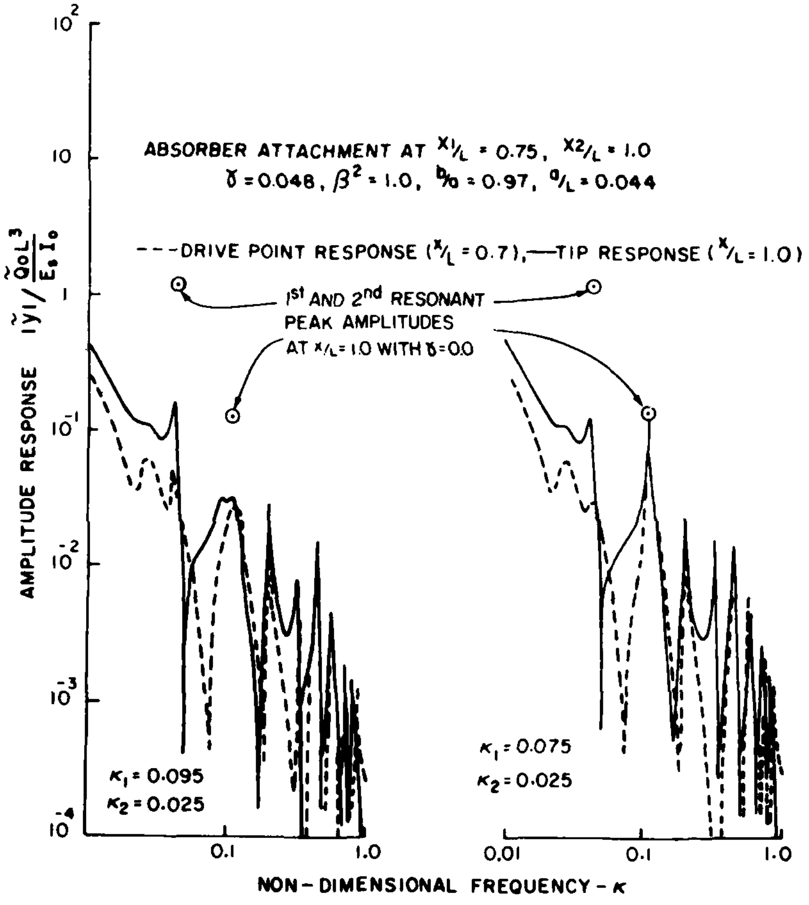

N5983-4

Figure 6. Amplitude Response of Free-Free Beam Carrying an Attached Absorber/In-Water Effect of Secondary Resonant Tuning

DISCUSSION

Mr. Galef (TRW): Given the fact that the beam has to be long and slender for aspects of your solution how important do the Timoshenko terms become? Can you throw those out and have practically the same results?

Mr. Sandman: We found that you would have to get up to the fifth or sixth mode before you would see any significant influence. It turns out that in the case of the hollow beam it is more significant because you would have less material along the shear axis. But you could probably get by with fairly reasonable results without using Timoshenko beam theory. You will note that the fluid solution was considered for essentially a circumferential displacement distribution of N=1. We are extending this type of approach now to cylindrical shells. It is directly applicable to cylindrical shells as well as beams. This beam approach was chosen to prove out the idea.

DYNAMIC STABILITY OF FIBROUS COMPOSITE CYLINDERS UNDER PULSE LOADING

Robert J. Stuart, Sangiahnadar Dharmarajan
College of Engineering
San Diego State University
San Diego, CA 92182

The stability of composite cylindrical shells with general boundary conditions subjected to pressure pulse loads is investigated. The governing differential equations of motion of an orthotropic cylindrical shell subjected to normal pressure are reduced to generalized Donnell's cylindrical shell theory. By neglecting higher order terms, these equations are further reduced to a single eighth-order differential equation in terms of the radial displacement. The governing differential equation is solved by assuming a solution in the form of a product. A simple computational algorithm is presented for finding the growth of deflections when the pressure pulse exceeds the static buckling pressure. The method may be used for all boundary conditions that may be solved in the vibrating beam problem.

INTRODUCTION

Fibrous composite structures such as missile cones, nose fairings and afterburner nozzels of jet engines which can be treated as orthotropic cylinders are at times subjected to fluctuating pressure loads. Yao (1) has investigated the dynamic stability of isotropic cylinders with simply supported boundary conditions. He showed that for isotropic cylinders, if the periodic load has only one harmonic term, the stability equation can be reduced to Mathieu's stability equation. Stuart, Dharmarajan and Penzes (2) extended Yao's work to orthotropic cylinders with general boundary conditions. In this paper, the stability of orthotropic cylinders with general boundary conditions subjected to pulse loads is investigated. It is apparent that if the static buckling pressure for a cylinder is exceeded for an appreciable length of time, the structure will fail; however, if the pulse duration is sufficiently brief, inertial effects will prevent failure. This paper relates the pulse amplitude, the pulse duration and the increase of structural deflections.

THEORY

Defining orthotropic stress-strain relations for inplane and bending loads separately as in Hoppman (3), one obtains for inplane loads

$$\sigma_x'' = \frac{1}{C^*}\left[C_{22}\,\varepsilon_x'' - C_{12}\,\varepsilon_\phi''\right] \qquad (1A)$$

$$\sigma_\phi'' = \frac{1}{C^*}\left[C_{11}\,\varepsilon_\phi'' - C_{12}\,\varepsilon_x''\right] \qquad (1B)$$

$$\tau_{x\phi}'' = \gamma_{x\phi}''/C_{66} \qquad (1C)$$

where

$$C^* = C_{11}\,C_{22} - C_{12}^{\;2} \qquad (2)$$

Similarly stresses associated with bending and twisting loads are related to strains as

$$\sigma_x' = \frac{1}{S^*}\left[S_{22}\,\varepsilon_x' - S_{12}\,\varepsilon_\phi'\right] \qquad (3A)$$

$$\sigma_\phi' = \frac{1}{S^*}\left[S_{11}\,\varepsilon_\phi' - S_{12}\,\varepsilon_x'\right] \qquad (3B)$$

$$\tau_{x\phi}' = \frac{\gamma_{x\phi}'}{S_{66}} \qquad (3C)$$

where

$$S^* = S_{11}\,S_{22} - S_{12}^{\;2} \qquad (4)$$

In Equations (1) and (3), C_{ij} and S_{ij} are orthotropic elastic constants associated with elastic axes of symmetry which correspond to the geometric axes of the cylinder as shown in Figure 1.

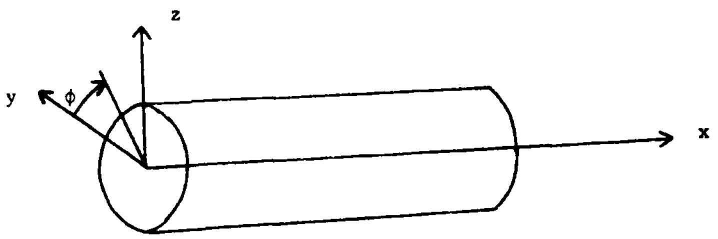

Figure 1. Coordinate System

For cylindrical shells the strain displacement functions are

$$\varepsilon_x'' = \frac{\partial u}{\partial x} \tag{5A}$$

$$\varepsilon_\phi'' = \frac{1}{a}\left(\frac{\partial v}{\partial \phi} - w\right) \tag{5B}$$

$$\gamma_{x\phi}'' = \left(\frac{\partial v}{\partial x} + \frac{1}{a}\frac{\partial u}{\partial \phi}\right) \tag{5C}$$

$$\varepsilon_x' = -z\frac{\partial^2 w}{\partial x^2} \tag{5D}$$

$$\varepsilon_\phi' = -\frac{z}{a^2}\left(\frac{\partial^2 w}{\partial \phi^2} + \frac{\partial v}{\partial \phi}\right) \tag{5E}$$

$$\gamma_{x\phi}' = \frac{z}{a}\left(\frac{\partial^2 w}{\partial x \partial \phi} + \frac{\partial v}{\partial x}\right) \tag{5F}$$

where a is the mean radius of the cylinder and u, v, w are displacements in the longitudinal, circumferential and radial directions.

Introducing h_s, h_b and h_m to denote shell thicknesses associated with inplane loading, bending and mean thickness of the shell respectively, one obtains the conventional stress resultants and moments as

$$N_x = \frac{h_s}{C^*}\left[C_{22}\frac{\partial u}{\partial x} - \frac{C_{12}}{a}\left(\frac{\partial v}{\partial \phi} - w\right)\right] \tag{6A}$$

$$N_\phi = \frac{h_s}{C^*}\left[\frac{C_{11}}{a}\left(\frac{\partial v}{\partial \phi} - w\right) - C_{12}\frac{\partial u}{\partial x}\right] \tag{6B}$$

$$N_{x\phi} = \frac{h_s}{C_{66}}\left[\frac{\partial v}{\partial x} + \frac{1}{a}\frac{\partial u}{\partial \phi}\right] \tag{6C}$$

$$M_x = -\frac{h_b^3}{12\,S^*}\left[S_{22}\frac{\partial^2 w}{\partial x^2} - \frac{S_{12}}{a^2}\left(\frac{\partial^2 w}{\partial \phi^2} + \frac{\partial v}{\partial \phi}\right)\right] \tag{6D}$$

$$M_\phi = -\frac{h_b^3}{12\,S^*}\left[\frac{S_{11}}{a^2}\left(\frac{\partial^2 w}{\partial \phi^2} + \frac{\partial v}{\partial \phi}\right) - S_{12}\frac{\partial^2 w}{\partial x^2}\right] \tag{6E}$$

$$M_{x\phi} = \frac{h_b^3}{12\,S_{66}}\left[\frac{1}{a}\left(\frac{\partial^2 w}{\partial x\,\partial \phi} + \frac{1}{a}\frac{\partial v}{\partial \phi}\right)\right] \tag{6F}$$

The differential equations of motion for a cylinder subject to normal pressure can be written as

$$\frac{\partial N_x}{\partial x} + \frac{1}{a}\frac{\partial N_{\phi x}}{\partial \phi} = \rho h_m \frac{\partial^2 u}{\partial t^2} \tag{7}$$

$$\frac{1}{a}\frac{\partial N_\phi}{\partial \phi} + \frac{\partial N_{x\phi}}{\partial x} + \frac{1}{a}\frac{\partial M_{x\phi}}{\partial x} - \frac{1}{a^2}\frac{\partial M_\phi}{\partial \phi} = \rho h_m \frac{\partial^2 v}{\partial t^2} \tag{8}$$

$$\frac{1}{a}N_\phi + \frac{1}{a}\frac{\partial^2 M_{\phi x}}{\partial x \partial \phi} + \frac{\partial^2 M_x}{\partial x^2} - \frac{1}{a}\frac{\partial^2 M_{x\phi}}{\partial x \partial \phi} + \frac{1}{a^2}\frac{\partial^2 M_\phi}{\partial \phi^2} = \frac{p}{a h_s}\left(w + \frac{\partial^2 w}{\partial \phi^2}\right) + \rho h_m \frac{\partial^2 w}{\partial t^2} \tag{9}$$

where p = normal pressure

ρ = density of the shell

By substituting Equations (6) into (7), (8) and (9), and dropping higher order terms as in the buckling analysis for long thin cylinders in Penzes (4), Penzes and Kraus (5), and Penzes and Bhat (6), the above equations are reduced to a single eighth-order differential equation in the radial displacement.

$$\frac{h_b^3 C^*}{12\,h_s} L_8(w) + \frac{C_{11}^2}{a^6}\left(1 - \frac{C_{11}}{a^2\gamma}\right)\frac{\partial^4 w}{\partial \phi^4} + \frac{h_b^3\, C^* S_{11} C_{11}^2}{6a^{10} h_s S^* \gamma}\frac{\partial^6 w}{\partial \phi^6} + \frac{C^*}{a^2}\frac{\partial^4 w}{\partial x^4} \tag{10}$$

$$= -\rho\left(\frac{h_m}{h_s}\right)\frac{\partial^2}{\partial t^2}\left\{\frac{C^* C_{11}}{a^4}\frac{\partial^4 w}{\partial \phi^4} - \frac{C^* C_{11}}{a^4}\frac{\partial^2 w}{\partial \phi^2} - \frac{h_b^3\, C^*}{12 h_s a^6 S^*}\left(C^* + C_{11}C_{66}\right) S_{11}\frac{\partial^6 w}{\partial \phi^6}\right\}$$

(continued on next page)

$$- \frac{C_{11}C^{*}p}{a^{5}h_{s}} \left(\frac{\partial^{4}w}{\partial\phi^{4}} + \frac{\partial^{6}w}{\partial\phi^{6}} \right)$$

where

$$\frac{h_{b}^{3}\ C^{*}}{12h_{s}} L_{8}(w) = \frac{h_{b}^{3}\ C^{*}C_{11}S_{11}}{12\ h_{s}a^{8}S^{*}} \frac{\partial^{8}w}{\partial\phi^{8}} \tag{11A}$$

$$\gamma = \frac{C_{11}}{a^{2}} + \frac{h_{b}^{3}\ C^{*}S_{11}}{12\ a^{4}h_{s}S^{*}} \tag{11B}$$

Equation (10) may be written in compact form as

$$a_{11} \frac{\partial^{8}w}{\partial\phi^{8}} + a_{13} \frac{\partial^{6}w}{\partial\phi^{6}} + a_{12} \frac{\partial^{4}w}{\partial\phi^{4}} + a_{14} \frac{\partial^{4}w}{\partial x^{4}}$$

$$= a_{15} \left(- \frac{\partial^{6}w}{\partial t^{2}\ \partial\phi^{4}} + \frac{\partial^{4}w}{\partial t^{2}\ \partial\phi^{2}}\right) + a_{16} \frac{\partial^{8}w}{\partial t^{2}\ \partial\phi^{6}} \tag{12}$$

$$- pa_{17} \left(\frac{\partial^{4}w}{\partial\phi^{4}} + \frac{\partial^{6}w}{\partial\phi^{6}} \right)$$

The a_{ij}'s are defined in terms of the constants previously introduced by comparing Equations (11) and (12). The a_{ij}'s may also be defined in terms of the composite theory stiffness parameters given in Jones (7)

$$a_{11} = \frac{h_{b}^{3}\ C^{*}C_{11}S_{11}}{12h_{s}a^{8}S^{*}} = \frac{h^{2}A_{22}D_{22}}{a^{8}(A^{*})^{2}} \tag{13A}$$

$$a_{12} = \frac{C_{12}^{2}}{a^{6}} \left(1 - \frac{C_{11}}{a^{2}\ \gamma} \right) =$$

$$\frac{h^{2}\ (A_{12})^{2}}{a^{6}\ (A^{*})^{2}} \left[\frac{\frac{D_{22}}{a^{2}}}{A_{22} + \frac{D_{22}}{a^{2}}} \right] \tag{13B}$$

$$a_{13} = \frac{h_{b}^{3}\ C^{*}S_{11}C_{11}^{\ 2}}{6\ a^{10}h_{s}S^{*}\ \gamma} = \frac{2\ h^{2}D_{22}(A_{22})^{2}}{a^{8}(A^{*})^{2}(A_{22}+\frac{D_{22}}{a^{2}})} \tag{13C}$$

$$a_{14} = \frac{C^{*}}{a^{2}} = \frac{h^{2}}{a^{2}\ A^{*}} \tag{13D}$$

$$a_{15} = \frac{\rho\ h_{m}C^{*}C_{11}}{h_{s}\ a^{4}} = \frac{\rho\ h^{3}A_{22}}{a^{4}(A^{*})^{2}} \tag{13E}$$

$$a_{16} = \frac{\rho\ h_{m}\ h_{b}^{3}\ C^{*}\ (C^{*}+ C_{11}C_{66})S_{11}}{12\ h_{s}^{2}\ a^{6}\ S^{*}}$$

$$= \frac{\rho\ h^{3}\ D_{22}}{a^{6}(A^{*})^{2}} \left[1 + \frac{A_{22}}{A_{66}} \right] \tag{13F}$$

$$a_{17} = \frac{C_{11}\ C^{*}}{a^{5}\ h_{s}} = \frac{h^{2}\ A_{22}}{a^{5}(A^{*})^{2}} \tag{13G}$$

where $A^{*} = A_{11}\ A_{22} - A_{12}^{2}$ (13H)

If p = 0, Equation (12) reduces to the case of free vibration of the cylinder.

SOLUTION TECHNIQUE

A separation of variable technique will be used to solve Equation (12). By letting

$$w = X(x)F(\phi,t) \tag{14}$$

and substituting into Equation (12), there results

$$\frac{1}{a_{14}F} \left[- a_{11} \frac{\partial^{8}F}{\partial\phi^{8}} - a_{13} \frac{\partial^{6}F}{\partial\phi^{6}} - a_{12} \frac{\partial^{4}F}{\partial\phi^{4}} \right.$$

$$- a_{15} \frac{\partial^{6}F}{\partial t^{2}\partial\phi^{4}} + a_{15} \frac{\partial^{4}F}{\partial t^{2}\partial\phi^{2}} + a_{16} \frac{\partial^{8}F}{\partial t^{2}\partial\phi^{6}}$$

$$\left. - pa_{17}\left(\frac{\partial^{4}F}{\partial\phi^{4}} + \frac{\partial^{6}F}{\partial\phi^{6}}\right)\right] = \frac{X''''}{X} \tag{15}$$

Since the variables x, ϕ and t are independent, the only way that equality in Equation (15) can hold is if both sides are equal to a constant. By calling the constant $(\beta/\ell)^{4}$, where ℓ is the length of the cylinder, from Equation (15)

$$X'''' - (\beta/\ell)^{4}X = 0 \tag{16}$$

As is well known from the vibrating beam problem, non-trivial solutions of Equation (16) for a given set of boundary conditions exist only for certain values of β^{4}, i.e., the eigenvalues. The problem has been investigated several times, e.g., Bisplinghoff, Ashley and Halfmann (8), with results that are summarized below

Boundary Conditions	Characteristic equation	Approximate solutions n = 1,2...
Fixed-fixed	$\cos\beta\ \cosh\beta = 1$	$\beta_{n} \simeq (n + \frac{1}{2})\ \pi$
Fixed-hinged	$\tan\beta = \tanh\beta$	$\beta_{n} \simeq (n + \frac{1}{4})\ \pi$
Hinged-hinged	$\sin\beta = 0$	$\beta_{n} = n\pi$

Since Equation (16) has an infinite number of solutions, by making use of linearity, Equation (14) is now written as

$$w = \sum_{n=1}^{\infty} X_n(x) \quad F_n(\phi,t) \tag{17}$$

where each term in the summation corresponds to a different eigenvalue β_n. $X_n(x)$ may be found from Equation (16) and the given boundary conditions; however, its precise form is not germane. An attempt to separate the variables x and ϕ in Equation (15) fails unless p is independent of time, i.e., the normal pressure is constant. Since F must be periodic in ϕ with period 2π, a Fourier series in ϕ is suggested. By trying a solution

$$F_n(\phi,t) = \sum_{m} \cos\left(m\phi + \theta_m\right) T_{mn}\ (t) \tag{18}$$

in Equation (15), the resulting equation for $T_{mn}(t)$ is

$$T''_{mn} + \omega^2_{mn} T_{mn} = 0 \qquad \text{where} \tag{19}$$

$$\omega^2_{mn} = \frac{\begin{bmatrix} a_{11}\, m^8 + a_{12}\, m^4 - a_{13}\, m^6 + \\ a_{17}\, (m^4 - m^6)\, p + a_{14}\, \beta_n^4/\ell^4 \end{bmatrix}}{a_{15}(m^4 + m^2) + a_{16}\, m^6} = \tag{20A}$$

$$\frac{\begin{bmatrix} A_{22}\, D_{22}\, m^8 + A^2_{12} \left[\dfrac{D_{22}}{A_{22} + \dfrac{D_{22}}{a^2}} \right] m^4 - \\ \dfrac{2\, D_{22}\, A^2_{22}}{A_{22} + \dfrac{D_{22}}{a^2}}\, m^6 + a^6\, A^* \beta_n^4/\ell^4 + \\ a^3\, A_{22}\, (m^4 - m^6)\, p \end{bmatrix}}{\rho\, h\, [\, a^4\, A_{22}\, (m^4 + m^2) + a^2\, D_{22}\, (1 + \dfrac{A_{22}}{A_{66}})\, m^6\,]} \tag{20B}$$

In order to display the effects of boundary conditions and normal pressure on ω^2_{mn} Equations (20B) may be written as

$$\omega^2_{mn} = a_{19} + a_{20}\, \beta^4 + a_{21}\, p \tag{21}$$

where

$$a_{18} = \rho\, h\, [\, a^4\, A_{22}\, (m^4 + m^2) + a^2\, D_{22}\, (1 + \frac{A_{22}}{A_{66}})\, m^6\,] \tag{22}$$

$$a_{19} = \frac{1}{a_{18}} [\, A_{22}\, D_{22}\, m^8 + A^2_{12}\, (\frac{D_{22}}{A_{22} + \frac{D_{22}}{a^2}})\, m^4 - (\frac{2D_{22}\, A^2_{22}}{A_{22} + \frac{D_{22}}{a^2}})\, m^6\,] \tag{23}$$

$$a_{20} = \frac{a^6\, A^*}{a_{18}\ell^4} \tag{24}$$

$$a_{21} = \frac{a^3\, A_{22}\, (m^4 - m^6)}{a_{18}} \tag{25}$$

From Equation (21) it is apparent that ω^2_{mn} varies linearly with the normal pressure p. Since a_{21} is negative, ω^2_{mn} decreases linearly with p. When ω^2_{mn} is reduced to zero, the pressure is the static buckling pressure for that mode. If p is increased past the static buckling pressure, ω^2_{mn} will become negative. In this case, by writing

$$\omega^2_{mn} = -\alpha^2_{mn} \tag{26}$$

the solution to Equation (19) in an interval where p is constant is

$$T_{mn}(t) = A_{mn} \exp(\alpha_{mn} t) + B_{mn} \exp(-\alpha_{mn} t) \tag{27}$$

When p does not exceed the static buckling pressure, ω^2_{mn} will be positive and the solution to Equation (19) in an interval where p is constant is

$$T_{mn}(t) = A_{mn} \cos \omega_{mn} t + B_{mn} \sin \omega_{mn} t \tag{28}$$

As intuition would suggest for an interval where p is constant, Equations (27) and (28) show that the amplitude of displacement in a mode increases only when the static buckling pressure for that mode has been exceeded.

When the static buckling pressure is exceeded by a pulse whose duration is τ seconds, the increasing exponential in Equation (27) increases by a factor

$$K = \exp(\alpha_{mn} \tau) \tag{29}$$

or

$$\frac{\tau}{\ell n K} = \frac{1}{\alpha_{mn}} \tag{30}$$

Thus a relationship between the normal pressure, the amount of time it exceeds the static buckling pressure and the growth of the displacement has been extablished. Clearly only the wave number m corresponding to the largest value of α_{mn}, i.e., the most negative ω^2_{mn} need be considered. Similarly only n = 1 need be considered since β_n increases monotonically with n.

COMPUTATIONAL ALGORITHM

A simple computational method for finding the growth of displacement when the pressure p exceeds the static buckling over an interval τ can now be stated.

1) Calculate the composite theory stiffness parameters A_{11}, A_{12}, A_{22}, A_{66}, A^*, and D_{22}.

2) For m = 2,3,4... plot ω^2_{mn} versus p using Equation (21). Continue until the wave number m is found that yields the minimum ω^2_{mn} for the desired normal pressure p is found. As noted above, only n = 1 need be considered.

3) For the desired value of pressure, read the minimum value of ω^2_{mn}. If this value is positive, there is no instability. If it is negative, calculate α_{mn}.

4) Using Equation (29), calculate the growth factor K.

NUMERICAL EXAMPLE

A fibrous composite cylinder of length ℓ = 49.0 in. and radius a = 7.0 in. is fabricated with five plies of graphite epoxy. Each ply has a thickness of 0.02 in. yielding h = 0.10 in. The outer plies are oriented along the axis of the cylinder (0°), while the three inner plies are oriented in the hoop direction. The following ply properties are assumed:

$E_1 = 25 \times 10^6$ lb/in^2

$E_2 = 1 \times 10^6$ lb/in^2

$G_{12} = 0.5 \times 10^6$ lb/in^2

$\gamma = 0.25$

$$\rho = 150 \times 10^{-6} \frac{\text{lb sec}^2}{\text{in}^4}$$

Find the growth factor when the pressure is 35 lb/in^2 for a duration of 2 msec for the case of simply supported (hinged) ends.

1) The values for the composite stiffness parameters are:

   $A_{11} = 1.06 \times 10^6$ lb/in

   $A_{12} = 0.012 \times 10^6$ lb/in

   $A_{22} = 1.54 \times 10^6$ lb/in

   $A^* = 1.63 \times 10^{12}$ lb^2/in^2

   $A_{66} = 0.05 \times 10^6$ lb/in

   $D_{22} = 516$ lb in

2) For simply supported ends, $\beta_1 = \pi$. Using Equations (21) through (25), the quantities in Table 1 were calculated. The results for ω^2_{mn} are plotted in Figure 2.

3) For p = 35 lb/in^2, $\omega^2_{mn} = -1.46 \times 10^6$ rad^2/sec^2 for m = 4 and α_{mn} = 1208 rad/sec.

4) From Equation (29), K = 11.2, i.e., a deflection will grow by a factor of approximately 11.2 during the 2 msec duration of the 35 lb/in^2 pressure pulse.

REFERENCES

1. J. C. Yao, "Dynamic Stability of Cylindrical Shells Under Static and Periodic Axial and Radial Loads," AIAA J. 1, 1391-1396 (1963).
2. R. J. Stuart, S. Dharmarajan, and L. E. Penzes, "Dynamic Stability of Fibrous Composite Cylinders," Proceedings of the Fourth Conference on Fibrous Composites in Structural Design, San Diego, November 1978.
3. W. H. Hoppman II, "Some Characteristics of the Flexural Vibrations of Orthogonally Stiffened Cylindrical Shells," J. Acoust. Soc. 30, 77-82 (1958).
4. L. E. Penzes, "Effect of Boundary Conditions on Flexural Vibrations of Thin Orthogonally Stiffened Cylindrical Shells," J. Acoust. Soc. 42, 901-903 (1967).
5. L. E. Penzes and H. Kraus, "Free Vibrations of Prestressed Cylindrical Shells Having Arbitrary Homogeneous Boundary Conditions," AIAA J. 10, 1309-1313 (1972).
6. L. E. Penzes and S. K. Bhat, "Generalized Hydrodynamic Effects of a Double Annulus on a Vibrating Cylindrical Shell," Proceedings of the Third International Conference on Structural Mechanics in Reactor Technology, London, September 1975.
7. R. M. Jones, Mechanics of Composite Materials, McGraw-Hill (1975).
8. R. L. Bisplinghoff, H. Ashley, and R. L. Halfmann, Aeroelasticity, Addison-Wesley (1955).

m	a_{18}, $lb^2 sec^2$	a_{19}, $\frac{1}{sec^2}$	a_{20}, $\frac{1}{sec^2}$	a_{21}, $\frac{in^2}{lb\ sec^2}$	ω^2_{mn} rad^2/sec^2
2	1.11×10^6	91.7×10^3	30.0×10^3	-22.8×10^3	$2.77 \times 10^6 - 22.8 \times 10^3 p$
3	5.00×10^6	811×10^3	6.65×10^3	-68.5×10^3	$1.46 \times 10^6 - 68.5 \times 10^3 p$
4	15.1×10^6	3.02×10^6	2.20×10^3	-134×10^3	$3.23 \times 10^6 - 134 \times 10^3 p$

TABLE 1 Numerical Example

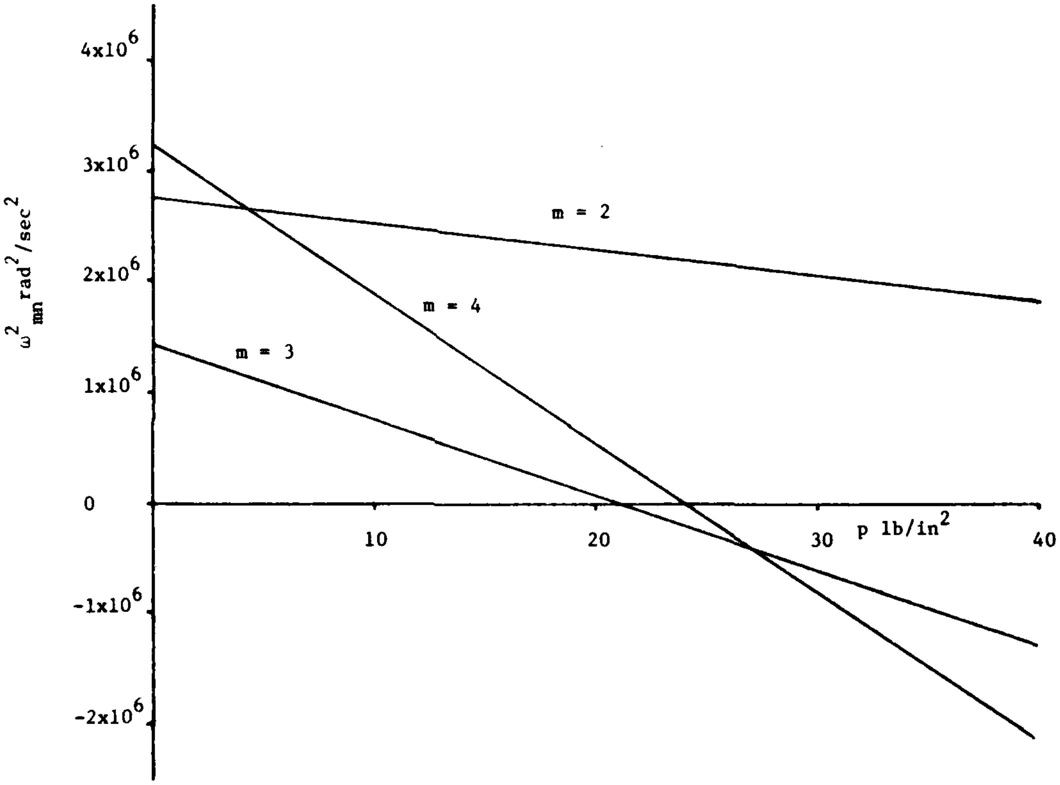

Figure 2. ω^2_{mn} for simply supported ends.

TRANSFER-MATRIX ANALYSIS OF DYNAMIC RESPONSE OF COMPOSITE-MATERIAL STRUCTURAL ELEMENTS WITH MATERIAL DAMPING

M. M. Wallace and C. W. Bert
The University of Oklahoma
Norman, Oklahoma

A simple one-dimensional finite-element technique utilizing transfer-matrix analysis is used to calculate the flexural and torsional natural frequencies for specimens made from planar anisotropic materials. The theory is based on Lekhnitskii's theory for static torsional-flexural coupling and Timoshenko's beam theory for transverse shear and rotatory inertia. This method was used to evaluate a specific structural element with length-to-width ratio of 6.6. This particular structural element was previously investigated experimentally and analytically as a thin-plate element. Good agreement among all of the techniques for natural frequencies and the associated nodal contours was demonstrated.

INTRODUCTION

The increasing demand for light-weight but strong structural elements in advanced aerospace vehicles has resulted in the increasing use of advanced composite materials, such as boron-aluminum, graphite-epoxy, and boron-epoxy. It has become extremely important to be able to predict the dynamic response (including the effect of material damping) in addition to the more common static and buckling behavior for composite structures elements. One cannot directly relate dynamic and damping experience for metal structural elements to prediction of dynamic response of composite structural elements, since the relative stiffnesses are quite different and other effects (i.e., bending-twisting coupling, transverse shear deformation, etc.) come into play. These factors make the dynamic analysis of structural elements made of composite materials more complicated than for homogeneous, isotropic-material elements.

Most general forced-vibration analysis techniques are rather complicated and sometimes difficult to formulate in the case of composite materials, but the formulation described in this paper is a simple finite-element technique employing the transfer-matrix approach to calculate the response spectrum for specimens with planar anisotropic symmetry.

The prediction of vibrational behavior of a composite-material component necessitates the incorporation of perturbations in the torsional and flexural resonant frequencies due to the coupling of normal and shear stresses. The method of using a simple finite-element technique for dynamic analysis was pioneered by Myklestad [1]. Later Pestel and Leckie [2] applied this method, better known as the transfer-matrix technique, to many varied engineering problems. The work done by Pestel and Leckie was strictly Bernoulli-Euler type beam analysis, i.e., transverse-shear deformation and rotatory-inertia effects were omitted. In 1972 Abarcar and Cunniff [3] showed that Timoshenko's theory of flexure [4] and Lekhnitskii's theory of static torsional-flexural coupling [5] could be incorporated into the transfer-matrix technique. More recently Ritchie, Rosinger, and Fleury [6] reconfirmed the incorporation of Timoshenko's and Lekhnitskii's theories into this method. They also extended the application from that for fixed-free (cantilever) resonant modes for a beam with orthotropic symmetry to that for a beam with planar anisotropic symmetry vibrating in free-free resonant modes.

In the present paper, the material model employed for the composite material is the complex-modulus model. In this model, the real material moduli are replaced by complex moduli of the form

$$E(1 + ig)$$

Here E may be either a Young's modulus or a shear modulus and g is the loss tangent for that particular modulus. We know from experience that the material properties vary with frequency as shown by Chang and Bert [7] and that the complex-modulus model does not take into account varying frequency. However, in this paper, the structural element in question was excited by a sinusoidally varying force, and we are verifying the response at certain discrete frequencies, not over a random-frequence spectrum.

THEORY

Due to the coupling between normal and shear stresses, a beam made of material with planar anisotropic symmetry and subjected to a bending moment will exhibit concurrent bending and twisting. Also a beam subjected to a torque will also respond with joint bending and twisting. Lekhnitskii [5] has derived equations for the relative deflection (v) and relative angle of twist ($\bar{\phi}$) for a cantilever beam (Fig. 1) with general anisotropy subjected to both bending and twisting moments. These equations reduce to the following when the beam is planar anisotropic

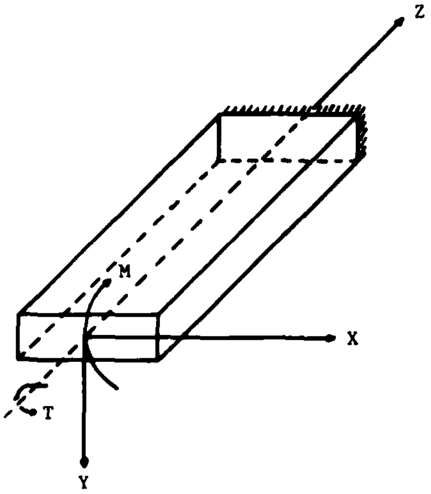

Fig. 1 - Lekhnitskii Cantilever Beam Subjected to Joint Bending Twisting Moments

$$v = \frac{-1}{2I_x}\left(MS'_{33} - \frac{TS'_{35}}{2}\right)(\ell - z)^2 \tag{1}$$

and

$$\bar{\phi} = \frac{T}{C_T} - \frac{MS'_{35}}{2I_x} \tag{2}$$

However, the beam element that is utilized in this paper is the one depicted in Fig. 2. Therefore, Eqs. (1) and (2) become

$$v = \frac{-1}{2I_x}\left(MS'_{33} - \frac{TS'_{35}}{2}\right)(z')^2 \tag{3}$$

and

$$\bar{\phi} = \frac{T}{C_T} - \frac{MS'_{35}}{2I_x} \tag{4}$$

It was assumed by Ritchie, et al. [6] that Eqs. (3) and (4), which represent the static theory of torsional-flexural coupling, can be used without modification to describe a differential beam element subjected to dynamic bending moments and torques.

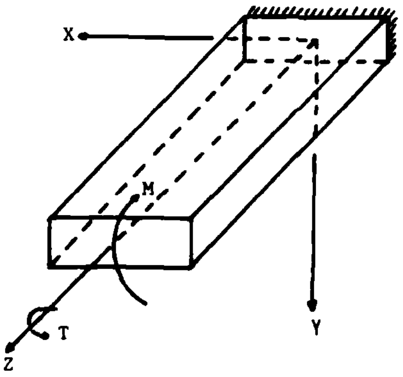

Fig. 2 - Present Cantilever Beam Subjected to Joint Bending and Twisting Moments

In Timoshenko beam theory [4], the shear forces contribute to the slope of the beam element and this change in slope is given by the following equation:

$$\alpha = \frac{V}{KG_{zy}A} \tag{5}$$

One can show that, for harmonic excitation, the equilibrium conditions as shown in Fig. 3 lead to six coupled equations of motion

$$\frac{dv}{dz} = \psi - \frac{V}{KG_{zy}A} \tag{6}$$

$$\frac{d\psi}{dz} = -\frac{MS'_{33}}{I_x} + \frac{TS'_{35}}{2I_x} \tag{7}$$

$$\frac{dV}{dz} = m\omega^2 v \tag{8}$$

$$\frac{dM}{dz} = V - m\omega^2 K_x^2 \psi \tag{9}$$

$$\frac{d\phi}{dz} = \frac{T}{C_T} - \frac{MS'_{35}}{2I_x} \tag{10}$$

$$\frac{dT}{dz} = -I_{pi}\,\omega^2\phi \tag{11}$$

In the transfer-matrix technique, the inertial and elastic properties of a vibrating beam element are considered separately. The beam is divided up into "N" masses each of which is concentrated in the middle of a massless beam element of length

$$\Delta ZI = \ell/N \tag{12}$$

The points at which the masses are concentrated are called stations while the massless beam element between two adjacent stations is

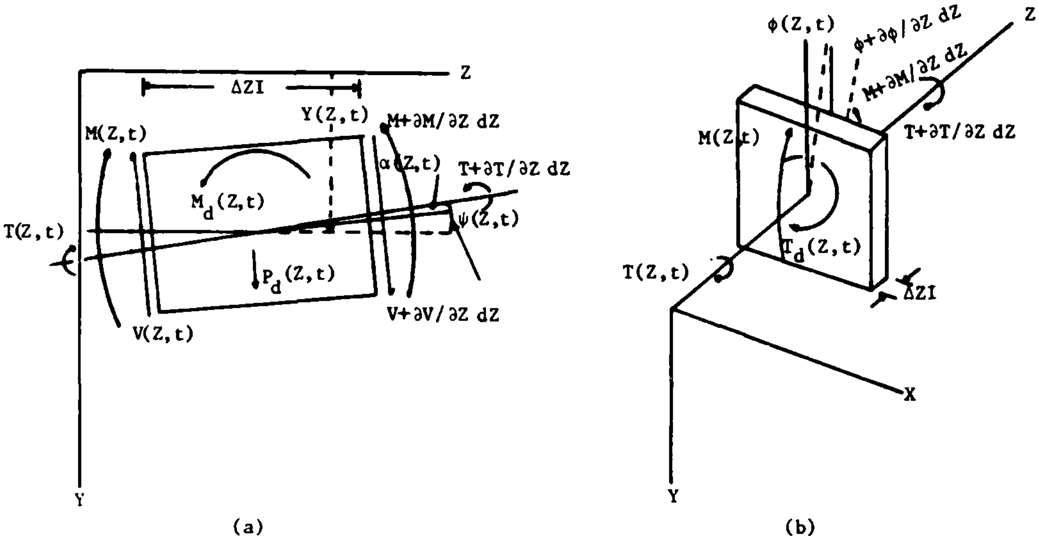
Z
ΔZI
Y(Z,t)
M(Z,t)
M+∂M/∂Z dZ
α(Z,t)
T+∂T/∂Z dZ
M_d(Z,t)
T(Z,t)
ψ(Z,t)
P_d(Z,t)
V(Z,t)
V+∂V/∂Z dZ
Y
(a)
φ(Z,t)
φ+∂φ/∂Z dZ
Z
M+∂M/∂Z dZ
M(Z,t)
T+∂T/∂Z dZ
T_d(Z,t)
T(Z,t)
ΔZI
X
Y
(b)

Fig. 3 - (a) Flexural Configuration of a Beam Element; (b) Torsional Configuration of a Beam Element

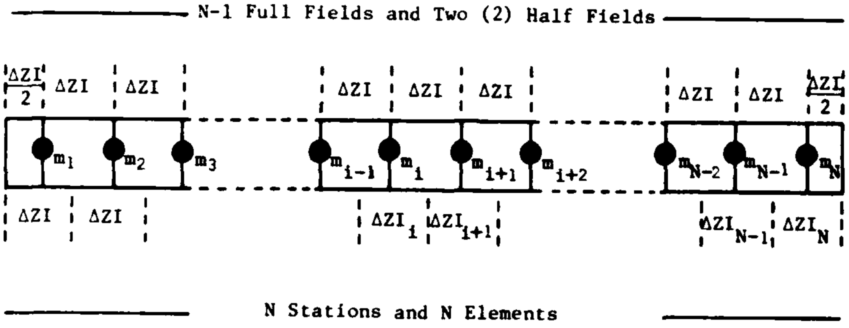
N-1 Full Fields and Two (2) Half Fields
ΔZI/2
ΔZI
ΔZI
ΔZI
ΔZI
ΔZI
ΔZI
ΔZI
ΔZI/2
m1
m2
m3
mi-1
mi
mi+1
mi+2
mN-2
mN-1
mN
ΔZI
ΔZI
ΔZIi
ΔZIi+1
ΔZIN-1
ΔZIN
N Stations and N Elements

Fig. 4 - Field and Station Model of a Beam

called a field (Fig. 4). The transfer-matrix technique utilizes field and station matrices which transfer the displacements (v,ψ,φ) and forces (M,V,T) from the left side of the field or station to the right side of the same field or station.

Figure 5 shows the flexural and torsional configuration of the i-th station. Mass m_i is a point rotatable mass which does not undergo any elastic deformation; therefore, from equilibrium and continuity considerations of Fig. 5 the following were derived

$$v_i^L = v_i^R = v_i \qquad (13)$$

$$\psi_i^L = \psi_i^R = \psi_i \qquad (14)$$

$$\phi_i^L = \phi_i^R = \phi_i \qquad (15)$$

$$M_i^L = M_i^R + m_i K_x^2 \omega^2 \psi_i \qquad (16)$$

$$V_i^L = V_i^R - m_i \omega^2 v_i \qquad (17)$$

$$T_i^L = T_i^R + I_{pi} \omega^2 \phi_i \qquad (18)$$

The above equations, when non-dimensionalized by using the techniques outlined in Pestel and Leckie's book [2], can then be put into the following matrix notation

$$\begin{bmatrix} v' \\ \psi' \\ \phi' \\ M' \\ V' \\ T' \end{bmatrix}_i^R = \begin{bmatrix} 1 & 0 & 0 & 0 & 0 & 0 \\ 0 & 1 & 0 & 0 & 0 & 0 \\ 0 & 0 & 1 & 0 & 0 & 0 \\ 0 & C_2 & 0 & 1 & 0 & 0 \\ C_1 & 0 & 0 & 0 & 1 & 0 \\ 0 & 0 & C_3 & 0 & 0 & 1 \end{bmatrix} \begin{bmatrix} v' \\ \psi' \\ \phi' \\ M' \\ V' \\ T' \end{bmatrix}_i^L \qquad (19)$$

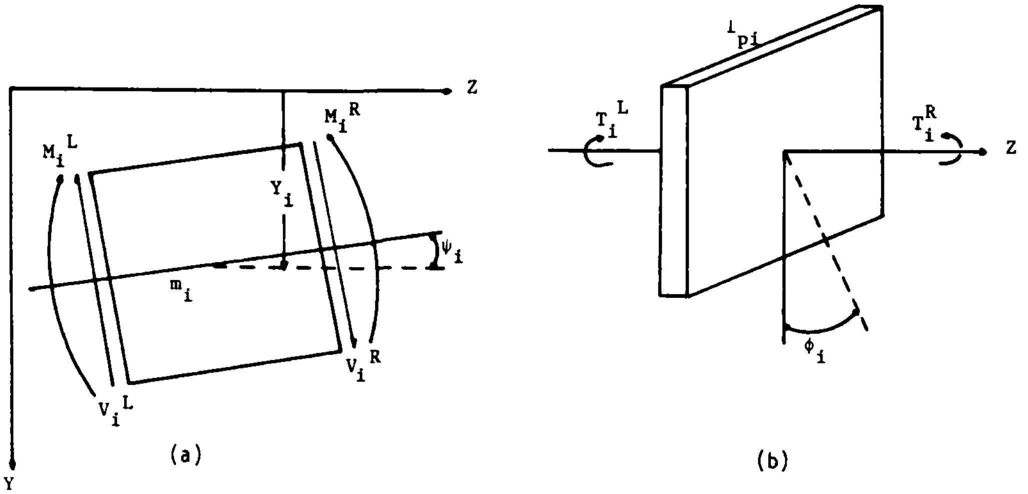
Z
M_i^L
M_i^R
Y_i
ψ_i
m_i
V_i^R
V_i^L
(a)
Y
I_{pi}
T_i^L
T_i^R
Z
ϕ_i
(b)

Fig. 5 - (a) Flexural Configuration of Station i; (b) Torsional Configuration of Station i

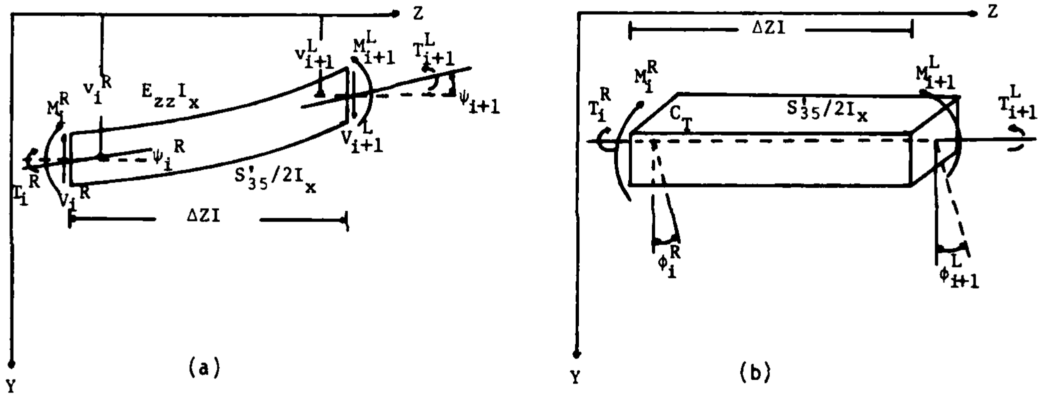
Z
v_{i+1}^L
M_{i+1}^L
T_{i+1}^L
M_i^R
v_i^R
$E_{zz}I_x$
ψ_{i+1}
V_{i+1}^L
ψ_i^R
T_i^R
V_i^R
$S'_{35}/2I_x$
ΔZI
(a)
Y
Z
ΔZI
M_i^R
T_i^R
C_T
$S'_{35}/2I_x$
M_{i+1}^L
T_{i+1}^L
ϕ_i^R
ϕ_{i+1}^L
Y
(b)

Fig. 6 - (a) Flexural Configuration of Field i; (b) Torsional Configuration of Field i

where

$$C_1 = m_i \omega^2 (\Delta ZI)^3 / E_{zz} I_x$$

$$C_2 = m_i \omega^2 \Delta ZI / E_{zz} A \qquad (20)$$

$$C_3 = - I_{pi} \omega^2 \, \Delta ZI / 2I_x$$

which can also be written as

$$[S]_i^R = [T_s]_i \, [S]_i^L \qquad (21)$$

Figure 6 illustrates the torsional and flexural configuration for the i-th massless beam element (field). Here $[S]_i^R$ (station i) = $[S]_i^L$ (field i) and $[S]_i^R$ (field i) = $[S]_{i+1}^L$ (station i+1). The total deflection of the right end of field i is determined by calculating the displacement of the right end relative to the left end together with the displacement of the left end. Therefore, the total deflection is equal to the sum of the displacement of the left end, slope at the left end times the length, the deflection at the right end due to bending-twisting coupling [Eq.(3)], the transverse shear displacement [Eq.(5)], and the deflection due to the shear load on the left end. Thus

$$v_{i+1}^L = v_i^R - \psi_i^R \Delta ZI - \frac{M_{i+1}^L (\Delta ZI)^2}{2E_{zz} I_x} + \frac{T_{i+1}^L S'_{35} (\Delta ZI)^2}{2I_x} + \frac{V_{i+1}^L (\Delta ZI)^3}{3E_{zz} I_x} + \frac{V_{i+1}^L \, \Delta ZI}{KG_{zy} A} \qquad (22)$$

From Eq. (7) the following equation can be written by taking an average of the moments and torques at each end of the field

$$\psi_{i+1}^L = \psi_i^R + \frac{\Delta ZI (M_i^R + M_{i+1}^L)}{2E_{zz} I_x} - \frac{\Delta ZI \; S'_{35} (T_i^R + T_{i+1}^L)}{4I_x} \qquad (23)$$

From Fig. 6 (a,b) the following equilibrium considerations are evident

$$V_{i+1}^{L} = V_{i}^{R} \tag{24}$$

$$M_{i+1}^{L} = M_{i}^{R} + V_{i}^{R}\,\Delta ZI \tag{25}$$

$$T_{i+1}^{L} = T_{i}^{R} \tag{26}$$

and from Eq. (9) it is found that

$$\phi_{i+1}^{L} = \phi_{i}^{R} + \frac{(T_{i+1}^{L} + T_{i}^{R})\Delta ZI}{2C_T} - \frac{\Delta ZI\ S'_{35}(M_{i}^{R} + M_{i+1}^{L})}{4I_x} \tag{27}$$

Using the same non-dimensionalization technique and matrix techniques, one can rearrange Eq. (22)-(27) to give

$$\begin{bmatrix} V' \\ \psi' \\ \phi' \\ M' \\ V' \\ T' \end{bmatrix}_{i+1}^{L} = \begin{bmatrix} 1 & -\beta & 0 & F_1 & F_2 & F_3 \\ 0 & 1 & 0 & -\beta & F_1 & F_4 \\ 0 & 0 & 1 & F_5 & F_6 & F_7 \\ 0 & 0 & 0 & 1 & \beta & 0 \\ 0 & 0 & 0 & 0 & 1 & 0 \\ 0 & 0 & 0 & 0 & 0 & 1 \end{bmatrix} \begin{bmatrix} V' \\ \psi' \\ \phi' \\ M' \\ V' \\ T' \end{bmatrix}_{i}^{R} \tag{28}$$

where

$$\begin{aligned} F_1 &= -\beta^2/2 \\ F_2 &= [(\beta E_{zz}\cdot I_x)/(K\cdot G_{zy}\cdot A\cdot \Delta ZI^2)] - \beta^3/6 \\ F_3 &= \beta^2 S'_{35}/2 \\ F_4 &= \beta S'_{35} \\ F_5 &= -\beta S'_{35}E_{zz}/2 \\ F_6 &= -\beta^2 S'_{35}E_{zz}/4 \\ F_7 &= 2\beta I_x/C_T \end{aligned} \tag{29}$$

and where $\beta=1$ for a full field between stations and $\beta={}^1/2$ for the half fields on each end of the beam.

Equations (19) and (28) can now be used to calculate the resonant frequencies and the associated mode shapes. The boundary conditions for the beam for free-free modes are

$$[S]_0^R = \begin{bmatrix} V' \\ \psi' \\ \phi' \\ 0 \\ 0 \\ 0 \end{bmatrix}_0^R \quad ; \quad [S]_{N+1}^L = \begin{bmatrix} V' \\ \psi' \\ \phi' \\ 0 \\ 0 \\ 0 \end{bmatrix}_{N+1}^L \tag{30}$$

The boundary conditions along with the station and field matrices, Eqs. (19) and (28), can be used to give the relationship between the ends of the beams by systematically applying the matrices to each station and field as follows

$$[S]_{N+1}^{L} = [T_f]_{\beta=1/2}\,[T_s]\,\prod_{i=1}^{N-1}\{[T_f]_{\beta=1}\,[T_s]\}_i\ [T_f]_{\beta=1/2}\,[S]_o^R \tag{31}$$

which can be written as

$$[S]_{N+1}^{L} = [B][S]_o^{R} \tag{32}$$

Here [B] is a six-by-six beam matrix. Equation (32) holds for the free-free mode, only if

$$\mathrm{DET}\begin{vmatrix} B_{41} & B_{42} & B_{43} \\ B_{51} & B_{52} & B_{53} \\ B_{61} & B_{62} & B_{63} \end{vmatrix} = 0 \tag{33}$$

Therefore, the frequencies can be varied until the DET = 0, thereby giving the resonant frequencies for the beam. Once the resonant frequencies have been determined, the generalized displacements v_i', ϕ_i', and ψ_i' at each station can be calculated, and hence the mode shapes for each resonant frequency by arbitrarily setting v_o' equal to 1.0 and hence ψ_o' and ϕ_o' are calculated from

$$\begin{bmatrix} B_{41} & B_{42} & B_{43} \\ B_{51} & B_{52} & B_{53} \\ B_{61} & B_{62} & B_{63} \end{bmatrix} \begin{bmatrix} 1 \\ \psi_o' \\ \phi_o' \end{bmatrix} = \begin{bmatrix} 0 \\ 0 \\ 0 \end{bmatrix} \tag{34}$$

Finally the rest of the generalized displacements are calculated as follows

$$\begin{bmatrix} V' \\ \psi' \\ \phi' \end{bmatrix}_1 = [T_s][T_f]_{\beta=1/2}\,[S]_0$$

$$\begin{bmatrix} v' \\ \psi' \\ \phi' \end{bmatrix}_2 = [T_s][T_f]_{\beta=1}\,[T_s][T_f]_{\beta=1/2}\,[S]_0$$

$$\vdots \tag{35}$$

$$\begin{bmatrix} v' \\ \psi' \\ \phi' \end{bmatrix}_{N+1} = [T_f]_{\beta=1/2}\cdots[T_s][T_f]_{\beta=1/2}\,[S]_0$$

Now that the resonant frequencies and mode shapes for a free-free, nonforced beam have been found, the damping ratio for a forced vibration, free-free beam problem can be calculated, since material damping does not affect frequency and mode shape. First, the station and field transfer matrices are expanded to include damping and the force terms. The matrices are of the form

$$[B]^* = \left[\begin{array}{c|c|c} B^R & -B^I & F^R \\ \hline B^I & B^R & F^I \\ \hline 0 & 0 & 1 \end{array}\right] \tag{36}$$

Here B^R and B^I are the real and imaginary parts of the previously defined beam matrix with all of the material constants replaced by their complex forms, F^R and F^I are the real and imaginary parts of the forcing term.

The Pendered-Bishop modification [10] of the Kennedy-Pancu method [11] defines the resonant frequency (ω_R) as the point on the argand-plot curve where the arc length change (ΔS) is maximum for a fixed incremental change in frequency ($\Delta\omega$). When $\Delta S/\Delta\omega$ is plotted versus frequency, the resonant frequencies correspond to the maximum points on the plot. The quantity $\Delta S/\Delta\omega$ is defined as

$$\Delta S/\Delta\omega \equiv (v_{i\,\mathrm{max}}/\tilde{q})\cdot(\Delta\phi^*/\Delta\omega) \tag{37}$$

where $\phi_i^* = \tan^{-1}(v_i{}^I\mathrm{max}/v_i{}^R\mathrm{max})$ and $\Delta\phi^* = \phi_{i+1}^* - \phi_i^*$. Once the Kennedy-Pancu resonant frequencies have been determined, the corresponding damping ratios (ζ) are calculated by

$$\zeta = [\omega_R(\Delta\phi^*/\Delta\omega)_R]^{-1} \tag{38}$$

where $\omega_R \equiv$ resonant frequency and $(\Delta\phi/\Delta\omega)_R \equiv$ phase angle change per fixed change in frequency at resonance.

RESULTS AND DISCUSSION

A boron-fiber/epoxy plate having free edges and consisting of twenty-four parallel plies was analyzed as a beam. The unidirectional plies were oriented at various angles to the longitudinal axis of the beam. The computer program used as input data, Young's and shear moduli (E_{11}, E_{22}, G_{12}, G_{23}, G_{31}), major Poisson's ratio (ν_{12}) and their corresponding loss tangents, which were generated by Chang and Bert [7](Table 1). The size, shape, and orientation of the beam corresponded to the plate used by Clary [8] as follows:

TABLE 1
Material Properties

Material Property and Units	Frequency Range (Hz)			
	40-205	205-370	370-535	535-700
E_{11} - GN/m^2 (x 10^6psi)	184.10 (25.8)	182.00 (25.5)	179.95 (25.2)	177.70 (24.9)
gE_{11} - %	0.153	0.160	0.164	0.169
E_{22} - GN/m^2 (x 10^6psi)	8.2 (1.15)	7.9 (1.10)	7.5 (1.05)	7.1 (1.00)
gE_{22} - %	1.8	2.0	2.2	2.4
G_{12} - GN/m^2 (x 10^6psi)	4.6 (0.65)	4.3 (0.6)	3.6 (0.5)	3.2 (0.45)
gG_{12} - %	1.96	2.08	2.20	2.30
ν_{12} - dimensionless	0.275	0.275	0.260	0.250
$g\nu_{12}$ - %	0.055	0.055	0.055	0.055
G_{31} - GN/m^2 (x 10^6psi)	2.8 (.395)	2.8 (.395)	2.8 (.395)	2.7 (.385)
gG_{31} - %	0.125	0.18	0.18	0.185
G_{23} - GN/m^2 (x 10^6psi)	5.7 (0.8)	5.4 (0.76)	5.1 (0.71)	4.6 (0.65)
gG_{23} - %	0.255	0.285	0.315	0.345

TABLE 2

Natural Frequencies for Laminate Composite Plates

Angle (Deg)	Mode No.	Freq(Hz) Ref.[8][1]	Freq(Hz) Ref.[9]	Freq(Hz) Present Results
0	1	141.8	140.0	136.8
	2	182.2	170.4	153.4
	3	386.2	360.1	306.7
	4	401.1	390.2	375.2
	5	649.5	639.6	629.6
10	1	100.6	92.0	92.1
	2	234.0	225.2	224.6
	3	275.2	265.5	232.5
	4	485.3	495.0	425.8
	5	523.4	511.0	494.8
30	1	57.2	58.7	51.5
	2	163.4	165.0	139.9
	3	314.9	320.0	283.1
	4	378.4	387.2	358.3
	5	534.2	565.0	446.6
45	1	46.2	45.1	43.3
	2	131.4	124.0	119.1
	3	257.6	251.0	232.2
	4	278.4	293.4	292.1
	5	433.3	430.0	392.8
60	1	44.1	42.3	42.4
	2	127.0	122.0	116.9
	3	226.8	288.1	223.1
	4	239.9	237.5	230.0
	5	405.1	401.5	387.9
90	1	48.0	48.0	48.2
	2	137.6	136.1	132.7
	3	188.9	164.4	154.3
	4	250.9	259.0	260.0
	5	331.7	331.0	308.6

Thickness, a = 2.74 mm (0.111 in.)
Width, b = 69.8 mm (2.75 in.)
Length, c = 462 mm (18.19 in.)
Density, ρ = 0.00208 gm/mm^3 (0.000194 lb-sec^2/in.^{4})
Fiber volume fraction, 0.48 to 0.50

Comparison of the frequency results obtained by Clary [8], Siu and Bert [9], and the present method is given in Table 2. The associated mode shapes are presented in Figs. 7-12, while the associated damping ratios are presented in Table 3. There is very good agreement among the two plate analyses and the present beam analysis of the same composite-material structural element. The length-to-width ratio of the structural element was 6.6 which is less than that usually accepted (10) for a beam.

It should also be noted that the transfer-matrix technique necessitates the use of repeatedly calculating Eq. (33) until it approaches zero. This iterative technique is extremely sensitive to the frequency increment used. Extreme care should be exercised in selecting the frequency increment since the value of the determinant could pass through zero twice within a frequency increment.

TABLE 3

Damping Ratio

Angle (Deg)	Mode No.	Damping Ratio (%) Clary [8][1]	Siu & Bert [7]	Present
0	1	0.1	0.22	0.21
	2	1.9	1.83	1.71
	3	0.9	0.97	0.82
	4	0.2	0.24	0.22
	5	1.4	0.95	0.92
10	1	0.6	1.19	1.16
	2	3.4	1.28	1.32
	3	0.9	1.06	0.93
	4	1.6	1.09	1.40
	5	0.9	0.66	0.61
30	1	1.0	1.37	1.21
	2	1.0	0.82	0.71
	3	1.1	1.03	0.97
	4	1.6	1.64	1.54
	5	1.4	0.97	1.10
45	1	0.9	0.98	0.93
	2	1.2	1.25	1.27
	3	1.1	0.95	0.93
	4	2.2	1.59	1.63
	5	1.5	1.18	1.09
60	1	0.9	1.00	0.98
	2	1.5	1.60	1.53
	3	3.9	2.05	2.16
	4	1.1	1.06	1.14
	5	1.5	1.17	1.22
90	1	0.8	0.87	0.84
	2	1.2	1.23	1.16
	3	5.3	3.31	3.45
	4	1.0	1.10	1.14
	5	2.1	1.98	1.91

CONCLUSION

The transfer-matrix technique was used to determine the sinusoidal response of a laminated anisotropic beam (including the effects of transverse shear deformation, material damping, and rotatory inertia) that had the same dimensions as a plate analyzed by Clary [8] and Siu and Bert [9].

The first five resonant frequencies were calculated for a beam free on both ends. The associated mode shapes and damping ratios were also calculated. The only significant deviation from the previously determined results were the mode shapes for the second, third, and fifth resonant frequencies for the zero-degree and ninety-degree orientations. This was because these mode shapes are pure plate bending modes. Therefore, it has been shown that the analysis of a thin plate with a length-to-width ratio less than the more commonly accepted value of ten, namely 6.6, is feasible and that the transfer-matrix technique can be used to determine damping ratios.

---

[1] Data shown are those obtained through Clary's experiments.

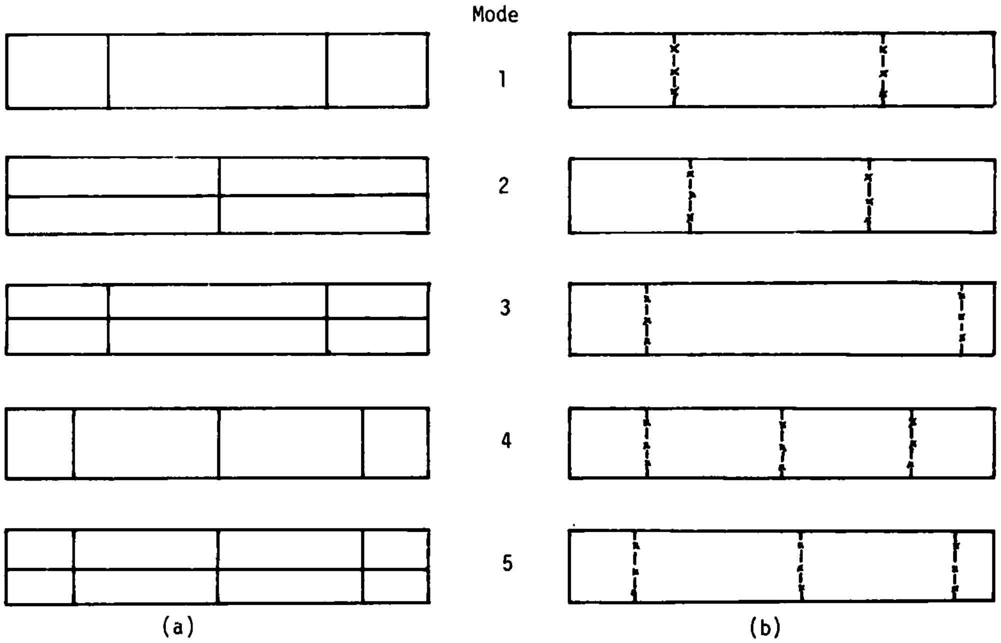

Figure 7. Nodal Pattern of First Five Modes with Fiber Orientation θ=0 deg; (a) Plate Analysis by Clary, and Siu and Bert; (b) Beam Analysis of Plate by Transfer-Matrix Techniques

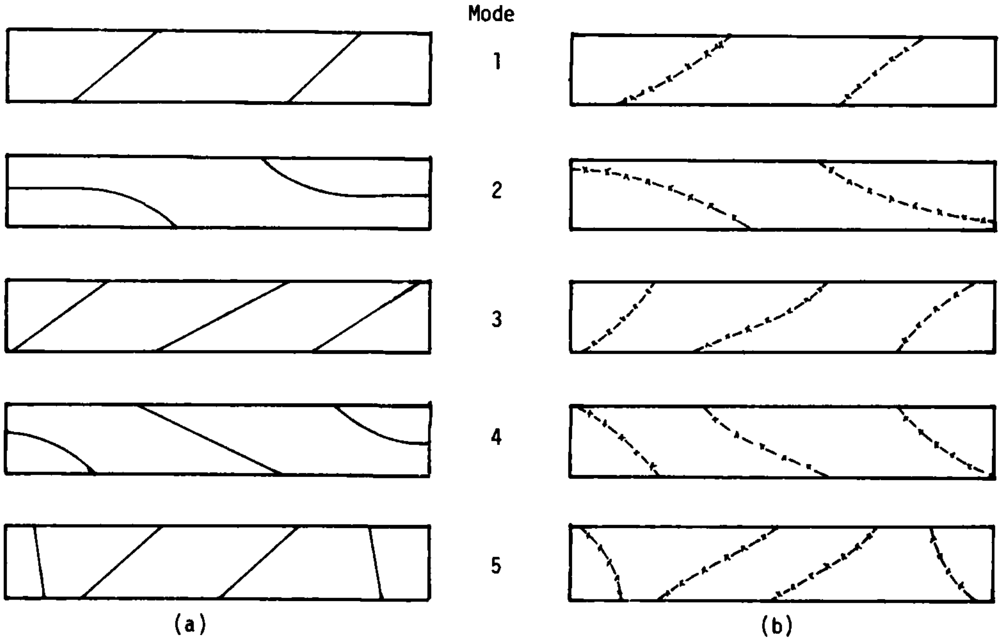

Figure 8. Nodal Pattern of First Five Modes with Fiber Orientation θ=10 deg; (a) Plate Analysis by Clary, and Siu and Bert; (b) Beam Analysis of Plate by Transfer-Matrix Techniques

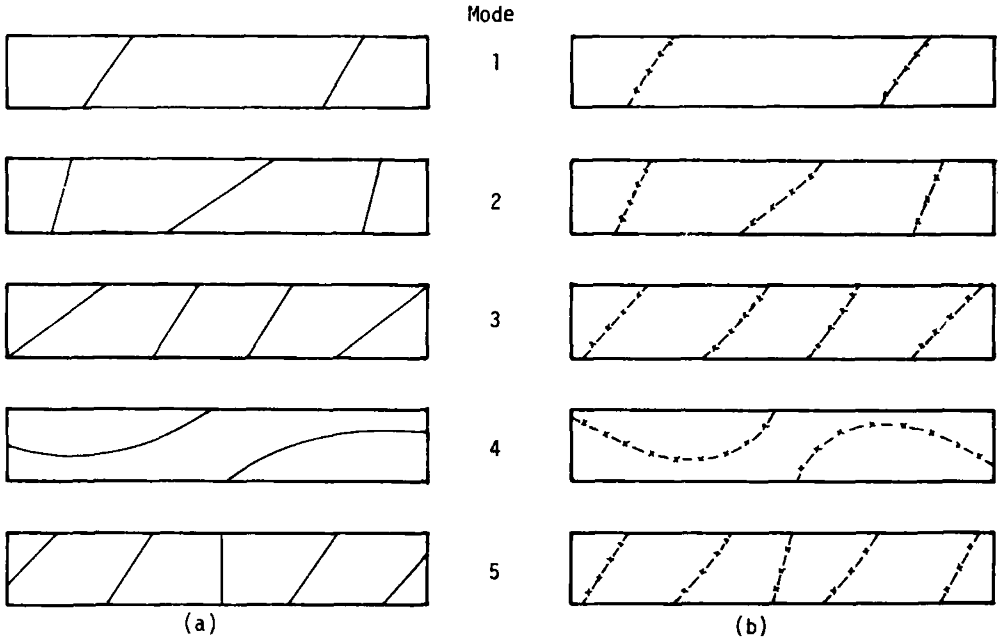

Figure 9. Nodal Pattern of First Five Modes with Fiber Orientation θ=30 deg; (a) Plate Analysis by Clary, and Siu and Bert; (b) Beam Analysis of Plate by Transfer-Matrix Techniques

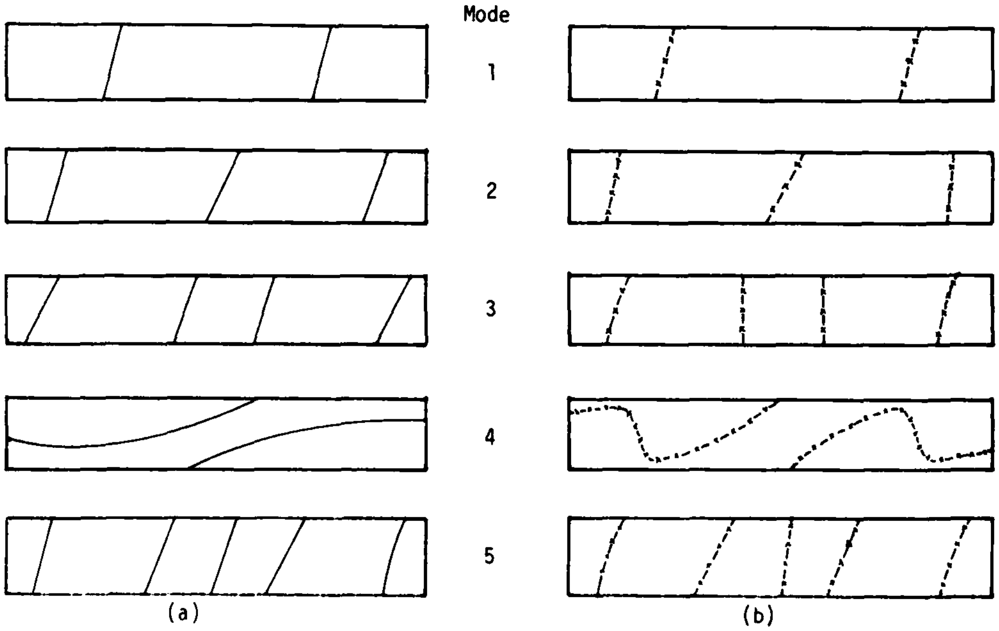

Figure 10. Nodal Pattern of First Five Modes with Fiber Orientation θ=45 deg; (a) Plate Analysis by Clary, and Siu and Bert; (b) Beam Analysis of Plate by Transfer-Matrix Techniques

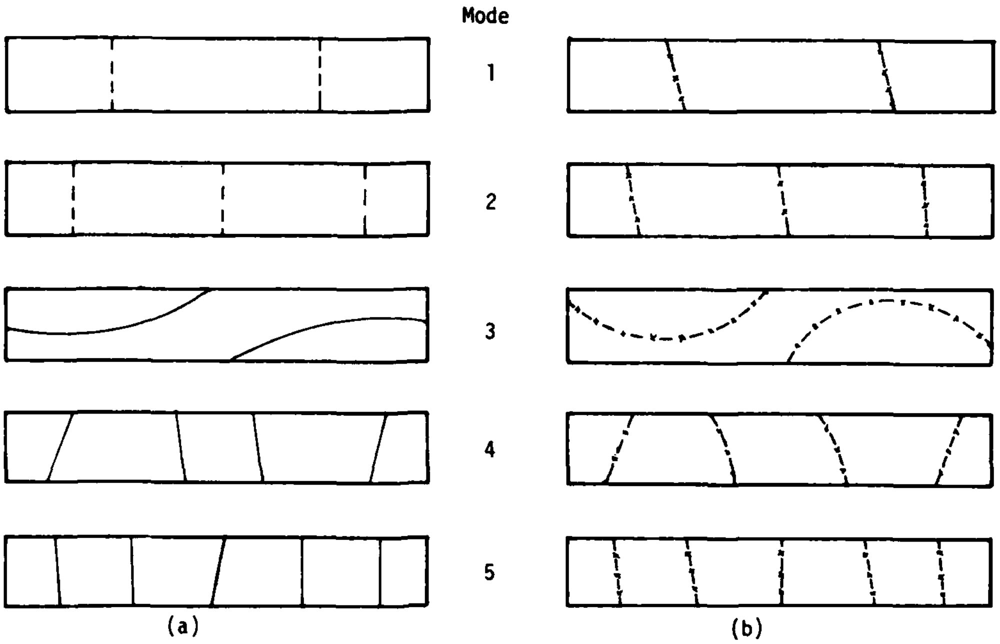

Figure 11. Nodal Pattern of First Five Modes with Fiber Orientation θ=60 deg; (a) Plate Analysis by Clary, and Siu and Bert; (b) Beam Analysis of Plate by Transfer-Matrix Techniques

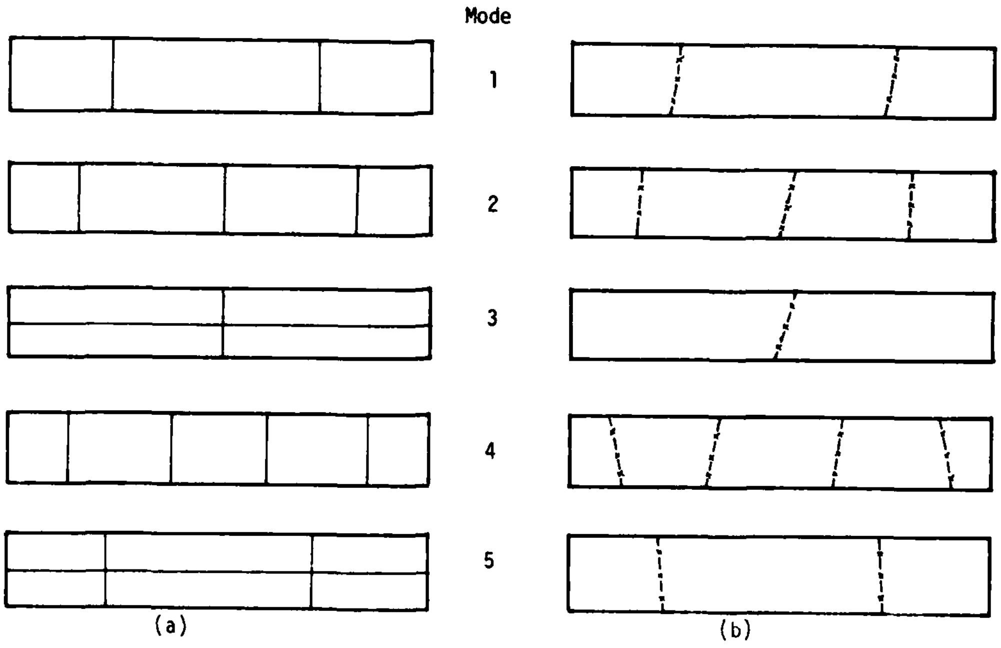

Figure 12. Nodal Pattern of First Five Modes with Fiber Orientation θ=90 deg; (a) Plate Analysis by Clary, and Siu and Bert; (b) Beam Analysis of Plate by Transfer-Matrix Techniques

REFERENCES

1. N.O. Myklestad,"Fundamentals of Vibration Analysis," McGraw-Hill, New York, 1956.

2. E.C. Pestel and F.A. Leckie, "Matrix Methods in Elastomechanics," McGraw-Hill, New York, 1963.

3. R.B. Abarcar and P.F. Cunniff, "The Vibrations of Cantilever Beams of Fiber Reinforced Materials", J. Composite Materials, Vol. 6, 1972, pp. 504-517

4. S.P. Timoshenko, "Vibration Problems in Engineering," 3rd ed., Van Nostrand, Princeton, NJ, 1955, pp. 312-313.

5. S.G. Lekhnitskii, "Theory of Elasticity of an Anisotropic Body," Holden-Day, San Francisco, 1963, sections 27 and 28.

6. I.G. Ritchie, H.E. Rosinger, and W.H. Fleury, "Dynamic Elastic Behavior of a Fibre Reinforced Composite Sheet. Part 2: Transfer Matrix Calculation of the Resonant Frequencies and Vibrational Shapes," J. Physics D: Applied Physics, Vol. 8, 1975, pp. 1750-1768.

7. S. Chang and C.W. Bert, "Analysis of Damping for Filamentary Composite Materials", Composite Materials in Engineering Design (Proc. 6th St. Louis Symposium, 1972), Amer. Soc. for Metals, Metals Park, OH, 1973, pp. 51-62.

8. R.R. Clary, "Vibration Characteristics of Unidirectional Filamentary Composite Material Panels," Composite Materials: Testing and Design (Second Conference), American Society for Testing and Materials, Special Technical Publication 497, 1972, pp. 415-438.

9. C.C. Siu and C.W. Bert, "Sinusoidal Response of Composite-Material Plates with Material Damping," J. of Engineering for Industry, Trans. ASME, Vol. 96B, May 1974, pp. 603-610.

10. J.W. Pendered and R.E.D. Bishop, "Critical Introduction to Some Industrial Resonance Testing Techniques," J. of Mechanical Engineering Science, Vol. 5, 1963, pp. 345-367.

11. C.C. Kennedy and C.D.P. Pancu, "Use of Vectors in Vibration Measurement and Analysis," J. of Aeronautical Sciences, Vol. 14, 1947, pp. 603-630.

NOMENCLATURE

$[B]^*$ = expanded beam matrix

$[B]$ = beam matrix

$[S]$ = state vector containing generalized displacements and forces in the system

$$[S] = \left[\begin{array}{c} v' \\ \psi' \\ \phi' \\ M' \\ V' \\ T' \end{array}\right] \begin{array}{l} \text{displacement of beam} \\ \text{angle of rotation due to bending} \\ \text{angle of twist} \\ \text{bending moment} \\ \text{shear force} \\ \text{torque} \end{array}$$

$[T_f]$ = field transfer matrix

$[T_s]$ = station transfer matrix

A = cross-sectional area of the beam

C_i = constants defined in equations (20); $i=1,2,3$

C_T = generalized torsional rigidity of speciemn

$\left.\begin{array}{l} E_{11} \\ E_{22} \end{array}\right\}$ = principal Young's moduli (longitudinal and transverse to the fiber direction)

E_{zz} = longitudinal Young's modulus of specimen (see S'_{33})

F_i = constants defined in equations (29); $i=1,\ldots,7$

$\left.\begin{array}{l} G_{12} \\ G_{23} \\ G_{31} \end{array}\right\}$ = principal shear moduli

G_{zy} = effective longitudinal-width shear modulus of specimen

g = loss tangent

I_{pi} = polar mass moment of inertia

I_x = moment of inertia about x-axis

K = Timoshenko's shear constant (5/6)

K_x = radius of gyration $(h^2/12)^{1/2}$ of cross section about x-axis

ℓ = length of beam

m_i = mass per station

M = moment

N = number of a beam element (station or field)

S'_{33} = $1/E_{zz}$, compliance

S'_{35} = $2(\sin^2\theta/E_{22}-\cos^2\theta/E_{11})\sin\theta\cos\theta + (1/G_{21}-2\nu_{12}/E_{11})(\cos^2\theta-\sin^2\theta)\sin\theta\cos\theta$

ΔS = arc length on argand plot

ΔZI = full field length = ℓ/N

α = transverse shear strain

β = field parameter (β=1 implies full field, β=$^1/2$ implies half field at each end of beam)

ϕ = rotation of beam about z axis

ϕ^* = phase angle

$\Delta\phi^*$ = change in phase angle

ψ = bending slope

ω = frequency

ω_R = resonant frequency

$\Delta\omega$ = fixed incremental change in frequency

ρ = density

ζ = damping ratio

ν = Poisson's ratio

CONTRIBUTIONS TO THE DYNAMIC ANALYSIS OF MAGLEV VEHICLES ON ELEVATED GUIDEWAYS

K. Popp
Technical University Munich, West Germany

Maglev vehicles on elevated guideways can be economically used to solve transportation problems involving speeds of up to 400 km/h. Here, feedback control methods for the dynamic analysis of Maglev vehicles moving on flexible guideways are reviewed. From models for the vehicle, suspension and guideway, the mathematical open-loop description is obtained systematically. The result is a high order linear state equation with periodic time-varying coefficients and jumping states. However, the control system design calls for simple low order models which are approached in different ways. For the resulting closed-loop system a stability analysis is given and steady state responses to deterministic and stochastic disturbances are calculated using common numerical simulation techniques as well as procedures which are based on Floquet theory. The methods are demonstrated by an example which also shows the influence of the different design parameters.

1. INTRODUCTION

Magnetically levitated vehicles are under development for applications in rapid transit systems in highly populated areas as well as for high speed transportation over large distances. The feasibility of electromagnetic guidance and control, particularly for high speed operations in connection with the use of linear induction motors for propulsion, has been shown by various test-vehicle runs, cf. Table 1. In tests speeds of more than 400 km/h already have been reached. Just recently the first public Maglev vehicle TRANSRAPID 05, see Fig. 1, has been presented at the International Transportation Exhibition in Hamburg. In order to reduce guideway construction costs, Maglev vehicles are going to be operated on flexible elevated guideways. Thus, there is a strong dynamic coupling between vehicle motion and guideway vibration and also an interaction with the suspension control system. For the evaluation of motion stability, ride comfort and safety as well as for overall system optimization a dynamic analysis of the entire system consisting of vehicle, guideway and suspension control is required.

A short literature review indicates the number of different fields which are involved in the present problem area. The basic concept for Maglev vehicles was described by Kemper [21-23] in his patent forty years ago. The present state of the development in Germany is summarized by Reister, Zurek [43] and Zurek [52], while Bahke [1], Muckli [29] give a comparison of different high speed ground transportation systems. The future role of tracked levitated transportation systems is critically evaluated by Ward [50]. The research on vibration of structures under moving loads has a long tradition, going back to the mid 19th century. A summary of the classical cases is given by Frýba [5]. Recent results particularly on research in air cushion vehicle-guideway systems are reviewed by Richardson, Wormley [44]. Vehicle models are usually achieved by the multibody approach. The dynamics of multibody systems is treated in Magnus [26], Müller, Schiehlen [32]. Other important subjects are guideway irregularity models and ride comfort evaluation, cf. Hedrick et. al. [13], [14], Müller, Popp [33], Hullender [16], [17], Snyder, Wormley [48], ISO 2631 [18], Smith et. al. [46].

TABLE 1 Maglev Vehicles in Germany

VEHICLE	YEAR	VEHICLE LENGTH	VEHICLE MASS	REACHED SPEED	GUIDE-WAY LENGTH
MAGNETMOBIL	1971	7.6 m	5.8 t	90 km/h	660 m
TRANSRAPID 02	1971	11.7 m	11.3 t	164 km/h	930 m
TRANSRAPID 04	1975	15.0 m	20.0 t	253 km/h	2400 m
KOMET	1975	8.5 m	8.8 t	401 km/h	1300 m
KOMET M	1977	8.5 m	11.0 t	400 km/h	1300 m
TRANSRAPID 05	1979	26 m	36.0 t	75 km/h	908 m
TRANSRAPID 06	PLANNED FOR 1982	54 m	120 t	300-400 km/h	31.400 m

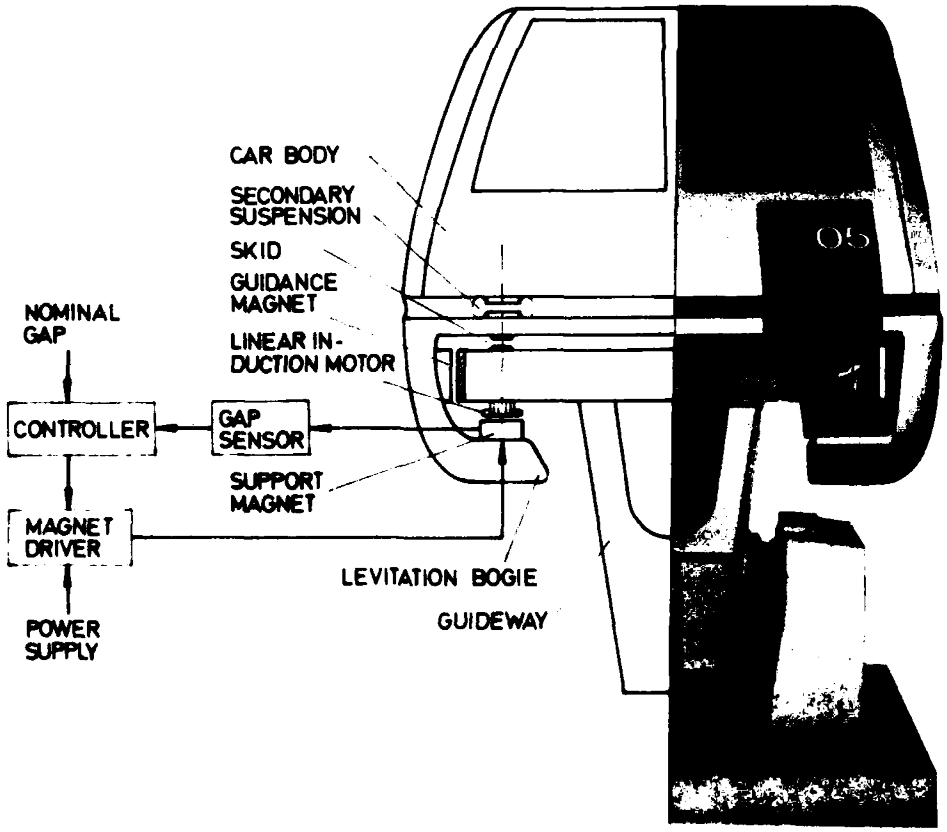
CAR BODY
SECONDARY SUSPENSION
SKID
GUIDANCE MAGNET
LINEAR INDUCTION MOTOR
NOMINAL GAP
CONTROLLER
GAP SENSOR
SUPPORT MAGNET
MAGNET DRIVER
LEVITATION BOGIE
GUIDEWAY
POWER SUPPLY
05

Fig. 1 - Front view at TRANSRAPID 05 and electromagnetic levitation principle

Guideway roughness measurements have been performed by Sussman [49] and Caywood, Rubinstein [3]. An integrated analysis of irregularities and comfort may be found in Müller et. al. [34].

Control concepts for Maglev vehicles are reported in Gottzein [6-11], Rothmayer [45], a number of experimental results being included in the first cited papers. Müller et. al. [30], [31] used disturbance accomodation techniques to investigate deterministic disturbances. In all cases, a rigid guideway and/or a vehicle in standstill is assumed for the control system design and linear time invariant control laws are obtained. On the other hand, Meisinger [27], [28] considers the control system of a moving flexible vehicle on a flexible guideway which results in linear periodic time variable feedback laws. Günther [12] treats the secondary suspension control. Other related contributions are due to Katz et. al. [20], Pollard, Williams [35], Jayawant [19] and Yamamura [51]. The numerical analysis of the closed-loop dynamics of Maglev vehicles can effectively be performed using the simulation programs reported in Caywood et. al. [2], Kortüm et. al. [24], [25], and Duffek et. al. [4]. The author's work on research concerning the Maglev vehicle-guideway system comprises [36-42].

In the present paper mathematical models for the suspension control of Maglev vehicles traveling on flexible guideways are given. First, the dynamic equations are described in state space notation which is well-suited to multivariable problems of large dimension. Then, the control system design for the magnetic suspension is discussed, based on reduced order models. For the resulting closed-loop system a stability analysis is given and steady state responses to deterministic and stochastic disturbances are calculated. Beside the common numerical simulation techniques, procedures derived from Floquet theory are used. Finally, the efficiency of the methods is demonstrated by an example which also shows the influence of the different design parameters. In what follows, basic ideas are emphasized rather than any computational details.

2. MATHEMATICAL SYSTEM DESCRIPTION

The vehicle-guideway system under consideration is a very complex system with many degrees of freedom. Here, only the motions in a vertical plane, i.e. heave, pitch and vertical bending, are considered. These dominant motions are decoupled from the other motions in the usual case of a symmetric construction. Furthermore, we assume small displacements except the forward motion of the vehicle which may take place on a straight track with constant speed v . The dynamical equations are obtained by separating the vehicle from the guideway and introducing magnetic suspension forces according to the principle of interaction. The subsystems are then mathematically described and put together, resulting in the open-loop description of the entire system.

2.1. VEHICLE MODEL

The vehicles are modeled as mass point systems or multibody systems, cf. Fig. 2. The complexity of the models depends on the purpose of the analysis. The general mathematical description has the form

$$\underline{M}\ddot{\underline{z}}(t)+\underline{D}\dot{\underline{z}}(t)+\underline{K}\underline{z}(t)=-\underline{J}^T\underline{f}(t),$$

$$\underline{z}(0)=\underline{z}_0,\ \dot{\underline{z}}(0)=\dot{\underline{z}}_0. \qquad (2.1)$$

where $\underline{z}$ denotes the f×1-vector of the f generalized vehicle coordinates measured from an inertial frame traveling with the vehicle at constant speed v_T and $\underline{M} = \underline{M}^T > \underline{0}$, $\underline{D} = \underline{D}^T$ and $\underline{K} = \underline{K}^T$ are the inertia, the damping and the stiffness matrix, respectively. The action of the magnetic primary suspension is replaced by single magnet forces, where $\underline{J}$ is the input matrix corresponding to the m×1-force vector $\underline{f}$,

$$\underline{f}(t) = \underline{F}(t) - \underline{F}_0 , \qquad (2.2)$$

which represents the deviation from the static forces $\underline{F}_0$. In case of an active secondary suspension or if the vehicle is subjected to vertical accelerations, e.g. during up and downhill trips, similar additional terms appear on the right hand side, cf. [42].

2.2. MAGNETIC SUSPENSION MODEL

Although electromagnets are highly nonlinear elements a linearized first order model has proven itself well, cf. Gottzein, Lange [10],

$$\dot{\underline{f}}(t)=-\underline{K}_f\underline{f}(t)-\underline{K}_s\underline{s}(t)-\underline{K}_{\dot{s}}\dot{\underline{s}}(t)+\underline{K}_u\underline{u}(t),$$

$$\underline{f}(0) = \underline{f}_0 . \qquad (2.3)$$

Here, $\underline{s}(t)$ is the m×1-vector of gap width variation, $\underline{u}(t)$ is the m×1-control vector and $\underline{K}_{f,s,\dot{s},n}$ denote m×m-diagonal matrices containing the parameters of the magnetic primary suspension. In technical applications all magnets are usually identical, thus these matrices reduce to scalar constants. The air gap variation $\underline{s}(t)$ is the difference between the vehicle and guideway displacements at the position

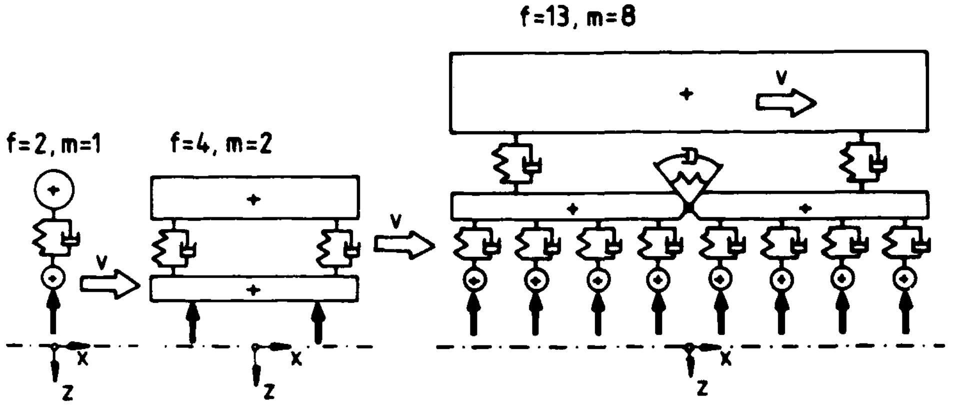

Fig. 2 - Vehicle models of different complexity

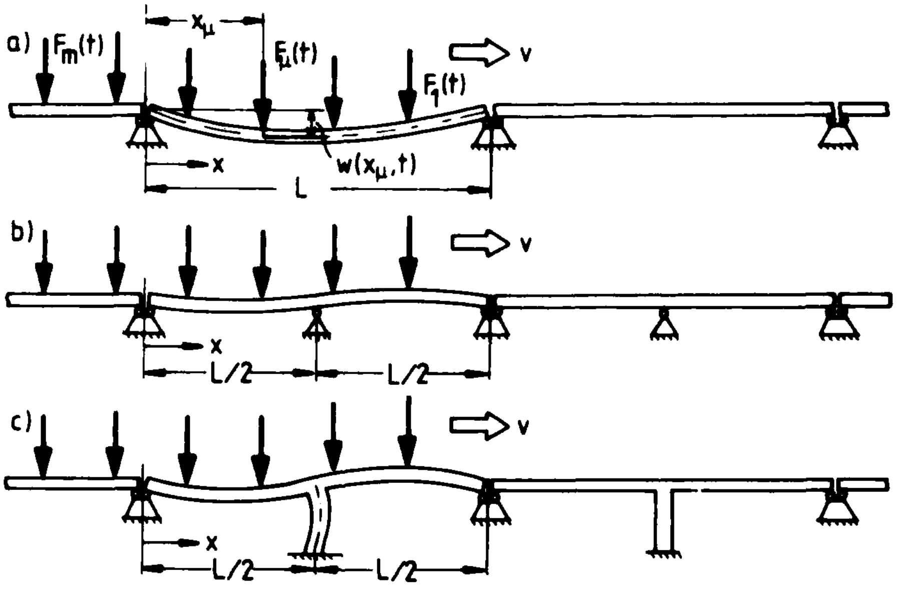

Fig. 3 - Guideway elements a) simple span, b) double span, c) double span frame

$\underline{\xi}(t)$ where the magnetic forces are acting,

$$\underline{s}(t)=\underline{J}\underline{z}(t)-\underline{w}[\underline{\xi}(t),t] \ . \qquad (2.4)$$

Here, $\underline{J}$ is the same matrix as in (2.1).

2.3. GUIDEWAY MODEL

In technical applications the guideway is long and it is generally constructed of prefabricated elements. For modeling reasons it is assumed that the guideway consists of an infinite sequence of identical and uncoupled Bernoulli-Euler beam-structure elements of length L , see Fig. 3. The total guideway deflection can be split into a deterministic part, $\underline{w}_d[\underline{\xi}(t),t]$ caused by the loading of the moving magnetic forces, and a stochastic part, $\underline{w}_s[\underline{\xi}(t),t]$, produced by random guideway irregularities,

$$\underline{w}[\underline{\xi}(t),t]=\underline{w}_d[\underline{\xi}(t),t]+\underline{w}_s[\underline{\xi}(t),t] \ . \qquad (2.5)$$

The mathematical description of the deterministic guideway deflections $\underline{w}_d[\underline{\xi}(t),t]$ is achieved in three steps:

I) Analysis of a single guideway element.

II) Setup of the guideway model by combining those guideway elements which are deflected under the traveling magnetic forces $\underline{F}(t)$ during the period of time $T = L/v$.

III) Calculation of the guideway deflections due to the traveling magnetic forces.

I) The deflections $w_i(x_i,t)$ of a single element i are governed by the wellknown fourth-order beam equation. The approximate solution reads due to the expansion theorem

$$w_i(x_i,t) = \sum_{j=1}^{\bar f} \bar w_j(x_i)\bar z_{ij}(t) = \bar{\underline{w}}^T(x_i)\bar{\underline{z}}_i(t) \ , \qquad (2.6)$$

where only $\bar f$ terms are regarded. Here, $\bar w_j(x_i)$ denotes the jth eigenfunction and $\bar z_{ij}(t)$ the corresponding generalized coordinate. These quantities are summarized in the $\bar f \times 1$-element vectors $\bar{\underline{w}}(x_i)$ and $\bar{\underline{z}}_i(t)$. The eigenfrequencies and the corresponding eigenfunctions follow from a modal analysis which is done analytically in [38], [42] for the guideway elements of Fig. 3. More complex structures may be analyzed numerically using finite element methods. Since the guideway is assumed to consist of identical elements, the eigenfunctions summed up in $\bar{\underline{w}}(x_i)$ are the same for all elements. The time dependent generalized coordinates, however, are different and follow from

$$\ddot{\bar{\underline{z}}}_i(t)+\underline{\Delta}_i\dot{\bar{\underline{z}}}_i(t)+\underline{\Omega}_i\bar{\underline{z}}_i(t) = \underline{M}_i^{-1}\sum_{k=1}^{m} b_{ki}\bar{\underline{w}}[\xi_{ki}(t)]F_k(t) \ . \qquad (2.7)$$

Here, $\underline{M}_i$, $\underline{\Delta}_i$, $\underline{\Omega}_i$ are the diagonal inertia, the damping and the stiffness matrix, respectively; they are identical for all elements and they follow from a modal analysis, the b_{ki} are Boolean variables indicating whether the magnetic force $F_k(t)$ is acting on the guideway element i ($b_{ki}=1$) or not ($b_{ki}=0$).

II) In order to keep the mathematical description of the guideway as simple as poosible, only the minimum number, say $\bar n$, of elements is regarded in the guideway model, shown in Fig. 4, resulting in a control volume of length $\bar n \cdot L$. Summing up the element coordinate vectors $\bar{\underline{z}}_i(t)$, $i = 1,\dots,\bar n$, yields the guideway vector $\bar{\underline{z}}(t)$,

$$\bar{\underline{z}}(t)=[\bar{\underline{z}}_1^T(t),\dots,\bar{\underline{z}}_{\bar n}^T(t)]^T \ , \qquad (2.8)$$

where $i=1$ always denotes the element under $F_1(t)$, the force exerted by the first magnet. From now on the time t is related to the traveled distance ξ_1 of $F_1(t)$ and measured in multiples of the period T,

$$t=\xi_1/v=\nu T+\tau \ , \quad 0 \le \tau \le T = L/v \ ,$$

$$\nu = \text{entier}(\xi_1/L) = \text{entier}(t/T) \ , \qquad (2.9)$$

where entier(x) denotes the greatest integer $\le x$. It is obvious, that the guideway control volume has to follow the moving forces. This can be done by stepwise shifting at the instants when the first moving force $F_1(t)$ reaches the next element. Then a new and resting element comes into the system bounds and the last one is abandoned. Mathematically, this is expressed by renumbering the guideway elements and providing a new setup for the guideway vector at the times $t = \nu T$,

$$\bar{\underline{z}}_1(t=\nu T+0)=\underline{0}, \quad \dot{\bar{\underline{z}}}_1(t=\nu T+0)=\underline{0} \ , \ \nu=1,2,\dots,$$

$$\bar{\underline{z}}_i(t=\nu T+0)=\bar{\underline{z}}_{i-1}(t=\nu T-0), \dot{\bar{\underline{z}}}_i(t=\nu T+0)= \dot{\bar{\underline{z}}}_{i-1}(t=\nu T-0), \ i=2,\dots,\bar n, \qquad (2.10)$$

or in more compact form by adding the initial conditions,

$$\bar{\underline{z}}_{\nu+}=\bar{\underline{U}}\ \bar{\underline{z}}_{\nu-} \ , \ \dot{\bar{\underline{z}}}_{\nu+}=\bar{\underline{U}}\ \dot{\bar{\underline{z}}}_{\nu-} \ , \ \nu=1,2,\dots,$$

$$\bar{\underline{z}}_{0+}=\bar{\underline{z}}_0 \ , \ \dot{\bar{\underline{z}}}_{0+}=\dot{\bar{\underline{z}}}_0 \ ,$$

$$\bar{\underline{U}} = \begin{bmatrix} \underline{0} & \cdots & \cdots & \cdots & \underline{0} \\ \underline{E}_{\bar f} & \underline{0} & & & \vdots \\ \underline{0} & \underline{E}_{\bar f} & \ddots & & \vdots \\ \vdots & \ddots & \ddots & \ddots & \vdots \\ \underline{0} & \cdots & \underline{0} & \underline{E}_{\bar f} & \underline{0} \end{bmatrix} \ . \qquad (2.11)$$

Here, the indices "+" and "-" denote the limit values after and before shifting, respectively, and the $\bar n\bar f \times \bar n\bar f$-matrix $\bar{\underline{U}}$ describes the changes in the guideway vectors. The row of zeros in $\bar{\underline{U}}$ is due to the fact that the vehicle front which coincides here with $F_1(t)$ is traveling onto a resting guideway element at times $t=\nu T$, $\nu=1,\dots$.

III) The guideway deflection $\underline{w}_d(t) = \underline{w}_d[\underline{\xi}(t),t]$ under the moving forces is found by combining (2.6-2.8),

$$\underline{w}_d(t) = \bar{\underline{J}}(t)\bar{\underline{z}}(t) \ ,$$

$$\ddot{\bar{\underline{z}}}(t)+\bar{\underline{\Delta}}\ \dot{\bar{\underline{z}}}(t)+\bar{\underline{\Omega}}\ \bar{\underline{z}}(t) = \bar{\underline{M}}^{-1}\bar{\underline{J}}^T(t)\underline{F}(t) \ , \qquad (2.12)$$

where the following $\bar n\bar f \times \bar n\bar f$-guideway matrices are introduced,

$$\bar{\underline{\Delta}}=\underline{\text{diag}}(\underline{\Delta}_i), \bar{\underline{\Omega}}=\underline{\text{diag}}(\underline{\Omega}_i),$$

$$\bar{\underline{M}}=\underline{\text{diag}}(\underline{M}_i), \ i = 1,\dots,\bar n \ . \qquad (2.13)$$

The $\bar n \times \bar n\bar f$-matrix $\bar{\underline{J}}(t)$ is more complex; it is worked out in detail in [42] and [40]. It contains the actual values of the eigenfunctions under the moving forces as well as the Boolean variables b_{ki}; both are periodic functions of time with period $T = L/v$, as long as constant vehicle speed v and identical guideway elements (length L) are assumed. Thus

$$\bar{\underline{J}}(t+T) = \bar{\underline{J}}(t) \ . \qquad (2.14)$$

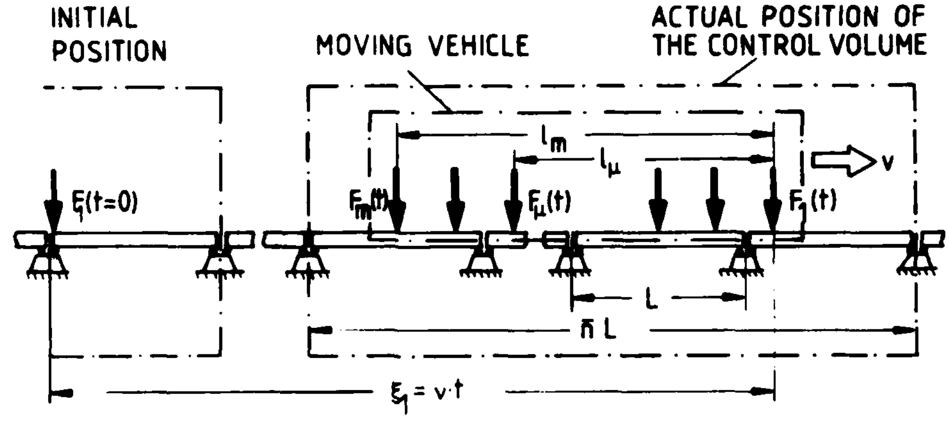

Fig. 4 - Guideway model consisting of simple spans

2.4. GUIDEWAY ROUGHNESS MODELS AND RANDOM VEHICLE EXCITATION

Irregularities of elevated guideways are caused by vertical offset, random walk, camber, and surface roughness of its elements, cf. Snyder, Wormley [48]. Measurements have proven that the total guideway roughness $\zeta(x)$ can be modeled as a stationary, Gaussian, ergodic random variable with zero mean value. The mathematical description is usually given by the (one sided) power spectral density $\Phi_\zeta(\Omega)$ or equivalently by the autocorrelation function $R_\zeta(x)$. A very simple but useful model reads, cf. Sussman [49],

$$R_\zeta(s)=E\{\zeta(x)\zeta(x-s)\}=\sigma^2 e^{\gamma|s|},$$
$$\Phi_\zeta(\Omega)=\frac{2\sigma^2}{\pi}\,\frac{\gamma}{\gamma^2+\Omega^2}\;, \tag{2.15}$$

where $E\{\cdot\}$ denotes the expected value, s a distance, Ω the (space) angular frequency, and where γ, σ^2 are constants. From the roughness model (2.15) the vehicle random excitation $\underline{w}_s(\xi(t),t)$ can be obtained in the frequency domain as well as in time domain. Here the time domain approach is preferred. This leads to the autocorrelation function of the excitation $w(t)$,

$$w(t)=\zeta(x=vt)\,,\; R_w(\theta)=E\{w(t)w(t-\theta)\}$$
$$=\sigma^2 e^{\gamma|\theta|}\;, \tag{2.16}$$

where $dx = vdt$ has been used. The random excitation $w(t)$ is a colored noise process and associated with the vehicle front, i.e. the position where the first magnet force $F_1(t)$ acts. Based on the time delay l_k/v between vehicle front and the position where $F_k(t)$ (distance l_k) is acting, the other $m-1$ excitations are found to be

$$\underline{w}_s(t)=\underline{w}_s[\underline{\xi}(t),t]=[w_1(t),\ldots,w_m(t)]^T\;,$$
$$w_k(t)=w(t-l_k/v)\,,k=1,\ldots,m,$$
$$0=l_1<l_2<\ldots<l_m\;. \tag{2.17}$$

For simplicity the time delays are sometimes neglected; the excitation vector $\tilde{\underline{w}}_s(t)$ then reads

$$\tilde{\underline{w}}_s(t) = \underline{h}\,w(t)\;,\; \underline{h} = [1,\ldots\ldots,1]^T. \tag{2.18}$$

In either case, the stochastic vehicle excitation is represented by a colored noise process. However, colored noise can be generated for $t \to \infty$ from a white noise process $\underline{r}(t)$ by means of a shape filter, i.e. a system of linear differential equations with white noise input,

$$\underline{w}_s(t) = \underline{H}\,\underline{v}_s(t)\;,$$
$$\dot{\underline{v}}_s(t)=\underline{F}\,\underline{v}_s(t)+\underline{G}\,\underline{r}(t)\,,\; \mathrm{Re}\lambda_i(\underline{F})<0\;,$$
$$i = 1,\ldots,\bar{s},\; 1 \le \bar{s} \le m\;,$$
$$\underline{v}_s(0) = \underline{v}_{so} \sim (\underline{0},\underline{P}_o)\;. \tag{2.19}$$

Here, $\underline{v}_s(t)$ is the $\bar{s}\times 1$-shape filter vector, $\underline{v}_s(0)$ has to be assumed as a random vector (mean value zero, covariance matrix $\underline{P}_o$), and $\underline{F}$, $\underline{G}$, $\underline{H}$ are the shape filter matrices. The modeling of vehicle excitations with time delays is extensively discussed in Müller, Popp [33] and Müller, Popp, Schiehlen [34]. The simpler case (2.18) results in a scalar shape filter ($\bar{s} = 1$)

$$\tilde{\underline{w}}_s = \underline{h}\,w(t)\,,\; \underline{h} = [1,\ldots\ldots,1]^T\;,$$
$$\dot{w}(t)=-fw(t)+gr(t)\,,\; f>0,\; R_r(\theta)=q_r\delta(\theta)\,,$$
$$w(0)=w_o\sim(0,P_o)\,,\; (f=\gamma v,\; g^2q_r=2\gamma v\sigma^2)\,, \tag{2.20}$$

where the shape filter quantities f and g as well as the white noise intensity q_r corresponding to the excitation model (2.16) are given in brackets.

2.5. OPEN-LOOP SYSTEM MODEL

Although the details of mathematical description of the total open-loop system depend on the chosen subsystem models, the resulting state equation always has the same structure. The introduction of the n×1-state vector $\underline{x}(t)$,

$$\underline{x}(t)=[\underline{z}^T(t),\ \dot{\underline{z}}^T(t),\ \underline{f}^T(t),\ \bar{\underline{z}}^T(t),$$
$$\dot{\bar{\underline{z}}}^T(t),\ \underline{v}_s^T(t)]^T\ , \qquad (2.21)$$

and the use of $\dot{\underline{w}}_d(t)=\dot{\bar{\underline{J}}}(t)\bar{\underline{z}}(t)+\bar{\underline{J}}(t)\dot{\bar{\underline{z}}}(t)$, $\dot{\underline{w}}_s(t)=\underline{H}\ \underline{F}\ \underline{v}_s(t)+\underline{H}\ \underline{G}\ \underline{r}(t)$ together with (2.1-2.5), (2.11-2.12), (2.19) results in the state equation

$$\boxed{\begin{aligned}&\dot{\underline{x}}(t)=\underline{A}(t)\underline{x}(t)+\underline{B}\underline{u}(t)+\underline{V}(t)\underline{F}_0+\underline{W}\ \underline{r}(t)\\&\underline{x}_{\nu+}=\underline{U}\ \underline{x}_{\nu-}\ ,\ \underline{x}_{0+}=\underline{x}_0,\ \nu=1,2,\ldots,\end{aligned}}\ \Sigma(2.22)$$

where ($\underline{\Omega}=\underline{M}^{-1}\underline{K}$, $\underline{\Delta}=\underline{M}^{-1}\underline{D}$)

$$\underline{A}(t)=\left[\begin{array}{cc|c|cc|c}\underline{0} & \underline{E}_f & \underline{0} & \underline{0} & \underline{0} & \underline{0}\\ -\underline{\Omega} & -\underline{\Delta} & -\underline{M}^{-1}\underline{J}^T & \underline{0} & \underline{0} & \underline{0}\\ \hline -\underline{K}_s\underline{J} & \underline{K}_{\dot{s}}\underline{J} & -\underline{K}_f & \underline{K}_s\bar{\underline{J}}(t)-\underline{K}_{\dot{s}}\dot{\bar{\underline{J}}}(t) & -\underline{K}_{\dot{s}}\bar{\underline{J}}(t) & \underline{K}_s\underline{H}-\underline{K}_{\dot{s}}\underline{H}\ \underline{F}\\ \hline \underline{0} & \underline{0} & \underline{0} & \underline{0} & \underline{E}_{\bar{n}\bar{f}} & \underline{0}\\ \underline{0} & \underline{0} & \bar{\underline{M}}^{-1}\bar{\underline{J}}^T(t) & -\bar{\underline{\Omega}} & -\bar{\underline{\Delta}} & \underline{0}\\ \hline \underline{0} & \underline{0} & \underline{0} & \underline{0} & \underline{0} & \underline{F}\end{array}\right]$$

$$\underline{U}=\underline{\text{diag}}\ (\underline{E}_f,\ \underline{E}_f,\ \underline{E}_m,\ \bar{\underline{U}},\ \bar{\underline{U}},\ \underline{E}_{\bar{s}}) \qquad (2.23)$$

$$\underline{B}=\left[\begin{array}{c}\underline{0}\\ \underline{0}\\ \hline \underline{K}_u\\ \hline \underline{0}\\ \underline{0}\\ \hline \underline{0}\end{array}\right]\ ,\qquad \underline{V}(t)=\left[\begin{array}{c}\underline{0}\\ \underline{0}\\ \hline \underline{0}\\ \hline \underline{0}\\ \bar{\underline{M}}^{-1}\bar{\underline{J}}^T(t)\\ \hline \underline{0}\end{array}\right],\qquad \underline{W}=\left[\begin{array}{c}\underline{0}\\ \underline{0}\\ \hline \underline{K}_s\underline{H}\ \underline{G}\\ \hline \underline{0}\\ \underline{0}\\ \hline \underline{0}\end{array}\right]\ .$$

The system matrix $\underline{A}(t)$ and the input matrix $\underline{V}(t)$ of deterministic disturbances are periodic, $\underline{A}(t+T)=\underline{A}(t)$, $\underline{V}(t+T)=\underline{V}(t)$, while the control input matrix $\underline{B}$ and the input matrix $\underline{W}$ of stochastic disturbances are constant. Furthermore, the state vector $\underline{x}(t)$ has periodic jumps due to (2.11). The dimension n of the state vector which corresponds to the order of the system matrix is given by

$$n=2f+m+2\bar{n}\bar{f}+\bar{s},\quad 1\le\bar{s}\le m\ , \qquad (2.24)$$

where f and $\bar{f}$ represent the degrees of freedom of the vehicle and of the guideway element, $\bar{n}$ is the number of guideway elements within the system bounds (control volume), m is the number of magnet forces and $\bar{s}$ is the order of the shape filter. In a realistic system description the total system order n is quite large. Thus, the open-loop system can be mathematically described by a

- linear, periodic high order state equation with periodically jumping states.

In addition, an equivalent system description should be mentioned, where the jumps are incorporated in the system matrix by Dirac delta functions; that is,

$$\dot{\underline{x}}(t)=[\underline{A}(t)+\underline{I}\sum_{\nu=-\infty}^{\infty}\delta(t-\nu T)]\underline{x}(t)+$$
$$+\underline{B}\ \underline{u}(t)+\underline{V}(t)\underline{F}_0+\underline{W}\ \underline{r}(t),\ \underline{I}=e^{\underline{U}}\ . \qquad (2.25)$$

Due to Hsu [15], this system type is called parametric excited. However, the description (2.22) is preferred here.

The state equation (2.22) has to be completed by the measurement equation

$$\underline{y}(t)=\underline{C}\ \underline{x}(t)+\underline{q}(t)\ , \qquad (2.26)$$

where the measurement vector $\underline{y}(t)$ represents the real output of the system and provides information about the states, $\underline{C}$ is the measurement matrix and $\underline{q}(t)$ the sensor noise. In technical applications one usually measures the vertical accelerations, air gaps, magnetic flux and current of the suspension magnets.

3. CONTROL SYSTEM DESIGN

The most important technical design criteria for the control system are

- asymptotic stability of all motions, best possible safety and reliability, sufficient ride comfort, low power consumption.

Since the Maglev vehicle is unstable without active control of the primary suspension, the first criterion is essential to operate the system. But the other criteria are important as well. The vehicle must not touch the guideway, not even under unusual dynamical conditions. The comfort specifications based e.g. on ISO 2631, have to be met, along with redundancy specifications. On the other hand the costs have to be as small as possible, calling for low power consumption.

There are different feasible control concepts for Maglev vehicles which should be touched upon:

i) Centralized mode control or decentralized single magnet control (magnetic wheel).
ii) Level control or air gap control.

i) In a centralized mode control all data processing is done in an onboard computer so that information about distinct modes, e.g. heave or pitch, is available. The central computed mode signals are fed back in mode controllers. Thus, changes in feedback gains for example, can easily be realized. The suspension magnets are usually fixed on the car body. In a decentralized control regime the magnets are decoupled from each other and flexibly mounted on the car body. Each magnet has an individual power supply, sensors and controller. These components result in a single unit which is sometimes called a magnetic wheel. Here, redundancy is realized by configuration. Single magnet control also offers benefits in the control system design.
ii) Level or z-control provides an active decoupling from the real track, i.e. each magnet and thus the car body are kept at a constant level, z=const., above an ideal track. Level control results in good ride comfort, since the vertical accelerations are very small. However, the nominal air gap has to be large (≈ 15 mm). In contrast, the gap or s-control keeps the nominal gap width constant, s=const, and results in best safety conditions. The nominal air gap can be small (≈ 6-8 mm). In order, to meet the comfort specifications, an active secondary suspension might be necessary.

Naturally, centralized control and level control are often combined as well as decentralized control and gap control. In early test vehicles, cf. Table 1, centralized mode control was implemented, while in recent vehicles decentralized gap control has been used. For any control concept the control system design must start with lower order models. The control design philosophy is outlined in Fig. 5. As a first step, the sophisticated higher order model Σ , cf. (2.22), has to be simplified to a lower order model $\tilde{\Sigma}$. The problem of order reduction can be solved either mathematically by mode truncation (condensation) or, as in the present case, by physical assumptions such as zero speed and/or a rigid guideway. In addition, the disturbances are usually neglected since they are assumed to be small. Thus, the simplified low order model can be stated as

$$\dot{\underline{\tilde{x}}}(t)=\underline{\tilde{A}}(t)\ \underline{\tilde{x}}(t)+\underline{\tilde{B}}\ \underline{u}(t),\ \underline{\tilde{A}}(t+T)=\underline{\tilde{A}}(t),$$

$$\underline{\tilde{x}}_{\nu+}=\underline{\tilde{U}}\ \underline{\tilde{x}}_{\nu-},\ \underline{\tilde{x}}_{o+}=\underline{\tilde{x}}_{o}\ ,\ \nu = 1,2,\ldots,\tilde{\Sigma} \quad (3.1)$$

$$\underline{\tilde{y}}(t) = \underline{\tilde{C}}(t)\ \underline{\tilde{x}}(t).$$

The system order now is

$$\tilde{n} = 2\tilde{f}+\tilde{m}+2\tilde{\tilde{n}}\tilde{\tilde{f}}\ ,\quad 1 \le \tilde{m} \le m\ . \qquad (3.2)$$

In many cases the relation between $\underline{x}$ and $\underline{\tilde{x}}$ can be given explicitely as

$$\underline{\tilde{x}}(t) = \underline{T}\ \underline{x}(t) \qquad (3.3)$$

where $\underline{T}$ is a $\tilde{n}\times n$-transformation matrix. The impact of different measures on system simplification is shown in detail in Table 2. As can be seen, best results are gained by assuming a rigid guideway, particularly in connection with single magnet control, cf. the example in Chapter 5. Then, the simplified system can be mathematically described by a

- linear constant reduced order state equation without jumping states.

The next step after system reduction, cf. Fig. 5, is the actual control synthesis. Only a few remarks concerning this topic shall be made here. More details about these methods may be found in [42] and practical solutions are given in Gottzein et.al. [6-11]. The aim of the control synthesis is the computation of a control law, i.e. a relation between the control vector $\underline{u}(t)$ and state vector $\underline{\tilde{x}}(t)$ or output vector $\underline{\tilde{y}}(t)$. Only linear control laws are considered,

$$\underline{u}(t) = -\underline{K}_x(t)\ \underline{\tilde{x}}(t)\ , \qquad (3.4)$$

$$\underline{u}(t) = -\underline{K}_y(t)\ \underline{\tilde{y}}(t)\ , \qquad (3.5)$$

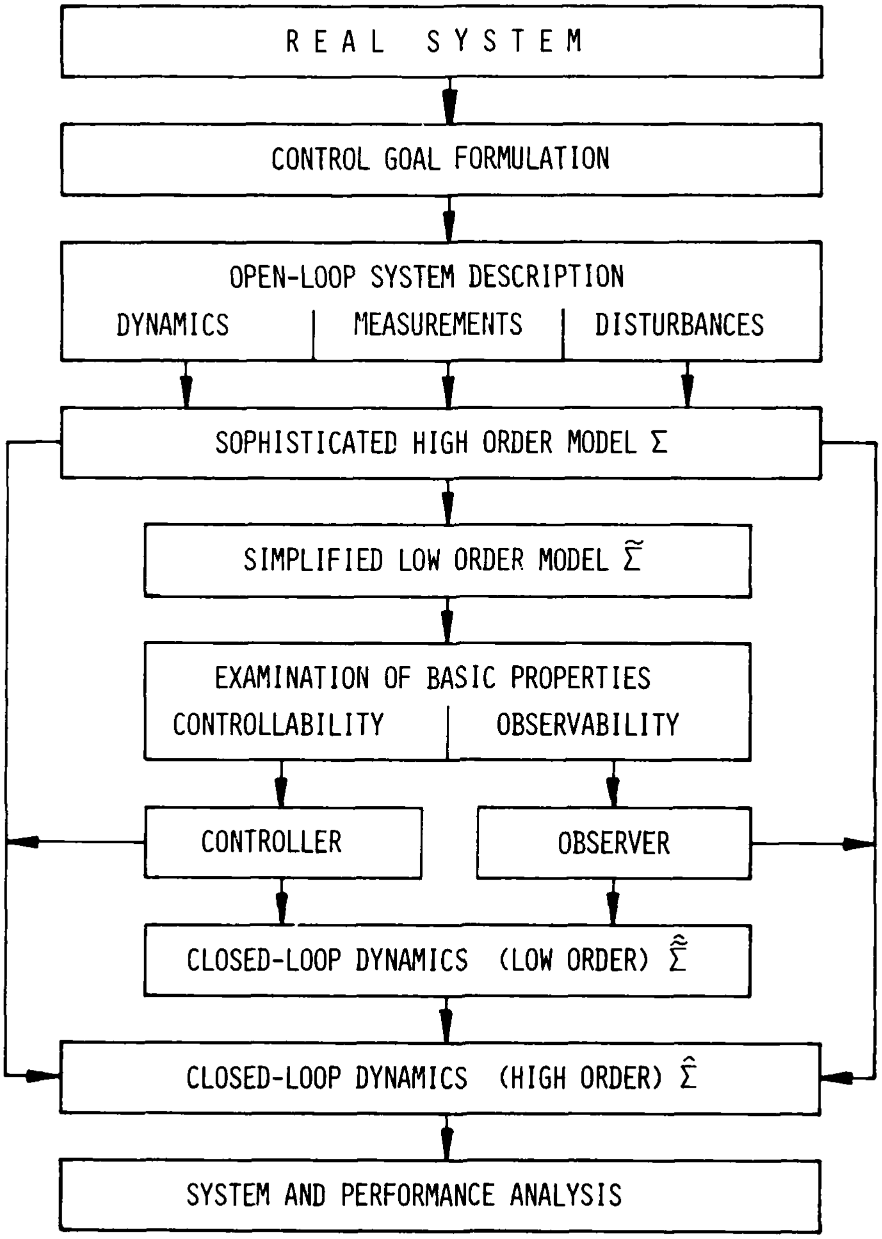
REAL SYSTEM
CONTROL GOAL FORMULATION
OPEN-LOOP SYSTEM DESCRIPTION
DYNAMICS
MEASUREMENTS
DISTURBANCES
SOPHISTICATED HIGH ORDER MODEL Σ
SIMPLIFIED LOW ORDER MODEL $\tilde{\Sigma}$
EXAMINATION OF BASIC PROPERTIES
CONTROLLABILITY
OBSERVABILITY
CONTROLLER
OBSERVER
CLOSED-LOOP DYNAMICS (LOW ORDER) $\hat{\tilde{\Sigma}}$
CLOSED-LOOP DYNAMICS (HIGH ORDER) $\hat{\Sigma}$
SYSTEM AND PERFORMANCE ANALYSIS

Fig. 5 - Flow chart of system analysis

where the feedback matrices $\underline{K}_x(t)$, $\underline{K}_y(t)$ comprise the control gains. Although it is possible to solve the optimal state feedback problem for linear periodic time-varying systems $\Sigma(t)$ (3.1) with jumping states, resulting in a periodic gain matrix $\underline{K}_x(t+T)=\underline{K}_x(t)$, cf. Meisinger [27], [28], one is more interested in constant gain matrices $\underline{K}_x=\underline{\mathrm{const}}$, $\underline{K}_y=\underline{\mathrm{const}}$, since they are much easier to implement. Starting from $\tilde{\Sigma}$ (3.1), where $\underline{\tilde{A}}=\underline{\mathrm{const}}$, $\underline{\tilde{U}} = \underline{E}$, the constant gains can be obtained using pole assignment, for example, or optimal control with respect to quadratic cost functionals. Both methods are suitable for multivariable systems and allow the design of state controllers as well as state observers. In the case of output feedback design, parameter optimization methods may be used.

As the final step in getting the closed-loop system description, the con-

TABLE 2
Impact of different measures on system complexity reduction

MEASURE	IMPACT ON		
	SYTEM ORDER	TIME DEPENDENCE	JUMPS
MODE TRUNCATION	$\tilde{\tilde{f}} \approx 1$ or 2 $\tilde{f}$ small	NO	NO
SINGLE MAGNET CONTROL	$\tilde{m} = 1$	NO	NO
SPEED v = 0	NO	$\tilde{\Sigma} = \text{const}$	$\tilde{\underline{U}} = \underline{E}$
RIGID GUIDEWAY	$\tilde{\tilde{f}} \equiv 0$	$\tilde{\Sigma} = \text{const}$	$\tilde{\underline{U}} = \underline{E}$

trol law (3.4), (3.5) based on the reduced order system $\tilde{\Sigma}$ (3.3) is introduced in the original higher order system Σ (2.22). This results in

$$\boxed{\begin{array}{l} \dot{\underline{x}}(t)=\hat{\underline{A}}(t)\ \underline{x}(t)+\underline{V}(t)\underline{F}_0+\underline{W}\ \underline{r}(t) \\ \underline{x}_{\nu+} = \underline{U}\ \underline{x}_{\nu-}\ ,\ \underline{x}_{0+} = \underline{x}_0 \end{array}}\ .\ \hat{\Sigma}(t) \quad (3.6)$$

Whenever eq. (3.3) applies, equations (3.4), (3.5) may be used to obtain

$$\hat{\underline{A}}(t) = \underline{A}(t) - \underline{B}\ \underline{K}_x(t)\ \underline{T}\ , \qquad (3.7)$$

$$\hat{\underline{A}}(t) = \underline{A}(t) - \underline{B}\ \underline{K}_y(t)\tilde{\underline{C}}(t)\underline{T}\ , \qquad (3.8)$$

where the periodicity condition $\hat{\underline{A}}(t+T)=\hat{\underline{A}}(t)$ holds. However, even if an optimal state feedback law (3.4) with respect to $\tilde{\Sigma}(t)$ is computed and implemented in the original higher order system $\Sigma(t)$, then this results in an incomplete state feedback with respect to $\Sigma(t)$ and nothing can be said about the stability of $\hat{\Sigma}(t)$ or other properties. Thus, a performance analysis of the closed-loop system $\hat{\Sigma}(t)$ is required.

4. SYSTEM ANALYSIS

The dynamic analysis of the closed-loop system $\hat{\Sigma}(t)$ is carried out starting with the homogeneous solution followed by a stability investigation. The performance of the Maglev vehicle-guideway system depends essentially on the system responses to the present disturbances. Since linearity is given, the responses due to deterministic and stochastic disturbances can be calculated separately and then superposed. Generally, exact methods are preferred, but some approximate results are also dealt with. Usually, for steady-state response calculations, numerical simulation methods are employed. Here, the wellknown analytical methods for periodic systems based on Floquet theory are applied and extended to jumping states. But only the main results are shown; derivations and proofs may be found in [42].

4.1. HOMOGENEOUS SOLUTION AND STABILITY ANALYSIS

Consider the homogeneous part of the closed-loop system $\hat{\Sigma}(t)$ (3.5),

$$\dot{\underline{x}}(t)=\hat{\underline{A}}(t)\underline{x}(t),\ \hat{\underline{A}}(t+T)=\hat{\underline{A}}(t),\ \underline{x}_{\nu+}=\underline{U}\ \underline{x}_{\nu-},$$

$$\underline{x}_{0+} = \underline{x}_0\ ,\ \nu = 1,2,\dots\ . \qquad (4.1)$$

The solution of (4.1) is obtained by piecewise calculation using the time representation (2.9) and Floquet theory, cf. [42],

$$\underline{x}(t=\tau+\nu T)=\underline{\Phi}(\tau)[\underline{U}\ \underline{\Phi}(T)]^{\nu}\underline{x}_0\ ,\ 0 \le \tau \le T\ ,$$

$$\nu = 1,2,\dots, \qquad (4.2)$$

where the transition matrix $\underline{\Phi}(\tau)$ follows from

$$\dot{\underline{\Phi}}(\tau)=\hat{\underline{A}}(\tau)\ \underline{\Phi}(\tau),\ \underline{\Phi}(0) = \underline{E}\ . \qquad (4.3)$$

For $\underline{U} = \underline{E}$ eq. (4.2) represents the wellknown result for a periodic system without jumping states. The stability of the system (4.1) can be determined by investigating the solution (4.2) for $t \to \infty$ or equivalently for $\nu \to \infty$. It is obvious that the stability behavior depends uniquely on the eigenvalues σ of the growth matrix $\underline{U}\ \underline{\Phi}(T)$ which is abbreviated by $\underline{\Psi}$. The characteristic equation thus becomes

$$\det(\sigma\underline{E} - \underline{\Psi}) = 0\ , \qquad (4.4)$$

and the following stability theorem applies, cf. [42] and Hsu [15]:

Theorem: The homogeneous system (4.1) is

i) asymptotically stable if and only if all eigenvalues of the growth matrix $\underline{\Psi}$ have absolute values less than one,

$$|\sigma_i| < 1,\ i = 1, \dots, n\ ,$$

ii) stable if and only if all eigenvalues have absolute values not greater than one, $|\sigma_i| \leq 1$, $i = 1,\ldots,n$, and for all eigenvalues λ_r with absolute values equal to one the defect d_r of the characteristic matrix $(\sigma_r \underline{E} - \underline{\Psi})$ is equal to the multiplicity m_r of these eigenvalues, $d_r = m_r$.

iii) unstable if and only if there is at least one eigenvalue which has absolute value greater than one, $|\sigma_i| > 1$, or there are multiple eigenvalues σ_s which have absolute value equal to one $|\sigma_s| = 1$, and the corresponding defect d_s of the characteristic matrix $(\sigma_s \underline{E} - \underline{\Psi})$ is less than the multiplicity m_s of these eigenvalues, $d_s < m_s$.

We are interested only in asymptotic stability. For this purpose, it is convenient to introduce the spectral radius $\mathrm{spr}(\underline{\Psi})$ of the growth matrix,

$$\mathrm{spr}(\underline{\Psi}) = \max_i |\sigma_i| \ , \quad i = 1,\ldots,n \ . \tag{4.5}$$

The practical stability analysis requires the following steps which can easily be written into a computer program:

i) Computation of the transition matrix $\underline{\Phi}(T)$ by integration of (4.3) over one single period.

ii) Construction of the growth matrix $\underline{\Psi} = \underline{U}\ \underline{\Phi}(T)$.

iii) Computation of the spectral radius $\mathrm{spr}(\underline{\Psi})$ (4.5).

iv) Stability test: System (4.1) is asymptotically stable if and only if

$$\mathrm{spr}(\underline{\Psi}) < 1 \tag{4.6}$$

is the case.

Some sufficient stability conditions follow immediately: For any lub norm $\|\cdot\|$ the conditions $\mathrm{spr}(\underline{\Psi}) \leq \|\underline{\Psi}\| = \|\underline{U}\underline{\Phi}(T)\|$ and $\|\underline{U}\| = 1$ are satisfied cf. (2.23), (2.11); it follows that system (4.1) is asymptotically stable if

$$\|\underline{\Psi}\| < 1 \text{ or } \|\underline{\Phi}(T)\| < 1 \tag{4.7}$$

holds. From $\|\underline{\Psi}\| \leq \|\underline{\Phi}(T)\|$ it can be concluded that the stability behavior in general is not affected by state variable jumps of the present type, something which is also evident from physical considerations.

4.2. STEADY-STATE RESPONSE TO DETERMINISTIC DISTURBANCES

The inhomogeneous deterministic part of the closed-loop system $\hat{\Sigma}(t)$ (3.5) can be written as

$$\begin{aligned}
&\dot{\underline{x}}(t) = \hat{\underline{A}}(t)\underline{x}(t) + \underline{b}_d(t), \quad \hat{\underline{A}}(t+T) = \hat{\underline{A}}(t), \\
&\underline{b}_d(t+T) = \underline{b}_d(t), \quad \underline{x}_{\nu+} = \underline{U}\ \underline{x}_{\nu-} , \\
&\underline{x}_{o+} = \underline{x}_o , \quad \nu = 1,2,\ldots \ .
\end{aligned} \tag{4.8}$$

The application of the usual simulation methods requires that eq. (4.8) be numerically integrated over a sufficiently long time. However, the steady-state response of an asymptotically stable system can also be found from the general solution, cf. [42],

$$\begin{aligned}
&\underline{x}(t=\tau+\nu T) = \underline{\Phi}(\tau)\Big[\underline{\Psi}^{\nu}\underline{x}_o + \sum_{k=1}^{\nu}\underline{\Psi}^{k}\underline{c}_d(T) + \underline{c}_d(\tau)\Big], \\
&\nu = 0,1,\ldots, \quad \underline{c}_d(\tau) = \int_0^{\tau}\underline{\Phi}^{-1}(\overset{*}{\tau})\underline{b}_d(\overset{*}{\tau})\,d\overset{*}{\tau} \\
&\qquad 0 \leq \tau \leq T \ ,
\end{aligned} \tag{4.9}$$

where the time representation (2.9) has again been used and where the calculation has been performed for each section individually. The steady-state solution $\underline{x}_\infty(t)$ is obtained for $t \to \infty$ or equivalently $\nu \to \infty$. Then, since asymptotic stability is assumed, the first term in brackets vanishes and the remaining infinite geometrical matrix series converges to $\underline{S}_d$,

$$\underline{S}_d = \sum_{k=1}^{\infty}\underline{\Psi}^k = (\underline{E}-\underline{\Psi})^{-1} - \underline{E} = (\underline{E}-\underline{\Psi})^{-1}\underline{\Psi} \ . \tag{4.10}$$

Thus, the steady-state response corresponding to deterministic disturbances is given by

$$\begin{aligned}
\underline{x}_\infty(t) &= \lim_{\nu\to\infty}\underline{x}(t=\tau+\nu T) = \underline{\Phi}(\tau)[\underline{S}_d\underline{c}_d(T) + \underline{c}_d(\tau)] = \\
&= \underline{x}_\infty(t+T), \quad 0 \leq \tau \leq T \ ,
\end{aligned} \tag{4.11}$$

which is a periodic *function of* time. Here, numerical integrations have to be carried out only over one single period. The simulation method can be recommended only for highly damped systems, while the computation of the formal solution (4.11) yields good results in all other cases.

4.3. STEADY-STATE RESPONSE TO STOCHASTIC DISTURBANCES

Analogous to (4.8) the stochastic part of the closed-loop system $\hat{\Sigma}(t)$ (3.5) is

$$\begin{aligned}
&\dot{\underline{x}}(t) = \hat{\underline{A}}(t)\ \underline{x}(t) + \underline{b}_s(t), \quad \hat{\underline{A}}(t+T) = \hat{\underline{A}}(t), \\
&\underline{b}_s(t) \sim (\underline{0}, \underline{Q}_b), \quad \underline{x}_{\nu+} = \underline{U}\ \underline{x}_{\nu-}, \\
&\underline{x}_{o+} = \underline{x}_o \sim (\underline{0}, \underline{P}_{xo}), \quad \nu = 1,2,\ldots \ .
\end{aligned} \tag{4.12}$$

Here, $\underline{b}_s(t)$ is assumed to be a Gaussian white noise vector process with zero mean characterized by the constant intensity matrix $\underline{Q}_b$. The initial condition $\underline{x}_o$ is now a random vector, where a vanishing mean value is assumed and where $\underline{P}_{xo}$ is the covariance matrix. Since the system is periodic and linear, the response $\underline{x}(t)$ is generally a nonstationary Gaussian vector process which can be characterized by the mean vector $\underline{m}_x(t)$ and the covariance matrix $\underline{P}_x(t)$,

$$\begin{aligned}
&\underline{m}_x(t) = E\{\underline{x}(t)\} \ , \\
&\underline{P}_x(t) = E\{[\underline{x}(t) - \underline{m}_x(t)][\underline{x}(t) - \underline{m}_x(t)]^T\} = \underline{P}_x^T(t) \ .
\end{aligned} \tag{4.13}$$

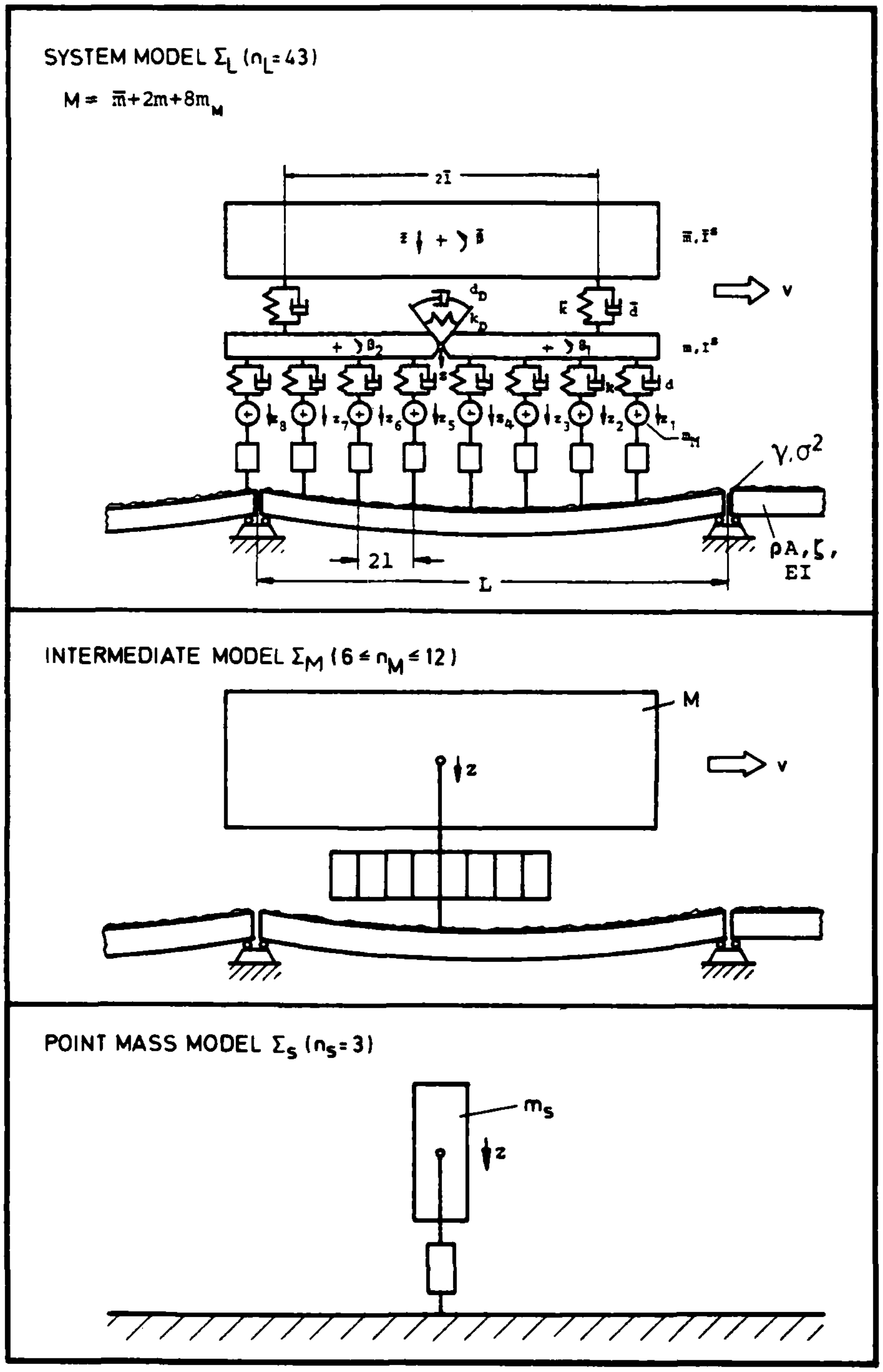
SYSTEM MODEL Σ_L ($n_L = 43$)
$M = \bar{m} + 2m + 8m_M$
$2\bar{l}$
z + $\bar{\beta}$
$\bar{m}, \bar{I}^s$
v
d_D
k_D
$\bar{k}$
$\bar{d}$
+ β_2
+ β_1
m, I^s
s
k
d
z_8
z_7
z_6
z_5
z_4
z_3
z_2
z_1
m_M
γ, σ^2
$\rho A, \zeta,$
EI
2l
L
INTERMEDIATE MODEL Σ_M ($6 \le n_M \le 12$)
M
z
v
POINT MASS MODEL Σ_S ($n_S = 3$)
m_S
z

Fig. 6 - System models of different complexity

However, due to the vanishing initial mean vector, $\underline{m}_x(0)=\underline{0}$, the mean vector $\underline{m}_x(t)$ vanishes identically. The covariance matrix $\underline{P}_x(t)$ is the solution of the Liapunov differential equation

$$\dot{\underline{P}}_x(t)=\hat{\underline{A}}(t)\underline{P}_x(t)+\underline{P}_x(t)\hat{\underline{A}}^T(t)+\underline{Q}_b \ ,$$

$$\underline{P}_{x\nu+}=\underline{U}\ \underline{P}_{x\nu-}\underline{U}^T,\ \underline{P}_{x0+}=\underline{P}_{x0},\ \nu=1,2,\ldots, \quad (4.14)$$

where the jump condition for the covariance matrix follows upon introduction of the state jumps in the definition (4.13). Eq. (4.14) is the starting point for the numerical calculation of $\underline{P}_x(t)$. However, the analytical solution is preferable here, cf. [42]; it is given by

$$\underline{P}_x(t=\tau+\nu T)=\underline{\Phi}(\tau)\left[\sum_{k=1}^{\nu}\underline{\Psi}^k\underline{C}_s(T)(\underline{\Psi}^k)^T+\underline{C}_s(\tau)\right]\underline{\Phi}^T(\tau)$$

$$\nu = 0,1,\ldots, \quad (4.15)$$

$$\underline{C}_s(\tau)=\int_0^{\tau}\underline{\Phi}^{-1}(\overset{*}{\tau})\underline{Q}_b(\underline{\Phi}^{-1}(\overset{*}{\tau}))^T d\overset{*}{\tau}\ ,\ 0\le\tau\le T\ .$$

The steady-state solution $\underline{P}_{x\infty}(t)$ follows from (4.15) for $t\to\infty$ or $\nu\to\infty$

$$\underline{P}_{x\infty}(t)=\lim_{\nu\to\infty}\underline{P}_x(t=\tau+\nu T)=\underline{\Phi}(\tau)[\underline{S}_s+\underline{C}_s(\tau)]\underline{\Phi}_s^T(\tau)=$$
$$=\underline{P}_{x\infty}(t+T)\ , \quad (4.16)$$

where asymptotic stability has again been assumed. Here, $\underline{S}_s$ is solution of the algebraic Stein equation,

$$\underline{S}_s-\underline{\Psi}\ \underline{S}_s\underline{\Psi}^T = \underline{\Psi}\ \underline{C}_s(T)\underline{\Psi}^T\ . \quad (4.17)$$

The steady-state solution $\underline{P}_{x\infty}(t)$ is periodic and can be obtained by a numerical integration over only a single period along with some algebraic operations. The simulation method can be recommended only for highly damped systems of low order, while in all other cases the solution (4.16) is more advantageous. In any case, the time dependent solution is laborious. Thus, a simple time invariant approximation shall briefly be mentioned. It starts with the reduced order system $\tilde{\Sigma}$(3.1) , where a rigid guideway is assumed but the stochastic disturbances due to guideway irregularities are not neglected. The state equation of the closed-loop system then has the form

$$\dot{\tilde{\underline{x}}}(t)=\hat{\tilde{\underline{A}}}\ \tilde{\underline{x}}(t)+\tilde{\underline{b}}_s(t),\ \tilde{\underline{x}}_0\sim(\underline{0},\tilde{\underline{P}}_{x0})\ ,$$

$$\tilde{\underline{b}}_s(t)\sim(\underline{0},\tilde{\underline{Q}}_b)\ , \quad (4.18)$$

which is time invariant and exhibits no jumps in the state variables. The steady-state covariance matrix $\tilde{\underline{P}}_{x\infty}$ now is constant and follows from the algebraic Liapunov equation

$$\hat{\tilde{\underline{A}}}\ \tilde{\underline{P}}_{x\infty}+\tilde{\underline{P}}_{x\infty}\hat{\tilde{\underline{A}}}^T+\tilde{\underline{Q}}_b = \underline{0}\ , \quad (4.19)$$

which can easily be solved using Smith's method [47], for example. Comparisons by means of examples show, that $\tilde{\underline{P}}_{x\infty}$ is a good approximation of $\underline{P}_{x\infty}(t)$, cf. Chapter 5.

5. EXAMPLE

As an example a vehicle model Σ_L with f=13 degrees of freedom and m=8 suspension magnets is considered, cf. Fig. 6, and single magnet control is chosen for the control implementation. The vehicle may be operated on a single span guideway, where $\bar{n}=2$ spans are coupled during the period T . If we only regard $\bar{f}=2$ modes to describe the guideway deflection and use the simple shape filter of order $\bar{s}=1$, then the total system order is $n_L=43$. Prior to analyzing the model Σ_L, as is done in [42], two simplified models, Σ_M and Σ_s , are investigated. The point mass model Σ_s (system order $n_s=3$) characterizes a single magnet on an ideal smooth and rigid guideway and serves as model for the control design. The intermediate model Σ_M (system order $6\le n_M\le 12$, depending on the number of included guideway modes $\bar{f}$) contains all m=8 magnets in parallel which is sufficient to levitate the total vehicle mass M. Since there is only one contact point on the guideway, model Σ_M can be considered as a worst case model with respect to guideway loading. It allows a check on the developed analysis methods and provides information about the influence of different design parameters. In the following, the models Σ_s and Σ_M are investigated and a few results are shown. More results and an extensive discussion may be found in [38] and [42].

5.1. CONTROL SYSTEM DESIGN FOR SINGLE MAGNET MODEL Σ_s

The mathematical description of model Σ_s is

$$\underset{\dot{\underline{x}}(t)=}{\begin{bmatrix} z(t)\\ \dot{z}(t)\\ f(t)\end{bmatrix}^{\cdot}}=\underset{\underline{A}}{\begin{bmatrix}0 & 1 & 0\\ 0 & 0 & -1/m_s\\ -k_s & k_{\dot{s}} & -k_f\end{bmatrix}}\underset{\underline{x}(t)}{\begin{bmatrix} z(t)\\ \dot{z}(t)\\ f(t)\end{bmatrix}}+\underset{\underline{b}}{\begin{bmatrix}0\\ 0\\ k_u\end{bmatrix}}\underset{u(t)\ ,}{u(t),}$$

$$m_s = M/8\ . \qquad \Sigma_s \quad (5.1)$$

System Σ_s is completely controllable; thus, a complete state feedback is possible,

$$u(t)= -\underline{k}^T\underline{x}(t)= -k_1 z(t)-k_2\dot{z}(t)-k_3 f(t).\quad (5.2)$$

Here, pole assignment methods are used in the computation of the feedback gains k_i= 1,2,3. If the desired eigenvalues, $\hat{\lambda}_i$, of the closed-loop system are chosen, and

TABLE 3
System parameters

SPEED RATIO	$\alpha = \frac{\omega}{\omega_1} = \frac{\pi v/L}{\omega_1}$
MASS RATIO	$\mu = \frac{M}{\rho A L}$
DAMPING RATIO	ζ
CONTROL PARAMETER	$\beta = \frac{\delta}{\omega_1}$
MAGNET PARAMETERS	$\kappa_s = \frac{k_s}{\omega_1{}^3 M}$, $\kappa_{\dot{s}} = \frac{k_{\dot{s}}}{\omega_1{}^2 M}$
ROUGHNESS PARAMETERS	$\overline{\gamma} = \gamma \frac{v}{\omega_1}$, $\overline{q} = \frac{\pi}{2L} \frac{\omega_1{}^4}{\mu^2 g^2} \frac{\sigma^2}{\alpha\gamma}$

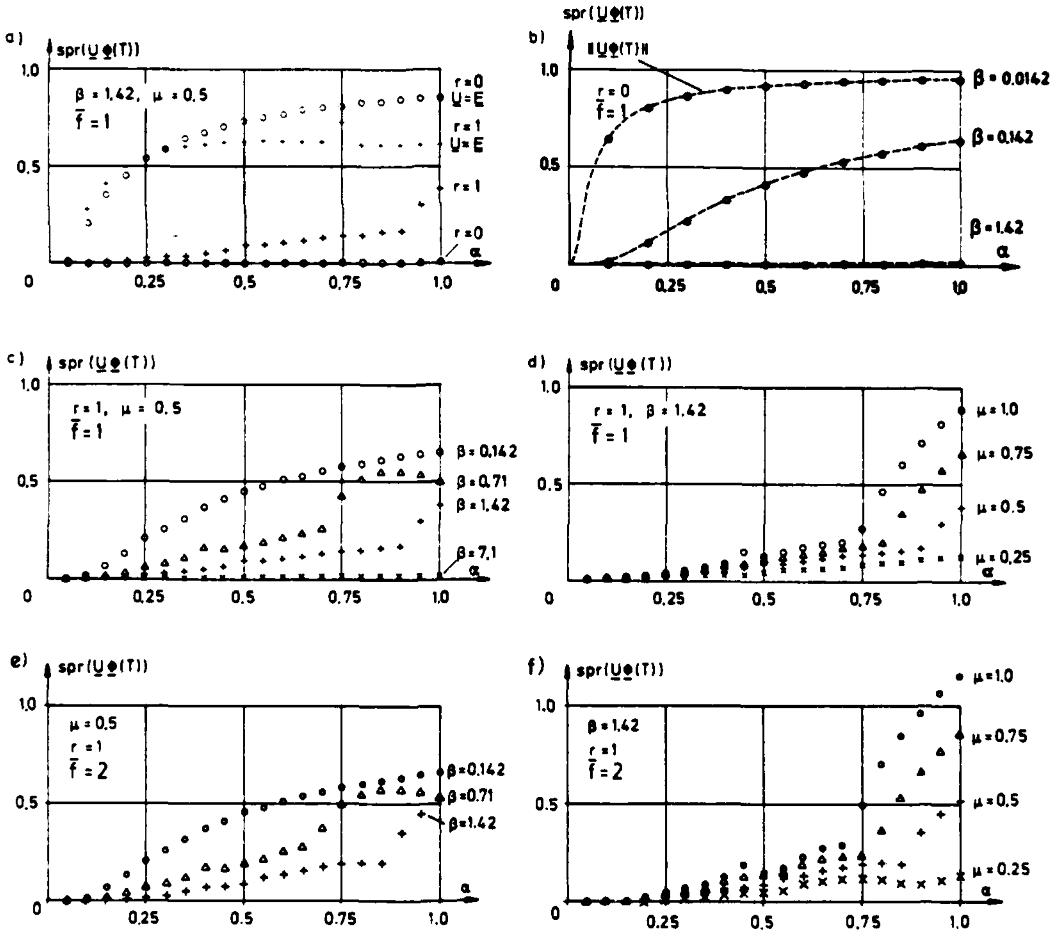

Fig. 7 - Results of the stability analysis

the corresponding characteristic polynominal is $p(\lambda)=(\lambda-\hat{\lambda}_1)(\lambda-\hat{\lambda}_2)(\lambda-\hat{\lambda}_3) = \lambda^3+\hat{a}_1\lambda^2+\hat{a}_2\lambda+\hat{a}_3$, then a comparision of coefficients yields

$$
\begin{aligned}
k_1 &= -\frac{1}{k_u}(m_s\hat{a}_3+k_s) , \\
k_2 &= -\frac{1}{k_u}(m_s\hat{a}_2-k_{\dot{s}}) , \\
k_3 &= \frac{1}{k_u}(\ \hat{a}_1-k_f) , \\
k_1 &= -\frac{1}{k_u}[-m_s\hat{\lambda}_1\hat{\lambda}_2\hat{\lambda}_3+k_s] , \\
k_2 &= -\frac{1}{k_u}[\ m_s(\hat{\lambda}_1\hat{\lambda}_2+\hat{\lambda}_2\hat{\lambda}_3+\hat{\lambda}_3\hat{\lambda}_1)-k_{\dot{s}}], \\
k_3 &= -\frac{1}{k_u}[\ \hat{\lambda}_1+\hat{\lambda}_2+\hat{\lambda}_3+k_f] .
\end{aligned}
\tag{5.3}
$$

In many investigations the eigenvalue pattern

$$\hat{\lambda}_1 = -2\delta,\ \hat{\lambda}_{2,3}=(-1\pm j\sqrt{3})\delta \tag{5.4}$$

has proven effective, where the only remaining adjustable parameter is δ .

5.2. SYSTEM DESCRIPTION FOR THE MODEL Σ_M

The control gains (5.3) are kept unchanged for the intermediate model Σ_M , but the guideway elasticity is regarded. However, different output vectors, $\underline{y}_z(t)$ and $\underline{y}_s(t)$, are fed back corresponding to level or z-control and gap or s-control,

$$
\begin{aligned}
u_z(t)&=-\underline{k}^T\underline{y}_z(t)=-k_1z(t)-k_2\dot{z}(t)-k_3f(t), \\
u_s(t)&=-\underline{k}^T\underline{y}_s(t)=-k_1s(t)-k_2\dot{s}(t)-k_3f(t).
\end{aligned}
\tag{5.5}
$$

Using $s(t)=z(t)-[w_d(t)+w_s(t)]$, cf. (2.4), (2.5), and the Boolean variable r , the control law for model Σ_M can be written as

$$
\begin{aligned}
u(t)=u_z(t)+r\{k_1[w_d(t)+w_s(t)] &+ \\
+k_2[\dot{w}_d(t)+\dot{w}_s(t)]\}& ,
\end{aligned}
\tag{5.6}
$$

where $r=0$ means z-control and $r=1$ represents s-control.
The total system description for model Σ_M is analogous to Chapter 2. Here, the result is shown for the case where only the first eigenmode of the single span guideway element (length L, mass ρAL, bending stiffness EI, first eigenfrequency $\omega_1=(\pi/L)^4EI/\rho A$, first eigenfunction $w_1(t)=\sin\frac{\pi V}{L}\tau)$ is included.
In addition, the nondimensional time

$$\bar{t}=\omega_1t=\bar{\tau}+\nu\bar{T},\ 0\le\bar{\tau}\le\bar{T}=\frac{\omega_1L}{V}=\frac{\pi}{\alpha} ,$$

$$\frac{d}{dt}()\equiv()^{\cdot} = \omega_1\frac{d}{d\bar{t}}() \equiv \omega_1()' , \tag{5.7}$$

has been introduced and all displacements are normalized with respect to the maximum static beam deflection at mid span,

$$w_{sm}=\frac{MgL^3}{48EI} \approx \frac{2}{\pi^4}\frac{MgL^3}{EI} = \frac{2g\mu}{\omega_1^2} . \tag{5.8}$$

The nondimensional mathematical closed-loop description of model Σ_M then is given by

$$
\begin{aligned}
&\underline{\bar{x}}'(\bar{t})=\underline{\hat{A}}(\bar{t})\underline{\bar{x}}(\bar{t})+\underline{\bar{b}}_d(\bar{t})+\underline{\bar{b}}_s\bar{r}(\bar{t}),\bar{r}(\bar{t})\sim(0,\bar{q}), \\
&\underline{\bar{x}}_{\nu+}=\underline{U}\ \underline{\bar{x}}_{\nu-} ,\ \underline{\bar{x}}_{0+} = \underline{\bar{x}}_0 ,\ \nu = 1,2,\dots,
\end{aligned}
$$

$$\Sigma_M \tag{5.9}$$

where

$$\underline{\bar{x}}(\bar{t})=[z(\bar{t})\ \ z'(\bar{t})\ \ z''(\bar{t})\ \ \bar{z}(\bar{t})\ \ \bar{z}'(\bar{t})\ \ w(\bar{t})]^T/w_{sm},$$

$$\underline{\bar{b}}_d(\bar{t})=[\ 0\quad 0\quad 0\quad 0\quad \sin\alpha\bar{\tau}\quad 0\ ]^T$$

$$\underline{\bar{b}}_s\ =[\ 0\quad 0\quad -\bar{\gamma}\gamma_{\dot{s}}\quad 0\quad 0\quad -\bar{\gamma}\ ]^T ,$$

$$\underline{U}=\underline{\mathrm{diag}}[1\quad 1\quad 1\quad 0\quad 0\quad 1\ ] ,$$

$$\underline{\hat{A}}(\bar{t})=\left[\begin{array}{cc|c|cc|c}
0 & 1 & 0 & 0 & 0 & 0 \\
0 & 0 & 1 & 0 & 0 & 0 \\
\hline
-8\beta^3 & -8\beta^2 & -4\beta & a(\bar{\tau}) & b(\bar{\tau}) & c \\
\hline
0 & 0 & 0 & 0 & 1 & 0 \\
0 & 0 & d(\bar{\tau}) & -1 & -2\zeta & 0 \\
\hline
0 & 0 & 0 & 0 & 0 & -\gamma
\end{array}\right] \tag{5.10}$$

$$
\begin{aligned}
a(\bar{\tau}) &= \gamma_s\sin\alpha\bar{\tau}+\alpha\gamma_{\dot{s}}\cos\alpha\bar{\tau} & c &= \gamma_s-\bar{\gamma}\gamma_{\dot{s}} \\
b(\bar{\tau}) &= \gamma_{\dot{s}}\sin\alpha\bar{\tau} & d(\bar{\tau}) &= -2\mu\sin\alpha\bar{\tau}
\end{aligned}
$$

$$\gamma_s = \kappa_s(r-1)+r\ 8\beta^2,\ \gamma_{\dot{s}}=-\kappa_{\dot{s}}(r-1)+r\ 8\beta^2 .$$

5.3. SYSTEM ANALYSIS FOR MODEL Σ_M

The following analysis is carried out using the parameter values

$$
\begin{aligned}
&\kappa_s=0.0269,\ \kappa_{\dot{s}}=0.00218,\ \bar{\gamma}=0.492\alpha, \\
&\bar{q}=0.788/(\alpha\mu^2),\ \zeta=0.05,\ \omega_1=51\ \mathrm{rad/sec}, \\
&L = 30\ \mathrm{m} .
\end{aligned}
\tag{5.11}
$$

The remaining parameters α , μ , β and the Boolean variable r are varied in order to exhibit their influence on the system response.

5.3.1 STABILITY ANALYSIS

The stability analysis is performed as outlined in Chapter 4.1. The results are shown in Fig. 7, where the spectral radius $\mathrm{spr}(\underline{U}\ \underline{\Phi}(T))$ of the growth matrix is plotted versus the speed ratio α . In Figs. 7a)-d) only the first beam mode is included, $\bar{f}=1$, while Figs. 7e), f) show

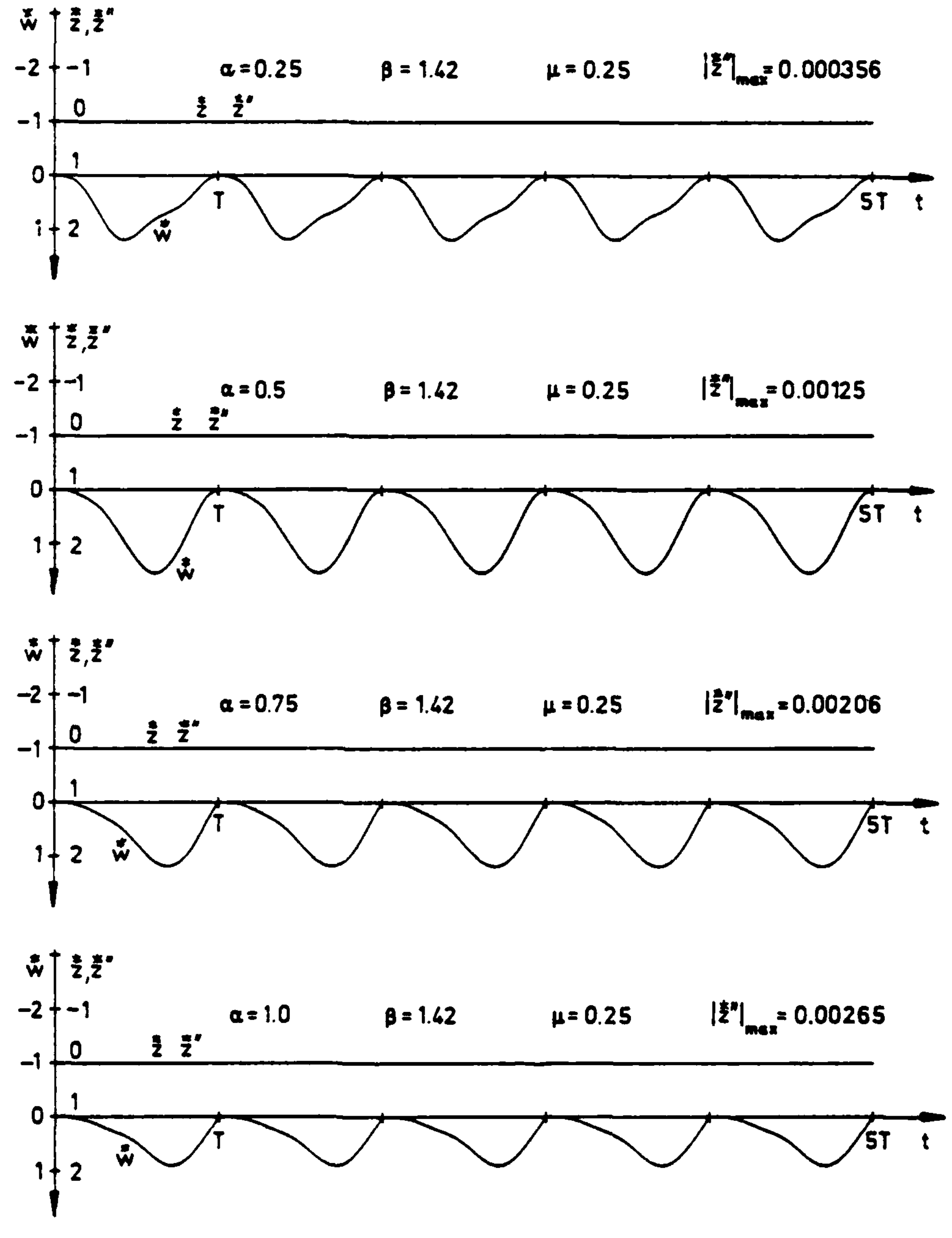

Fig. 8 - Time histories of vehicle and guideway motion for level or z-control ($\overset{*}{w} = w_d(t)/w_{sm}$, $\overset{*}{z} = z(t)/w_{sm}$, $\overset{*}{z}'' = \ddot{z}(t)/(\omega_1^2 w_{sm})$)

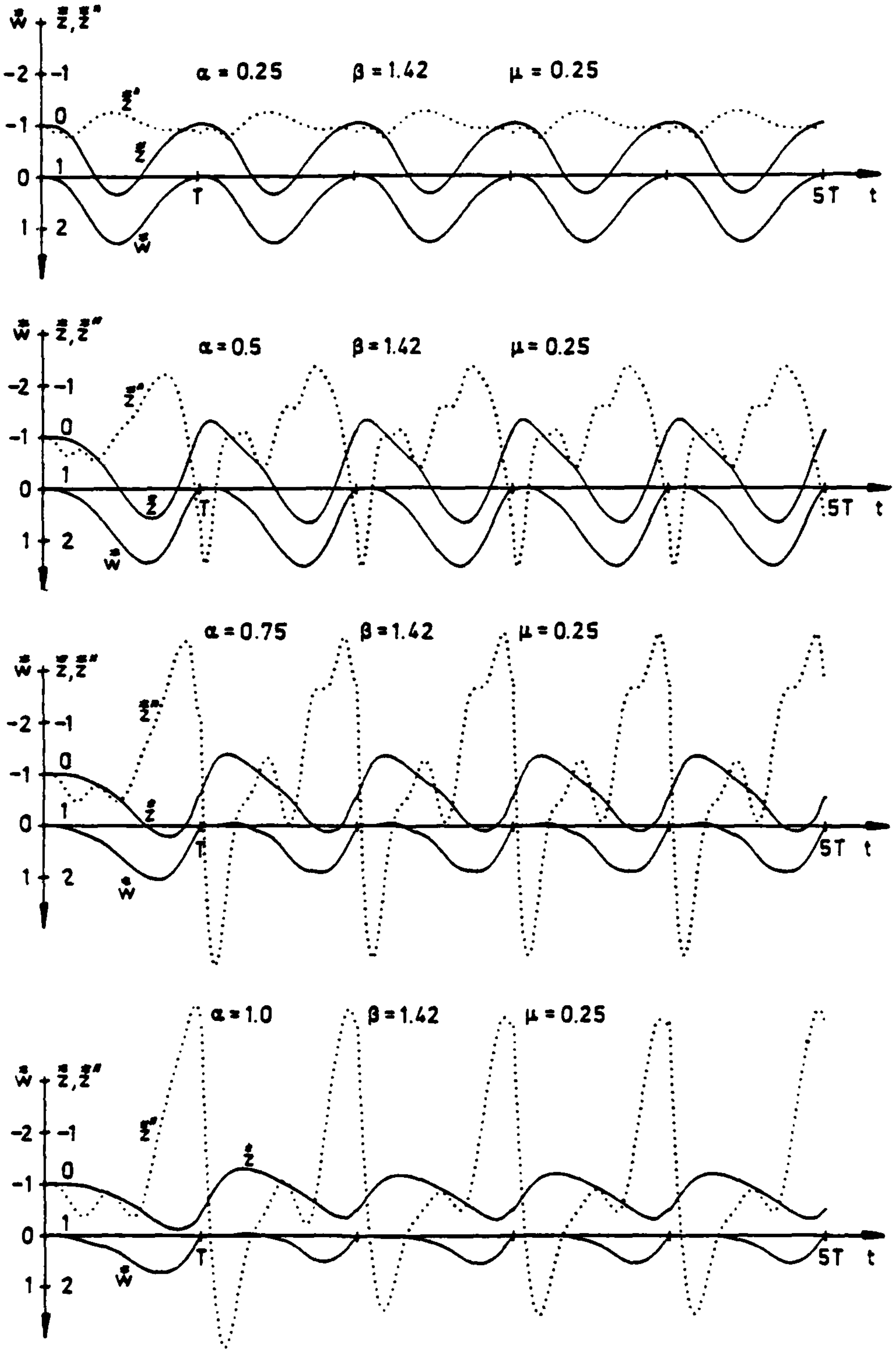

Fig. 9 - Time histories of vehicle and guideway motion for gap or s-control ($\overset{*}{w} = w_d(t)/w_{sm}$, $\overset{*}{z} = z(t)/w_{sm}$, $\overset{*}{z}'' = \ddot{z}(t)/(\omega_1^2 w_{sm})$)

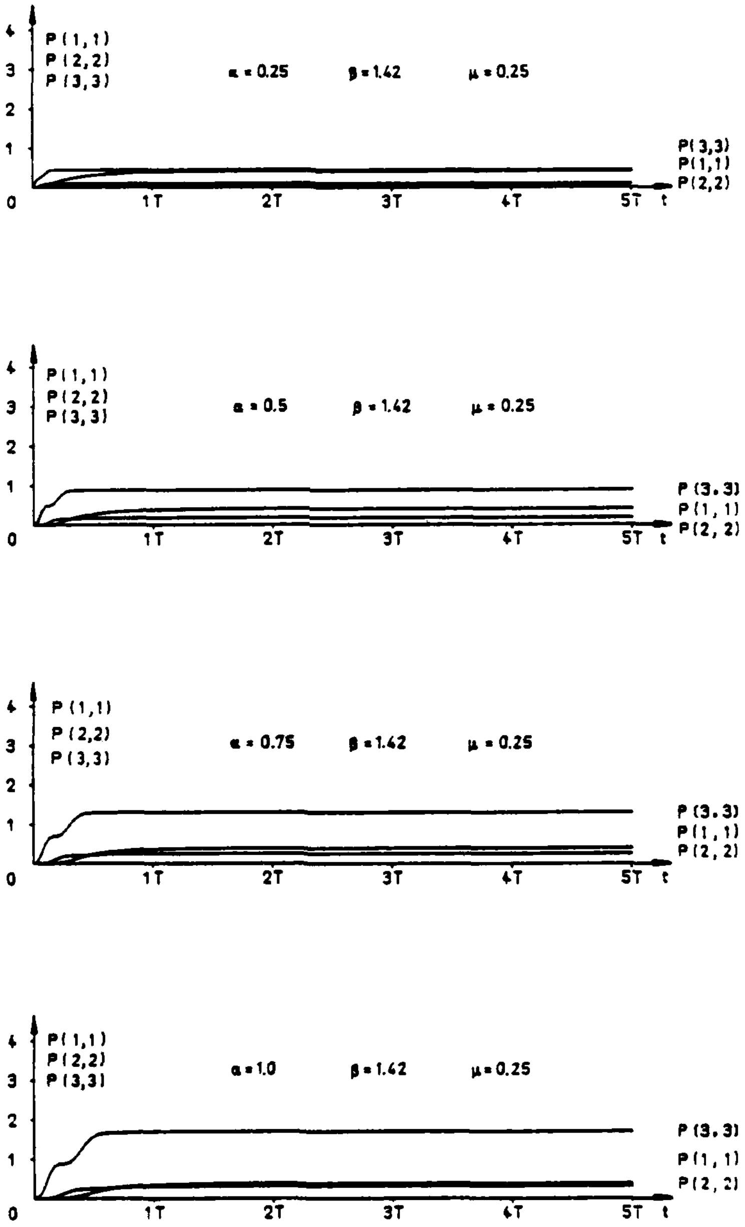

Fig. 10 - Time histories of vehicle motion variances for level or z-control ($P(i,i) = 10^5 \bar{P}_{ii}$)

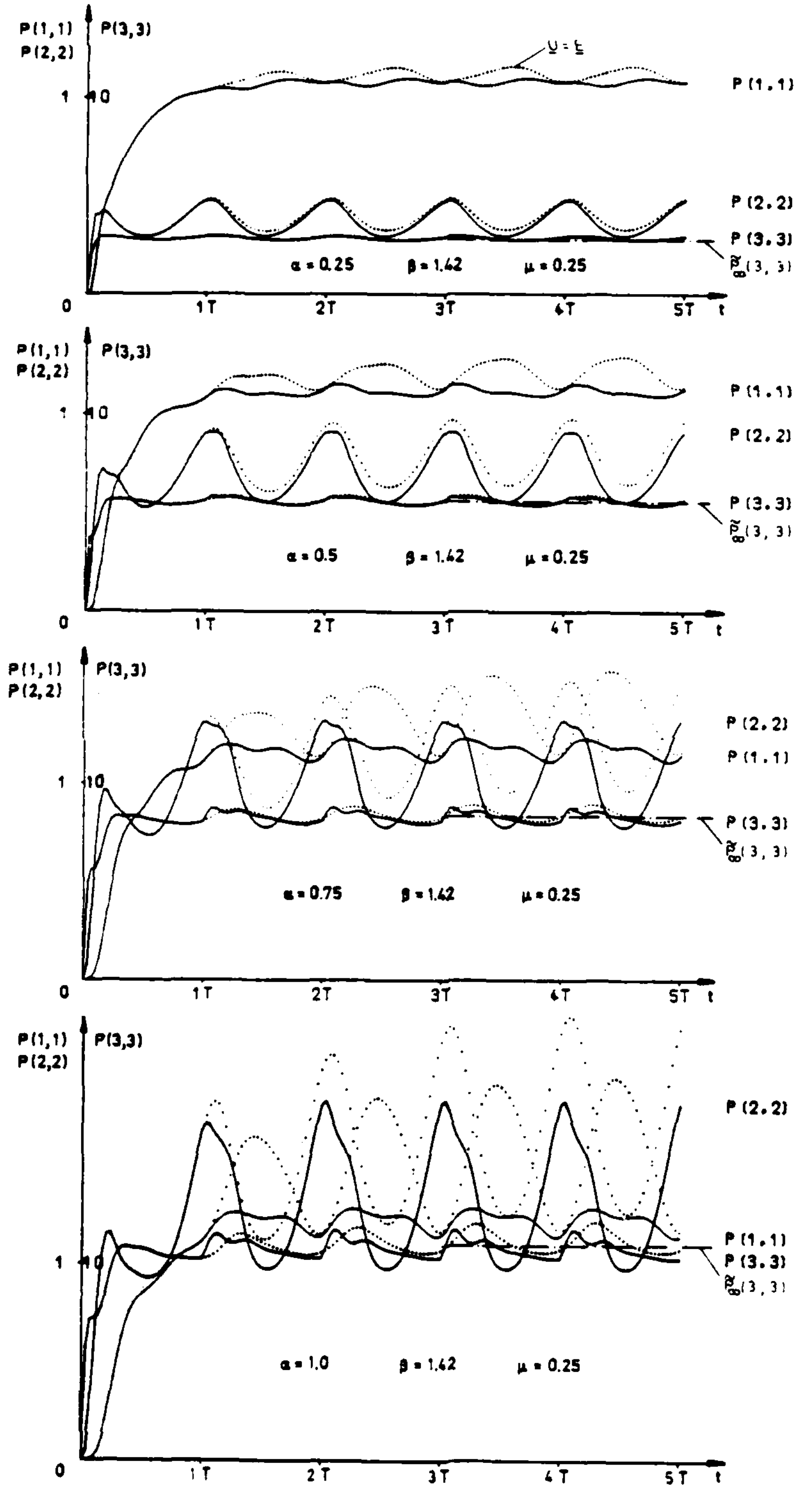

Fig. 11 - Time histories of vehicle motion variances for gap or s-control ($P(i,i) = P_{ii}/\bar{\sigma}^2$, $\bar{\sigma}^2 = 0.1933/\mu^2$)

the results when the first two modes, $\bar{f}=2$, are taken into account. In either case the damping ratio is assumed to be $\zeta_1=\zeta_2=0.05$. It can be seen that the spectral radius $\mathrm{spr}(\underline{U}\,\underline{\Phi}(T))$ increases with higher speeds α, larger mass ratio μ and smaller control parameter ε. For $\bar{f}=1$ asymptotic stability is given for all considered parameters, while for $\bar{f}=2$ the parameter combinations $\alpha = 1$, $\mu = 1$, $\varepsilon = 1.42$, $r = 1$ leads to instability. Fig. 7a) shows that the results are highly incorrect if the jump phenomenon is neglected. Furthermore, the spectral radii are generally smaller for level or z-control than for gap or s-control. In case of z-control (r=0) the lub-approximation $\|\underline{U}\,\underline{\Phi}(T)\|$ agrees very well with the exact results, Fig. 7b).

5.3.2 RESPONSES TO DETERMINISTIC DISTURBANCES

In order to observe the transient behavior, the time histories of the vertical vehicle motion and the guideway motion under the vehicle are plotted until steady state is reached. The results are shown in Fig. 8 for level or z-control and in Fig. 9 for gap or s-control, where $\bar{f}=2$ guideway modes are regarded and the speed ratio α is varied. In either case steady-state is reached after two or three periods and the control goals are almost completely realized. However, for s-control, Fig. 9, the car body acceleration increases considerably with the speed α which may restrict the validity of the model. The results for other parameters and particularly an extensive guideway analysis are given in [42].

5.3.3 RESPONSES TO STOCHASTIC DISTURBANCES

In accord with the previous section, time histories of vehicle motion variances are given in Fig. 10 for level or z-control and in Fig. 11 for gap or s-control. Again, steady-state is obtained after two or three periods. Due to the active decoupling, the steady-state variances are nearly constant in the case of z-control, while for s-control periodic steady-state variances appear. It can be seen, that the variances increase with the speed α. In Fig. 11 the dotted lines show the variances for neclected jumps, clearly leading to incorrect results. In the present example the approximate solution based on (4.18), (4.19) can be analytically calculated. The results are nearly identical with the constant steady state in case of z-control and are between maximum and minimum steady-state variances for s-control. Fig. 11 shows the approximation for the vehicle accelearation variances which are of particular interest for ride comfort evaluations. The results agree very well with the exact value. A numerical comparision shows, cf. [42], that the relative error of the approximation is smaller than 10 % for parameter combinations $\alpha\mu < 0.5$. Thus, for many purposes the approximate solution is sufficient.

6. CONCLUSIONS

Maglev vehicles are complex dynamical system comprising the vehicle, magnetic suspension and guideway dynamics as well as measurement, disturbance and control dynamics. The mathematical description of the open-loop system results in a linear, high order state equation with periodic coefficients and periodically jumping states. However, the control system design calls for low order models, which are obtained mathematically by mode truncation or, physically, by assuming a rigid guideway or zero speed and vanishing disturbances. The controller design results in output feedback or reduced state feedback laws which complete the closed-loop system description. An integrated analysis is given, where stability and steady-state responses to deterministic and stochastic disturbances are investigated. Here, common simulation techniques can be used or the wellknown methods for the analysis of linear periodic systems, which are extended to jumping states. Beside the exact covariance analysis a simple approximation is proposed.

The methods are applied to a simple worst case model which exhibits the influence of the different design parameters. The numerical results show asymptotic stability except for unrealistic design parameters. Furthermore, the responses to deterministic disturbances prove that the control goals are met. A comparison of the responses to stochastic disturbances based on the exact covariance analysis with the proposed approximation shows a very good agreement. For many applications the simple approximate solutions seems to be sufficient. All numerical investigations lead to highly incorrect results if the jumping state phenomenon is neglected.

REFERENCES

1. Bahke, E.: Transportsysteme heute und morgen. Krauskopf-Verlag, Mainz, 1973.

2. Caywood, W.C., Dailey, G., O'Connor, J.S., Stadter, J.T.: A General Purpose Computer Program for the Dynamic Simulation of Vehicle-Guideway Interactions. The Johns Hopkins University, Applied Physics Laboratory, Report No. APL/JHU CP 008, TPR 021, Silver Spring, Md.,1972.

3. Caywood, W.C., Rubinstein, N.: Ride Quality and Guideway Roughness Measurements of the Transpo '72 PRT System. High Speed Ground Transp. J.8, No. 3, 1974, pp. 214-225.

4. Duffek, W., Kortüm, W., Wallrapp, O.: A General Purpose Program for the Simulation of Vehicle-Guideway Interaction Dynamics. 5th VDS - 2nd IUTAM Symposium on Dynamics of Vehicles on Roads and Tracks, Wien, 1977.

5. Frýba, L.: Vibration of Solids and Structures Under Moving Loads. Noordhoff Int. Publ., Groningen, 1972.

6. Gottzein, E., Brock, K.-H., Schneider, E., Pfefferl, J.: Control Aspects of a Magnetic Levitation High Speed Test Vehicle. Automatica 13, 1977, pp. 201-223.

7. Gottzein, E., Crämer, W., Ossenberg, F.W., Roche, Ch.: Optimal Control of a Maglev Vehicle. Proc. of the IUTAM Symposium on the Dynamics of Vehicles on Roads and Railway Tracks, Delft, 1975, pp. 504-530.

8. Gottzein, E., Crämer, W.: Critical Evaluation of Multivariable Control Techniques based on Maglev Vehicle Design. 4th IFAC Symp. Multivariable Technological Systems, Fredericton, N.B., Canada, July 4-7, 1977.

9. Gottzein, E., Lange, B.: Magnetic Suspension Control System for the German High Speed Train. 5th IFAC Symposium Automatic Control in Space, Genua, Juni 1973, In: Automatica 11, No. 5, 1975.

10. Gottzein, E., Lange, B., Ossenberg-Franzes, F.: Control System Concept for a Passenger Carrying Maglev Vehicle. High Speed Ground Transp. J. 9, No. 1, 1975, pp. 435-447.

11. Gottzein, E., Miller, L., Meisinger, R.: Magnetic Suspension Control System for High Speed Ground Transportation Vehicles. World Electrotechnical Congress. Section 7, Paper 07, Moscow, 1977.

12. Guenther, Chr.: A New Approach to High-Speed Tracked Vehicle Suspension Synthesis. In: Leondes, C.T. (Ed.), Control and Dynamic Systems, Vol.13, New York, San Francisco, London, 1977, pp. 71-133.

13. Hedrick, J.K., Billington, G.F., Dreesbach, D.A.: Analysis, Design and Optimization of High Speed Vehicle Suspensions Using State Variable Techniques. J. Dyn. Syst. Meas. Control, Trans. ASME 96, Ser. G, 1974, pp. 193-203.

14. Hedrick, J.K., Ravera, R.J., Anderes, J.R.: The Effect of Elevated Guideway Construction Tolerances on Vehicle Ride Quality. J. Dyn. Syst. Meas. Control, Trans. ASME 97, Ser. G, 1975, pp. 408-416.

15. Hsu, C.S.: Impulsive Parametric Excitation: Theory. J. Appl. Mechanics, Trans. ASME, Juni 1972, pp. 551-558.

16. Hullender, D.A.: Analytical Models for Certain Guideway Irregularities. J. Dyn. Syst. Meas. Control, Trans. ASME 97, Ser. G, 1975, pp. 417-423.

17. Hullender, D.A., Bartley, T.M.: Defining Guideway Irregularity Power Spectra in Terms of Construction Tolerances and Constraints. High Speed Ground Transp. J. 9, No. 1, 1975, pp. 356-368.

18. ISO 2631: Guide for the Evaluation of Human Exposure to Whole-body Vibration, 1st Ed. 1974.

19. Jayawant, B.V.: Dynamical Aspects of Passenger Carrying Vehicles using Controlled D.C. Electromagnets. 5th VSD - 2nd IUTAM Symposium on Dynamics of Vehicles on Roads and Tracks. Wien, 1977.

20. Katz, R.M., Nene, V.D., Ravera, R.J., Skalski, C.A.: Performance of Magnetic Suspensions for High Speed Vehicles Operating over Flexible Guideways. J. Dyn. Syst. Meas. Control, Trans. ASME 96, Ser. G, 1974, pp. 204-212.

21. Kemper, H.: Schwebebahn mit räderlosen Fahrzeugen, die an eisernen Fahrschienen mittels magnetischer Feder entlang geführt wird. Patentschrift Nr. 643316, 1937 (Patenterteilung 1934).

22. Kemper, H.: Schwebende Aufhängung durch elektromagnetische Kräfte: Eine Möglichkeit für eine grundsätzlich neue Fortbewegungsart. ETZ, April 1938, pp. 391-395.

23. Kemper, H.: Elektrisch angetriebene Eisenbahnfahrzeuge mit elektromagnetischer Schwebeführung. ETZ-A, Januar 1953, pp. 11-14.

24. Kortüm, W., Lehner, M., Richter, R.: Multibody Systems Containing Active Elements: Algorithmic Generation of Linearized System Equations, System Analysis and Order-Reduction. IUTAM Symposium Dynamics of Multibody Systems, Munich, Aug. 1977.

25. Kortüm, W., Richter, R.: Simulation of Multibody Vehicles Moving over Elastic Guideways. Vehicle System Dynamics 6, 1977, pp. 21-35.

26. Magnus, K. (Ed.): Dynamics of Multibody Systems. Proc. IUTAM Symp. Munich 1977. Springer, Berlin, Heidelberg, New York, 1978.

27. Meisinger, R.: Optimale Regelung periodischer Systeme mit sprungförmiger Zustandsänderung. ZAMM 57, 1977, pp. 79-81.

28. Meisinger, R.: Beiträge zur Regelung einer Magnetschwebebahn auf elastischem Fahrweg. Dissertation, TU München, 1977.

29. Muckli, W.: Bahnsysteme mit berührungsfreier Fahrtechnik. ZEV-Glasers Annalen 100, No. 1, 1976, pp. 16-19.

30. Müller, P.C., Bremer, H., Breinl, W.: Tragregelsysteme mit Störgrößen-Kompensation für Magnetschwebefahrzeuge. Regelungstechnik 24, 1976, pp. 257-265.

31. Müller, P.C.: Design of Optimal State-Observers and its Application to Maglev Vehicle Suspension Control. 4th IFAC Symp. Multivariable Technological Systems, Fredericton, N.B., Canada, July 4-7, 1977.

32. Müller, P.C., Schiehlen, W.: Lineare Schwingungen. Akademische Verlagsgesellschaft, Wiesbaden, 1976.

33. Müller, P.C., Popp, K.: Kovarianzanalyse linearer Zufallsschwingungen mit zeitlich verschobenen Erregerprozessen. ZAMM 59, 1979, pp. T 144-T 146.

34. Müller, P.C., Popp, K., Schiehlen, W.: Covariance Analysis of Nonlinear Stochastic Guideway-Vehicle-Systems. 6th IAVSD Symp. on Dynamics of Vehicles on Roads and Tracks, Berlin 1979.

35. Pollard, M.G., Williams, R.A.: The Dynamic Behaviour of a Low Speed Electro-Magnetic Suspension. Proc. IUTAM Symp. on the Dynamics of Vehicles on Roads and Railway Tracks, Delft, 1975, pp. 445-478.

36. Popp, K.: Näherungslösung für die Durchsenkungen eines Balkens unter einer Folge von wandernden Lasten. Ing.-Arch. 46, 1977, pp. 85-95.

37. Popp, K.: Stabilitätsuntersuchung für das System Magnetschwebefahrzeug-Fahrweg. ZAMM 58, 1978, pp. T 165 - T 168.

38. Popp, K., Habeck, R., Breinl, W.: Untersuchungen zur Dynamik von Magnetschwebefahrzeugen auf elastischen Fahrwegen. Ing.-Arch. 46, 1977, pp. 1-19.

39. Popp, K., Müller, P.C.: On the Stability of Interactive Multibody Systems with an Application to Maglev-Vehicle-Guideway Control System. IUTAM Symposium Dynamics of Multibody Systems, München, 1977.

40. Popp, K., Schiehlen, W.: Dynamics of Magnetically Levitated Vehicles on Flexible Guideways. Proc. IUTAM Symp. on the Dynamics of Vehicles on Roads and Railway Tracks, Delft, Aug. 1975, pp. 479-503.

41. Popp, K.: Zufallsschwingungen von Fahrzeugen auf elastischem Fahrweg am Beispiel einer Magnetschwebebahn. Appears in ZAMM 60, 1980.

42. Popp, K.: Beiträge zur Dynamik von Magnetschwebebahnen auf geständerten Fahrwegen. Habilitationsschrift, TU München 1978. Fortschr.-Ber. VDI-Z. Series 12, No. 35, Düsseldorf 1978.

43. Reister, D., Zurek, R.: Entwicklungsstand der elektromagnetischen Schwebetechnik für eine Hochleistungs-Schnellbahn. ETR 25, No. 3, 1976, pp. 155-160.

44. Richardson, H.H., Wormley, D.N.: Transportation Vehicle/Beam-Elevated Guideway Dynamic Interactions: A State-of-the-Art Review. J. Dyn. Syst. Meas. Control, Trans. ASME 96, Ser. G, 1974, pp. 169-179.

45. Rothmayer, W.: Elektromagnetische Trag- und Führsysteme (EMS). In: Lehrgang der Carl-Cranz-Gesellschaft O R2.2 Simulationsmodell für Spurgebundene Fahrzeuge, Oberpfaffenhofen, 1977.

46. Smith, C.C., McGehee, C.Y., Healey, A.J.: The Prediction of Passenger Riding Comfort from Acceleration Data. J. Dyn. Syst. Meas. Control, Trans. ASME 100, Ser. G, 1978, pp. 34-41.

47. Smith, R.A.: Matrix Equation $XA + BX = C$. SIAM J. Appl. Math. 16, 1968, pp. 198-201.

48. Snyder III, J.E., Wormley, D.N.: Dynamic Interactions Between Vehicles and Elevated, Flexible Randomly Irregular Guideways. J. Dyn. Syst. Meas. Control, Trans. ASME 99, Ser. G, 1977, pp. 23-33.

49. Sussman, N.E.: Statistical Ground Excitation Models for High Speed Vehicle Dynamic Analysis. High Speed Ground Transp. J. 8, No. 3, 1974, pp. 145-154.

50. Ward, J.D.: The Future Roles for Tracked Levitated Systems, J. Dyn. Syst. Meas. Control, Trans. ASME 96, Ser. G, 1974, pp. 1-11.

51. Yamamura, S.: Performance Analysis of Electromagnetically Levitated Vehicle. World Electrotechnical Congress, Section 7, Paper 09, Moscow, 1977.

52. Zurek, R.: Method of Levitation for Tracked High-Speed Traffic. Endeavour, Vol. 2, No. 3, 1978.

DISCUSSION

Mr. Dorland (Federal Railroad Administration): Are your solutions complicated by the curves in the guideway due to superelevation and by the fact that the inner row of magnets will be shorter than the outer row of magnets and that the velocities will be different?

Mr. Popp: This has been done; particularly curving has been put into the mathematical model. It is nonlinear and you can only use the simulation method for this. I looked for this problem but it is not periodic anymore and so you cannot use Floquet theory to analyze this system, you must rely on simulation methods.

DYNAMICS OF LONG VERTICAL CABLES

F. H. Wolff
Westinghouse R&D Center
Pittsburgh, Pennsylvania

Natural periods of vibration of cables are determined from the homogeneous solution to the equation of motion for a flexible string (with gravity effects) which is fixed at both ends and stretched under applied tension (T_o). Curves containing fundamental periods of vibration for cables of various weights per unit length and applied tension conditions are presented as a function of cable length. Comparisons to the solutions of the classical vibrating string are made to illustrate the discrepancies that would occur if the massive cables were modeled as the classical vibrating string.

LIST OF SYMBOLS

x = distance along cable (ft, m)

y = lateral displacement of cable (ft, m)

t = time (sec)

γ = weight per unit length of cable (lb/ft, N/m)

T_o = applied tension (lb, N)

$T(x)$ = total tension (lb, N)

L = length of cable (ft, m)

ϕ = mode shape

G = time varying modal amplitude

ω_n = cable natural frequency (rps)

n^{th} Period = natural period for n^{th} mode (sec)

Fundamental Period = natural period for 1st mode (sec)

$(\dot{\ })$ = derivative with respect to time

$(')$ = derivative with respect to space variable

INTRODUCTION

To determine the cable natural periods of vibration, they are represented as flexible strings which are fixed at their extremeties. In addition, the cables consist of a weight per unit length (γ) and are assumed to be stretched under a tension (T_o). Also, the effects of gravity are included which causes the total tension ($T(x)$) to vary along the cable - a departure from the classical vibrating string formulation which assumes a uniform tension along its length. The governing equation of motion for the cable modes of vibration is a Bessel equation whose solution involves Bessel's function of the first and second kind. The natural periods of vibration are presented as a function of cable lengths for various weights per unit length and applied tension values.

The natural periods of vibration for the long cables with gravity effects are compared with those of the classical vibrating string. The solutions agree closely for the shorter lengths; however, for the longer cable lengths, the comparable modes of vibration differ substantially. In addition, an approximate solution is presented for the natural periods of vibration for the long cables which agrees closely to the more rigorous Bessel solutions over a wide range of cable parameters.

CABLE FORMULATION (WITH GRAVITY EFFECTS

Consider a flexible cable of weight per unit length γ and length L to be vibrating laterally with displacement motion $y(x,t)$ - Fig. 1A. The partial differential equation which describes these lateral motions can be derived with the aid of the free body diagram - Fig. 1B.

A summation of forces in the vertical direction x gives

$$\gamma\, dx + T \cos \Theta - (T+dT) \operatorname{Cos} \left(\Theta + \frac{\partial \Theta}{\partial x} dx\right) = 0 \qquad (1)$$

which after assuming small angle motions,

$$\operatorname{Cos} \Theta \approx 1 \text{ and } \operatorname{Sin} \Theta \approx \Theta$$

rearranging, and reducing provides the variation in total tension along the cable as

$$\frac{dT}{dx} = \gamma \qquad (2)$$

Integrating Eq. (2) over the cable length gives the total tension (including both the applied tension T_o and tension due to cable weight) as a function of position x.

$$T = \gamma x + T_o \qquad (3)$$

A summation of lateral forces

$$(T + dT) \operatorname{Sin} \left(\Theta + \frac{\partial \Theta}{\partial x} dx\right) - T \operatorname{Sin} \Theta - \frac{\gamma}{g} dx \frac{\partial^2 y}{\partial t^2} = 0 \qquad (4)$$

for small angle motion and neglecting differentials of higher order (dx^2) results in

$$\frac{\gamma}{g} \frac{\partial^2 y}{\partial t^2} = \frac{dT}{dx} \Theta + T \frac{\partial \Theta}{\partial x} \qquad (5)$$

where g is the gravitational constant. Since the slope of the cable is $\Theta = \frac{\partial y}{\partial x}$, substituting Eq. (2) and Eq. (3) into Eq. (5) gives

$$\frac{\partial^2 y}{\partial t^2} = g \left\{\frac{\partial y}{\partial x} + \left(x + \frac{T_o}{\gamma}\right) \frac{\partial^2 y}{\partial x^2}\right\} \qquad (6)$$

which is the governing equation of motion for the lateral vibration of the cable shown in Fig. 1.

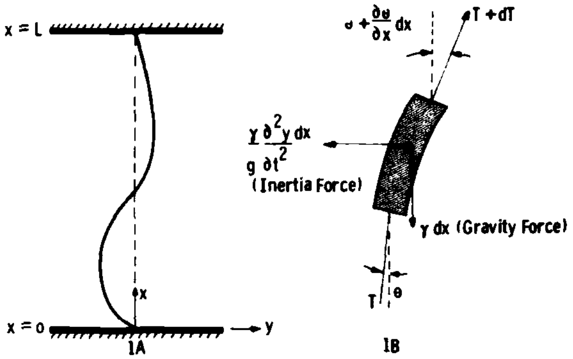
x = L
x = 0
x
y
1A
$\Theta + \frac{\partial \Theta}{\partial x} dx$
T + dT
$\frac{\gamma}{g} \frac{\partial^2 y}{\partial t^2} dx$
(Inertia Force)
γ dx (Gravity Force)
T
θ
1B

Fig. 1 - Flexible cable (length L, weight per unit length γ) supported at both ends while stretched under tension T_o and free body diagram of cable element of length dx

NATURAL VIBRATION CHARACTERISTICS

The cable natural frequencies and characteristic mode shapes can be determined by finding the solution to Eq. (6). In any normal mode

$$y_n (x,t) = \Phi_n (x)\, G_n (t) \qquad (7)$$

where $\Phi_n (x)$ is the characteristic shape for the nth mode and $G_n(t)$ is the time varying modal amplitude. Substitution of Eq. (7) into Eq. (6) leads to

$$\frac{\ddot{G}_n(t)}{G_n(t)} = g \left\{\frac{\Phi'_n(x)}{\Phi_n(x)} + \left(x + \frac{T_o}{\gamma}\right) \frac{\Phi''_n(x)}{\Phi_n(x)}\right\} = - \omega_n^2 \qquad (8)$$

where ω_n is the cable natural frequency (rad/sec) for mode n. Equation (8) furnishes two ordinary differential equations

$$\ddot{G}_n(t) + \omega_n^2 G_n(t) = 0 \qquad (9)$$

$$\left(x + \frac{T_o}{\gamma}\right) \Phi''_n(x) + \Phi'_n(x) + \frac{\omega_n^2}{g} \Phi_n(x) = 0 \qquad (10)$$

The solution to Eq. (10) provides the characteristic shapes.

Introducing a change of independent variable to X by substituting for

$$x = X - \frac{T_o}{\gamma} \qquad (11)$$

into Eq. (10) gives

$$X\Phi''_n(X) + \Phi'_n(X) + \frac{\omega_n^2}{g} \Phi_n(X) = 0 \qquad (12)$$

A further change in the independent variable according to

$$Z^2 = 4 \frac{\omega_n^2}{g} X = 4 \frac{\omega_n^2}{g} \left(x + \frac{T_o}{\gamma}\right) \qquad (13)$$

where

$$\frac{dZ}{dX} = 2 \frac{\omega_n^2}{g} \frac{1}{Z}$$

$$\Phi'_n(X) = 2 \frac{\omega_n^2}{g} \frac{1}{Z} \Phi'_n(Z) \qquad (14)$$

$$\Phi''_n(X) = \left(2 \frac{\omega_n^2}{g}\right)^2 \frac{1}{Z^2} \left\{\Phi''_n(Z) - \frac{1}{Z} \Phi'_n(Z)\right\}$$

results in the more familiar form of Bessel's equation of order 0.

$$\Phi''_n(Z) + \frac{1}{Z} \Phi'_n(Z) + \Phi_n(Z) = 0 \qquad (15)$$

The complete solution to Eq. (15) involves Bessel functions of the first $J_o(Z)$ and second $Y_o(Z)$ kinds of order 0[1].

$$\Phi_n(Z) = A_n J_o(Z) + B_n Y_o(Z)$$

or

$$\Phi_n(x) = A_n J_o\left(2 \omega_n \sqrt{\frac{\gamma x + T_o}{g\gamma}}\right) + B_n Y_o\left(2 \omega_n \sqrt{\frac{\gamma x + T_o}{g\gamma}}\right) \qquad (16)$$

Applying the fixed end conditions

$$y_n(0,t) = \Phi_n(0) = A_n J_o\left(2 \omega_n \sqrt{\frac{T_o}{g\gamma}}\right) + B_n Y_o\left(2 \omega_n \sqrt{\frac{T_o}{g\gamma}}\right) = 0 \qquad (17)$$

$$y_n(L,t) = \Phi_n(L) = A_n J_o\left(2 \omega_n \sqrt{\frac{\gamma L + T_o}{g\gamma}}\right) + B_n Y_o\left(2\omega_n \sqrt{\frac{\gamma L + T_o}{g\gamma}}\right) = 0 \qquad (18)$$

yields the characteristic shapes

$$\left(\frac{B}{A}\right)_n = - \frac{J_o\left(2 \omega_n \sqrt{\frac{T_o}{g\gamma}}\right)}{Y_o\left(2 \omega_n \sqrt{\frac{T_o}{g\gamma}}\right)} = - \frac{J_o\left(2 \omega_n \sqrt{\frac{\gamma L + T_o}{g\gamma}}\right)}{Y_o\left(2 \omega_n \sqrt{\frac{\gamma L + T_o}{g\gamma}}\right)} \qquad (19)$$

and the frequency equation

$$f(\omega_n) = Y_o\left(2 \omega_n \sqrt{\frac{\gamma L + T_o}{g\gamma}}\right) J_o\left(2 \omega_n \sqrt{\frac{T_o}{g\gamma}}\right) - Y_o\left(2 \omega_n \sqrt{\frac{T_o}{g\gamma}}\right) J_o\left(2 \omega_n \sqrt{\frac{\gamma L + T_o}{g\gamma}}\right) = 0 \qquad (20)$$

The roots of the polynominal $f(\omega_n) = 0$ are identically the natural frequencies ω_n for all

$$Y_o\left(2 \omega_n \sqrt{\frac{T_o}{g\gamma}}\right) \neq 0 \text{ and } Y_o\left(2 \omega_n \sqrt{\frac{\gamma L + T_o}{g\gamma}}\right) \neq 0$$

Note, a trivial solution exists for

$$J_o\left(2 \omega_n \sqrt{\frac{T_o}{g\gamma}}\right) = J_o\left(2 \omega_n \sqrt{\frac{\gamma L + T_o}{g\gamma}}\right) = 0$$

The roots of Eq. (20) were found numerically for a range of values of L, γ, and T_o to obtain the fundamental natural frequencies or periods. The corresponding mode shapes were determined from

$$\Phi_n(x) = J_o\left(2 \omega_n \sqrt{\frac{\gamma x + T_o}{g\gamma}}\right) + \left(\frac{B}{A}\right)_n Y_o\left(2 \omega_n \sqrt{\frac{\gamma x + T_o}{g\gamma}}\right) \qquad (21)$$

NATURAL PERIODS OF VIBRATION

Fig. 2 illustrates the fundamental natural periods of vibration (solution to Eq. (20) for n = 1) of the flexible cable (with gravitational effects) as a function of cable length for a range of

$$v = \sqrt{\frac{gT_o}{\gamma}}\ \frac{ft}{sec}$$

values. Incidentally, the v parameter is the wave velocity of the classical vibrating string.

As the applied tension to weight per unit length ratio (T_o/γ) is decreased, the cable length becomes the dominant variable. Accordingly, in the extreme case where the applied tension is zero, Eq. (6) reduces to

$$\frac{\partial^2 y}{\partial t^2} = g \left[\frac{\partial y}{\partial x} + x\,\frac{\partial^2 y}{\partial x^2}\right]$$

which is the equation of motion for the heavy chain vibration[2]. The fundamental natural period for the heavy chain oscillation is a function of length only

$$\text{Fundamental Period} = \frac{\sqrt{L}}{1.08} \qquad (22)$$

as shown on Fig. 2.

For very large values T_o/γ, the fundamental natural periods decrease and the curves approach a linear function of length as exhibited by the classical vibrating string solutions shown later.

The natural periods of vibration for the higher modes (2nd, 3rd, etc.) are very nearly related to the fundamental mode according to

$$n^{th}\ \text{period} = \frac{\text{Fundamental Period}}{n}$$

$$\text{for } n = 2, 3, \text{etc.} \qquad (23)$$

CHARACTERISTIC MODE SHAPES

Fig. 3 demonstrates the characteristic shape associated with the first two modes of vibration of a cable with $\sqrt{gT_o/\gamma}$ = 500 ft/sec. Note, if a first mode vibration was prevalent the peak motion would not occur at the center of the cable; but, instead somewhere ($x \cong 0.4$ L) below the mid-point. Similarly, for a predominant second mode vibration, the peak responses would not be located at the 1/4 and 3/4 positions. Fig. 4, which shows the first and second modes of a cable with $\sqrt{gT_o/\gamma}$ = 100 ft/sec, indicates the weight parameter accentuates the asymmetric shape of the cable vibrations. In this case the peak amplitude for a first mode vibration would occur at the $x \cong 0.23$ L point.

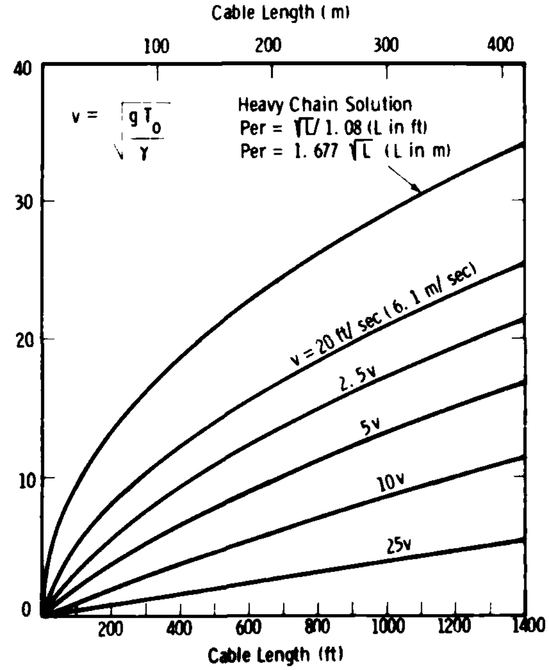

Fig. 2 - Fundamental natural periods of vibration for a flexible cable (γ weight/length) fixed at both ends under tension T_o

COMPARISON TO FUNDAMENTAL MODE OF CLASSICAL VIBRATING STRING

The fundamental natural period of the classical vibrating string which neglects gravity effects by considering uniform tension along its length is given by

$$\text{Fundamental Period} = \frac{2}{\sqrt{\frac{gT_o}{\gamma}}}\,L$$

$$= \frac{2}{\text{wave velocity}}\,L = \frac{2}{v}\,L \qquad (24)$$

which is a linear function of length.

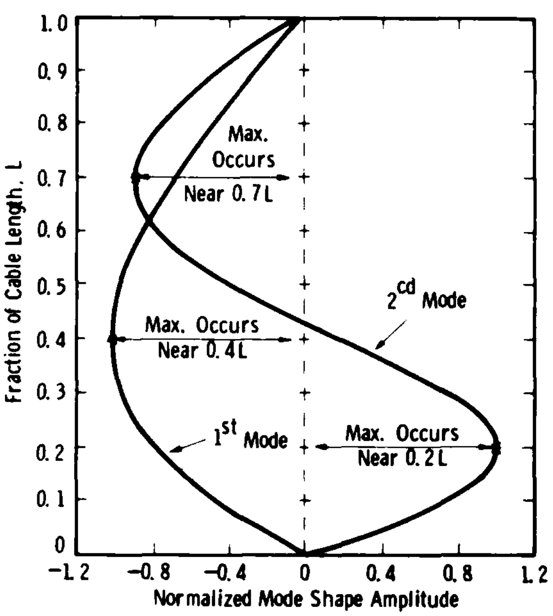

Fig. 3 - 1st and 2nd mode shapes for a cable with v = 500 ft/sec (152.4 m/sec)

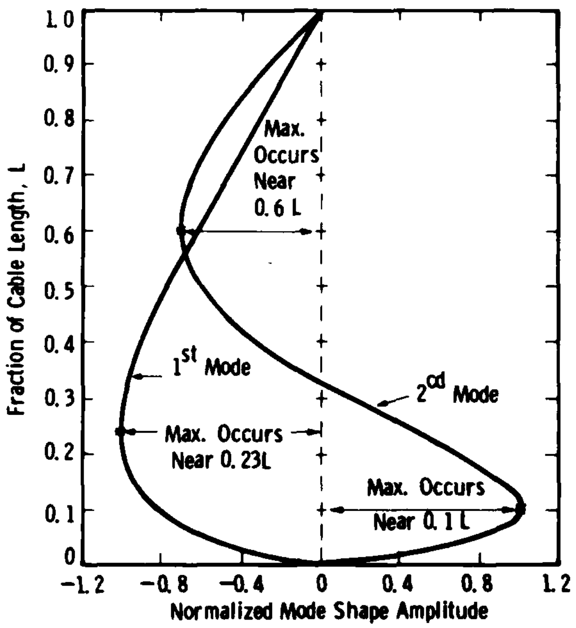

Fig. 4 - 1st and 2nd mode shapes for a cable with v = 100 ft/sec (30.5 m/sec)

Fig. 5 demonstrates for a selected few cable configurations ($v = \sqrt{gT_o/\gamma}$ = 500, 200, 100) the natural period comparison between the varying tension cable (cable with gravity effects) and the classical vibrating string in the fundamental modes. Once again for large values of T_o/γ (hence v), the curves nearly coincide; however, for smaller values T_o/γ, the curves diverge rapidly as the cable length is increased. Also, for the very short cable lengths the two formulations give close results; i.e., as the length → 0 the varying tension curves asymptotically approach the classical vibrating string straight lines.

The foregoing remarks indicate that large discrepancies would occur if the classical vibrating string solutions were used to predict normal modes of long heavy cables.

APPROXIMATE SOLUTION TO FLEXIBLE CABLE (GRAVITY EFFECTS)

Fig. 6 shows the first and second kind Bessel's functions of order 0 for values of the argument, $Z \leq 8$. Further, for values of $Z > 8.654$ and $Z > 10.222$ the first kind $J_o(Z)$ and the second kind $Y_o(Z)$ are for all practical purposes periodic with period 2π. As a consequence of this near periodicity there exist trignometric approximations to these functions for large values of the Z argument[3].

For large values of Z; e.g., Z > 15.

$$J_o(Z) \approx \sqrt{\frac{2}{\pi Z}}\,[\text{Sin}\,(Z + \tfrac{1}{4}\pi) + \frac{1}{8Z}\,\text{Sin}\,(Z - \tfrac{1}{4}\pi)]$$

$$\approx \sqrt{\frac{2}{\pi Z}}\,\text{Sin}\,(Z + \tfrac{1}{4}\pi) = \sqrt{\frac{2}{\pi Z}}\,\text{Cos}\,(Z - \tfrac{1}{4}\pi) \tag{25}$$

and

$$Y_o(Z) \cong \sqrt{\frac{2}{\pi Z}}\,[\text{Sin}\,(Z - \tfrac{1}{4}\pi) - \frac{1}{8Z}\,\text{Sin}\,(Z + \tfrac{1}{4}\pi)]$$

$$\approx \sqrt{\frac{2}{\pi Z}}\,\text{Sin}\,(Z - \tfrac{1}{4}\pi) \tag{26}$$

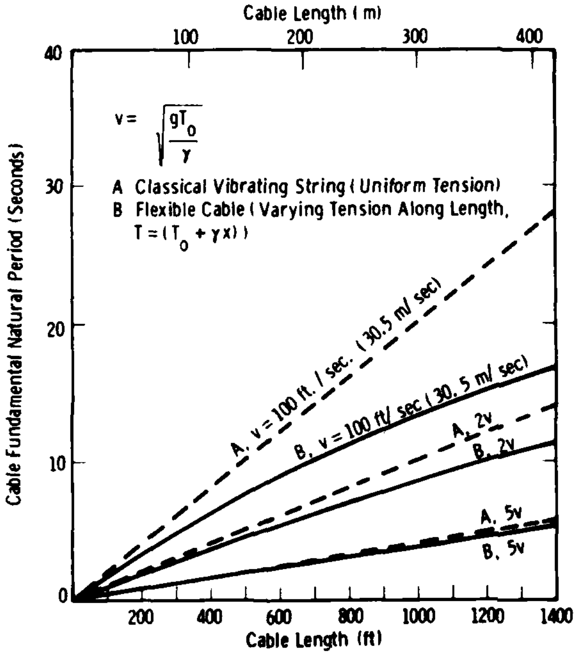

Fig. 5 - Comparison of fundamental periods between uniform (classical vibrating string) and varying tension formulations

Let

$$Z_1 = 2\,\omega_n\sqrt{\frac{T_o}{g\gamma}} \tag{27}$$

$$Z_2 = 2\,\omega_n\sqrt{\frac{\gamma L+T_o}{g\gamma}} \tag{28}$$

Eq. (20) becomes

$$Y_o(Z_2)\,J_o(Z_1) - Y_o(Z_1)\,J_o(Z_2) = 0 \tag{29}$$

Substituting Eq. (25), Eq. (26) in Eq. (29) gives

$$\frac{2}{\pi Z}\,\text{Sin}\,(Z_2 - \tfrac{\pi}{4})\,\text{Cos}\,(Z_1 - \tfrac{\pi}{4}) - \frac{2}{\pi Z}\,\text{Sin}\,(Z_1 - \tfrac{\pi}{4})\,\text{Cos}\,(Z_2 - \tfrac{\pi}{4}) \tag{30}$$

$$= \frac{2}{\pi Z}\,\text{Sin}\,(Z_2 - Z_1) = 0$$

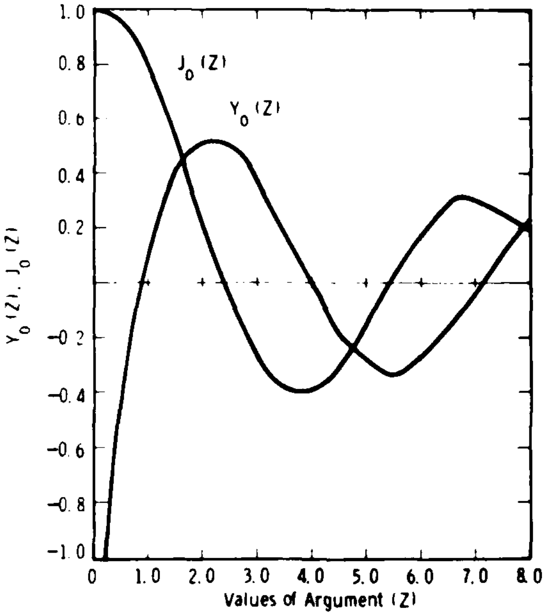

Fig. 6 - Graphical representations of Bessel's Functions of the 1st and 2nd kinds of order 0

Therefore,

$$Z_2 - Z_1 = 2\,\omega_n\sqrt{\frac{\gamma L+T_o}{g\gamma}} - 2\,\omega_n\sqrt{\frac{T_o}{g\gamma}} = n\pi \tag{31}$$

Since $\omega_n = 2\pi/n^{th}$ Period, the fundamental period becomes

$$\text{Fundamental Period} = 4\left[\sqrt{\frac{\gamma L+T_o}{g\gamma}} - \sqrt{\frac{T_o}{g\gamma}}\right] \tag{32}$$

$$= .7049\left(\sqrt{L + \frac{T_o}{\gamma}} - \sqrt{\frac{T_o}{\gamma}}\right)$$

Table I lists the fundamental periods for the flexible cable with gravity effects using the approximate solution from Eq. (32), the more rigorous solution to Eq. (20), and the fundamental periods of the classical vibrating string of the same dimensions.

For the range of values shown in Table I the fundamental periods obtained from the approximate solution are within 5% of those from the more rigorous solution to the Bessel equation.

TABLE 1
Fundamental Periods of Flexible Cable (With Gravity Effects) Using Eq. (20), Eq. (32) and of the Classical Vibrating String

V ft/sec (m/sec)		Fundamental Periods (Sec) For Various Cable Lengths (ft)								
		50	100	200	400	600	800	1000	1200	1400
500	A	0.20	0.40	0.80	1.60	2.40	3.20	4.00	4.80	5.60
(152.5)	B	--	--	--	1.58	2.35	3.12	3.88	4.63	5.37
	C	--	--	--	1.58	2.36	3.12	3.88	4.627	5.368
200	A	0.50	1.00	2.00	4.00	6.00	8.00	10.00	12.00	14.00
(61)	B	--	--	--	3.72	7.02	7.02	8.54	10.00	11.41
	C	--	--	--	3.72	5.41	7.01	8.53	9.99	11.38
100	A	1.00	2.00	4.00	8.00	12.00	16.00	20.00	24.00	28.00
(30.5)	B	.962	1.86	3.51	6.38	8.88	11.12	13.18	15.09	16.88
	C	.96	1.86	3.50	6.37	8.85	11.07	13.09	14.97	16.73
50	A	2.00	4.00	8.00	16.00	24.00	32.00	40.00	48.00	56.00
(15.24)	B	1.75	3.19	5.56	9.29	12.31	14.93	17.27	19.42	21.40
	C	1.75	1.75	5.53	9.19	13.13	14.67	16.93	18.98	20.88
20	A	5.00	10.00	20.00	40.00	60.00	80.00	100.0	120.0	140.0
(6.1)	B	3.11	5.06	7.97	12.23	15.57	18.41	20.43	23.23	25.34
	C	3.08	4.99	7.79	11.83	14.96	17.61	19.94	22.06	24.00
(m)		(15.2)	(30.5)	(61)	(122)	(183)	(244)	(305)	(366)	(427)

A = Classical Vibrating Solutions.

B = Flexible Cable with gravity effects using Eq. (20).

C = Flexible Cable with gravity effects using Eq. (32).

EXPERIMENTAL RESULTS OF LONG VERTICAL CABLE

To verify the theory, experiments were conducted on a long vertical cable. Snap back vibration tests were performed on two lengths of cable. Table II lists the measured and theoretical fundamental periods of vibration of the two lengths. Initially, with 718 feet of cable, the cable was pulled back and released from a location ≈363 feet. The cable was found to have a fundamental period of 10.9 seconds. Secondly, a cable (1376 foot length) was excited from a location about 700 feet. The measured period was 17.9 seconds. The theoretical fundamental periods of vibration for these two cable lengths are 11.14 and 17.71 seconds, respectively. Figure 7 shows the theoretical curve for the cable tested.

TABLE II
Theoretical and Measured Cable Fundamental Periods of Vibration for Long Vertical Cable

Cable				Fundamental Periods (Seconds)		Percent Difference
Length		v		Theoretical	Measured	
(Ft)	(m)	Ft/Sec	m/sec			
718	218.8	84.03	25.6	11.14	10.9	2.20
1375	419.1	84.03	25.6	17.71	17.9	1.06

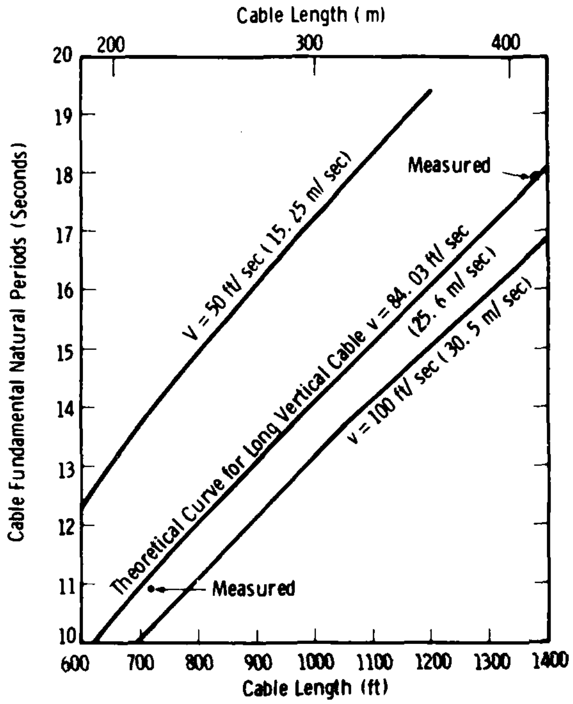

Fig. 7 - Comparison of measured and theoretical fundamental periods for long vertical cable

CONCLUSIONS

The fundamental natural periods curves of Fig. 2 (obtained by solving Eq. (20)) or the approximate solution of Eq. (32) provide accurate means of determining the resonant conditions of long cables. The mode shapes obtained from Eq. (21) indicate where cable motions would be the greatest.

The analysis shows that a classical vibrating string formulation of the cables could produce misleading results, particularly for the long and heavy cables.

REFERENCES

1. Relton, F. E., "Appliied Bessel Functions", Blackie and Son Limited, 1946.

2. Rayleigh, Lord, "Theory of Sound", Dover Publications, 1945.

3. McLachlan, N. W., "Bessel Functions for Engineers", OXFORD at the Clarendon Press, 1934.

Discussion

Mr. Galef (TRW Systems): This problem is constantly encountered in the off shore drilling business. This is especially true when you are in deep water so that to a very good first approximation you can completely forget about the EI of the 18 inch pipe. That sounds a little startling perhaps but the tension dominates up to about the 4th or 5th mode. Some years ago we developed a program for the Subsea Division of TRW using complex Bessel functions where the complex tension was used to include the damping. Now obviously that is not quite true, but if you argue that the damping is important only when you get near a natural period it is not bad and we use this program to make some extended stability studies of a proposed positioning system. It worked very well.

RESPONSE AND FAILURE OF UNDERGROUND REINFORCED CONCRETE PLATES SUBJECTED TO BLAST*

C. A. Ross and C. C. Schauble
University of Florida Graduate Engineering Center
Eglin Air Force Base, Florida

and

P. T. Nash
USAF Armament Laboratory
Eglin Air Force Base, Florida

This paper presents the results of an analytical study to determine plate response and subsequent failure of buried reinforced slabs subjected to a small explosive. Failure is described here as actual material fracture of concrete and reinforcing element at some point in the slab.

Experimentally for underground slabs with fixed or simply supported edges four failure modes have been observed, i.e., 1) stationary hinge mechanism with hinges at edges and extending from corners to slab center, 2) a moving hinge mechanism with fixed hinges at the edges and interior hinges moving toward the center of the slab, 3) localized failure of concrete and reinforcing elements when small explosive is very close to slab, and 4) complete shear of the edges of the slab before hinge mechanisms begin. This study is concerned with modes 1 and 2 and the equations of motion to describe these response modes are derived. The analysis is based on an assumed plastic hinge or yield line response used previously for metal plates and statically loaded reinforced concrete slabs.

Numerical solutions are obtained and results give good qualitative and quantitative agreement with experimental data.

INTRODUCTION

Experimentally observed [1,2] response and failure of underground reinforced concrete slabs subjected to small localized explosions show four definite failure mechanisms. Failure, in this study, is defined as actual combined concrete and reinforcing element fracture at some point in the slab.

The response of reinforced concrete plates can be described using plastic hinges or yield lines, hinge moments and static collapse load.

Plastic hinges are described in detail by Timoshenko [3] and are localized gross rotations in beams and plates at points where localized yielding has occured. A schematic of this type beam deformation is shown in Fig. 1. Plastic hinges are usually used to describe the hinge response in beams [4,6] and are associated with a hinge moment which is determined by assuming a rigid-perfectly plastic constitutive relation for the material. This assumption gives a moment-rotation curve as shown in Fig. 2 and rotation will occur without bounds when the hinge moment M_u is reached, assuming the load remains on the structure. The maximum bending moments for beams and plates tend to occur at fixed edges and at the center of the structure for symmetrical loads. The static collapse load is defined as the static load which is just sufficient to cause plastic

---

*Funded by Joint Technical Coordinating Group/Surface Target Surface Target Survivability Program through AFOSR Grant 78-3592 with cooperation of the USAF Armament Laboratory.

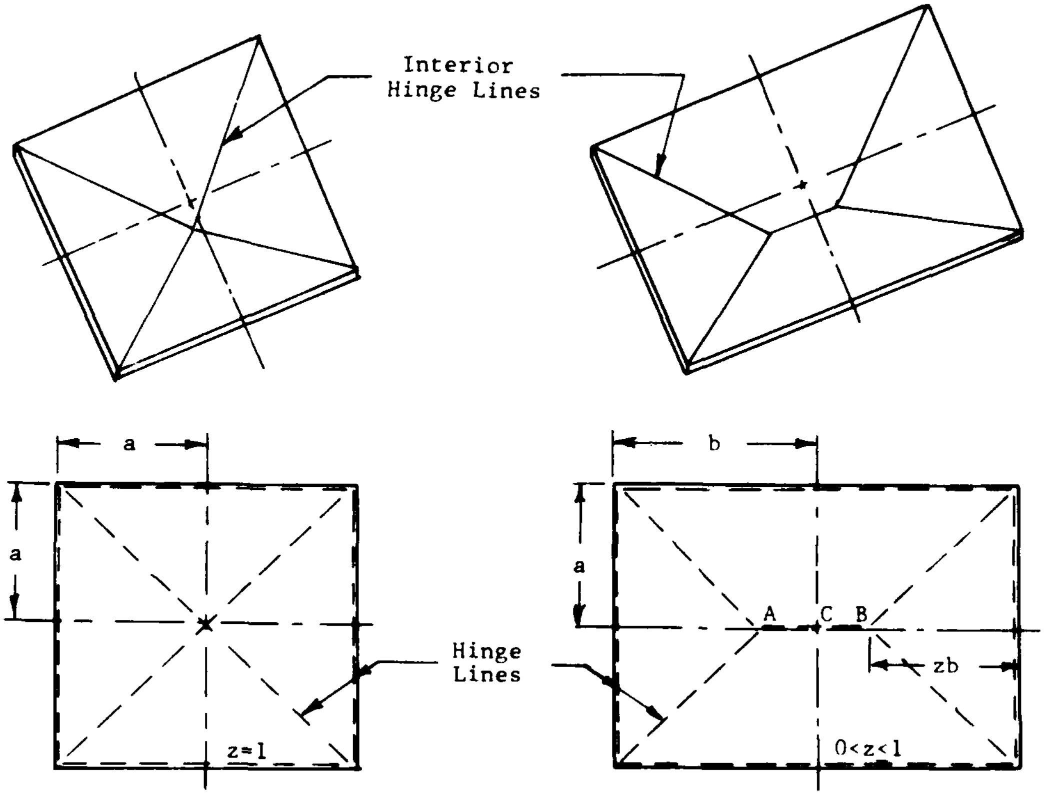

a) square plate b) rectangular plate

Fig. 1 - Yield line locations for mechanism 1 mode response

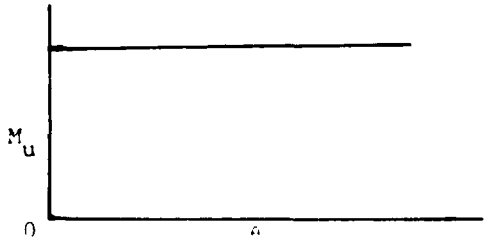

Fig. 2 - Yield line moment/length versus rotation at yield line

hinges to form. Yield lines defined by Szilard [7] are used to describe the hinge motion in plates and are essentially the hinge moments per unit length. The static collapse load of plates is defined as the static load which is just sufficient to cause formation of the yield lines. The static collapse load may vary spatially and in the case of plates has a direct effect on the yield line locations. A typical yield line pattern or hinge location is shown in the schematic of Fig. 3 for static loading of a plate or slab.

The response of buried four edge slabs and two edge beams to loadings caused from localized small underground explosions are best described in terms of a constant size exploding device at varying distances from the structure element. The device is placed on a line passing through and normal to the center of the beam or slab. The pressure time history of the loading pulse at the structure is assumed to have an instantaneous pressure jump and decay to zero in some finite time with the magnitude of the instantaneous pressure and the decay time a function of the distance from the structure. For a given explosive size moved closer and closer to the structure an increase in initial pressure occurs until the mechanism 1 failure

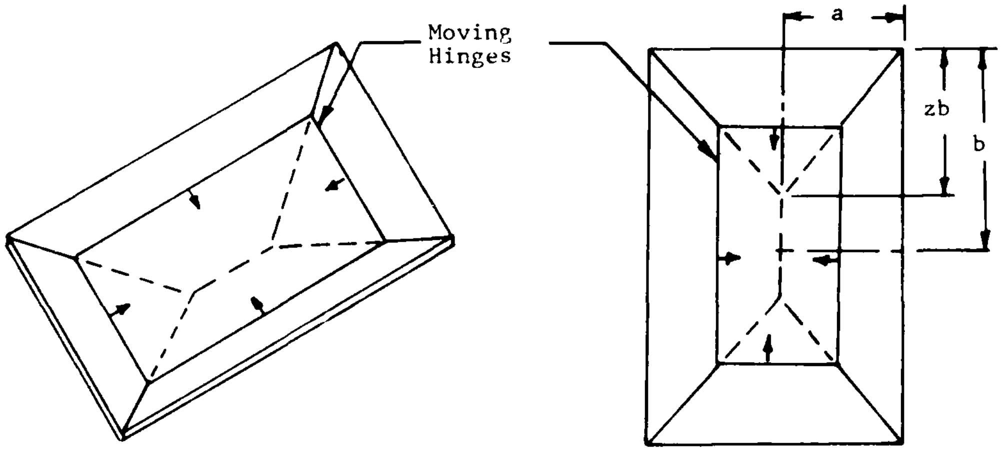

a) 3D schematic b) top view

Fig. 3 - Yield line positions for mechanism 2 mode response

occurs by a stationary hinge mechanism as shown in Fig. 1. The beam response has been described previously by the authors [4] and only the plate or slab response is given here. Analytically, mechanism 1 response will occur when the initial step of the dynamic load reaches the static collapse load of the structure. For dynamic loading, if the static collapse load is reached then rotation will start but due to unloading with time it may be possible that rotation will cease before fracture of the reinforcing element occurs.

As the explosive is moved closer the instantaneous pressure increases. At a critical explosive standoff distance corresponding to a critical pressure load, the interior hinge or yield lines form at distances away from the interior static mechanism 1 positions and move toward the midspan mechanism 1 position. This response mode is a mechanism 2 case and is shown schematically in Fig. 3. This critical load may be determined but is not required for the general overall response analysis. As the explosive is moved still closer a point is reached when a highly localized area of the concrete is blown away without overall plate response. This is defined as mechanism 3. Occasionally the loading may be high enough to cause complete shear at plate edges and is defined as mechanism 4. The analysis in this study is concerned only with mechanism 1 and 2 and it is assumed that the slabs will remain intact supporting the pressure load and will respond only in a mechanism 1 or 2 mode.

PRESSURE LOADING

More than likely the most critical portion of this problem is the description of the pressure loading. For this study an approximate loading, as shown schematically in Fig. 4, is described using a function with separable time and spatial elements of the general form

$$P(x,y,t) = P(x,y)f(t) \quad . \qquad (1)$$

The pressure function is assumed to be symmetric about the center of the plate and will be described over one quarter of the plate. Using Fig. 5 the pressure for the area ODC is expressed as

$$\left.\begin{aligned} P(x,y) &= P_E + P_C \frac{x}{a} \exp\beta\left(\frac{x}{a}-1\right) \quad , \\ & 0 \leq x \leq \left(x = \frac{ay}{b}\right) \quad , \end{aligned}\right| \qquad (2a)$$

and the pressure for area OEC is expressed as

$$\left.\begin{aligned} P(x,y) &= P_E + P_C \frac{y}{b} \exp\beta\left(\frac{y}{b}-1\right) \quad , \\ & 0 \leq y \leq \left(y = \frac{b}{a}x\right) \quad , \end{aligned}\right| \qquad (2b)$$

where P_E is a uniform load over all the plate, P_C is the magnitude at the slab center for the nonlinear superimposed pressure, β is the spatial decay

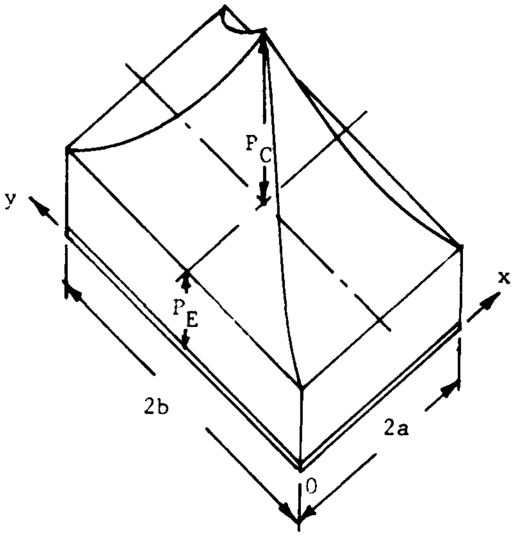

Fig. 4 - Schematic of assumed pressure load on plate

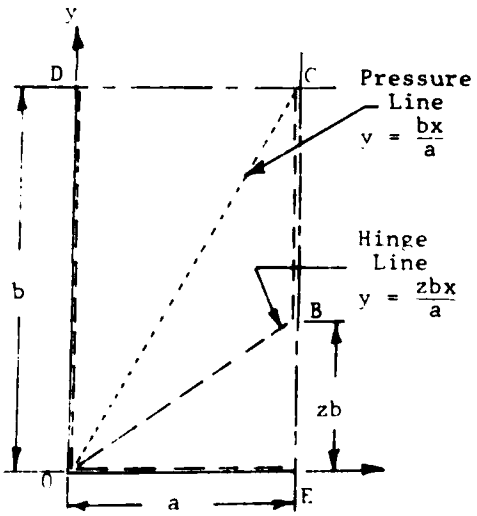

Fig. 5 - Static collapse load yield line positions

constant and x,y,a,b are plate coordinate and plate dimensions respectively. The time function f(t) for a square wave is given as

$$f(t) = 1 \quad , \quad 0 \le t \le \tau \qquad (3)$$
$$f(t) = 0 \quad , \quad t > \tau$$

and for a general decay time function

$$f(t) = (1-t/\tau)\exp(-\alpha t/\tau) \quad 0 \le t \le \tau \qquad (4)$$
$$f(t) = 0 \quad , \quad t > \tau$$

where t is time, α is the time decay constant and τ is the pressure duration.

The spatial portion of the pressure function was handled in closed form in deriving the equations of motion and the time variations were evaluated in the time steps of the numerical solution of the equations of motion. The use of the same β for both the x and y variations appears to be reasonable for plate aspect ratios of two or less. The linear varying load may be found by setting $\beta = 0$, however care must be exercised in closed form integration as β will appear in the denominator of integrated terms, so it is best to handle the linear case separately.

ANALYSIS

The basic assumption of this analysis is that the plate or slab will respond in a yield line or plastic hinge manner under the failure load. It is also important to note that this paper is concerned only with loadings that have an initial instantaneous step functions as shown in Fig. 6.

For mechanism 1 mode in beams, a stationary hinge is assumed to be at the midspan of the beam; whereas, for the mechanism 1 mode of the plate or slab the yield line location is dependent on the magnitude and distribution of the pressure load. For this reason a preliminary calculation must be made to determine the position of the yield lines for the mechanism 1 mode. It is also assumed that the interior traveling hinges of the mechanism 2 mode will move toward and terminate at the yield line locations of the mechanism 1 mode. It is also noted that the yield line positions of the mechanism 1 mode and the yield line positions for the static collapse loading coincide. Therefore calculation of the yield line positions, assuming a static collapse load, are required prior to determining which failure mechanism is operative. This calculated position is then used in both mechanism 1 and mechanism 2 mode calculations.

The yield line positions are based on a minimum energy method using Fig. 5 and a unit midline displacement along the line BC. The line BC, half of the line ACB of Fig. 1, is always assumed to be parallel to the long sides of the slab. The zb positions of the yield

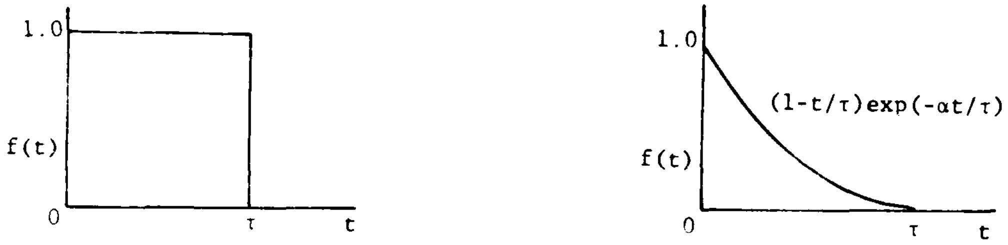

a) square wave b) general decay

Fig. 6 - Time function for pressure loading

lines may be determined by equating the internal energy to the external energy for unit midline displacement and minimizing the resulting expression with respect to z. Using Fig. 5 the external energy is

$$W_{ext} = 4ab\left[P_E\left(\frac{1}{2}-\frac{z}{6}\right)+\frac{P_C}{z^2\beta^4}f(\beta,z)\right] \qquad (5)$$

where

$$\begin{aligned} f(\beta,z) = {} & (3-\beta z)\exp\beta(z-1) \\ & -(2\beta z^2+9z^2+2\beta z+3)\exp(-\beta) \qquad (6) \\ & +2\beta^2-7\beta z^2+9z^2 \end{aligned}$$

and the internal energy is expressed as

$$W_{int} = 4FM_u\left(\frac{a}{zb}+\frac{b}{a}\right) \qquad (7)$$

where M_u is the yield line moment and F is a factor for edge conditions with F = 2 for fixed edges and F = 1 for simply supported edges. Equating W_{int} and W_{ext} and rearranging terms yields

$$\frac{P_C b^2}{FM_u} = \frac{(z+\overline{AR}^2z^2)\beta^4}{f(\beta,z)+K\beta^4z^2\left(\frac{1}{2}-\frac{z}{6}\right)} \qquad (8)$$

$$K = \frac{P_E}{P_C}$$

where $\overline{AR}$ is the aspect ratio b/a. If one plots Eq. (8) versus z a minimum value is realized. It was found that analytically only one minimum exists for $0<z\leq 1$, therefore z may be determined by differentiating Eq. (8) with respect to z and setting the right hand side to zero. The result of this for the nonlinear spatial case ($\beta\neq 0$) is

$$\begin{aligned} & \overline{AR}^2z\Big\{P_E\beta^4z^2\left(\frac{z}{6}\right) \\ & \quad +P_C[(6-4\beta z+\beta^2z^2)\exp\beta(x-1) \\ & \quad -(6+2\beta z)\exp(-\beta)]\Big\} \\ & +P_E\beta^4z^2\left(\frac{z}{3}-\frac{1}{2}\right)+P_C[(3-3\beta z+\beta^2z^2)\exp\beta(z-1) \\ & \quad +(2\beta z^2+9z^2-3)\exp(-\beta)] \\ & -2\beta^2z^2+7\beta z^2-9z^2 = 0 \qquad (9) \end{aligned}$$

and for the linear base ($\beta=0$)

$$\begin{aligned} & P_E(4\overline{AR}^2z+8z-12) \\ & +P_C(2\overline{AR}^2z^3+3z^2-5) = 0 \end{aligned} \qquad (10)$$

The derivation of the equations of motion are covered in detail previously by the authors [8] and only a summary is given here. Using Fig. 7 two equations are derived; one for the inner flat portion and one for the outer deformed portion and displacement continuity is insured at the hinge line. Shear is assumed to be zero at the hinge line and this assumption is discussed in some detail in Refs. 5 and 8. The equation for the inner portion using the symbols of Fig. 7 is

$$\begin{aligned} & m(1-X)(1-zX)\ddot{\delta} = f(t)\Big\{P_E(1-zX+zX^2-X) \\ & +\frac{P_C}{\beta^3}[2\beta-4+(\beta+\beta^2zX^2-\beta^2zX-\beta)\exp\beta(zX-1) \\ & \quad +(4+\beta-3\beta X-\beta^2X+\beta^2X^2)\exp\beta(X-1)]\Big\} \\ & -nw(1-X)(1-zX) \end{aligned} \qquad (11)$$

and the equation for the outer portion becomes

$$\begin{aligned}
&m\ddot{\theta}a^4\overline{AR}X^3\left[(z^2\overline{AR}+1)\left(\frac{1}{3}-\frac{X}{4}\right)+(1-z)\frac{X}{4}\right] = \\
&\frac{f(t)a^3\overline{AR}}{z^2\beta^4}\Big\{P_E\ \beta^4z^2X^2\left[\overline{AR}z^2\left(\frac{1}{2}-\frac{X}{3}\right)+\frac{1}{3}(1-z)X+1\right] \\
&\quad +P_C[-(2\overline{AR}\beta z^2+2\beta z^2+9z^2+6\overline{AR}z-3)\exp(-\beta) \\
&\quad +(\beta^3z^2X^2-\beta^3z^2X^3+4\beta^2z^2X^2)\exp\beta(X-1) \\
&\quad +(-2\beta^2z^2X-9\beta z^2X+2\beta z^2+9z^2)\exp\beta(X-1) \\
&\quad +\overline{AR}(-\beta^3z^4X^3+\beta^3z^4X^2+3\beta^2z^3X^2 \\
&\qquad -2\beta^2z^3X-6\beta z^2X+2\beta z^2+6z)\exp\beta(zX-1) \\
&\quad +(-\beta^2z^2X^2+3\beta zX-3)\exp\beta(zX-1)]\Big\} \\
&-nwa^3\overline{AR}X^2\left[\overline{AR}z^2\left(\frac{1}{2}-\frac{X}{3}\right)+(1-z)\frac{X}{3}+\frac{1}{2}-\frac{X}{3}\right] \\
&-FM_u(1+\overline{AR})a \quad . \qquad (12)
\end{aligned}$$

where

θ	rotation at yield line,
δ	plate center displacement,
$(\cdot\cdot)$	indicates the second derivative with respect to time,
n	an indicator of gravitational force, i.e., n = -1 for explosive above plate, n = +1 for blast below plate and n = 0 for vertical wall,
m	mass per unit area of plate,
w	weight per unit area of plate,
X	defined as x_h/a .

The displacement continuity required at the yield line is

$$\theta x_h = \theta aX = \delta \quad . \qquad (13)$$

As $\beta \to 0$ in Eqs. (10) and (11) the equation of motion for the linearly varying spatial load becomes

$$\begin{aligned}
&m(1-zX)\ddot{\delta} = \\
&f(t)\left\{P_E\ (1-zX)+P_C\left[\frac{1}{3}(X+1)-\frac{X}{2}\left(z^2+\frac{1}{3}\right)\right]\right\} \\
&-nw(1-zX) \quad , \qquad (14)
\end{aligned}$$

for the inner portion and

$$\begin{aligned}
&m\ddot{\theta}a\ \overline{AR}X^3\left[(z^2\overline{AR}+1)\left(\frac{1}{3}-\frac{X}{4}\right)+(1-z)\frac{X}{4}\right] \\
&= f(t)a^3\overline{AR}X^2\Big\{P_E\left[(z^2\overline{AR}+1)\left(\frac{1}{2}-\frac{X}{3}\right)+(1-X)\frac{X}{3}\right] \\
&\qquad +P_C\left[z^3X\overline{AR}\left(\frac{1}{3}-\frac{X}{4}\right)+\frac{X^2}{4}\left(\frac{11}{6}-\frac{z^2}{2}-X\right)\right]\Big\} \\
&-nwa^3\overline{AR}X^2\left[\overline{AR}z^2\left(\frac{1}{2}-\frac{X}{3}\right)+(1-z)\frac{X}{3}+\frac{1}{2}-\frac{X}{3}\right] \\
&-FM_u(1+\overline{AR})a \quad , \qquad (15)
\end{aligned}$$

for the outer portion.

The general solution procedure is to calculate the yield line position zb which then becomes a constant for the remainder of the problem. Next the initial hinge or yield line position must be determined from the initial condition

$$\left.\begin{aligned}\ddot{\theta}aX &= \ddot{\delta} \\ f(t) &= 1\end{aligned}\right\} \quad t = 0 \quad . \qquad (16)$$

The initial value of X then determines the mechanism which is operative. For *0<X<1 the mechanism 2 response is initi*ated, then rotation θ and deflection δ are determined using the Eqs. (11), (12), and (13) or similar Eqs. (14), (15), and (13) until X=1, at which time the yield line has reached the final position and the response is continued using Eqs. (12) or (15) with X=1. If the initial value of X is unity then the mechanism 1 mode is operative and the solution stays in that mode until failure or the motions ceases.

The yield line moment per unit length was derived by Szilard [7] to be

$$M_u = 0.9[d^2q\sigma_r(1-0.59q\sigma_r/\sigma_c)] \quad , \qquad (17)$$

based on the sketch of Fig. 8 and where d is distance from reinforcing element in tension to the opposite slab surface, q is the area of the tensile reinforcement per unit of cross section area, σ_r is the tensile yield of the reinforcing material and σ_c is the compressive strength of the concrete. This expression was used in this study to express the yield line moment in terms of the properties of the structure.

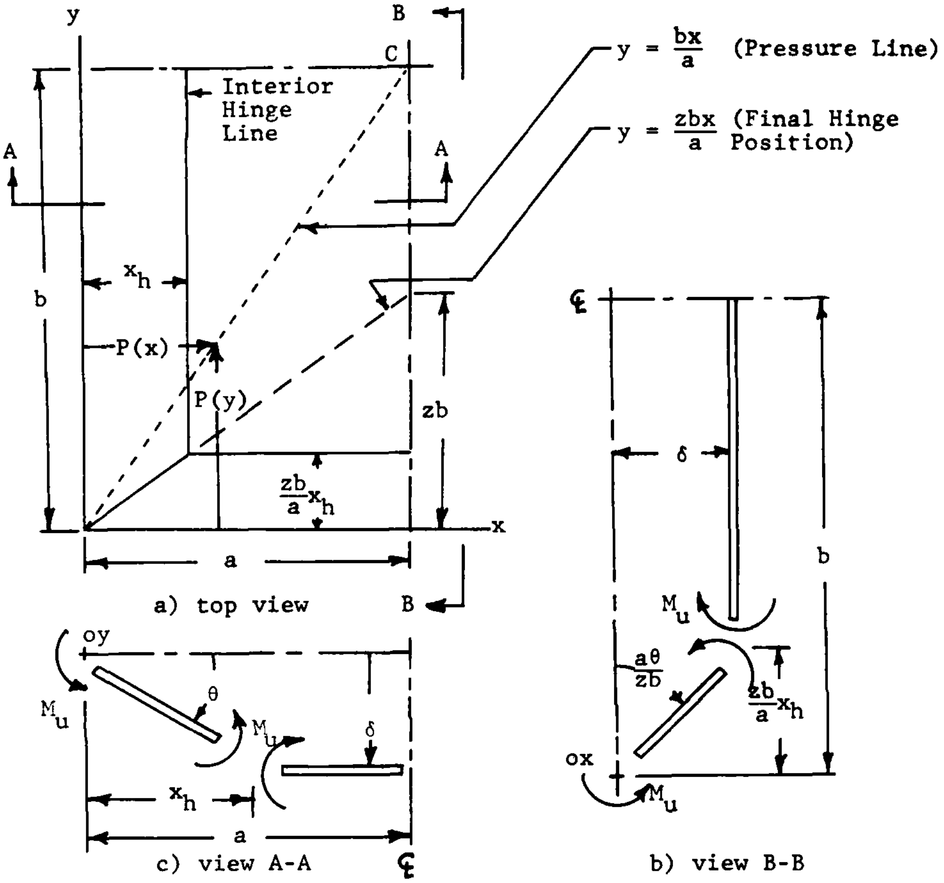
y
B
C
Interior Hinge Line
A
A
$y = \frac{bx}{a}$ (Pressure Line)
$y = \frac{zbx}{a}$ (Final Hinge Position)
b
x_h
P(x)
P(y)
zb
$\frac{zb}{a}x_h$
x
a
B
℄
δ
b
M_u
$\frac{a\theta}{zb}$
$\frac{zb}{a}x_h$
ox
M_u
oy
M_u
θ
M_u
δ
x_h
a
℄

a) top view

c) view A-A

b) view B-B

Fig. 7 - Sketch used for deriving general equations of motion

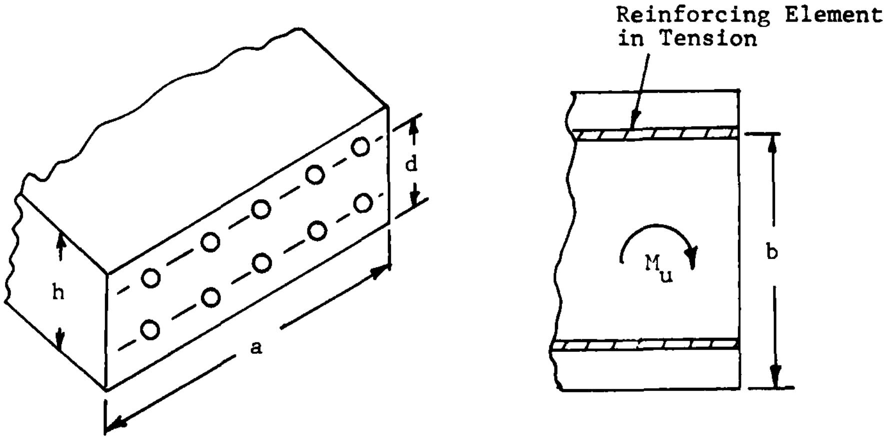
Reinforcing Element in Tension
d
h
a
M_u
b

Fig. 8 - Sketch showing hinge moment distance d used in Eq. (17)

In addition, expressions for kinetic energy, work done by the hinges, and external work were derived in Ref. 8 but are omitted here.

FAILURE CRITERION

Under the assumptions of the previous sections the rotations are highly localized and assumed to occur along a line of zero width. In a real structure the hinge width or damaged zone must be nonzero and intuitively the thicker the slab the larger or wider the damaged area. For an assumed damaged arc length of ℓ at the yield line the strain may be broken into two parts, i.e., a part due to bending ε_b and a part due to axial elongation in tension ε_t. The total strain will then be the sum of these or

$$\varepsilon = \varepsilon_b + \varepsilon_t \quad . \qquad (18)$$

Using the sketch of Fig. 9 the radius of curvature becomes ℓ/θ and the strain due to bending becomes

$$\varepsilon_b = \theta d/2\ell \quad . \qquad (19)$$

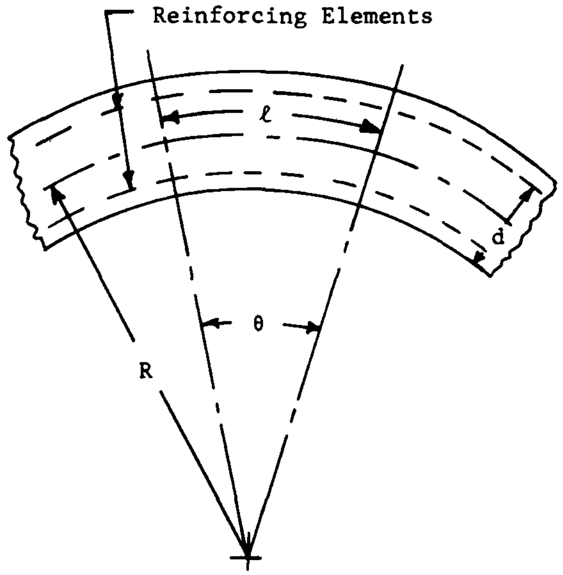

Fig. 9 - Sketch used for calculating strain due to bending

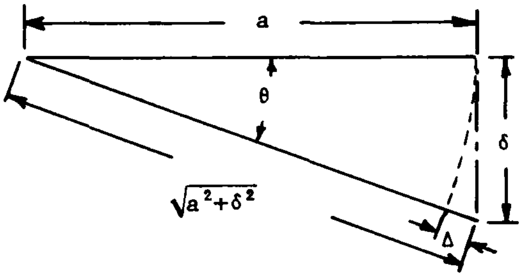

Fig. 10 - Sketch used for determining strain due to tensile elongation

As shown in Fig. 10 the change in length of the short length a may be approximated as $\Delta \simeq \delta^2/2a$ and with half of Δ at each end and small rotations $(\theta \simeq \delta/a)$ the strain due to axial elongation becomes

$$\varepsilon_t = \frac{a\theta^2}{4\ell} \quad . \qquad (20)$$

The total strain then becomes

$$\varepsilon = \frac{\theta a}{\ell}\left(\frac{\theta}{4}+\frac{d}{2a}\right) \quad , \qquad (21)$$

and the rotation θ_u required to produce ultimate strain ε_u becomes

$$\theta_u = \frac{d}{a}\left(\sqrt{\frac{4\ell a\varepsilon_u}{d^2}+1} -1\right) . \qquad (22)$$

For the general case for when the half span a is replaced with x_h the rotation for failure of the tensile reinforcing element becomes

$$\theta_u = \frac{d}{x_h}\left(\sqrt{\frac{4\ell x_h\varepsilon_u}{d^2}+1} -1\right) . \qquad (23)$$

RESULTS AND DISCUSSION

The solutions of the equations of motion were performed numerically using a bisection (binary search) method [9] for the initial hinge location X and the final hinge position zb, and a 4th order Runge-Kutta [10] for the simultaneous differential equations. The numerical solution is contained in a computer code included in Ref. [8] and only two examples are included here.

Calculations were performed on two experimental test cases [1,2] for the pressure loading as shown in Fig. 11. The loading for each case is based on a 8.0 lbf (36N) charge at 2 ft (.61m) from the slab on a line normal to the slab

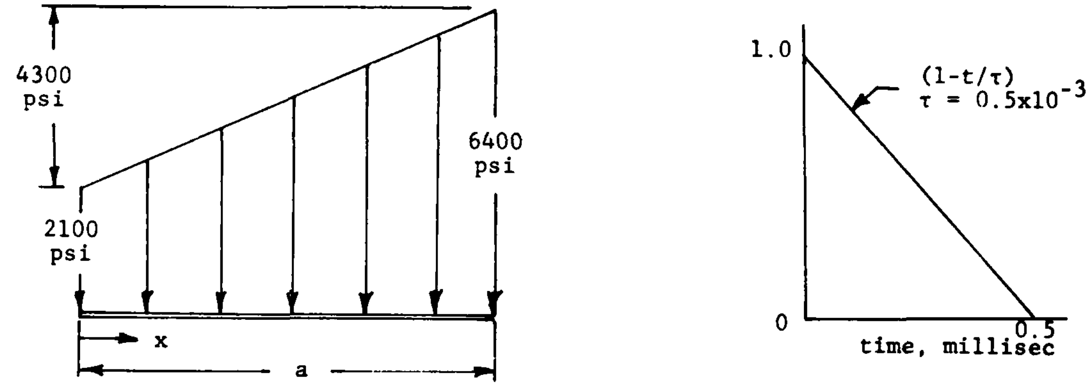

a) spatial variation

b) time variation

Fig. 11 - Pressure distributions used in analyses

center. The experimental slabs were constructed using a six sided box placed against a flat underground vertical wall and both wall and box covered with soil as shown schematically in Fig. 12. The dimensions and necessary information for solution are shown in Table I.

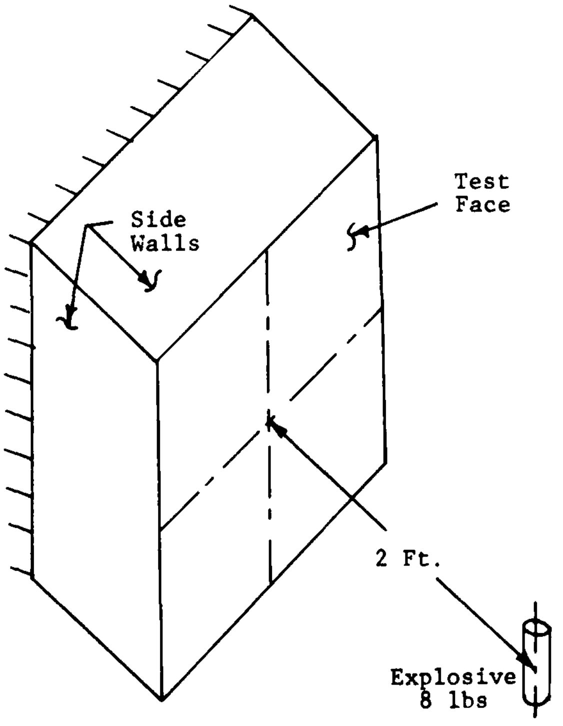

Fig. 12 - Experimental test schematic

In the results of the analysis the maximum displacement of case 1 was 4.4 in (110mm) with a maximum experimental displacement of 2.8 in (71mm). For case 2 the maximum predicted displacement of 5.25 in (133 mm) as compared to approximately 8.0 in (200mm). The analysis predicts that a failure, for ε_u=0.2, occured in case 2 and not in case 1. This was verified experimentally. The most important result of these two analyses is that the analytical procedure distinguishes between the severity of damage with just changes in the aspect ratio of the slab. The damaged slabs are shown in Figs. 13 and 14. In Fig. 13 the cracks tend to form circles rather than rectangles as assumed in the analysis. This appears to be a result of the cracks forming parallel to the edges and curving around the corners as one finds in classical metal plate response where the stresses are predominately membrane in nature.

CONCLUSIONS

Underground experiments using small scale explosive devices verify that concrete plates will exhibit a yield line or plastic hinge response when subjected to dynamic loadings of such devices.

Using failure mechanisms based on dynamic yield line or plastic hinge response, equations of motion for reinforced concrete plates or slabs are derivable and their solutions are in reasonable agreement with experiments. However, these solutions are restricted to slabs where the symmetric pressure load

TABLE I

Properties And Dimensions Of Test Cases

Parameter	Case 1	Case 2
Plate Dimensions in (m)	36x36x4 (.91x.91x.1)	48x36x4 (1.22x.91x.1)
Mass/area lbf-sec^2/in^3(kg/m^2)	$0.899\text{x}10^{-3}$ (244)	$0.899\text{x}10^{-3}$ (244)
P_C psi(MPa)	4300 (30)	4300 (30)
P_E psi(MPa)	2100 (14)	2100 (14)
α	0.	0.
τ, millisec	0.5	0.5
Edge Cond.	Fixed	Fixed
Explosive Position	Vert Wall	Vert Wall
β	0.	0.
σ_C psi(MPa)	6000 (40)	6000 (40)
σ_r psi(MPa)	70,000 (500)	70,000 (500)
Reinforcing ratio in tension	0.1	0.1
Reinforcing Dist in (m)	3.0 (.076)	3.0 (.076)

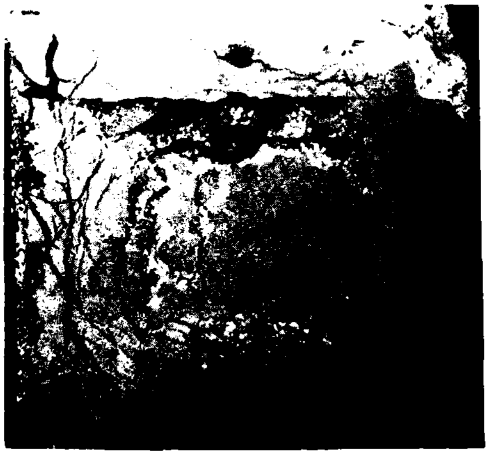

Fig. 13 - Post-test photograph for test case 1

extends over the entire plate whose boundary conditions are fixed or simply supported. The accuracy of the solution is heavily dependent on the accuracy of the pressure time predictions.

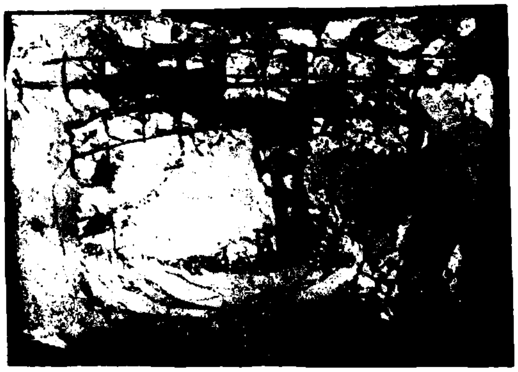

Fig. 14 - Post-test photograph of test case 2

NOMENCLATURE

a	beam half span, plate short side in, (m)
$\overline{AR}$	aspect ratio for plates b/a, dimensionless
b	beam width, plate long side in, (m)

d	distance from tensile reinforcing element to opposite face in compression of cross section in bending in, (m)
F	multiplier on hinge moment designating fixed or simply supported beam ends or plate edges, F = 1 for simple supports, F = 2 for fixed supports, dimensionless
ℓ	plastic hinge width or deformed length in, (m)
m	mass per unit area of plate or beam lbf-sec^2/in^3, (kg/m^2)
M_u	plastic hinge moment per unit length, lbf(N)
P_E	uniform pressure over plate or beam lbf/in^2, (N/m^2,Pa)
P_C	maximum pressure of linear or nonlinear loading lbf/in^2, (N/m^2,Pa)
q	reinforcement ratio, ratio of area of tensile reinforcement per unit cross section area, dimensionless
R	radius of curvature of deformed hinge, in, (m)
t	time sec
w	weight per unit area, lbf/in^2(N/m^2)
W_{int}	internal work, lbf-in(N-m)
W_{ext}	external work, lbf-in(N-m)
x,y	plate coordinates, in(m)
x_h	hinge length, in(m)
X	ratio x_h/a, dimensionless
z	ratio of final hinge position of plate to b, dimensionless
α	time decay constant of pressure, dimensionless
β	spatial decay constant of pressure, dimensionless
δ	midpoint displacement for beams or plates, in(m)
Δ	change in hinge length due to rotation, in(m)
ε	strain, unit deformation, dimensionless
ε_b	strain due to bending, dimensionless
ε_t	strain due to tensile elongation, dimensionless
ε_u	ultimate material strain, dimensionless
n	sign of potential energy term (+) for explosive below horizontal structure, (-) for explosive above horizontal structure, (0) for a vertical structure
σ	stress, lbf/in^2(N/m^2,Pa)
σ_c	concrete compressive strength, lbf/in^2(N/m^2,Pa)
σ_r	ultimate tensile strength reinforcing elements, lbf/in^2(N/m^2,Pa)

REFERENCES

1. Fuehrer, H. R., and Keeser, J. W., "Response of Buried Concrete Slabs to Underground Explosions," AFATL-TR-77-115, USAF Armament Lab., Eglin AFB, Florida, September 1977.
2. Fuehrer, H. R., and Keeser, J. W., "Breach of Buried Concrete Structures," AFATL-78-92, USAF Armament Lab., Eglin AFB, Florida, August 1978.
3. Timoshenko, S. P., and Gere, J. M., Mechanics of Materials, Van Nostrand Reinholt Co., 1972, pp. 289-316.
4. Ross, C. A., Nash, P. T., and Griner, G. R., "Failure of Underground Concrete Structures Subjected to Blast Loadings," 49th Shock and Vibration Bulletin, Part 3, pp 1-9, Sept. 1979.
5. Abrahamson, G. R., Florence, A. L., and Lindberg, H. E., "Radiation Damage Study (RADS) - Vol. XIII, Dynamic Response of Beams, Plates and Shells," BSDTR-66-372, Vol. XIII, Ballistic Systems Div., Norton AFB, CA, September 1966.
6. Florence, A. L., "Critical Loads for Reinforced Concrete Bunkers," DNA 4469F, Defense Nuclear Agcy, Washington, D. C., November 1977.
7. Szilard, R., Theory and Analysis of Plates, Prentice Hall, Inc., 1974, pp. 511-612.

8. Ross, C. A., and Schauble, C. C., "Failure of Underground Hardened Structures Subjected to Blast Loading," Final Report, AFOSR Grant 78-3592. USAF Office of Scientific Research, Bolling AFB, D. C., April 1979.

9. LaFara, R. L., Computer Methods for Science and Engineering, Hayden Book Co., 1973, pp. 82-84.

10. Hildebrand, F. B., Introduction to Numerical Analysis, McGraw Hill Book Co., 1956, pp. 236-239.

WHIPPING ANALYSIS TECHNIQUES FOR SHIPS AND SUBMARINES

Kenneth A. Bannister
Naval Surface Weapons Center
White Oak, Silver Spring, Maryland 20910

An important and difficult example of fluid-structure interaction is the whipping of ships and submarines caused by an underwater explosion. Models of whipping must treat (1) structural response, (2) explosion bubble hydrodynamics, and (3) fluid-structure interaction. The existing models and their computational realizations are reviewed, and illustrative calculations are given on, for example, predictions of the strong influence of submergence depth. Our new work is then described on whipping, using the advanced finite element code USA-STAGS, coupled with an advanced bubble model. Encouraging initial computational results obtained with USA-STAGS are described.

INTRODUCTION

"Whipping" is defined as the transient beam-like response of a ship or submarine to some form of external transient or impulsive loading. In the present context, the source of loading is the transient incompressible fluid flow field associated with a pulsating and migrating gas bubble created by a nearby, but noncontact, underwater explosion. We focus on the phenomenology and analysis of whipping as an interesting, albeit specialized, problem in fluid-structure interaction. Our discussion proceeds with the viewpoint that the treatment of explosion bubble-induced whipping requires a blend of structural dynamics, hydrodynamics, and fluid-structure interaction modeling techniques. The purpose is to briefly review the state-of-the-art on this subject and to show illustrative computations for an idealized surface ship and submerged submarine. Recent work with an advanced bubble model coupled to an advanced fluid-structure interaction analyzer is then discussed.

EARLY INVESTIGATIONS

Very little has been published on explosion bubble-induced whipping in comparison with the perhaps more familiar problem of whipping due to such at-sea events as slamming, ship collisions, or rough sea-states. A great deal has been written, of course, on the behavior of explosion bubbles [1-5] and the low-frequency vibrations of ships [6-10]. Rarely, however, have these two topics been combined so as to explore bubble-induced whipping response.

Apparently, the first investigator to present a comprehensive treatment of bubble-induced whipping is G. Chertock [11-14]. Chertock developed a theory applicable to an idealized ship-like body, possessing lateral and fore-aft symmetry, subjected to hydrodynamic forces generated by a distant non-migrating explosion bubble. The bubble is placed at a distance from the ship hull large in comparison with dimensions of the ship cross section. Thus, the presence of the ship does not cause the bubble to deviate significantly from its "free field" behavior. The ship is modeled as an undamped free-free elastic beam whose dynamic response is obtained by modal superposition. Chertock simplified the response problem greatly by assuming the ship to be a "proportional body," i.e., one whose wet and dry mode shapes are the same--although with different frequencies.

Chertock verified his theory experimentally with floating box ("surface ship") and submerged cylindrical shell ("submarine") models subjected to bubble loadings derived from small charges in the range 1-10 grams. These tests were carefully designed to not violate the underlying assumptions of the theory. Good, and in some cases excellent, agreement was obtained between experimental and theoretical results. Unfortunately, the small scale and idealized targets made extrapolation of these results to practical full-scale situations rather difficult. The following important limitations are inherent in this early theory:

1. Bubble migration is ignored. The inclusion of migration effects is very important in accurately modeling the behavior of full-scale bubbles;

2. Most ships have non-uniform mass and strength distributions and lack fore-aft symmetry;

3. There is no indication of how well the older theory does for close-in bubble positions. Also, the effects of hull-bubble coupling, which may be important for very close-in cases, are omitted;

4. Since modal superposition is employed and only elastic behavior permitted, it is difficult to extend Chertock's theory to problems with large deformations and inelastic response.

When Chertock developed his analysis, large digital computers were unavailable. Thus, the computer-based numerical analysis methods so familiar to us now in structural dynamics work were simply out of reach. The four points just mentioned would present formidable computational hurdles to anyone attempting to incorporate them into a "pencil and paper" method such as Chertock's. In retrospect, it is remarkable how well this pioneering attempt at modeling bubble-induced whipping turned out. Chertock's contributions led to later investigations which resulted in significant improvements in our ability to predict whipping motions.

In recent years, A. Hicks has conducted systematic studies into the phenomenology and analysis of ship and submarine whipping [15-17]. He has considerably extended and generalized the early work of Chertock so that reasonably accurate predictions can be made for elastic, or even mildly inelastic, whipping responses over wide ranges of target characteristics and charge size. Validation studies have been conducted to verify analytical results using experimental results. In regard to computational methods, Hicks has developed various versions of whipping computer programs--all based on a simple lumped mass finite element beam representation of the ship [15]. In the next section, we will give an outline of the underlying analytical formulation typically employed in such models.

ANALYSIS

As mentioned before, the whipping problem involves a blend of structural dynamics, hydrodynamics, and fluid-structure interaction. We therefore draw from the available analytical methods in each field to construct a model. It is possible to do this in a way that yields a model in which the main elements have about the same level of sophistication and accuracy. Attempts to improve one part of the model must include corresponding improvements in the other two to maintain consistency.

The model outlined here results in a matrix equation governing the forced response of the ship (or submarine). The number of equations number twenty or more, usually, so the need for computer-based numerical solution procedures should be clear. Details of the derivations are given in the references and will not be repeated here. Our intent is to point out the important phenomena and review relevant analytical methods.

1. Structural Model

The ship (or submarine) is modeled as an elastic beam floating at the free surface of (or submerged in) an ideal fluid. As shown in Fig. 1, a lumped mass-finite element beam representation is used for the ship. The twenty lumped masses are connected by nineteen elastic beam elements containing bending and shear properties. This is considered about the minimum number of lumped masses one should employ for low-frequency whipping motions.

The pulsating and migrating explosion bubble sets up a transient incompressible flow field that varies along the ship length. Only the vertical flow component is considered since vertical vibrations of the beam are of most interest. Real ships, of course may respond in a complex fashion--undergoing rigid body, flexural, and torsional motions. Whipping response, especially in surface ships, mainly involves vertical motions, that is, heave, pitch, and the first few flexural modes. Submarines may vibrate in any plane through the neutral axis and so it is more likely the whipping response will be three dimensional--unless the bubble loadings are in a principal plane of vibration.

2. Equations of Motion

The undamped equations of motion for the lumped mass positions of the ship-fluid system can be written in the matrix form,

$$[M+M_w]\{\ddot{y}\} + [K]\{y\} = [M_w+\bar{M}_w]\{\dot{u}\} \qquad (1)$$

where $[M]$, $[M_w]$, $[\bar{M}_w]$ and $[K]$ are ship mass, added mass, displaced water mass, and stiffness matrices, respectively. In this development, all these matrices are constant with time. Vectors $\{\ddot{y}\}$, $\{y\}$, and $\{\dot{u}\}$ are the vertical components of ship acceleration, displacement, and bubble flow field acceleration, respectively. The added mass matrix $[M_w]$ will be diagonal if classical strip theory is used, or full and slightly nonsymmetric if an alternative method of computing added mass to be discussed in Section 5 is used. $[\bar{M}_w]$ is a diagonal matrix whose elements are simply the displaced water masses for the ship segments lying at equilibrium in the water. For example, we have for the ith segment,

$$\bar{M}_{w_i} = \rho A_i \ell_i \qquad (2)$$

where ρ = fluid mass density

A_i = submerged cross sectional area of the ith segment

ℓ_i = length of the ith segment

The presence of this term arises from the buoyancy force imposed on the ship due to the acceleration of the fluid $\dot{u}$. When the fluid is at rest, $\dot{u} = g$, so then $\bar{M}_{w_i}\dot{u}$ yields the weight of displaced water.

3. Method of Modal Superposition

Since the ship behaves like a vibrating linearly elastic beam for low frequency motions, we may seek solutions to Eq. (1) by the well-known modal superposition method. This approach is convenient because whipping motions typically involve only the lowest few beam modes, i.e., the first three flexural modes. The existence of such modes can be demonstrated in real ships by steady-state vibration surveys or by impulsive loading tests (anchor-drop, explosions of mild intensity). Some care is needed in selecting the maximum number of modes to include in a whipping calculation, since tuning between bubble pulsation and ship frequencies is important.

We write the displacement history of the ship in the following form:

$$\{y(x_i,t)\} = \sum_{r=0}^{n} \alpha_r(t)\{\phi_r(x_i)\} \qquad (3)$$

where x_i = x-coordinate of the ith lumped mass

and where $\{\phi_r\}$, $r=0,1,2,\ldots,n$ are the first n+1 mode shapes of the ship-fluid system.

Note that Eq. (3) includes the r=0,1 modes corresponding to the rigid body modes of heave and pitch (vertical translation and rotation), respectively. For surface ships, these modes usually are of the same frequency but contribute less to the internal force resultants than the higher-frequency flexural modes. In the case of submarines fully submerged, these modes become simply rigid body displacement degrees of freedom with zero frequency.

The mode coefficient functions $\alpha_r(t)$ may be derived from Eq. (1) in the following manner. First, we write Eq. (1) in the simpler form,

$$[M_1]\{\ddot{y}\} + [K]\{y\} = [M_2]\{\dot{u}\} \qquad (4)$$

where now, $[M_1] = [M + M_w]$ and $[M_2] = [M_w + \bar{M}_w]$. Assuming that $[M_1]$ is, at worst, full and only slightly unsymmetric (so symmetrization does not lead to significant errors in the time-solution), we express it in the form:

$$[M_1] = [L]\,[L^T] \qquad (5)$$

Then, define a new vector $\{z\}$ by,

$$\{z\} = [L^T]\{y\}$$

$$\text{Thus,} \quad \{y\} = [L^T]^{-1}\{z\} \qquad (6)$$

where $[\,]^{-1}$ signifies the inverse of $[\,]$.

Substitution of Eq. (6) into Eq. (4) and rearranging terms yields an equation in terms of $\{z\}$:

$$\{\ddot{z}\} + [L]^{-1}[K]\ [L^T]^{-1}\{z\} = [L]^{-1}[M_2]\{\dot{u}\} \tag{7}$$

Eigenvectors and eigenvalues can be computed from the $\{z\}$-coefficient in Eq. (7) and we denote them by:

$$\{\zeta_r\}\ ,\ \omega_r^2$$

We assume the $\{\zeta_r\}$ are normalized such that,

$$\{\zeta_r\}^T\{\zeta_s\} = \begin{cases} 1 & r=s \\ 0 & r\neq s \end{cases} \tag{8}$$

We can write $\{z\}$ in terms of the normal modes:

$$\{z\} = \sum_{r=0}^{n} \alpha_r(t)\ \{\zeta_r\} \tag{9}$$

Substitution of this result into Eq. (7) and use of the orthonormality property (Eq. (8)) yields r uncoupled equations as follows:

$$\ddot{\alpha}_r + \omega_r^2\alpha_r = \{\zeta_r\}^T[L]^{-1}[M_2]\{\dot{u}\} \tag{10}$$

Hence, by solving Eq. (10) for the mode coefficient functions, given initial conditions $\{\alpha_r(0)\}$ and $\{\dot{\alpha}_r(0)\}$, a flow acceleration vector $\{\dot{u}\}$, and ship characteristics, $\{y\}$ can be computed from:

$$\{y\} = \sum_{r=0}^{n} \alpha_r(t)[L^T]^{-1}\ \{\zeta_r\} \tag{11}$$

Other quantities, such as internal moments, shear forces, strains and stresses can be computed by standard elastic beam relations.

4. Explosion Bubble Hydrodynamics

Ship-bubble flow field interactions occur through the $\{\dot{u}\}$ term on the right-hand-side of Eq. (1). We assume the bubble behaves in a "free field" manner, i.e., as though the ship is not present to perturb the flow. It is possible to account, at least approximately, for the presence of the free surface by the "method of images." Bubble flow loadings are imposed along the axis of the ship (vertical components only) but the true coupled nature of ship and bubble motions is not represented. This coupling problem is a difficult one and is beyond the scope of this discussion.

For the sake of completeness, we include here a brief derivation of the $\{\dot{u}\}$ term for two cases, (1) a free field bubble far from a free surface, and (2) a bubble near a free surface. Figs. 3a and 3b show schematically the problems we wish to solve (both reduce to calculating vertical flow acceleration components along the ship axis). Assuming the bubble remains spherical, does not migrate and the fluid is incompressible, the radial acceleration of the fluid at distance r from the bubble becomes:

$$\dot{u}_r = \frac{\ddot{V}(t)}{4\pi r^2} \tag{12}$$

where V(t) is the current bubble volume. For the case of the bubble far from the free surface, the vertical component is given by

$$\dot{u}_i = \frac{1}{4\pi}\left\{\frac{D-d}{((D-d)^2+H^2+(x_i-x_c)^2)^{3/2}}\right\}\ddot{V}(t) \tag{13}$$

The proximity of a free surface is approximated by placing a negative source at the location of the bubble image in the free surface (Fig. 3b). The total vertical flow acceleration then becomes:

$$\dot{u}_{iT} = \dot{u}_i + \dot{u}_{si} \tag{14}$$

where $\dot{u}_i$ is defined in Eq. (13) and

$$\dot{u}_{si} = \frac{1}{4\pi}\left\{\frac{D+d}{((D+d)^2+H^2+(x_i-x_c)^2)^{3/2}}\right\}\ddot{V}(t) \tag{15}$$

Note that if the body lies in the free surface with d=0, $\dot{u}_i=\dot{u}_{si}$ and $\dot{u}_{iT}=2\ \dot{u}_i$. Thus, $\dot{u}_{iT}$ becomes just twice the value obtained for the case in which the free surface is ignored.

Our assumption of bubble sphericity is an approximation since real bubbles undergo shape distortions, especially during the contraction phase. Physical boundaries such as the free surface, rigid surfaces such as the sea floor, and flexible surfaces such as a ship hull, tend to cause deviations from sphericity. A flat calm surface has been assumed in the derivation of Eq. (14). This also is an approximation since even a nonmigrating bubble tends to elevate the free surface above itself and generate surface (or gravity) waves.

An additional important phenomenon we have ignored so far is the tendency of a bubble, under the action of buoyant forces, to migrate. Boundary surfaces can also cause a certain amount of migration, e.g., free surfaces repel and rigid surfaces attract, but we are concerned here with gravity effects.

As the bubble expands and contracts, and migrates upward, it sets up an accelerating flow field around itself. Assuming that the fluid is ideal (incompressible, irrotational, and inviscid), then potential flow theory can be used to determine the $\{\dot{u}\}$ term in Eq. (1). In simplest form, the velocity potential can be expressed as a sum of pulsation and migration terms,

$$\phi = \phi_{\text{pulsation}} + \phi_{\text{migration}} \qquad (16)$$

Beginning at this point and invoking the First Law of Thermodynamics, Hicks derived a coupled pair of second-order non-linear differential equations governing the pulsation and migration degrees of freedom of the bubble motion [17]. These equations can be altered easily so as to eliminate migration effects and to include, at least approximately, free surface effects. For practical calculations, the equations can be transformed into a set of first-order equations which can be solved by Runge-Kutta or another numerical scheme.

5. Fluid-Structure Interaction

The last part of the analysis concerns the determination of the added mass terms in Eq. (1). The added mass effect arises whenever a body accelerates through a fluid--a certain amount of fluid is entrained and causes an apparent mass increase. In the case of a ship vibrating in a fluid, added masses can be calculated by (a) classical "strip theory" which is the simplest approach, or (b) a more sophisticated method developed by Hicks.

In strip theory, the ship is divided into a number of short segments along its length such that the submerged cross section shape does not vary much over each segment. (A finite element beam model is obviously compatible with strip theory.) Local flow around each segment is assumed perpendicular to the ship axis and to be purely two dimensional. No axial flow is permitted since cross-flow between segments is ruled out. The omission of axial flow means that strip theory does not accurately represent added masses near the free ends of the ship where three dimensional flow predominates. This is not a critical limitation since most conventional ships have fairly constant, or at worst gradually varying, cross sections over much of their lengths.

The use of strip theory is almost synonymous with Lewis coefficients [18]. For a segment of length L, waterline beam (width) B, and water mass density ρ, the added mass M_w is given by,

$$M_w = \frac{1}{2} \pi \rho \left(\frac{B}{2}\right)^2 C_L L . \qquad (17)$$

where C_L is the Lewis coefficient appropriate to the submerged cross section. C_L depends on the local shape of the wetted cross section and can be computed by conformal mapping for simple geometries. Complex shapes can be handled by comparing the hull form against published hull profiles for which C_L values have been tabulated [18]. It is customary to account for three dimensional flow by applying a reduction factor "J" ($0.0 \leq J \leq 1.0$) to the entire distribution of C_L values along the ship length. This reduction factor is usually applied uniformly to all vibration modes simultaneously, but more accurate results can be obtained by computing separate J's for each mode. Recent studies on the correct use of J factors are reported in [19].

An alternative to strip theory has been developed by Hicks [17]. This method accounts for three dimensional flow and accurately treats the velocity boundary condition between ship and fluid. A distribution of discrete vertically oriented fluid dipoles is placed at the lumped mass positions shown in Fig. 1. Their strengths are adjusted to satisfy the normal velocity boundary condition,

$$V_n(\text{hull}) = V_n(\text{fluid}) \qquad (18)$$

This procedure yields more accurate hydrodynamic force distributions for a larger class of ship geometries than strip theory, and especially for length/beam ratios $<$ 10. Otherwise, the new and old methods give about the same results for length/beam ratios $>$ 10 so long as the ship has smoothly varying cross sections versus length (even considering free ends).

Further refinements in the fluid-structure interaction portion of the analysis should probably focus on "higher order" effects. Such phenomena as unsteady flow, non-linear free surface behavior, and axial flow caused by local hull deformations could be important. The analysis of these effects is beyond our scope here, but an idea of the state-of-the-art along these lines can be found in [20] and [21].

EXAMPLE CALCULATIONS

We include here some typical whipping response results computed by the analytical approach just discussed. The three dimensional added mass approximation scheme of Hicks was used in these calculations. We choose for our examples an idealized "uniform beam" surface ship and submerged submarine. No attempt to represent any existing craft has been made here, but the dimensions chosen are typical of full-sized vessels in these categories. Both beams are subjected to bubble loadings arising from the underwater detonation of 100 Kg of TNT. It will be shown that remarkable differences can occur in whipping response (due to changes in added mass and buoyancy forces in the beams) and bubble behavior (due to hydrostatic pressure). We first show plots of basic bubble parameters. Secondly, beam whipping response plots for the amidship positions are shown.

A list of relevant structural, hydrodynamic, and material properties for the uniform beam models is given in Table 1. Both beams are right circular cylinders and are identical except that the submerged beam has twice the density and added mass of the surfaced beam. These differences will naturally lead to different modal characteristics and consequently different whipping response. In both cases, the burst point (bubble center) is positioned 30.48 m (100 feet) below the beam center of gravity. The surfaced beam is assumed to be half-submerged while the other is at a centerline depth of 100 m (328 feet).

Figs. 4-6 show comparisons of shallow and deep bubble radius, depth, and migration velocity histories. Depth effects are quite evident in these plots and it is apparent that a deep bubble produces higher frequency loadings on a target than a shallow one. Note that the bubble parameters are zeroed out just beyond the end of the first cycle. This is a consequence of the TNT bubble model used which is only valid for roughly one bubble cycle and so is terminated early in the second expansion.

Whipping responses are displayed in Figs. 7-10. The surfaced beam executes lower frequency and larger amplitude motions than the submerged beam. In both cases, the first five flexural modes are combined to give the response (plus heave and pitch modes for the surfaced beam).

Table 2 lists the frequencies of the beams along with the corresponding bubble first cycle frequencies. It can be seen that the shallow bubble oscillates at a frequency comparable to the lowest flexural mode of the surfaced beam. In contrast, tuning between the deep bubble and third flexural mode of the submerged beam occurs. Also, the increased density and added mass of the submerged beam causes it to have much lower frequencies.

There are many other ways to display whipping response, of course, in which non-time dependent parameters can be used. For example, a non-dimensional peak moment ratio such as the one discussed by Yuille [11] could be calculated at many bubble positions. With a sufficient density of such values, contours (or surfaces) of constant magnitudes could easily be interpolated for study.

ADVANCED WORK

The USA-STAGS computer code [23] has recently been developed for the analysis of nonlinear response of submerged or partially-submerged structures to underwater explosion-type loadings. By means of the Doubly Asymptotic Approximation (DAA) [24] implemented in the USA (Underwater Shock Analysis) portion of the code, high frequency (shock) and low frequency (bubble) loadings are accurately treated; between these limits a smooth (but approximate) transition is effected. USA, therefore, plays the role of a fluid-structure interaction analyzer that couples the fluid to the vibrating structure and also provides a scheme for applying fluid loadings generated by an explosion source.

The equations of motion solved in USA-STAGS can be written in the general form:

$$
\begin{aligned}
&[M_s]\{\ddot{x}\} + [C_s]\{\dot{x}\} + [K_s]\{x\} \\
&\quad = -[G][A_f]\{P_I + P_s\} + \{f_D\}
\end{aligned}
\tag{19}
$$

$$
\begin{aligned}
&[M_f]\{\dot{P}_s\} + \rho c\,[A_f]\{P_s\} \\
&\quad = \rho c\,[M_f]\{[G^T]\{\ddot{x}\} - \dot{u}_I\}
\end{aligned}
\tag{20}
$$

where in Eq. (19), $\{x\}$ is the structural displacement vector, $[M_s]$, $[C_s]$, and $[K_s]$ are the nonlinear structural mass, damping, and stiffness matrices, $[G]$ is a rectangular transformation matrix relating fluid and structural nodal point forces over the wetted body surface, $[A_f]$ is a diagonal area matrix associated with the elements of the fluid mesh (used in the DAA formulation) laid over the wetted surface of the body, $\{P_I\}$ and $\{P_s\}$ are vectors of the known incident and unknown scattered pressures defined over the fluid mesh nodal points, and $\{f_D\}$ is the dry-structure external nodal point force vector. Eq. (20) expresses the fluid-structure interaction (coupling) resulting from adoption of the DAA. In this equation, $[M_f]$ is the fluid mass matrix for the fluid mesh, ρ and c are the fluid mass density and sound speed, and $\{\dot{u}_I\}$ is the vector of known incident-wave fluid particle accelerations normal to the wetted surface. In the simple case of a spherical incident pressure wave (generated perhaps by an underwater explosion), the vectors $\{P_I\}$ and $\{\dot{u}_I\}$ become [23]:

$$
\begin{aligned}
p_{I_i}(t) &= \frac{S}{R_i}\,\bar{p}_I\left(t - \frac{R_i - S}{c}\right) \\
\dot{u}_{I_i} &= \left[\frac{1}{\rho c}\,\dot{P}_{I_i}(t) + \frac{1}{\rho R_i}\,P_{I_i}(t)\right]\gamma_i
\end{aligned}
\tag{21}
$$

where S is the distance between the incident wave origin and the nearest point on the wetted body surface, R_i is the distance between the wave origi and the ith fluid node on the wet surface, γ_i is the cosine of the angle between R_i and the local wet-surface normal, and $p_I(t)$ is the incident pressure profile at R_i=S. Note that although P_I and $\dot{u}_I$ happen to be easily related in this example, Eq. (20) allows $\dot{u}_I$ to vary independently of P_I.

Having introduced USA-STAGS as a new analytical tool for fluid-structure interaction problems, we now focus on the advantages it offers over the simpler methods discussed earlier. First, a considerable improvement in structural dynamics modeling is afforded. We are no longer limited to small deformation-small strain response of one-dimensional structures; now three dimensional nonlinear responses of quite general assemblages of beams and shells can be computed. Second, much more general types of fluid loadings are treated. Third, the source of fluid loading is arbitrary, i.e., so long as reasonable incident pressure and fluid particle acceleration histories can be generated, USA-STAGS will accept these regardless of source model.

An example of how USA-STAGS predictions compare with results from a simpler whipping model is shown in Fig. 11. In this analysis, the elastic whipping response of a submerged body of assumed form was computed with a simple beam element model (see Fig. 1) coupled with Hicks' added mass scheme and then by modeling the same problem with USA-STAGS. In the simpler case, a non-migrating bubble model like that outlined in Section 4 was used. Essentially the same beam element model was used in the USA-STAGS work but a new shock-bubble code, now under development, was used to calculate an incident spherical pressure wave history. This history was then input to Eqs. (21), which are built into USA, to calculate a corresponding fluid particle acceleration history. Note that the pressure history calculated this way contains both early-time shock wave and late-time bubble flow effects. Since the simpler bubble model is valid for only one pulsation, the comparison in Fig. 11 is terminated shortly past the end of the first cycle. No such limitation exists on the shock-bubble code, however, and if desired, it can be used to analyze several bubble pulsations. Fig. 11 shows good agreement between the two predictions over the interval of interest. This is very promising in regard to the usefulness of USA-STAGS in performing practical whipping calculations.

CONCLUSIONS

Analytical approaches have been summarized for the important problem of a ship interacting with fluid loadings due to an underwater explosion. The main elements of this problem, namely, structural response, fluid-structure interactions and bubble hydrodynamics, are each amenable to modeling at various levels of sophistication but it is important to maintain consistency among the three. It is demonstrated that the bubble behavior and target response can change strongly as a function of submergence--leading to much different whipping motions. This is done with the aid of simple uniform cylinder geometries which are intended to be "bench mark" problems for comparative calculations by methods other than those discussed here.

A new analytical tool, USA-STAGS, has been exercised on a trial whipping problem and reproduces quite well results obtained by present methods. It is important to note that this new code offers many advantages over our present modeling techniques due to the extensive structural analysis capability of STAGS. Also, the more realistic DAA formulation, which better handles fluid-structure interactions, allows both shock and bubble-type inputs. The problem still remains, of course, of supplying a model of the underwater explosion loadings suitable for input to USA-STAGS. This problem is mitigated by the inherent flexibility of the USA portion of the code which merely requires pressure and particle velocity inputs.

REFERENCES

1. Office of Naval Research, "Underwater Explosion Research: Volume II - The Gas Globe," Department of the Navy, 1950

2. Cole, R. H., Underwater Explosions, (New York: Dover Publications, 1965)

3. Snay, H. G., "Hydrodynamics of Underwater Explosions," in Naval Hydrodynamics, Publication 515, National Academy of Sciences, National Research Council, 1957

4. Plesset, M. S., "Bubble Dynamics and Cavitation," in Annual Review of Fluid Mechanics (Palo Alto: Annual Reviews, Inc., 1977) Vol. 9, pp. 145-185

5. Holt, M., "Underwater Explosions," in Annual Review of Fluid Mechanics (Palo Alto: Annual Reviews, Inc., 1977) Vol. 9, pp. 187-214

6. Young, T., (1814), in History of Strength of Materials (New York: McGraw-Hill, 1953)

7. Taylor, J. L., "The Theory of Longitudinal Bending of Ships," Trans. of the North East Coast Institution of Engineers and Shipbuilders, Vol. 41, 1924

8. McGoldrick, R. T., "Ship Vibration," DTMB Report 1451, 1960

9. Leibowitz, R. C., and Kennard, E. H., "Theory of Freely Vibrating Nonuniform Beams, Including Methods of Solution and Application to Ships," DTMB Report 1317, 1961

10. Bishop, R.E.D., Price, W. G., and Tam, P.K.Y., "A Unified Dynamic Analysis of Ship Response to Waves," Trans. of the Royal Institution of Naval Architects, 1977, pp. 363-390

11. Chertock, G., "The Flexural Response of a Submerged Solid to a Pulsating Gas Bubble," Journal of Applied Physics, Vol. 24, No. 2, 1953, pp. 192-197

12. Chertock, G., "Effects of Underwater Explosions on Elastic Structures," in Fourth Symposium on Naval Hydrodynamics, ACR-92, August 1962

13. Chertock, G., "Excitation of Transient Vibrations of Idealized Ship Models by Underwater Explosions," in Seventy-Seventh Meeting of the Acoustical Society of America, 8 April 1969

14. Chertock, G., "Transient Flexural Vibrations of Ship-like Structures Exposed to Underwater Explosions," Journal of the Acoustical Society of America, Vol. 48, No. 1 (Part 2), 1970, pp. 170-180

15. Hicks, A. N., and McKeeman, J. L., "The Elastic Theory of Explosion Induced Whipping; Computer Program Specification," NCRE Report R550, September 1968

16. Hicks, A. N., "The Whipping Forces Experienced by a Ship Very Close to an Underwater Explosion," DTNSRDC Report 3271, January 1970

17. Hicks, A. N., "A Method for Determining the Virtual Mass Distribution Around a Vibrating Ship," DTNSRDC Report 3272, January 1970

18. Wendel, K., "Hydrodynamic Masses and Moments of Inertia," DTMB Translation 260, 1956

19. Townsin, R. L., "Virtual Mass Reduction Factors:J-Values for ship Vibration Calculations Derived from Tests with Beams Including Ellipsoids and Ship Models," Trans. Royal Institution of Naval Architects, 1968, pp. 385-397

20. Schot, J. W., and Salvesen, N., eds., Proceedings: First International Conference on Numerical Ship Hydrodynamics, (David W. Taylor Naval Ship Research and Development Center, October 1975)

21. Wehausen, J. V., and Salvesen, N., eds., The Proceedings: Second International Conference on Numerical Ship Hydrodynamics, (University of California, Berkeley: University Extension Publications, September 1977)

22. Yuille, I. M., "Longitudinal Strength of Ships," Trans. Royal Institution of Naval Architects, Vol. 105, No. 1, 1963, pp. 1-33

23. DeRuntz, J. A., et al, "The Underwater Shock Analysis (USA) of Non-Linear Structures, A Reference Manual for the USA-STAGS Code," LMSC-D624355, February 1978

24. Geers, T. L., "Doubly Asymptotic Approximations for Transient Motions of Submerged Structures," Journal of the Acoustical Society of America, Vol. 64, No. 5, November 1978, pp. 1500-1508

TABLE 1

Structural and Hydrodynamic Properties of Surfaced and Submerged Uniform Beam Models

Maximum Beam (Diameter)	10 m
Overall Length	100 m
Section Length (L/20)	5 m
Moment of Inertia	10 m^4
Area Effective in Shear	1 m^2
Section Displacement	213075 Kg (Surfaced Beam) 426150 Kg (Submerged Beam)
Section Added Mass	213075 Kg (Surfaced Beam) 426150 Kg (Submerged Beam)
Young's Modulus, E	2.07×10^{11} Pa (30×10^6 psi)
Poisson's Ratio, ν	0.3
Seawater Density, ρ	1025.2 Kg/m^3 (64 lbm/ft^3)
Yield Stress, σ_y	3.45×10^8 Pa (50000 psi)

TABLE 2

Frequency Data for Surfaced and Submerged Beams

Mode No.	Frequency (Hz) Surfaced Beam	Submerged Beam
0 (Heave)	0.178	—
1 (Pitch)	0.182	—
2	1.860	1.314
3	4.990	3.530
4	9.380	6.632
5	14.650	10.360
6	20.470	14.470
Bubble First Cycle	2.273	6.211

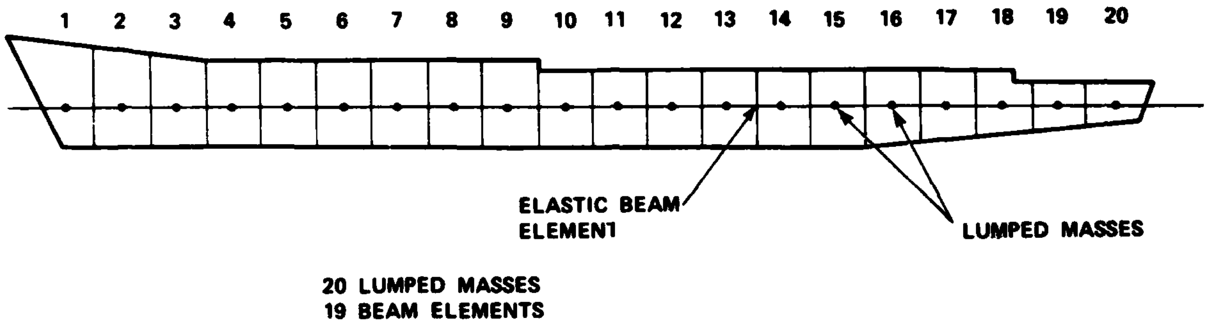
1
2
3
4
5
6
7
8
9
10
11
12
13
14
15
16
17
18
19
20
ELASTIC BEAM ELEMENT
LUMPED MASSES
20 LUMPED MASSES
19 BEAM ELEMENTS

FIGURE 1 LUMPED MASS FINITE ELEMENT BEAM MODEL OF A SHIP

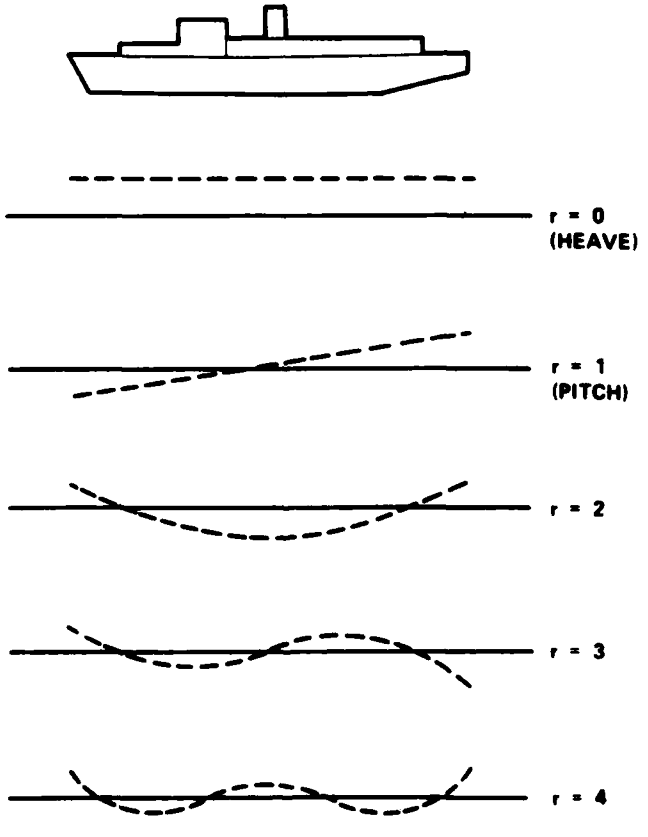
r = 0
(HEAVE)
r = 1
(PITCH)
r = 2
r = 3
r = 4

FIGURE 2 RIGID BODY AND FLEXURAL MODE SHAPES FOR A SURFACE SHIP

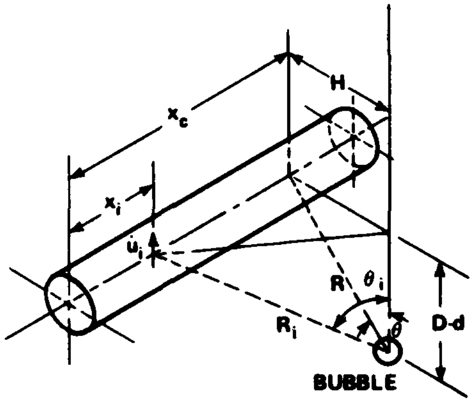
x_c
H
x_i
$\dot{u}_i$
R
θ_i
R_i
θ
D-d
BUBBLE

(a) BUBBLE FAR FROM FREE SURFACE ($\dot{u}_i$ = VERTICAL COMPONENT OF FLOW ACCELERATION AT x_i)

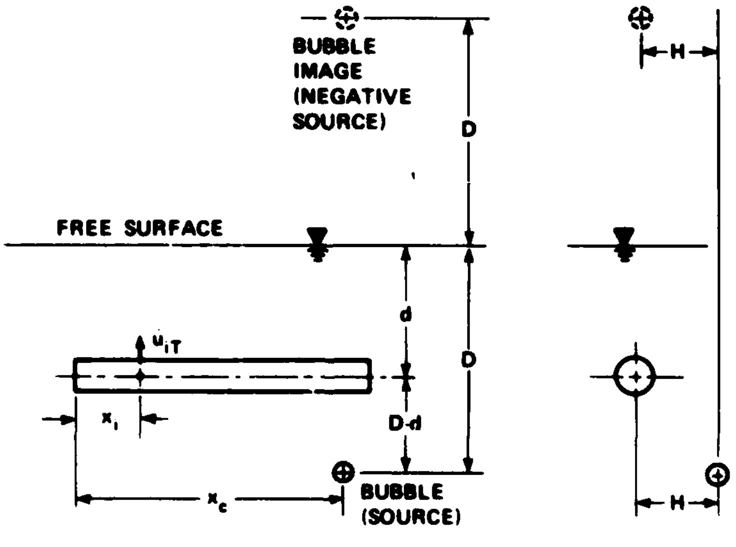
BUBBLE
IMAGE
(NEGATIVE
SOURCE)
D
FREE SURFACE
d
u_{iT}
D
x_i
D-d
x_c
BUBBLE
(SOURCE)
H
H

(b) BUBBLE NEAR A FREE SURFACE (u_{iT} = TOTAL VERTICAL COMPONENT OF FLOW ACCELERATION AT x_i)

FIGURE 3 GEOMETRIES FOR BUBBLE ANALYSES WITH, AND WITHOUT, FREE SURFACES

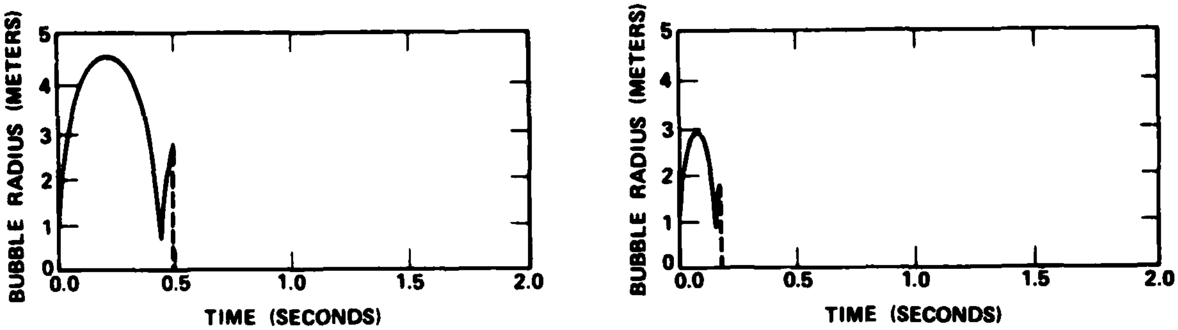

(a) 30.48 m DEPTH

(b) 130.48 m DEPTH

FIGURE 4 RADIUS VS TIME FOR 100 KG TNT EXPLOSION BUBBLE

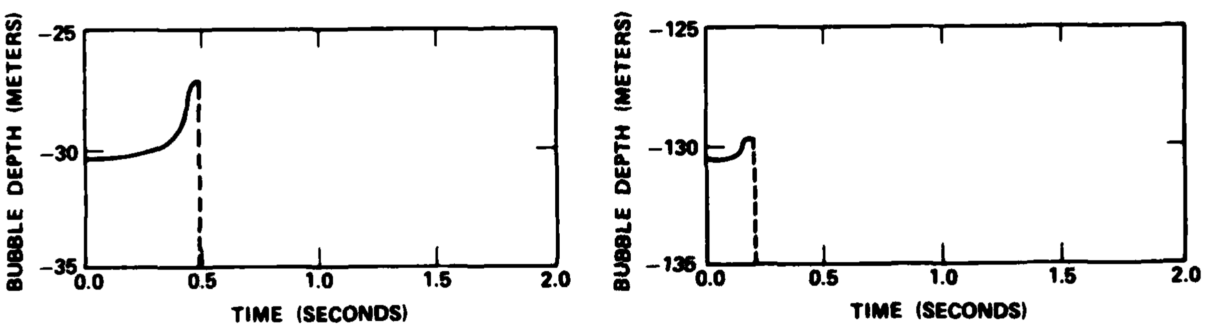

(a) 30.48 m DEPTH

(b) 130.48 m DEPTH

FIGURE 5 DEPTH VS TIME FOR 100 KG TNT EXPLOSION BUBBLE

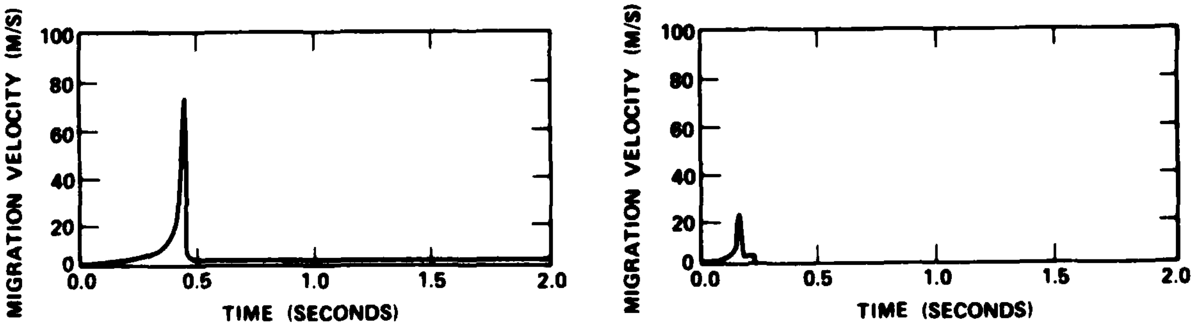

(a) 30.48 m DEPTH

(b) 130.48 m DEPTH

FIGURE 6 MIGRATION VELOCITY VS TIME FOR 100 KG TNT EXPLOSION BUBBLE

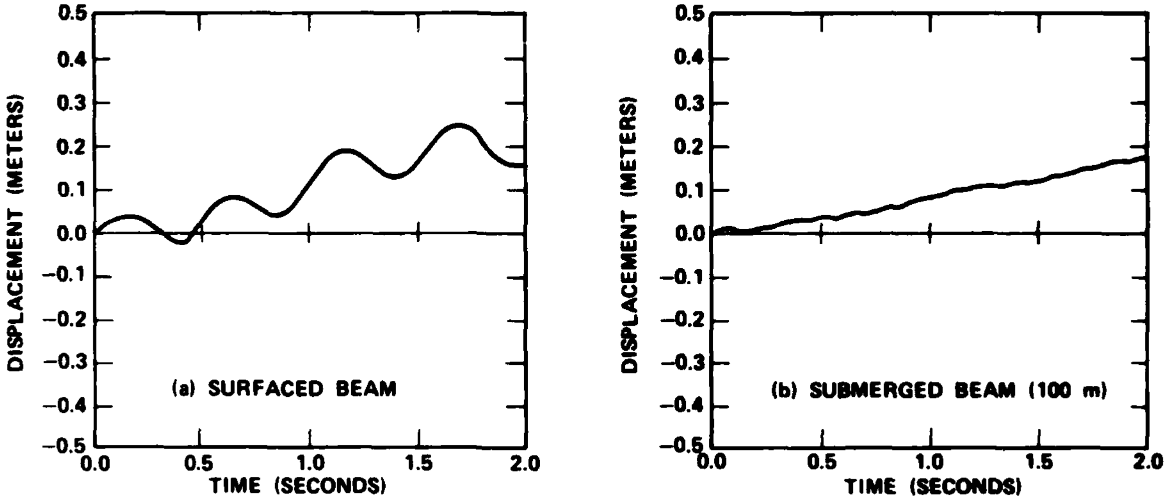

FIGURE 7 AMIDSHIP DISPLACEMENT VS TIME IN RESPONSE TO 100 KG TNT BUBBLE LOADING

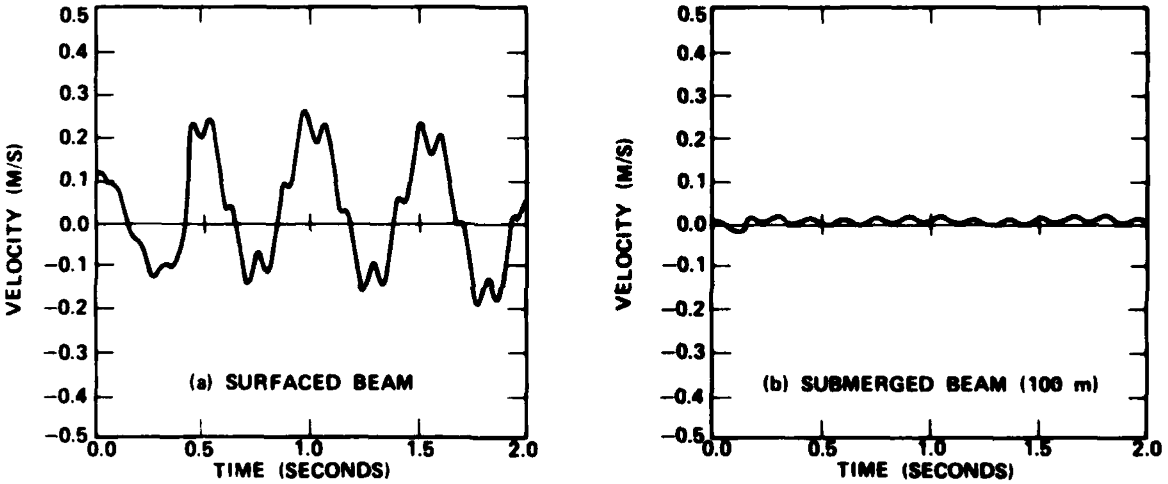

FIGURE 8 AMIDSHIP VELOCITY VS TIME IN RESPONSE TO 100 KG TNT BUBBLE LOADING

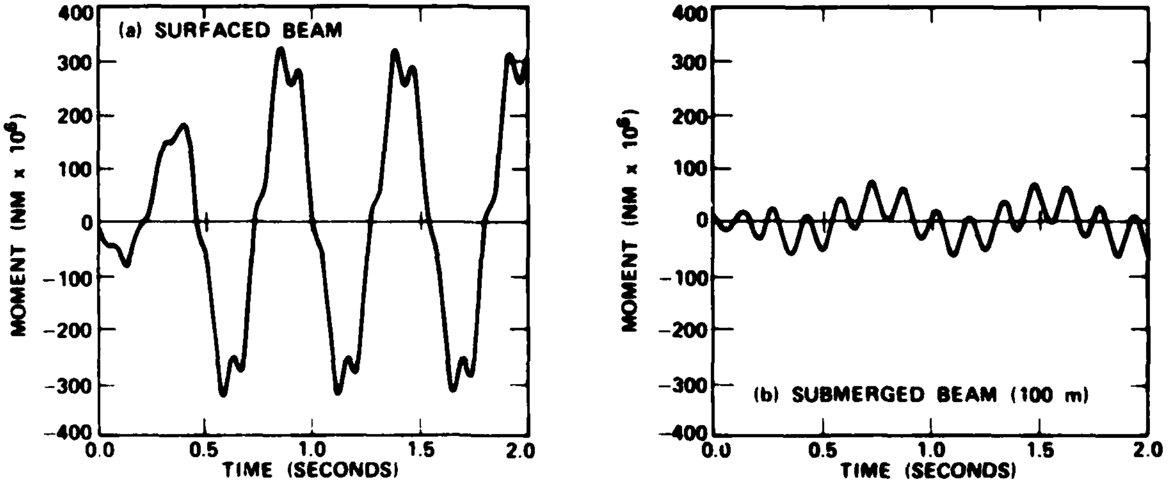

FIGURE 9 AMIDSHIP BENDING MOMENT VS TIME IN RESPONSE TO 100 KG TNT BUBBLE LOADING

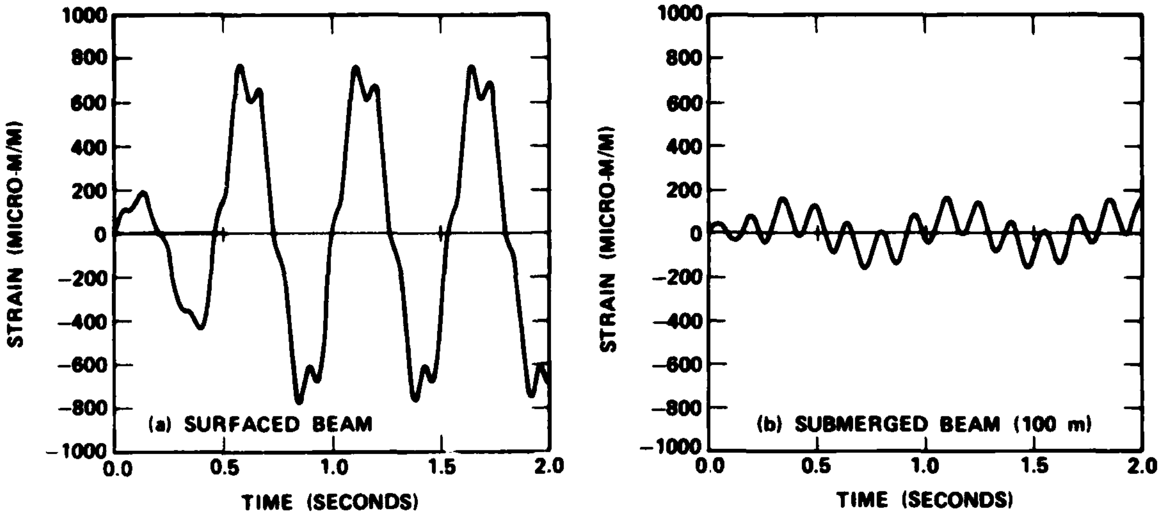

FIGURE 10 AMIDSHIP OUTER FIBER STRAIN VS TIME IN RESPONSE TO 100 KG TNT BUBBLE LOADING

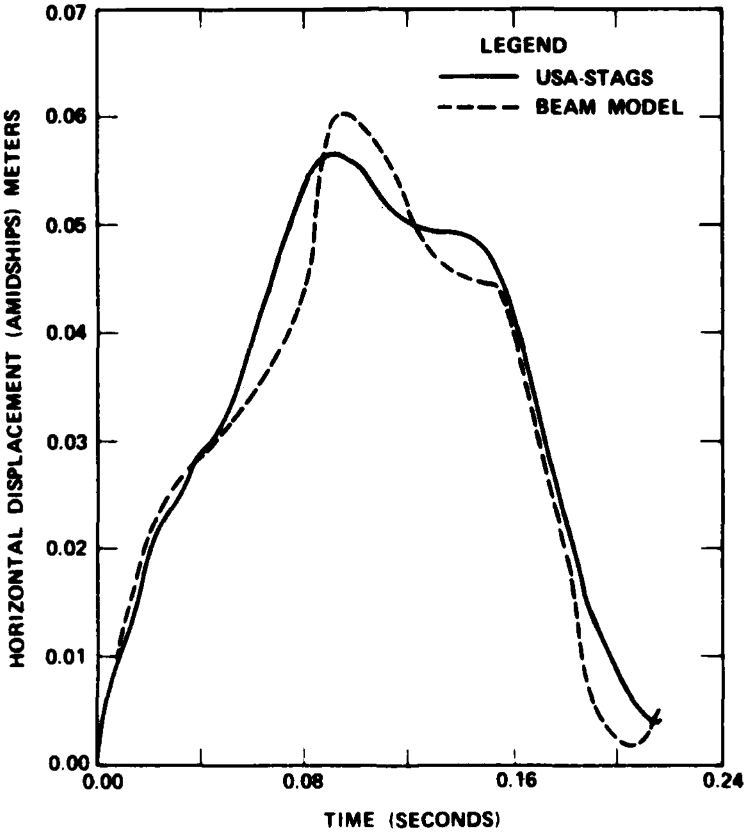

FIGURE 11 COMPARISON OF DISPLACEMENT HISTORIES CALCULATED BY USA-STAGS AND BEAM MODEL FOR A BODY OF ASSUMED FORM

DISCUSSION

Mr. Cole (Cambridge Acoustical Assoicates, Inc.): The reduction between the free surface, the ship surfaced and the ships submerged, is it obvious that it is primarily a free surface effect on the bubble? Is it the added mass on the ship?

Mr. Bannister: That is a complicated question. It turns out that in this case the submerged beam must have twice the density for equilibrium purposes because the geometries are the same and also the added mass is double that. Not only do the target modal characteristics change but the bubble behavior also changes significantly. I didn't show the modal changes in the target but at depth the frequencies drop off and the corresponding whipping frequencies between surfaced and submerged are much different.

Mr. Pepin (Electric Boat): Has there been any attempt to try to correlate the accelerations that would be induced by these various whipping modes with respect to any particular frequency? Did you try to tie together what acceleration is induced by the frequency that results from the whipping mode?

Mr. Bannister: I think, Dr. Hicks, in his thesis and in some of his reports, discusses the various contributions of the bubble motions. There are migration terms and expansion and contraction terms and he shows the relative effects of these various terms. We have not done studies of that kind.

Mr. Westine (Southwest Research Institute): Why did you stop with one bubble pulse? Depending on the frequencies of the bubble and the frequencies of the hull in the system you can get large amplification with subsequent pulses.

Mr. Bannister: You are right. It turns out that the bubble model in the code that I ran for these examples was not adequate beyond the first cycle. The reason is that the bubble continues oscillating to get the same behavior on each cycle. In reality you have losses at each minimum and the bubble damps out. Depending on the circumstances, it could go to five cycles. We have other codes which can handle as many as five cycles but they are still in checkout and they are not ready for public distribution.

LIMITATIONS ON RANDOM INPUT FORCES IN RANDOMDEC COMPUTATION FOR MODAL IDENTIFICATION

S. R. Ibrahim
Department of Mechanical Engineering
and Mechanics
Old Dominion University
Norfolk, Virginia

The condition of having white noise random input to test structures has been proven unnecessary for the purpose of using random decrement technique for modal identification of vibrating structures. In this paper it is shown that nonwhite, stationary narrow band random inputs will yield modal parameters as accurate as those obtained if the inputs were narrow band white noise. Seven simulated experiments are included in support of the material presented in this paper.

INTRODUCTION

With the increasing complexities of modern structures, aerospace and nonaerospace, verification of analytical mathematical models has become a necessity for successful operation, response prediction, stress levels evaluation, stability and control of such structures.

Before the introduction of functional and practical time domain techniques early in this decade, modal testing and identification was done primarily in the frequency domain. Although frequency domain techniques may vary in name or form, they are all based on the detection of some resonance or antiresonance phenomena assuming that the structure under test has light or proportional damping and behaves as a single degree-of-freedom system at its natural frequencies. From Kennedy and Pancu technique [1], in 1947 to the more sophisticated computerized Fast Fourier Transform, "FFT," approaches [2-4], it can be concluded that little advance in the state of the art of frequency domain techniques took place. All the advance was mainly in the data acquisition and manipulation to extract the modal parameters and this was primarily due to the introduction and use of minicomputers in modal testing.

Furthermore, a common feature in frequency domain methods is that they all require the knowledge of the input forces to the test structure. This criterion makes these techniques inapplicable to situations where the input forces are not known. Flight measurements and operational data are examples of these situations.

All of the above disadvantages of frequency domain techniques, were taken into account in the design and development of time domain approaches to the problem of modal testing and identification. A time domain approach referred to as the Ibrahim Time Domain, "ITD," brought the attention of researchers to the merits of time domain modal identification. The introduction of the "ITD" in 1973 and its later developments [5-11] resulted in a trend, by other researchers, to shift from frequency domain to time domain approach. Figure 1 summarizes the available options in modern modal identification.

As shown in Figure 2, experimental data for the "ITD" technique can be either free decay responses directly recorded from the structure in case of controlled experiments, or free decay responses computed from random responses using the random decrement technique for uncontrolled experiments or operational data.

BACKGROUND ON RANDOM DECREMENT TECHNIQUE

Random decrement technique is an ensemble averaging method for obtaining the free decary response from a forced response due to a random force input. The technique was first introduced by Henry A. Cole, Jr. [12-15]. Cole's technique dealt mainly with a single station single mode response and was designed for obtaining structure's signature for failure detection and damping measurements. The technique seemed useful in flutter testing [16-17] where damping of a single mode is to be determined. The original random decrement technique was modified and extended by Ibrahim [9] to apply to multi-station multi-mode situation mainly for use in time-domain modal identification techniques. Randomdec time domain modal identification has the outstanding advantage of identifying modal parameters of a structure under test without the knowledge of the force input(s) thus making the technique uniquely applicable to flight measurements and other situations where the luxury of knowing the force input(s) is nonexisting.

Since the introduction of the concept of random decrement technique, efforts have been directed to investigate the theoretical grounds for accuracy and convergence and any inherent assumptions, conditions, or limitations. One main assumption in these theoretical proofs was that the random input force(s) must be white noise.

The assumption of white noise input(s) is very convenient for theoretical proofs. The fact is such white noise does not exist in real life applications.

In this paper, it will be shown that the strict condition of having white noise, or flat power spectrum density, is not necessary, at least for the purpose of modal identification of structures. The only condition on the input force(s) is that it is of zero mean, stationary random.

PROOF

Considering a multi-degree-of-freedom linear system with [M], [K], and [C] as mass, stiffness and damping matrices and y as the response vector to a random force input vector f , such a system is governed by the equation:

$$[M]\{\ddot{y}(t)\} + [C]\{\dot{y}(t)\} + K\{y(t)\} = \{f(t)\}\ . \qquad (1)$$

The above equation is valid for any time t and any set of initial conditions. Replacing time t with the expression $t_i + \tau$ where t_i's are selected according to the method of triggering the start of ensembles for the randomdec computations [18], then equation (1) can be written as

$$\begin{aligned}[M]\{\ddot{y}(t_i + \tau)\} + [C]\ \dot{y}(t_i + \tau) \\ + [K]\{y(t_i + \tau)\} \qquad (2) \\ = \{f(t_i + \tau)\}(i = 1, 2\text{---}N)\end{aligned}$$

where N is the number of averages intended for use in randomdec computation.

By summing all of the N equations and dividing by N and replacing $\frac{1}{N}\sum\{y(t_i + \tau)\}$ by $\{x(\tau)\}$, the resulting summation can be written as:

$$\begin{aligned}[M]\{\ddot{x}(\tau)\} + [C]\{\dot{x}(\tau)\} + [K]\{x(\tau)\} \\ = \frac{1}{N}\sum_{i=1}^{N}\{f(t_i + \tau)\} \qquad (3)\end{aligned}$$

Noting that since t_i's were selected according to a specific randomdec triggering criterion, the resulting response $\{x(\tau)\}$ will not average to zero. Now considering the right hand side of equation (3), if $\{f\}$ is a stationary random signal, then

$$\frac{1}{N}\sum_{i=1}^{N}\{f(t_i + \tau)\} = 0$$

and equation (3) will be:

$$[M]\{\ddot{x}(\tau)\} + [C]\{\dot{x}(\tau)\} + [K]\{x(\tau)\} = 0. \qquad (4)$$

Equation (4) implies that $\{x(\tau)\}$ is a free-decay response that resulted from applying randomdec to random responses due to a force input vector $\{f\}$, where $\{f\}$ was assumed to be only some stationary random signals.

EXPERIMENTAL VERIFICATION

Figure 3 shows the system and procedure used to simulate the experimental data to be used in verifying the theory presented in this work. The system is a two-mass-spring-damper system with the following physical parameters:

$m_1 = m_2 = 4.53$ kg

$k_1 = k_3 = 17512$ kN/m

$k_2 = 8756$ kN/m

$C_1 = 10.51$ kN-sec/m

$C_2 = 7.00$ kN-sec/m

$C_3 = 3.5$ kN-sec/m

These physical parameters produce the following modal parameters

mode	percent damping	freq. (Hz)	Modal (x_2/x_1) Ampl.	Phase
1	1.24	9.86	100.10	1.42
2	2.63	13.94	99.85	180.00

A random input force of an assumed power spectral density was applied to mass number 1. Using Laplace transform, the frequency responses of the two masses were calculated and then transformed, together with the force frequency response, back to the time domain using a rectangular window over the frequency range 0.2 - 25 Hz. This resulted in the time histories of the random input force, and random responses of the two masses. The length of these time histories was one minute with 0.015 seconds between samples.

The multiple station random decrement technique [9] was applied to the three responses with the first station as a leading station and ensembles were triggered at every positive response point of the first station response. This resulted in the randomdec free-decay signatures of the two stations and the force. The record length of the signatures was 1.5 seconds (100 date point each). The number of averages was about 2000 averages.

To test this procedure and to judge the soundness of the hypothesis of this paper, two criteria were used:

1. The randomdec signatures of the two stations were used as data in the "ITD" identification program, and the accuracy of the identified parameters – frequencies, percent damping and mode shapes – are used as an indication of the validity of the random force input for this application.

2. To verify the fact that signature of a stationary random force will go to zero and thus free decay responses will result, the RMS of the force signature was compared to the RMS of the original random force.

RESULTS

Seven cases were studied with seven different force PSD. To be used as a reference, the first case was run with the input force as a narrow-band white noise.

The PSD of the input force for the seven cases were:

1 - Flat,

2 - Ramp,

3 - Triangular (saw tooth),

4 - Sinusoidal with random imposed on it,

5 - Flat with two 40% dips at the two resonant frequencies,

6 - Flat with two 40% peaks at the two resonant frequencies,

7 - Flat with a 60% peak in between the two resonant frequencies.

Figures 4 to 10 show in clockwise order starting from upper left corner:

a) PSD of input force,

b) Part of time history of the input force followed by the randomdec signature of the force. The RMS ratio written on this figure is computed as follows:

$$\text{RMS Ratio} = \frac{\text{RMS of input force signature}}{\text{RMS of input force}} \times 100 \qquad (5)$$

c) Random response of mass 1,

d) Randomdec signature of mass 1,

e) Random response of mass 2,

f) Randomdec signature of mass 2.

Table 1 summarizes the identified modal parameters for the seven cases.

False Modes:

To investigate the possibility of the introduction of false modes in the system's responses due to the existance of peaks in the spectrum of input force, the responses from cases 3 and 7 were identified as a four-degree-of-freedom systems. The identified parameters are listed in Tables 2 and 3.

DISCUSSION OF RESULTS

1. Accuracy of the Identified Modal Parameters:

Table 1 lists the identified modal parameters of the system under test for the seven cases that were studied. These parameters are the percentage damping factors, damped natural frequencies, modal deflection ratio (x_2/x_1) and the modal confidence factors [10] for the two test stations.

By examining the identified parameters for the seven test cases and comparing them to the theoretical parameters, it can be noticed that the accuracy of these identified parameters for nonwhite noise input force cases is as good as the accuracy in the white noise case. Furthermore, the identified frequencies and mode shapes have almost negligible errors while the damping factors have higher level of errors, nevertheless, these errors do not correlate to the form of the spectrum of the input force. In the author's opinion these errors in damping factors could be due to the transformation of responses from frequency domain to time domain. It is to be noted that this transformation is done only here to simulate required responses, something which does not need to be done in real experimental situations.

2. Randomdec Signatures of Input Forces:

According to the theory presented in this paper, to obtain free-decay responses from the test structure, the randomdec signature of the input force should average to zero.

For the seven cases, these RMS ratios, as defined in equation 5, are:

1.5% for flat PSD,
1.5% for ramp PSD,
1.7% for saw tooth PSD,
1.4% for random wave PSD,
2.2% for flat with dips PSD,
2.6% for flat with peaks PSD, and
1.5% for flat with one peak PSD.

For all practical purposes, it can be said that the random force input averaged to zero and thus the randomdec signatures of the responses can be used as free-decay responses. Analogous to the RMS ratio of the force, the same procedure was done for system's responses and the RMS ratio of the randomdec responses to the random responses ranged from about 35 to 60 percent. This means that contrary to the force, the system's responses did not average to zero.

3. False Modes:

The spectrums of the input forces for cases 3 and 7 were selected to have higher levels of energy at nonresonant frequencies to investigate if this would produce any false modes. Randomdec responses for these two cases were identified as four-degrees-of-freedom systems instead of two. The identification results are listed in Table 2 for case 3 and Table 3 for case 7. The modal confidence factors indicate only two good modes in each case. The other modes are just noise modes as indicated by the low MCF's. This excludes the possibility of the introduction of any false modes by having a nonflat spectrum for input forces.

CONCLUSIONS

The conclusion that can be made from the study conducted in this paper is that to obtain randomdec free-decay responses from random responses for the use in the "ITD" modal identification procedure, the input forces can be stationary random signals with zero mean. The condition of requiring white-noise is not at all necessary.

ACKNOWLEDGMENT

This work is supported by a research grant from NASA's Langley Research Center.

REFERENCES

1. Kennedy, C.C., and Pancu, C.D.P., "Use of Vectors in Vibration Measurement Analysis," Journal of Aeronautical Sciences, Vol. 14, No. 11, 1947.
2. Richardson, M., and Potter, R., "Identification of the Modal Parameters of and Elastic Structure from Measured Transfer Function Data," Instrument Society of America, ISA ASI 74250, 1974, pp. 239-246.
3. Klosterman, A., and Zimmerman, R., "Modal Survey Activity via Frequency Response Functions," SAE Paper No. 751068, 1975.
4. Brown, D.L., Allenang, R.J., and Zimmerman, R., "Parameter Estimation Techniques for Modal Analysis," SAE Paper No. 790221, 1979.
5. Ibrahim, S.R., "A Time Domain Vibration Test Technique," Ph.D. Thesis, The University of Calgary, Calgary, Alberta, Canada, 1973.
6. Ibrahim, S.R., and Mikulcik, E.C., "A Time Domain Vibration Test Technique," Shock and Vibration Bulletin, Bulletin 43, Part 4, 1973.
7. Ibrahim, S.R., and Mikulcik, E.C., "The Experimental Determination of Vibration Parameters from Time Domain Responses," Shock and Vibration Bulletin, Bulletin 46, 1976.
8. Ibrahim, S.R., and Mikulcik, E.C., "A Method for the Direct Identification of Vibration Parameters from Free Responses," Shock and Vibration Bulletin, Bulletin 47, 1977.
9. Ibrahim, S.R., "Random Decrement Technique for Modal Identification of Structures," The AIAA Journal of Spacecraft and Rockets, Vol. 14, No. 11, 1977.
10. Ibrahim, S.R., "Modal Confidence Factor in Vibration Testing," The AIAA Journal of Spacecraft and Rockets, Vol. 15, Sept.–Oct. 1978.
11. Hanks, B.R., and Ibrahim, S.R., "Comparison of Modal Test Methods on the Voyager Payload," SAE Paper No. 781044, Nov. 1978.
12. Cole, H.A., Jr., "On-The-Line Analysis of Random Vibrations," AIAA/ASME 9th Structures, Structural Dynamics and Materials Conference, Palm Springs, California, April 1-3, 1968, Paper No. 68-288.

13. Cole, H.A., Jr., "Failure Detection of a Space Shuttle Wing Flutter Model by Random Decrement," NASA TM X-62, 041, May 1971.

14. Cole, H.A., Jr., "Method and Apparatus for Measuring the Damping Characteristics of a Structure," United States Patent No. 3,630,069, November 16, 1971.

15. Cole, H.A., Jr., "On-Line Failure Detection and Damping Measurement of Aerospace Structures by Random Decrement Signatures," NASA CR-2205, March 1973.

16. Chang, C.S., "Study of Dynamic Characteristics of Aeroelastic Systems Utilizing Randomdec Signatures," NASA CR 132563, 1975.

17. Hammond, C.E., and Doggett, R.V., Jr., "Determination of Subcritical Damping by Moving-Block/Randomdec Applications," Proceedings of the NASA Symposium on Flutter Testing Techniques, October 9-10, 1975.

18. Caldwell, D.W., "The Measurement of Damping and the Detection of Damage in Linear and Nonlinear Systems by the Random Decrement Technique," Ph.D. Thesis, University of Maryland, 1978.

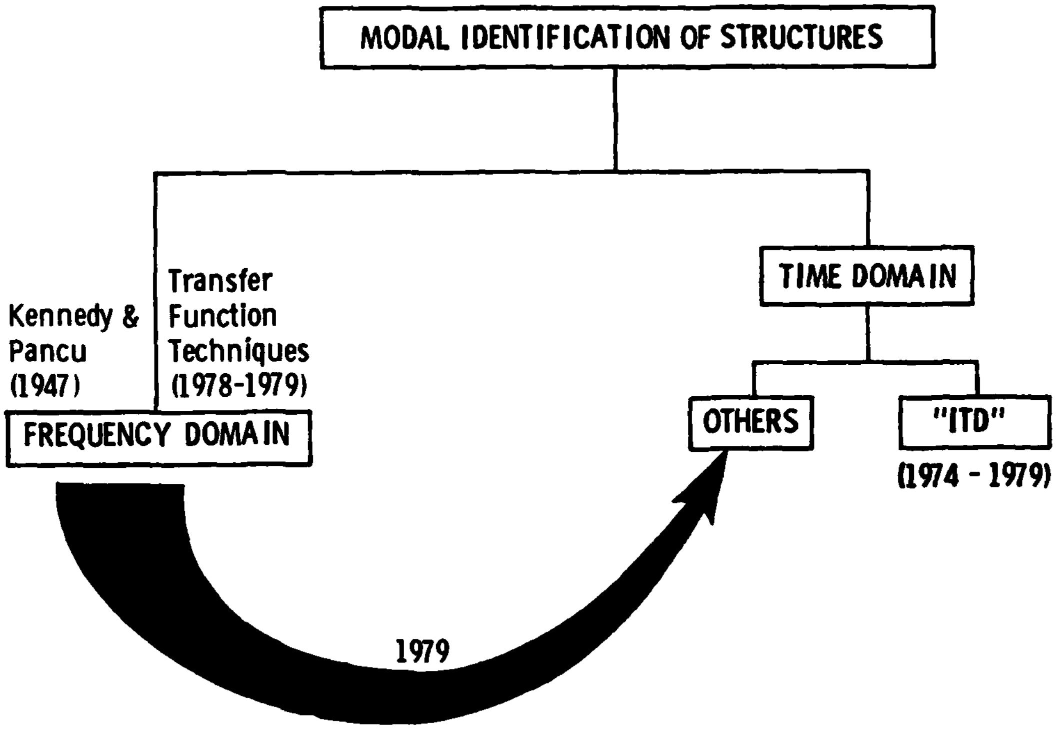
MODAL IDENTIFICATION OF STRUCTURES
Kennedy & Pancu (1947)
Transfer Function Techniques (1978-1979)
FREQUENCY DOMAIN
TIME DOMAIN
OTHERS
"ITD"
(1974 - 1979)
1979

Fig. 1 - Options and Trends in Modal Identification of Structures

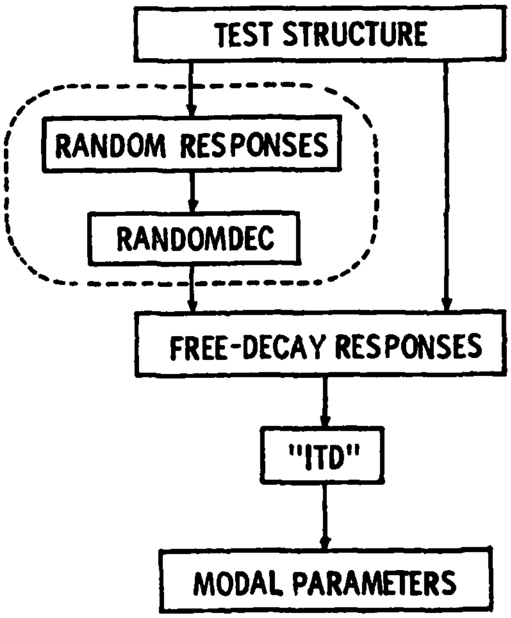
TEST STRUCTURE
RANDOM RESPONSES
RANDOMDEC
FREE-DECAY RESPONSES
"ITD"
MODAL PARAMETERS

Fig. 2 - Data for the "ITD" Technique

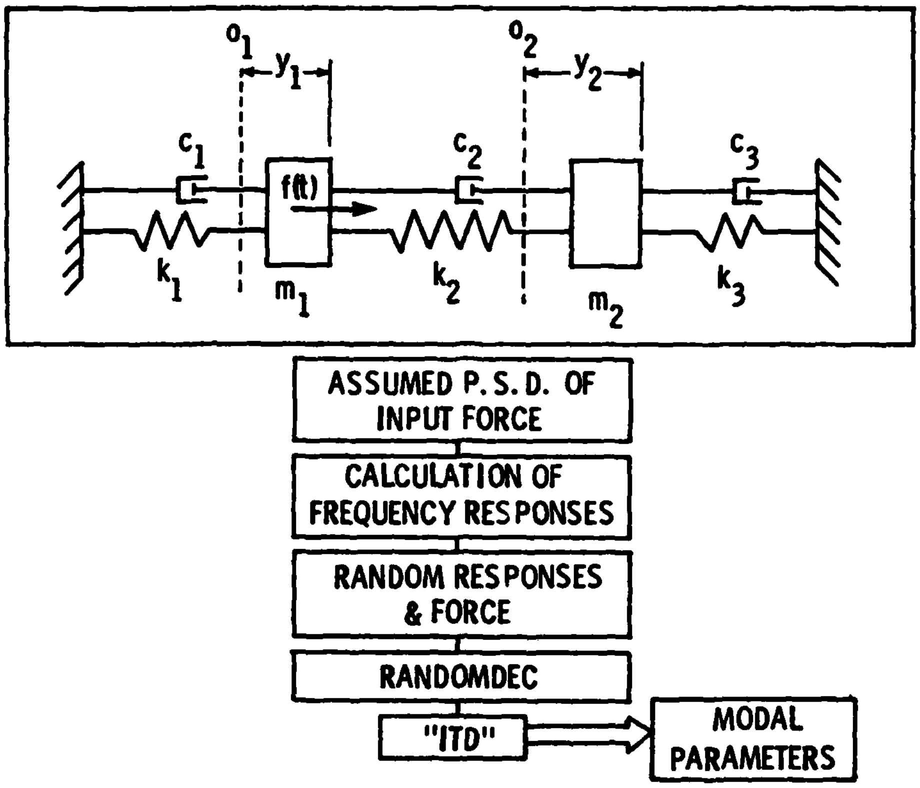
o_1
y_1
o_2
y_2
c_1
c_2
c_3
f(t)
k_1
m_1
k_2
m_2
k_3
ASSUMED P.S.D. OF INPUT FORCE
CALCULATION OF FREQUENCY RESPONSES
RANDOM RESPONSES & FORCE
RANDOMDEC
"ITD"
MODAL PARAMETERS

Fig. 3 - System, Simulation, and Identification Procedure

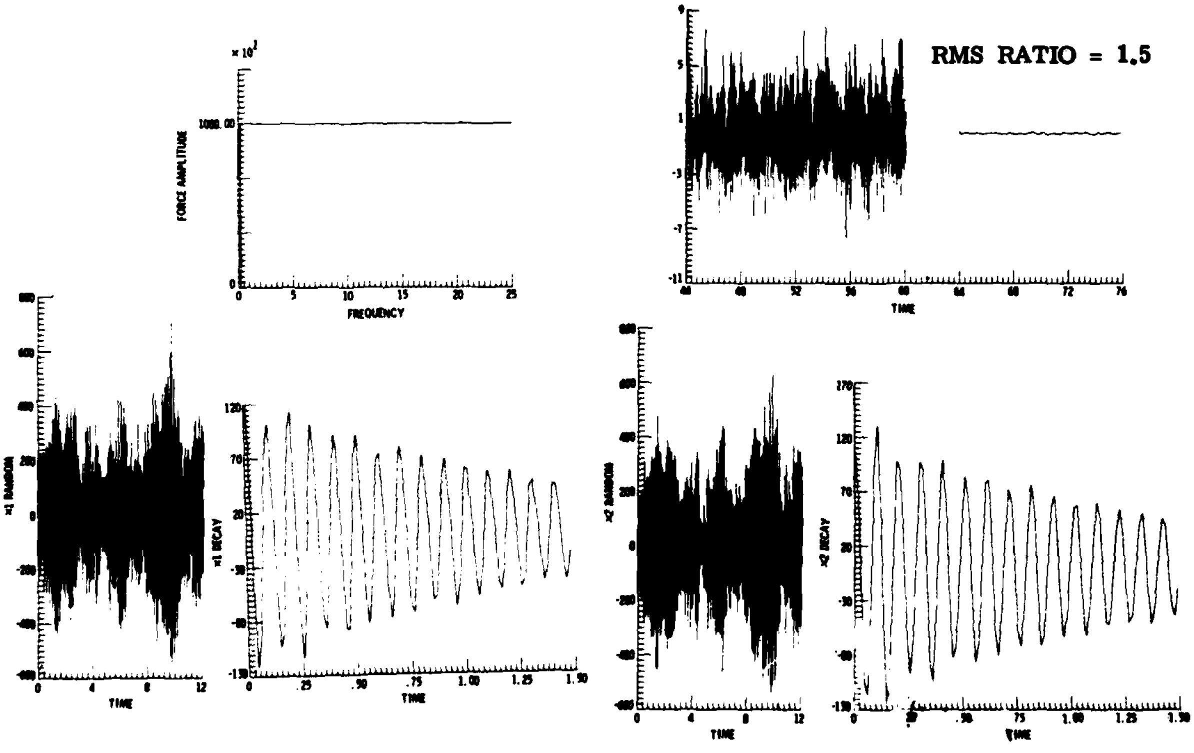

Fig. 4 - Responses for Case 1

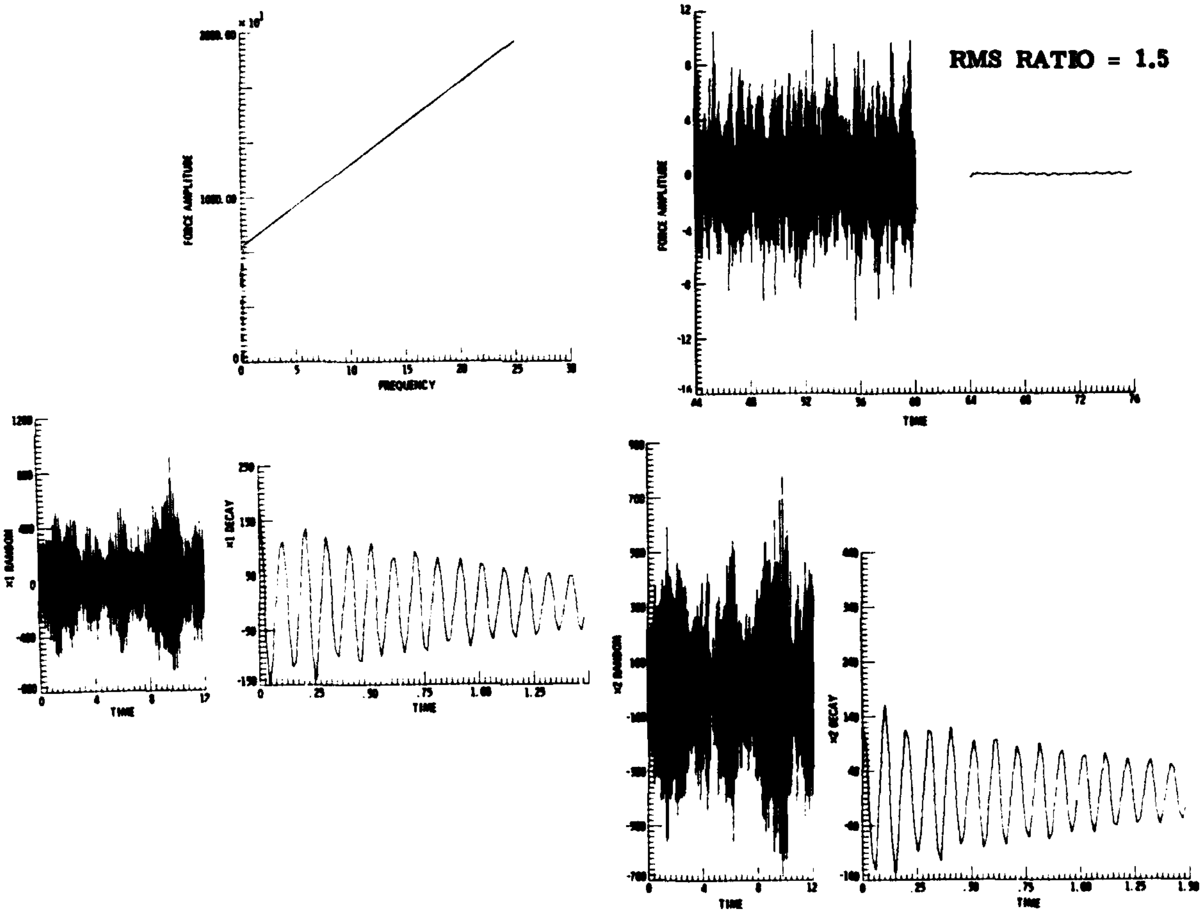

Fig. 5 - Responses for Case 2

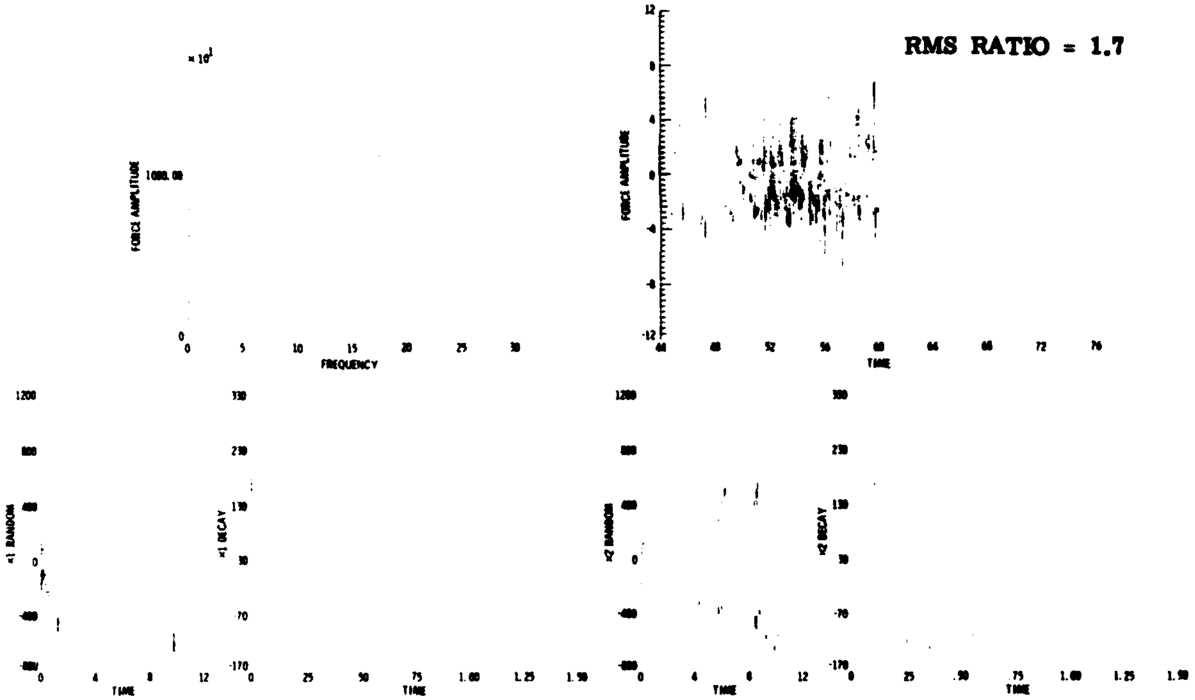

Fig. 6 - Responses for Case 3

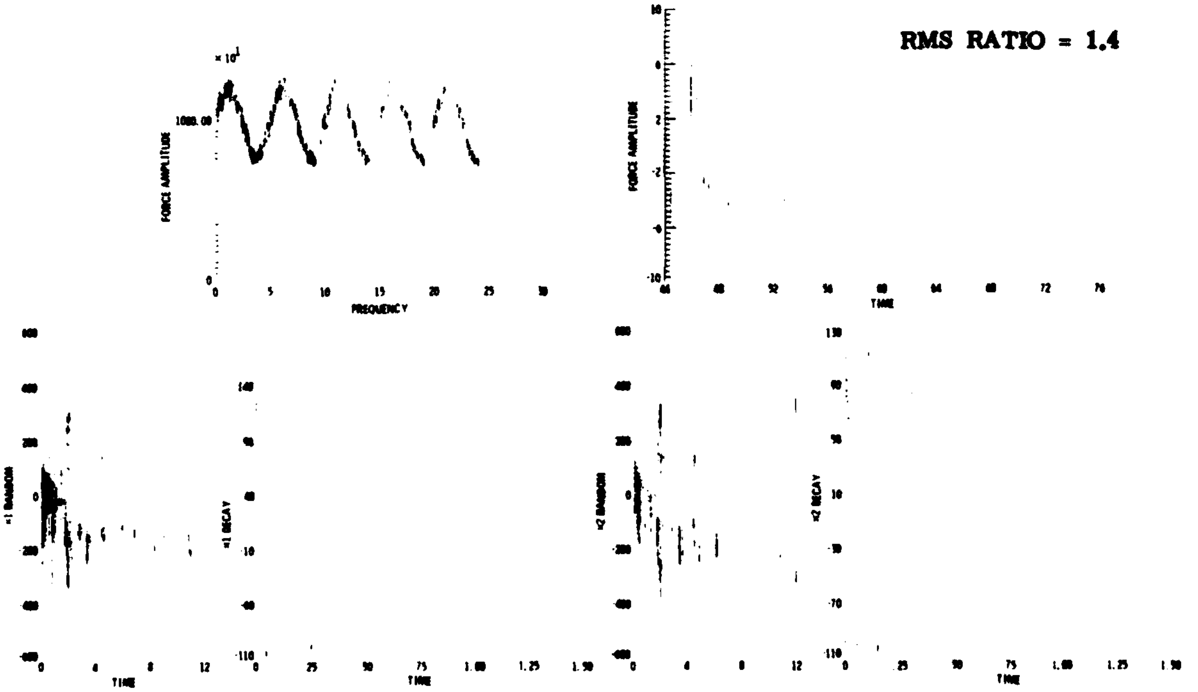

Fig. 7 - Responses for Case 4

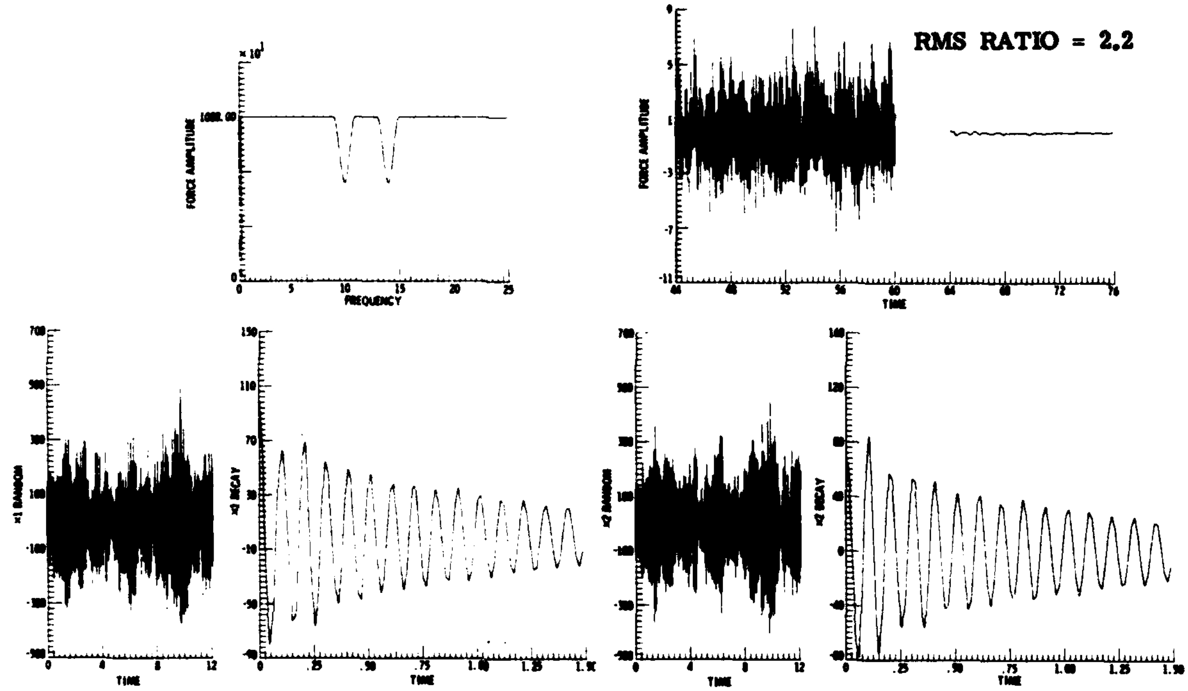

Fig. 8 - Responses for Case 5

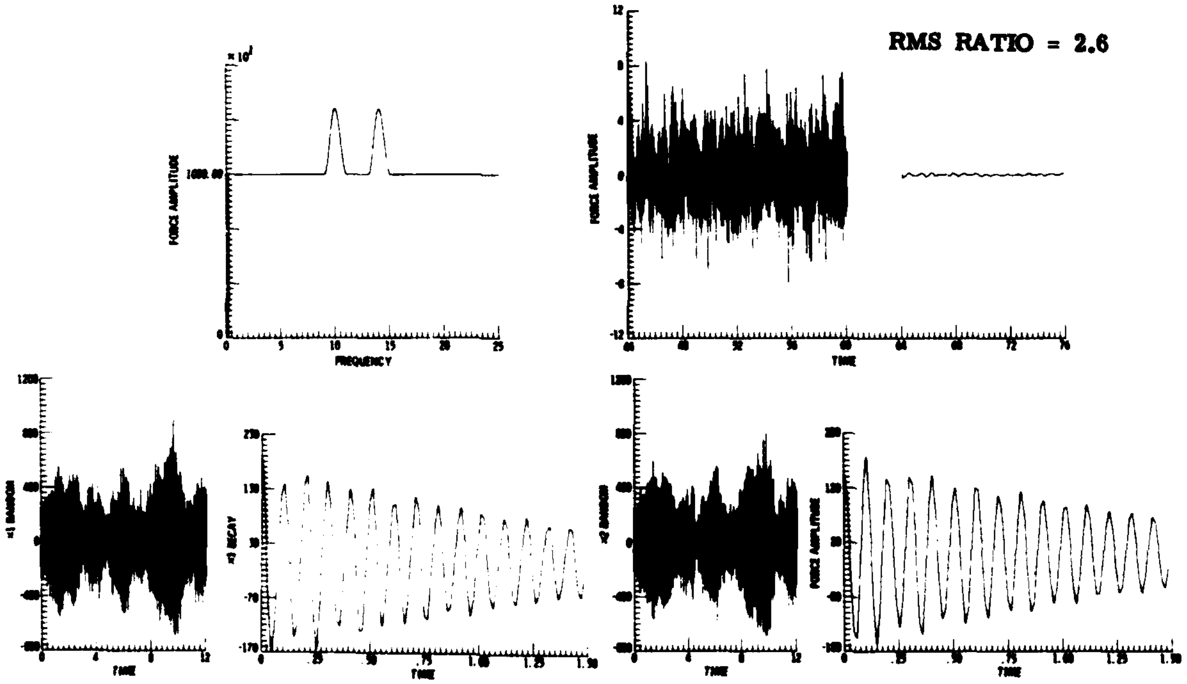

Fig. 9 - Responses for Case 6

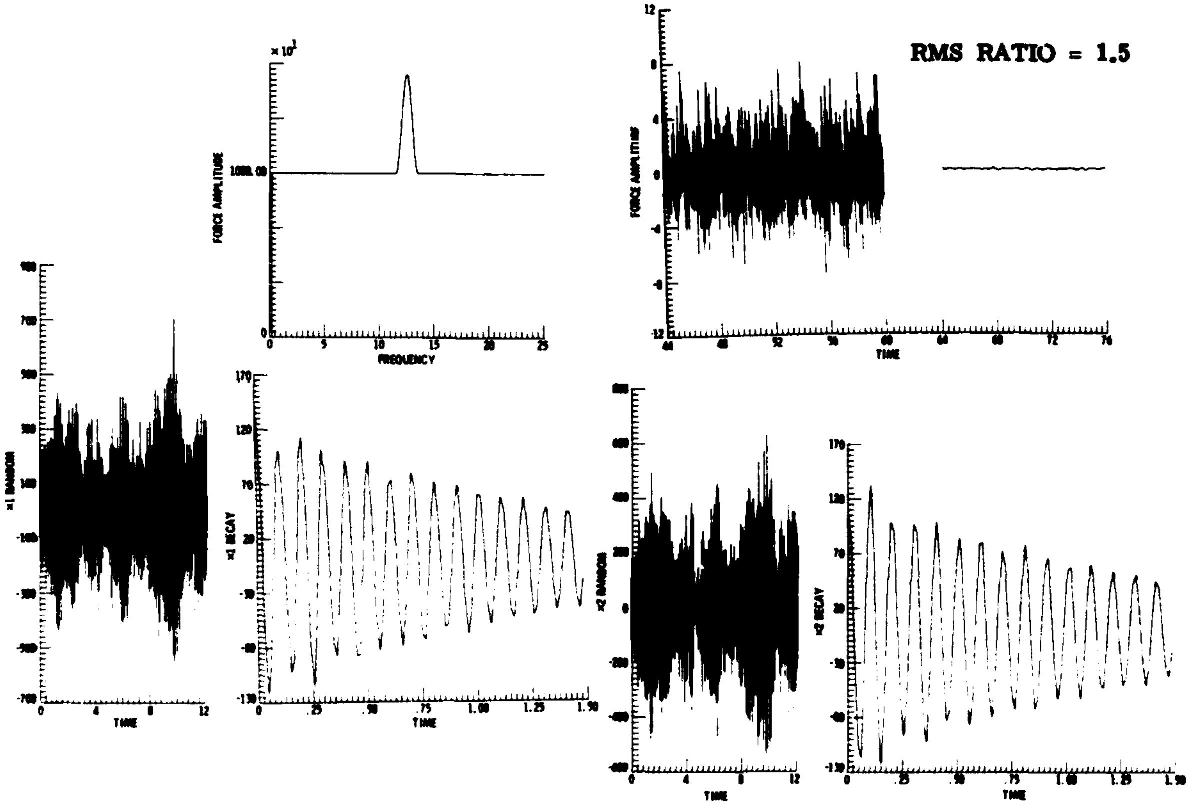

RMS RATIO = 1.5

Fig. 10 - Responses for Case 7

TABLE 1
Theoretical and Identified Modal Parameters

Case	Mode	%Damping	Frequency (Hz)	Mode Shape (x_2/x_1)		"MCF"	
				Ampl.	Phase°	Ampl.	Phase°
Theory	1	1.24	9.86	100.10	1.42	–	
	2	2.63	13.94	99.85	178.00	–	
1	1	1.12	9.87	100.57	1.12	100.0	-0.1
						99.9	0.1
	2	2.78	13.94	98.70	179.45	98.0	0.6
						96.8	0.6
2	1	1.18	9.87	100.20	1.31	99.9	0.1
						99.8	-0.1
	2	2.64	13.93	99.16	178.10	96.6	1.3
						94.9	0.1
3	1	1.16	9.87	100.26	1.33	99.9	0.1
						99.8	-0.2
	2	2.66	13.96	99.93	177.53	96.5	1.8
						94.1	0.2
4	1	1.22	9.86	100.2	1.21	100.0	-0.1
						99.9	0.1
	2	2.55	13.94	99.47	173.46	94.6	-2.7
						96.5	1.6
5	1	1.20	9.89	101.50	2.69	99.7	0.2
						97.6	-0.5
	2	3.15	13.98	107.27	172.27	99.7	-2.9
						91.3	-3.5
6	1	1.20	9.90	100.91	0.72	99.5	0.0
						98.9	0.2
	2	2.25	14.01	101.23	175.33	95.6	1.6
						94.0	3.2
7	1	1.13	9.87	100.57	1.12	100.0	-0.1
						99.8	0.1
	2	2.65	13.97	101.91	177.71	99.1	-1.4
						99.8	-2.0

TABLE 2
Identified Parameters for Case 3 as a Four Degrees of Freedom System

No.	%Damping	Frequency (Hz)	"MCF"	
			Ampl.	Phase°
1	1.14	9.87	99.9	0.0
			99.7	0.0
2	2.20	13.96	100.0	0.1
			99.8	0.9
3	13.09	14.86	54.6	52.0
			55.2	71.6
4	Overdamped	----	0.2	90.0
			4.4	-90.0
5	Overdamped	----	4.6	180.0
			4.2	180.0

TABLE 3
Identified Parameters for Case 7 as a Four Degrees of Freedom System

No.	%Damping	Frequency (Hz)	"MCF"	
			Ampl.	Phase°
1	1.4	9.88	100.0	-0.1
			99.8	-0.1
2	2.28	13.93	96.1	1.5
			95.4	1.4
3	21.64	12.93	28.2	95.1
			13.0	46.3
4	Overdamped	----	13.7	90.0
			57.7	90.0
5	Overdamped	----	00.0	180.0
			0.1	0.0

DISCUSSION

Mr. Dorland (Federal Railroad Administration): The one example of applying this technique that I know of in the railroad dynamics literature involved an input that was non stationary so the experimenters elected not to do a modal identification with it. Did they give up too easily?

Mr. Ibrahim: My last slide which was a conclusion was changed after I had a session with Larry Pinson at NASA Langley Research Center because I said that the input force only needs to be random. He said you have been using stationary random inputs and you better stay there. So I think the next step would be to use nonstationary random inputs and see what happens.

Mr. Dorland: What if it were a narrow band random and non stationary input?

Mr. Ibrahim: All of these inputs were narrow band.

Mr. Dorland: They seemed pretty wide to me because the waveforms didn't look like narrow band filter responses on the time history records.

Mr. Ibrahim: If you are dealing with a very narrow band random input the structural modes in this range would be excited. Outside of this range they wouldn't be excited or the excitation would be very low.

Mr. Dorland: The reason I am making this comment is that the time history these authors had in their paper looked like narrow band filtered responses for their input force and I'm not sure what limitation that put on their possible results.

Mr. Ibrahim: In this case when we have random responses due to some unknown random input force we will be able to identify the modes that have been excited by this random input force. Modes that haven't been excited because the forces didn't have enough power in some other frequency range will not appear in the responses.

Mr. Sattinger (Westinghouse Bettis Atomic Power Lab): How closely spaced can your modes be when you apply the random decrement technique?

Mr. Ibrahim: I don't think that "random dec" has any effect on the closeness of modes or their damping but the identification technique has been very successful in identifying very closely spaced natural frequencies. The closeness of the frequencies will not have any effect on the random decrement computation.

Mr. Sattinger: Do you feel that you can still apply the method even if the modes are close enough to have a cross coupling between them or a merging between them?

Mr. Ibrahim: The method still applies. This was the one main thing behind the development of this method, it doesn't have any restrictions on the closeness of natural frequencies or the level of damping.

Mr. Showalter (Shock and Vibration Information Center): Do you think you could use a "random dec" technique to get the mode shape of a naval vessel where the random inputs would be due to the wave motion of the ship underway?

Mr. Ibrahim: This is one subject that I would like to get some data on. I understand that some people are working on applying "random dec" and time domain identification techniques to offshore drilling platforms which are like ships due to the waves. Some professors in ocean engineering told me that wave motion can be classified as a stationary random narrow band process. So I think it can be done.

STRUCTURAL-DYNAMIC CHARACTERIZATION OF AN EXPERIMENTAL 1200-KILOVOLT ELECTRICAL TRANSMISSION-LINE SYSTEM

by
LEON KEMPNER, JR.
BONNEVILLE POWER ADMINISTRATION
PORTLAND, OREGON
and
STRETHER SMITH and RICHARD C. STROUD
SYNERGISTIC TECHNOLOGY INCORPORATED
CUPERTINO, CALIFORNIA

During the next decade the electrical-power industry will introduce new transmission systems capable of carrying significantly higher levels of electrical power. These systems will require taller towers to increase conductor/earth clearances. More conductors per phase will be required increasing dead loads and contributing to greater ice and wind loadings. These factors combine to produce a greater threat of static and dynamic loading conditions that can lead to mechanical failure. In addition to these technical considerations, economics and the limited availability of right-of-way will dictate more refined design procedures. These conditions result in the need for more accurate structural analysis and more effective structural testing in the development of future transmission systems.

In preparation for planned 1200-kV transmission lines, the Department of Energy's Bonneville Power Administration (BPA) has constructed two experimental ultra-high-voltage (UHV) transmission lines; an electrical prototype at Lyons, Oregon, and a mechanical test line at Moro, Oregon. The Mechanical Test Facility consists of an approximately 1.8-kilometer-long (1.1 mile) test line with six towers. It is intended to provide a facility for the assembly of various insulator/conductor designs and to help assess their behavior in response to artificial and natural excitation. The site is located approximately 210 kilometers (130 miles) east of Portland on the eastern rim of the Deschutes River Canyon, a site that provides an abundance of wind and ice loading. BPA has installed an extensive instrumentation and data- acquisition system for measurement of both environmental conditions and mechanical responses.

This paper describes an investigation conducted to establish, by correlation of analytically and experimentally derived results, credibility for structural and structural-dynamic modeling procedures under development at BPA. The approach was to formulate an analytical model of one of the suspension towers and compare the modal characteristics of that idealization with measured properties obtained with a modal survey.

The SPAR (1)* finite-element program was used for a theoretical analysis of the tower. The entire test sequence was performed analytically prior to the experimental phase to determine safe and adequate loadings and to establish instrumentation gains. The suitability of the instrument distribution was verified by an orthogonality check of theoretical eigenvectors, truncated to instrument locations.

In conjunction with the modal test of the tower, the dynamic behavior of the eight-conductor bundle and conductor-tower interaction were experimentally investigated.

Twang (i.e., transient response to an initial displacement) excitation was applied at several locations on the tower and conductors. Resulting tower and conductor motions were measured. Instrumentation included accelerometers on the tower and conductor, load cells at excitation points and at the tower-attachment points of the insulator strings, and swing-angle sensors on the insulators.

---

* Numbers in parentheses refer to references listed at the end of the paper.

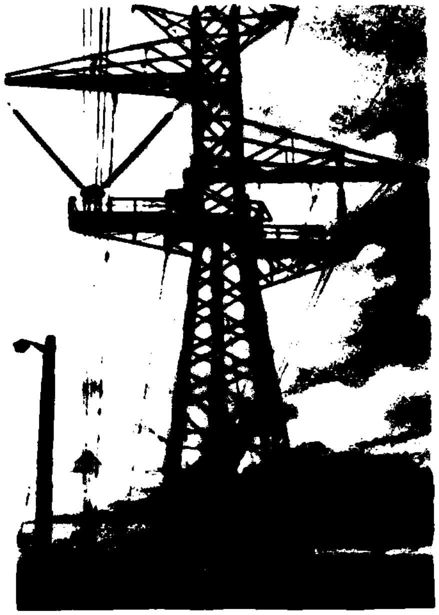

Figure 1 The Moro Test Line

Analysis of the test data was performed using STI-VAMP (Vibration Analysis and Measurement Processor) to determine the *modal and other dynamic properties of the* transmission tower and eight-conductor bundle.

Reliable measurements were made on a number of tower modes and the modal characterizations compare satisfactorily with computed values.

Experimental analysis of conductor motions was considerably more difficult. The very large dynamic range required of the accelerometers to measure phenomena ranging from traveling waves (high-amplitude, brief-duration accelerations) and aeolian vibration (high-frequency, high-amplitude accelerations) to "galloping" (low-frequency, high-amplitude displacement, low-amplitude acceleration) prevented measurements that were adequate for conventional analysis. This difficulty may be reduced in future experiments by preprocessing the accelerometer outputs (using analog techniques) to produce "velocity-like" signals before digitization.

In this paper, theoretical and experimental procedures are described and a comparison of measured and predicted behavior is presented. A critique of the methods used is presented and the concepts required for characterization of a complete transmission-line system are discussed.

THE MORO TEST LINE

Figure 1 shows the mechanical test line. It consists of two dead-end and four suspension towers. At the time of the test they were strung with single, twin, and eight-conductor-bundle configurations of 41-millimeter diameter (1.6-inch) "Aluminum Conductor Steel Reinforced" (ACSR) "Chukar" conductors. In addition, two 19-millimeter (0.75-inch) overhead ground wires and two 12.7-millimeter (0.5-inch) messenger wires (for suspension of conductor instrumentation leads) were strung.

Figure 2 shows the configuration of the eight-conductor bundle. This, or similar multiconductor systems, will be used in UHV transmission lines in order to reduce corona discharge, audible noise, and radio-frequency interference. The bundle is suspended at each tower by a "V-string" insulator pair. Its geometry is maintained by a yoke plate at each insulator pair and by "spacer-dampers" at approximately 70-meter (230-foot) intervals in the span.

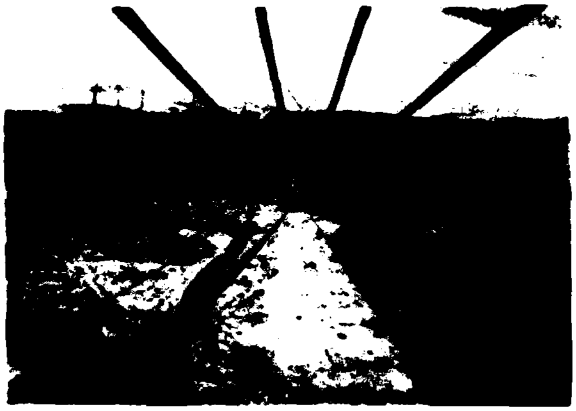

Figure 2 Eight-Conductor Bundle

The towers and conductors are instrumented with a variety of meteorological and structural-response transducers. The signals are appropriately conditioned and then acquired by a 256-channel, high-speed data-acquisition system. A minicomputer system is used to select data for storage on magnetic-cartridge disk.

INSTRUMENTATION

Figures 3 and 4 show the locations, orientations, and types of transducers used in the tests. The following devices were used:

1. Amplifier-followed piezoelectric accelerometers measured motions at 36 locations on the tower. These instruments were used to measure motions above 1 Hertz.

2. Capacitive accelerometers were used at six locations on the eight-conductor bundle. These devices provide accurate data from 0 to 50 Hertz and were used as the primary conductor-motion transducers.

3. Six tower/insulator loads were transduced using strain-gage load cells.

4. Applied loads were measured using strain-gage load cells.

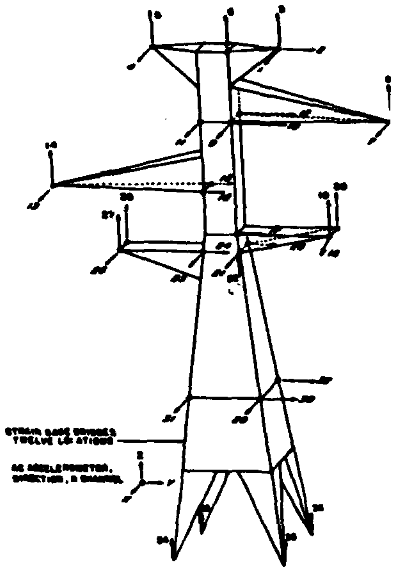

Figure 3 Tower Instrumentation

5. Pendulum actuated potentiometer swing-angle indicators were used to transduce the angular (along-line) motion of the twin-conductor insulator and eight-conductor bundle V-string insulator. These devices are restricted to measurements below 1.5 Hertz by a 3-Hertz resonance in the instrument.

6. Strains in the four tower legs and two of the tower diagonal members were measured using conventional foil strain gages. Four-arm bridges were used with temperature compensation provided by two unstrained gages per bridge.

Signal conditioning, data acquisition, and monitoring were performed using the system shown in Figure 5. Important features are:

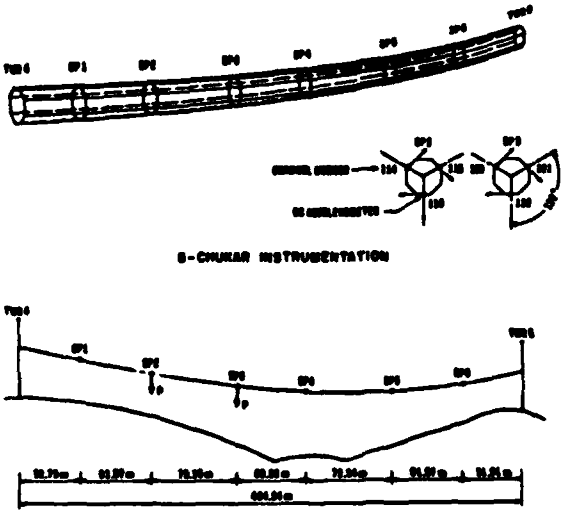
8-CHUKAR INSTRUMENTATION

Figure 4 Conductor Instrumentation

1. Low-level signals (from the strain gages and load cells) are amplified at the tower before being transmitted to the data system.

2. The signal-conditioning system has the following features:

    1. Differential input.

    2. AC coupling for piezoelectric accelerometers (all other instrumentation was DC coupled).

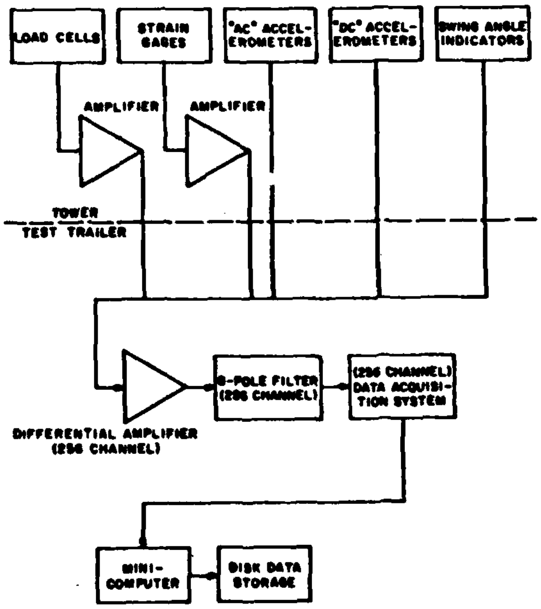
LOAD CELLS
STRAIN GAGES
"AC" ACCELEROMETERS
"DC" ACCELEROMETERS
SWING ANGLE INDICATORS
AMPLIFIER
AMPLIFIER
TOWER
TEST TRAILER
DIFFERENTIAL AMPLIFIER (256 CHANNEL)
8-POLE FILTER (256 CHANNEL)
(256 CHANNEL) DATA ACQUISITION SYSTEM
MINI-COMPUTER
DISK DATA STORAGE

Figure 5 Data System

3. Eight-pole low-pass filters for rejection of aliasing signals. For all tests reported here, filters were set at 40 Hertz. This, when combined with a 100 samples per second data acquisition rate, provided 40 dB of antialias protection for the signal range of interest (0 to 25 Hertz).

3. Filter outputs were digitized with a 256-channel analog-to- digital converter system. This system acquired data at 100 samples per channel per second with a resolution of 12 bits (i.e., one part in 4096).

PRETEST ANALYSIS

A pretest analysis was conducted to help select instrumentation and excitation locations and to give experimenters a prediction of response levels.

The analytical model of Tower #4 is shown in Figure 6. It contains 502 elements and 177 nodes. With the exception of the fixed groundline points, each node allows three translations and three rotations giving a total of 1038 degrees of freedom. Although the mass and stiffness of the insulators and conductors were not modeled, their weights were included.

After the model was specified, the SPAR finite-element program was used to determine the mass, stiffness, and geometric-stiffness matrices. An eigensolution was performed to estimate the resonant frequencies (eigenvalues) and associated mode shapes (eigenvectors).

The next step in the analysis was to perform an orthogonality check on the analytically derived modes which were truncated to contain only the degrees-of-freedom at the accelerometer locations. The mass matrix used in the orthogonality check was determined by Guyan reduction (2) of the full SPAR-generated mass matrix. The motive for this analyses was to verify adequacy of the instrument distribution. Ideally, the product of an orthogonality check;, i.e.:

$$\Phi^T M \Phi$$

where: Φ = eigenvector matrix

Φ^T = transpose of eigenvector matrix

M = mass matrix

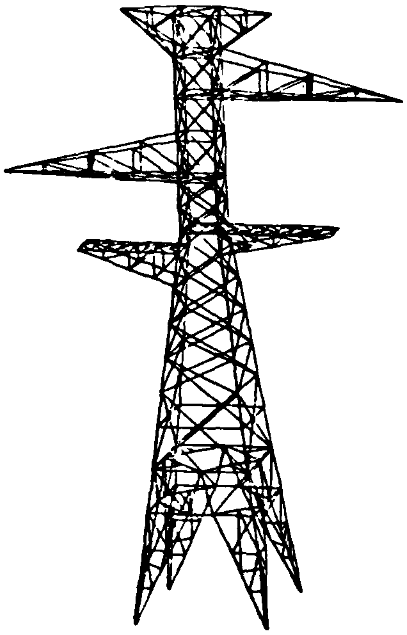

Figure 6 Tower Analysis Model

is approximately the unit matrix, i.e., ones along the diagonal and small off-diagonal terms. A large off-diagonal term would indicate that the instrument distribution is incapable of distinguishing between two similar modes. This study indicated that the accelerometer distribution used was satisfactory for characterization of the analytically-predictd modes.

The final step in the pretest analysis was to compute the dynamic response of the tower to each of the planned loadings. The objective was to estimate peak accelerations and loads to provide information required to set instrumentation gains and to assure that allowable stresses would not be exceeded.

TEST TECHNIQUE

The physical nature of the transmission system restricted the excitation alternatives for testing. The classical excitation procedures were considered; i.e., sine dwell, sine sweep, fast sine sweep or chirp, random, impulse, release from initial displacement or twang, and ambient.

The size and mass of the tower and conductors, the background noise levels (due to wind excitation), the requirement of producing realistically large motions, and available excitation methods, restricted the selection to twang excitation. Although other methods have significant signal-processing advantages, the capability of applying large loads, at several locations high on the tower, gives the twang-excitation concept a large practical advantage.

Forces were applied to the tower and conductor with the hydraulic-winch truck shown in Figure 7. The release was accomplished with the snap-shackle assembly shown in Figure 8.

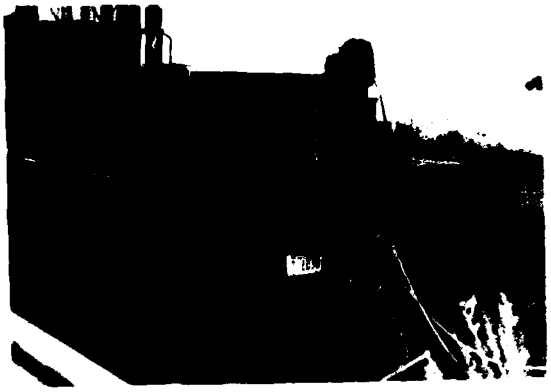

Figure 7 Winch Truck

Figure 8 Pully/Snap Shackle Assembly

The tower was loaded at the locations shown in Figure 9. Loads were applied to the conductor, both concentrically (vertical) and eccentrically (torsion), using the fixture shown in Figure 10.

In each instance, the test procedure was as follows:

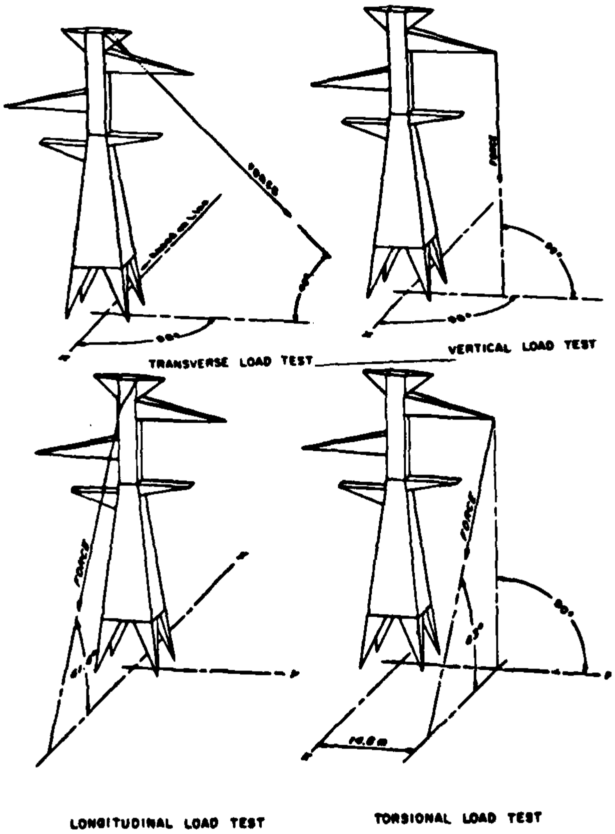

Figure 9 Tower Loading

1. Load was applied incrementally in ten steps to the maximum level of 45,000 Newtons (10,000 pounds) for tower tests, 18,000 Newtons (4000 pounds) for vertical conductor tests, and 4,500 Newtons (1000 pounds) for conductor torsion tests.
2. At each load level, static deflections were measured with theodolites to determine the stiffness of the tower and to determine the amount of permanent set (3).
3. After maximum load was reached, the data-acquisition system was activated and the load released. Data were acquired for periods ranging from 30 to 60 seconds, depending on the duration of transient response. In some conductor tests, data acquisition was restarted to provide more than one minute of data.

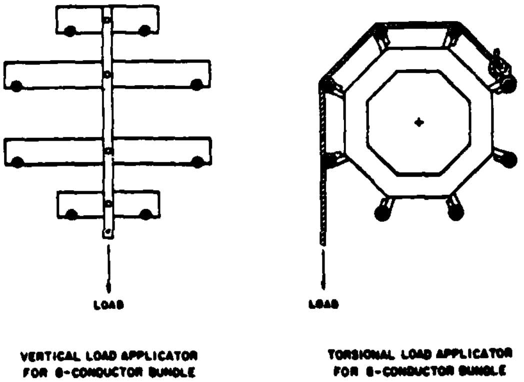

Figure 10 Conductor Loading Devices

ANALYSIS OF EXPERIMENTAL DATA

The discrete data acquired during the conductor and tower tests were processed to determine the dynamic characteristics of the system. The intent was to determine, wherever possible, the modal characteristics of the transmission-line system and to define interactions between the system elements.

The analysis was performed in two stages: A preprocessor was used for the following functions:

1. The time-series data was read in blocks of 1024 (10.24 seconds), 2048 (20.48 seconds), 4096 (40.96 seconds),8192 (81.92 seconds) or 16384 (163.84 seconds) points.
2. The conditioned time histories were converted to spectra by discrete Fourier Transform.
3. A block of 512 spectral values was selected. This process, combined with the four time-series-length options, resulted in up to a "16-to-1 zoom". For the tower and conductor-tower interaction analyses, a zoom ratio of 4 (producing a frequency range of 0 to 12.5 Hertz) was used. A ratio of 8 or 16 (frequency range of 0 to 3.12 or 6.25 Hertz) was used for conductor modal analysis.
4. The resulting spectra were stored in VAMP files and converted to engineering units (i.e., multiplication by calibration factors).
5. Transfer functions (i.e., the response spectra divided by the spectrum of the applied force) were calculated.
6. The transfer functions were fitted with an analytical expression for linear, multimode responses. The VAMP "global" fitting method, which produces a best-fit normal-mode set, was used to provide an estimate of the modal parameters.

Figure 11 shows a typical set of data for the tower with the fitted results superimposed. The transfer functions shown are for several displacement responses near the top of the tower during a "transverse" tower test. There are approximately 30 modes evident below 12 Hertz. Modal analysis was performed for each load condition for the 20 most-significant (from a global-response standpoint) modes below 12 Hertz. Very closely spaced modes were effectively separated by analysis of more than one transfer-function set. In particular, the first two modes of the tower have virtually identical resonant frequencies but, because of the distinct nature of their mode shapes, are easily separated by coordinated analysis of transverse and torsional tests.

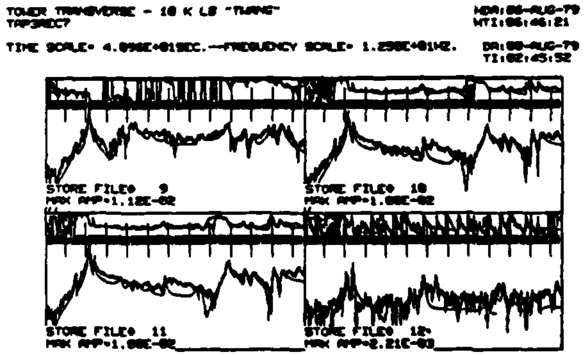

Figure 11 Tower Transfer Functions

The second minute of conductor motion was analyzed to determine modal frequencies and damping. During this period the traveling-wave motions were essentially dissapated leaving only "modal" activity. For these studies, a zoom ratio of eight was used to provide sufficient spectral resolution.

The first minute of data for the conductor-excited tests was analyzed to determine the interaction of the tower to large-amplitude, conductor-motion inputs. The data were analyzed by the following procedure:

1. Vertical motion of the spacers was determined by performing a vector addition of the accelerometer responses at each location.

2. Responses of the strain gages on the tower legs were plotted as a function of time as a measure of tower loading due to conductor excitation.

3. Vertical motions of the spacers were plotted, with the vertical motions of the arm tip (Accelerometer 8), for comparison of levels.

4. The spectra of these motions were determined by discrete Fourier transform.

5. The tower-motion/conductor-motion transmissability was calculated to determine tower/conductor interaction as a function of frequency.

RESULTS

The following table compares the determinations of the tower resonant frequencies, damping, and analytical/experimental orthogonality values for the first four experimentally determined modes.

TEST FREQUENCY	ANALYSIS FREQUENCY	TEST/ANALYSIS ORTHOGONALITY	STRUCTURAL DAMPING
1.54	no analysis	no analysis	.030
2.05	2.24	.949	.035
2.09	2.37	.907	.016
2.37	2.64	.969	.020

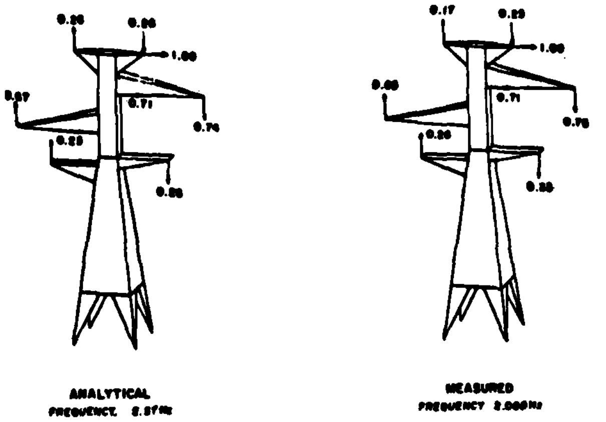

Figure 12b First Transverse Mode

Figure 12 shows the analytically and experimentally determined shapes for the first three tower modes.

Modes with nearly identical indicated shapes were identified at 1.54 and 2.05 Hertz. The similarity of these modes caused a large off-diagonal terms in the orthogonality matrix. The inability of the orthogonality check to distinguish between them indicates that at least one of the modes involves response of uninstrumented degrees of freedom. In addition, the lower-frequency mode was not predicted by the analytical model. Further testing of the eight-conductor insulator revealed a local resonance at approximately 1.5 Hertz. Insulator motion was not included in the finite-element model and is undoubtably the source of the unidentified mode.

The experimental results for the second, third and fourth modes show excellent agreement with the analysis values. The measured resonant frequencies were found to be about 10 percent below the analysis predictions. Refinement of the analytical model to include the effect of conductor and insulator mass would lower the theo-

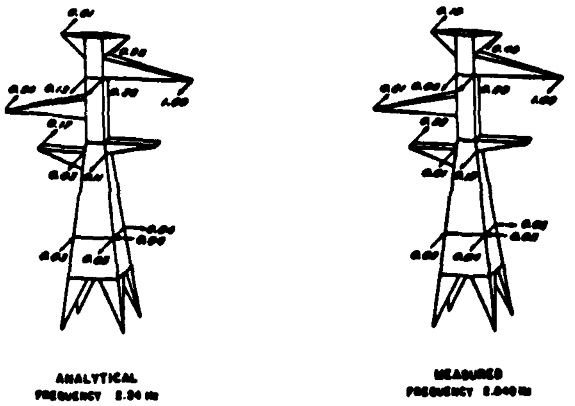

Figure 12a First Longitudinal Mode

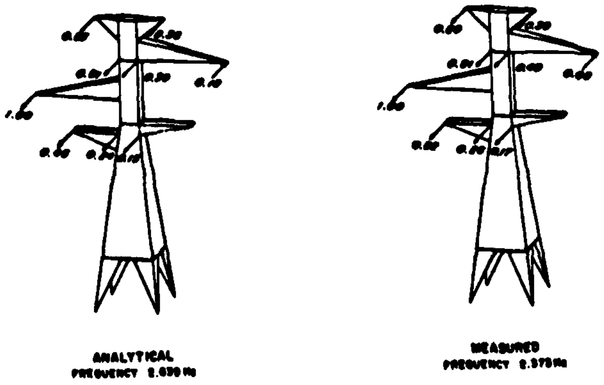

Figure 12c Second Longitudinal Mode

retical predictions. Other unaccounted effects that would improve correlation include joint slippage and base flexibility. However, the results produced were deemed satisfactory for the test requirements and further refinement was not attempted. The mode-shape determinations produced good correlation with analytical quantities.

Vertical motions of the third spacer during the second minute of the spacer #3 twang test was analyzed to determine natural frequencies and related damping coefficients. The following results were determined:

FREQUENCY	STRUCTURAL DAMPING COEFFICIENT
0.145	.084
0.272	.034
0.387	.026
0.420	.022
0.548	.017
0.682	.016
0.810	.012
1.100	.009
1.356	.008
1.635	.008
:	:
:	:
3.430	.005
3.577	.004
3.711	.004

It is interesting to note the progressive decrease in damping coefficient with increasing modal frequency. For the first few modes, the damping is very high (by normal structure standards) while, for the higher-frequency modes, the damping is quite low.

Figure 13 shows the response histories, due to a 18,000-Newton (4000-pound) vertical input at spacer #3, for the first fifty seconds after excitation at the second and third conductor spacers and the tower-arm tip. Several features of the response should be observed:

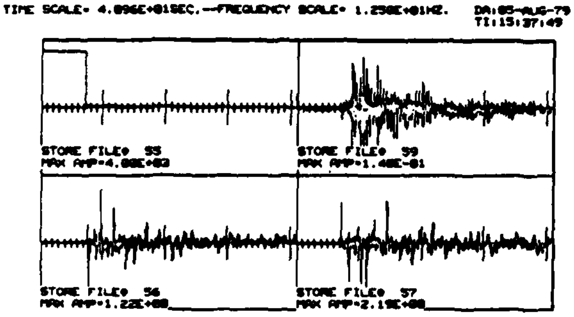

Figure 13 Conductor and Tower-Arm Response

1. Responses at the spacers are characterized by very sharp acceleration pulses that are due to traveling waves. These waves decay rapidly and the "modal" motions become dominant.

2. "Modal" behavior continues at very low damping well beyond the end of the data sample.

3. Despite displacement amplitudes of over three meters (ten feet). "Galloping" accelerations at approximately 0.1 Hertz are insignificant compared to other measured accelerations.

4. The tower responds at significantly lower peak acceleration levels (10%) than the conductor.

The transmissability (Figure 14) between the tower and conductor motions is significant (greater than 0.2) for a wide range of frequencies and exceeds unity at some tower resonances. The common assumption of insignificant interaction between the conductor and tower is not valid for this test line. Conductor motion in the frequency range of tower sensitivity (i.e., above two Hertz in this instance) will excite the tower to significant levels.

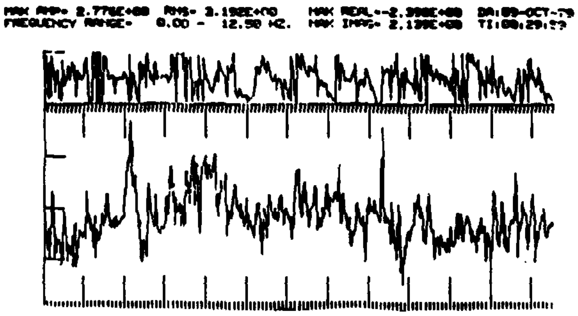

Figure 14 Tower Arm/Conductor Transmissability

CRITIQUE

One of the more important results of this test series was the experience gained which may be applied to future experiments.

The two primary problems encountered were:

1. The "twang" method of excitation causes several data-processing difficulties and greatly restricts the options available for analysis.

2. The use of acceleration signals was not entirely satisfactory for measuring conductor motions.

In spite of its utility in applying large loads far from the ground, "twang" excitation is probably not the best method available for transmission-line-system testing. It produces responses of inadequate duration. These signal's brevity and high-frequency content requires an impractically high sample rate and a very large discrete Fourier transform (i.e., many spectral lines) to provide the spectral density required for accurate modal analysis at low frequencies. Also, transient testing gives an "average" of the modal characteristics over the range of response amplitude. For structures with known nonlinearity, such as the transmission system, this procedure can lead to unconservative errors.

A solution is to provide a continuous excitation function that can be controlled in level and duration. A hydraulic shaker, driven by a sinusoidal or "chirp" (fast sine sweep) command, appears to be a likely solution. This excitation method will also allow the study of the system's response to a range of simulated "real" excitations.

The extremely wide range of accelerations that conductors experience, under both natural and artificial excitation, make acceleration an inappropriate measurement under many conditions. The detection of "galloping" motions at approximately 0.1 Hertz, requires an acceleration resolution of 0.0005 g's to measure 2.5 centimeters (1 inch). This must be done in the presence of high-frequency (above 20 Hertz) aeolian and traveling-wave motions of the order of 5 g's. Thus, a dynamic range of 10,000 to 1 is required of the instrumentation and acquisition system. This capability is well beyond the present state-of-the-art.

Characterization of traveling waves in the conductor is impractical with acceleration measurements. Initial motions of the conductor twang tests consisted primarily of waves with very brief intervals of high (theoretically infinite) acceleration. Effective characterization of these motions would require an impractically high data-acquisition rate.

A potential solution to both of these difficulties is to use high-resolution accelerometers and to perform analog integration to produce a "velocity-like" signal. For this response parameter, the required dynamic range of the data-acquisition system is reduced to the order of 150 to 1, a realizable capability, and the frequency range of significant signals is greatly reduced. This is presently being performed at the Moro test site by signal conditioning the conductor accelerometers with "AC-coupled integrators" (i.e., a two-pole bandpass filter centered at 0.2 Hertz). The success of this approach will be determined by analysis of conductor response to natural excitation over the 1979/1980 winter and during future forced-vibration tests.

The analytical/experimental comparison showed the techniques being used for analysis of tower motions are satisfactory. However, insulator motions have not been included in the analyses because they were thought to be insignificant and because available techniques do not accurately predict their behavior. Modeling techniques for the conductors and insulators must be upgraded to include more realistic (nonfixed) boundary conditions to provide improved correlation. It is necessary that these elements be adequately modeled to characterize the overall behavior of a transmission-line system.

CONCLUDING REMARKS

This test series has produced a number of conclusions. Four of the most significant are:

1. It was shown that the finite-element modeling of the tower provided adequate predictions of the measured tower behavior.

2. The widely accepted belief that conductor and tower dynamics are separable is not justified for this case. For transmission-line systems, in which the mass of the conductors is significant compared to the tower, interaction effects cannot be ignored. The insulator does not isolate the components and large loads can be transferred from the conductors to the tower. Such dynamic effects may threaten the structural integrity of the system.

3. Significant changes in instrumentation are needed to characterize conductor motions. Both traveling waves and the ever-present aeolian vibrations can produce high-frequency, high-acceleration signals that overwhelmingly dwarf the low-frequency signals related to galloping, making meaningful analysis of this phenomenon very unlikely. A measurement of velocity or displacement time histories would be less sensitive to

aeolian phenomena. In the long term, some radical developments in measurement methods may make such direct measurements possible. However, for the near future, analog processing of acceleration signals is the most likely solution.

4. The appearance of insulator resonances in tower-response measurements indicates that insulator and conductor characteristics must be included in the analysis of transmission-line systems.

The eventual objective of dynamic analysis of transmission towers or conductors should be an integrated analysis of all elements (i.e., towers, insulators, and conductors). This type of integrated approach is necessary to perform analysis of the accuracy required to design the electrical transmission systems of the future.

REFERENCES

1. Whetstone, W. D., "EISI/SPAR Reference Manual", Engineering Information Systems, Inc., Saratoga, California, August 1976.

2. Guyan, R.J., "Reduction of Stiffness and Mass Matrices", Journal of the American Institute of Aeronautics and Astronauutics, Vol. 3, No.2, February 1968, p380.

3. Kempner, L., "UHV Moro Mechanical Test Line, Structural Static Tests,, November 27-December 2, 1978", Moro 1200-kV Project Report No. ME-80-3, Bonneville Power Administration, 1980.

DISCUSSION

Mr. Volin (Shock and Vibration Information Center): The towers had walkways for instrumenting the conductors. How would that model be affected if you had removed those walkways? Would that make any difference in the mode shapes and natural frequencies of the tower?

Mr. Smith: The tower was modeled both with and without the walkways obviously. There were relatively small differences, the walkways are relatively small mass compared to the rest of the tower, but they were included because the objective was to verify the analytical techniques that we were using and so they had to be included to show that things were right.

Mr. Volin: Did you consider that the cables are very prone to being excited by wind loads? How would those interact with the tower?

Mr. Smith: For three of the six days of the test it was blowing so hard and the conductors were going so hard that we couldn't do any reasonable testing and let me tell you that the wind really does the job on it.

Mr. Stahle (General Electric Company): You said you missed the tower frequencies by ten percent?

Mr. Smith: The analytical predictions were consistently ten percent above the measured frequencies.

Mr. Stahle: And I think you also indicated that this was due to the fact that you had bolted joints.

Mr. Smith: That is one good reasonable assumption.

Mr. Stahle: Do you feel that ten percent gives you adequate analytical correlation and is there anything you can do to your math modeling that would improve it?

Mr. Smith: Yes you could improve it. No I don't think it is worth the trouble. We have found this ten percent difference to be fairly consistent when we use sophisticated finite programs like SPAR. These differences are due to small nonlinearities in the joints and such things as that, they will be very, very hard to characterize and I don't think they are worth chasing.

Mr. Stahle: We were recently involved in a wind turbine design using thrust towers. We did not miss it by ten percent, we used NASTRAN and the towers had bolted joints.

Mr. Smith: Have you assumed anything other than rigid joints?

Mr. Stahle: I think the towers had bolted joints so I have a little trouble understanding why you missed it by ten percent. I wonder if you have a cable problem that could cause your error?

Mr. Smith: A cable problem?

Mr. Stahle: Cable interaction problem.

Mr. Smith: That could be. The weight of the cables but not the mass of the cables was included in the analytical model and that could conceivably push it in the right direction.

Mr. Dyrdahl (Boeing Company): How about some of the other modes, were you off on those too?

Mr. Smith: The first three modes were all off by ten percent. Now we did not adjust the model after the test which is a standard procedure. I am sure we could have had very good agreement if we had done that.

Mr. Dyrdahl: In relating back to Bob Hager's speech this morning, when are you going to be ready to dispense with the test and do it all analytically and with a great deal of confidence?

Mr. Smith: With certain kinds of simple structures, not very long from now. And I would like to think that this kind of structure is one example.

Mr. Dyrdahl: How about the base of the foundation? Did you model the soil?

Mr. Smith: This analytical model had a rigid base. There have been some studies at Bonneville that showed that this doesn't make that much difference.

DESIGN TECHNIQUES

ANALYSIS AND DESIGN OF THE SHUTTLE REMOTE MANIPULATOR SYSTEM MECHANICAL ARM FOR LAUNCH DYNAMIC ENVIRONMENT

D.M. GOSSAIN, E. QUITTNER, S.S. SACHDEV
SPAR AEROSPACE LIMITED
TORONTO, CANADA

INTRODUCTION

The Remote Manipulator System (RMS) is a part of the payload handling system of the U.S. Space Shuttle Orbiter. It comprises the orbiter-mounted hardware installed in the payload bay and the crew compartment. The payload bay equipment consists essentially of a Manipulator Arm.

4/mcs490/1

The Manipulator Arm (MA) is a 15.24 m (50 ft.) long tubular structure consisting of six joints providing six rotational degrees- of-freedom. The joints correspond to the degrees-of-freedom of a human arm. The arm is attached at one end to the Manipulator Positioning Mechanism (MPM) of the Orbiter. The joints near the attachment, called "shoulder joints", provide two degrees-of-freedom and the joints at the tip, called "wrist joints" provide three degrees-of-freedom. An "elbow joint" in the middle of the arm, provides one degree-of-freedom. The "joints" are electro-mechanical structures, with the rotational degrees-of-freedom provided by motor-driven high-ratio gearboxes. The joints are connected by 34.29 cm (13.5") dia. tubular members, called "booms". The tip of the arm carries an End Effector which attaches to the payload.

During launch the arm is stowed in the payload bay. In this configuration three additional supports are provided to the arm by the Manipulator Retention Latches (MRL) - one near the elbow joint and two in the wrist joint area. Figure 1 is a schematic showing the arm in its stowed configuration. In orbit, the MPM deploys the Arm into an operational position. The MRL's are released and RMS is ready for use.

The launch dynamic environment specified for the stowed arm comprises very low frequency acceleration (applied as quasi-static g-levels) and random vibration inputs applied at the longeron. The random vibration spectrum extends from 20 Hz. to 2000 Hz.

This paper presents an overview of the design and analysis studies undertaken for the stowed MA, the problems encountered and their solutions. The data presented here are typical and for discussion only since they are subject to update/revision in the design/development process.

DESIGN FEATURES OF THE MECHANICAL ARM

The MA has been designed to meet stringent weight and stiffness requirements. The constraints of stowage require that the arm cross-section stay within a 38.1 cm (15") diameter dynamic envelope. The maximum diameter of the arm booms is limited to 34.29 cm (13.5") due to this constraint. The stiffness of the arm and the torque capacities of the joints are governed by considerations of the on-orbit operation of the arm. A design goal of stiffness of 0.885 N/cm (10 lbf/inch) at the tip of the arm, when fully extended, has been used. The torque and speed capabilities of the joints, given in Table 1, are based on the requirements to perform payload manoeuvres within specified time limits, stopping the payloads within specified distances, ability to apply forces at the arm tip, etc. References (1), (2) and (3) give details of RMS system requirements on which the design is based.

The stiffness and weight distribution of the arm structure along its length has been optimized within the constraints of keeping the design cost effective i.e. considering commonality

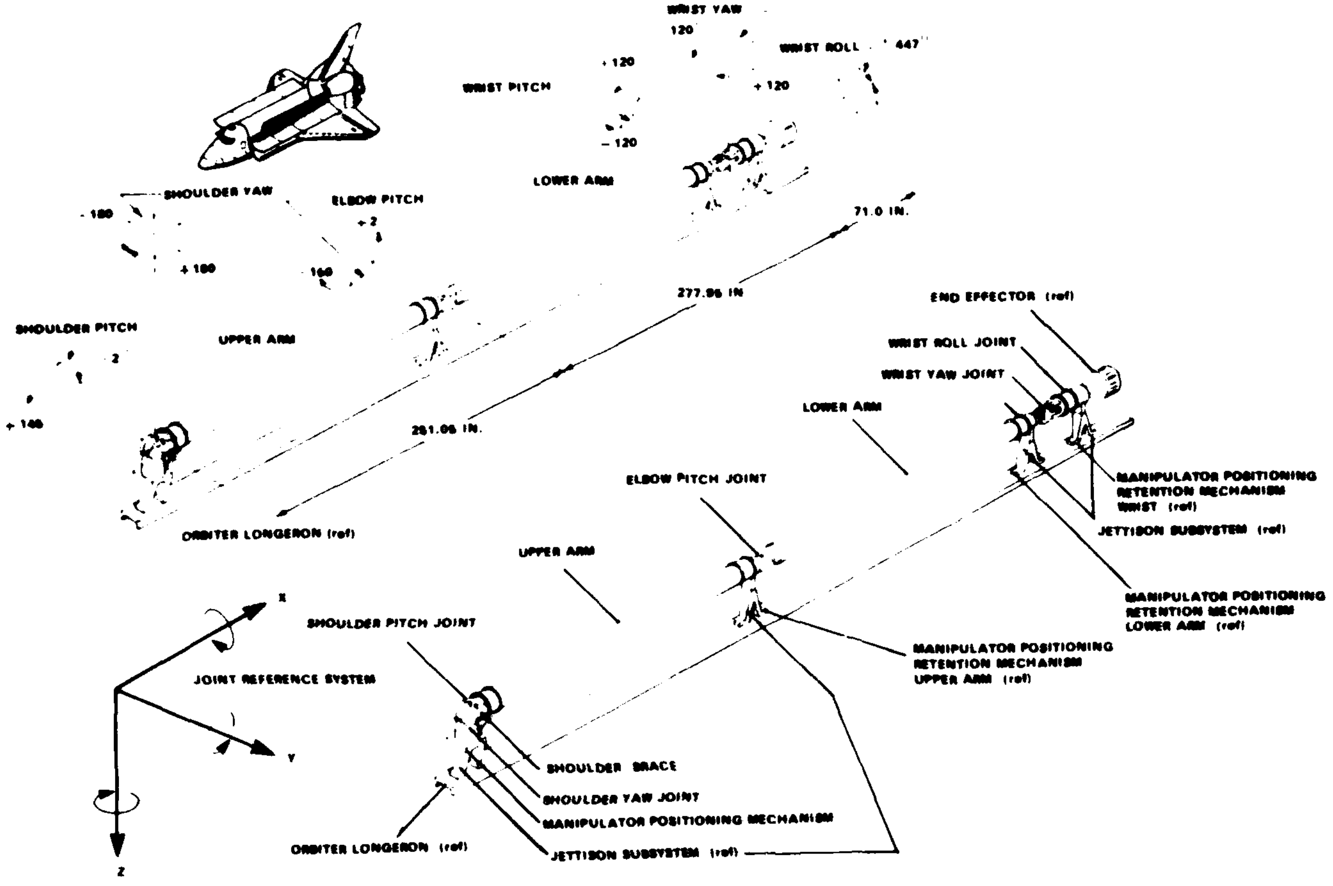
WRIST YAW
120
WRIST ROLL
447
WRIST PITCH
+120
+120
−120
LOWER ARM
SHOULDER YAW
ELBOW PITCH
−180
+2
+180
−160
71.0 IN.
277.96 IN
SHOULDER PITCH
UPPER ARM
2
+140
251.06 IN.
ORBITER LONGERON (ref)
END EFFECTOR (ref)
WRIST ROLL JOINT
WRIST YAW JOINT
LOWER ARM
ELBOW PITCH JOINT
MANIPULATOR POSITIONING RETENTION MECHANISM WRIST (ref)
JETTISON SUBSYSTEM (ref)
UPPER ARM
MANIPULATOR POSITIONING RETENTION MECHANISM LOWER ARM (ref)
X
SHOULDER PITCH JOINT
MANIPULATOR POSITIONING RETENTION MECHANISM UPPER ARM (ref)
JOINT REFERENCE SYSTEM
Y
SHOULDER BRACE
SHOULDER YAW JOINT
MANIPULATOR POSITIONING MECHANISM
ORBITER LONGERON (ref)
JETTISON SUBSYSTEM (ref)
Z

FIG. 1 MECHANICAL ARM ASSEMBLY GENERAL CONFIGURATION

of parts, manufacturing costs, schedules, etc. As a result, the wrist-region joint structures are within a smaller diametral envelope (and, thus, have lower stiffness) than the shoulder or elbow joints. The booms are made from graphite-epoxy composites. The inside diameters of the upper and lower arm booms are the same but the lower arm boom has a smaller thickness.

The structural components, other than the booms, are made of conventional engineering materials: stainless steel, aluminum alloys and titanium alloys.

Each joint in the arm has a drive module. The input and output sides of the drive module are attached to structural elements (referred to as "joint structures") which provide structural load paths and interfaces to other joints or structural components of the Arm. Figure 2 shows the configuration of shoulder joint, as an example. The drive modules have commonality of design. Each module consists of a brushless d.c. motor along with its drive/control hardware (tachometer, commutation scanner, brake) and a high-ratio gearbox. The gearbox comprises high-speed spur gear-trains and a low-speed bearingless-differential-planetary (epicyclic) drive. The differential planetary drive is at the output-end of the gearbox, and has a ratio of 40:1 for all joints. The gear-ratios for the spur gears are adjusted to get the required gear-ratios for different joints (Table 1). The gear-train schematic for the shoulder joint is shown in Figure 3, as an example.

The Arm structure is designed for 100 missions. The requirement is to demonstrate that the structual components can survive 100 missions with a scatter factor of 4 i.e. survive load cycles equivalent to 400 missions, including launch.

Detailed descriptions of the Manipulator Arm design are given in References (1) and (4).

INITIAL/PRELIMINARY LAUNCH STUDIES

At the preliminary design stage, all the joint-structures were designed to be within 34.29 cm (13.5") diameter envelope with an allowance of 3.81 cm (1.5") for arm deflections under acceleration/ vibration environment. The arm brace (Figure 1) was not a part of the design. It became apparent at this stage that the largest deflections, at the arm centre-line, were in the lateral direction (Y) and that the stiffness of the MPM structure was primarily responsible for these deflections. The deflections occur under the application of "quasi-static" launch accelerations in the lateral direction. Although the accelerations in the longitudinal direction (thrust) are the highest, the stiffness of the retention system in this direction is also significantly higher than that in the lateral direction. Also, a larger dynamic envelope is available along the length of the arm.

Analysis for random vibration input indicated very high loads in the arm, especially at the joints where the dynamic loads (bending moments) are carried by the gear-trains. A finite-element, lumped-mass, mathematical model of the system was used and is discussed in a later section.

The loads at the Arm joints in response to random input (Table 2) were calculated to be as given in the table below.

It is seen from the table that the random loads are far in excess of the maximum torque capability of the joints for on-orbit operation. Fatigue damage calculations, which included the effect of loads due to quasi-state acceleration, indicated that the application of

JOINT	RESPONSE BENDING MOMENT (N-m)(rms)	TORQUE CAPABILITY ON-ORBIT (N-m)
Shoulder-Yaw	542.3(400 lbf-ft)	1308.3(965 lbf-ft)
Shoulder-Pitch	3158.9(2330 lbf-ft)	1308.3(965 lbf-ft)
Elbow-Pitch	1532.0(1130 lbf-ft)	894.8(660 lbf-ft)
Wrist-Yaw	854.1(630 lbf-ft)	391.8(289 lbf-ft)
Wrist-Pitch	1586.2(1170 lbf-ft)	391.8(289 lbf-ft)
Wrist-Roll	583.0(430 lbf-ft)	391.8(289 lbf-ft)

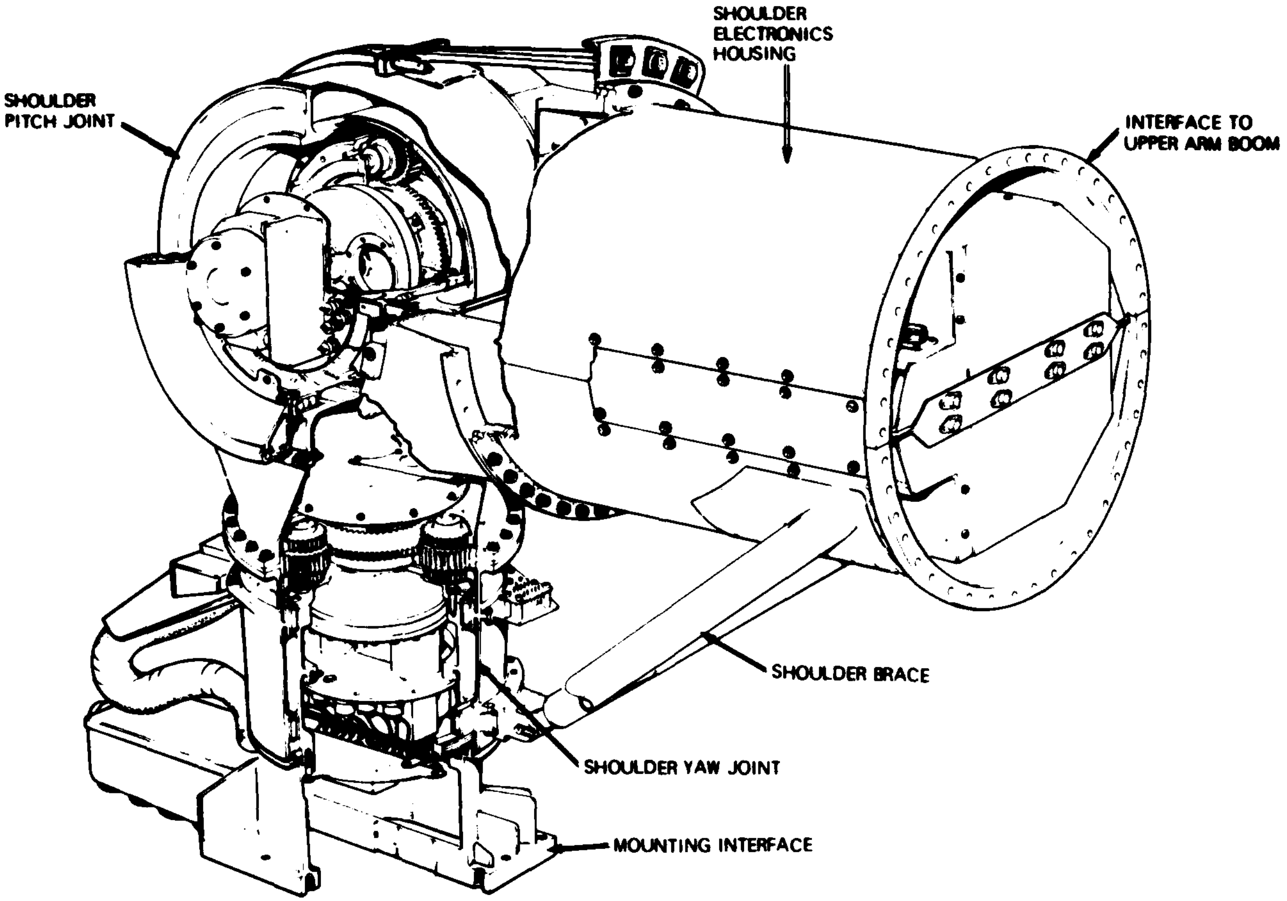
SHOULDER ELECTRONICS HOUSING
SHOULDER PITCH JOINT
INTERFACE TO UPPER ARM BOOM
SHOULDER BRACE
SHOULDER YAW JOINT
MOUNTING INTERFACE

FIG. 2 OVERALL CONFIGURATION OF THE SHOULDER JOINT

TABLE 1

ARM JOINT CHARACTERISTICS

		SHOULDER		ELBOW	WRIST		
PARAMETER	UNITS	YAW	PITCH	PITCH	PITCH	YAW	ROLL
Maximum Capability	N-m	1308.3	1303.3	894.8	391.8	391.8	391.8
(Nominal)	Ft-lbs	(965)	(965)	(660)	(289)	(289)	(289)
Output Speed Limits							
- Unloaded	Rad/sec	0.04	0.04	0.056	0.083	0.083	0.083
- Loaded	Rad/sec	0.004	0.004	0.0056	0.0083	0.0083	0.008
Gear Ratio	-	1842:1	1842:1	1260:1	738:1	738:1	738:1

4/mcs490/10

TABLE 2

PRELIMINARY RANDOM VIBRATION SPECIFICATION

(ACCELERATION POWER SPECTRAL DENSITY)

Level A

20-90 Hz : increasing at 6 db/Oct to 0.1 g^2/Hz
90-300 Hz : constant at 0.1 g^2/Hz
300-2000 Hz: decreasing at 6 db/Oct.
(Duration: 34 minutes)

Level B

20-40 Hz: increasing at 6 db/Oct to 0.05 g^2/Hz
40-150 Hz: constant at 0.5 g^2/Hz
150-2000 Hz: decreasing at 6 db/Oct.
(Duration: 14 minutes)

REVISED RANDOM VIBRATION SPECIFICATION

(ACCELERATION POWER SPECTRAL DENSITY

20-30 Hz: increasing at 6db/Oct. to 0.006 g^2/Hz
30-250 Hz: constant at 0.006 g^2/Hz
250-2000 Hz: decreasing at -6db/Oct. from 0.006g^2/Hz at 250 Hz
(Duration: 48 minutes)

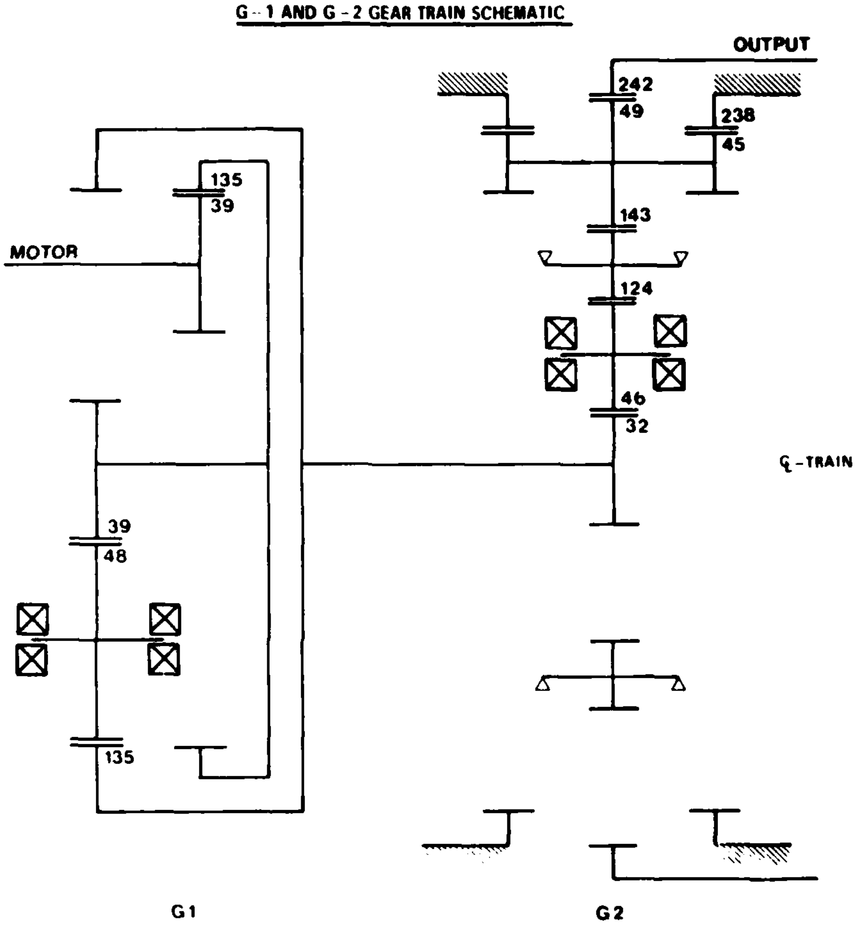
G – 1 AND G – 2 GEAR TRAIN SCHEMATIC
OUTPUT
242
49
238
45
135
39
143
MOTOR
124
46
32
℄ – TRAIN
39
48
135
G1
G2

FIG. 3 SHOULDER JOINT GEAR SCHEMATIC

these random loads for 48 minutes (equivalent to 100 launches with a scatter factor of 4) would consume practically all the fatigue life of the gear teeth which had been sized from on-orbit load considerations.

A system study of the stowed Arm was then undertaken, with the following design requirements:

(a) The primary design driver for the Arm shall be the on-orbit performance requirements of the RMS.

(b) The MA support and retention system shall be optimum within its own constraints of weight and cost. The system is being designed by the Orbiter Contractor, Rockwell.

(c) The effect of launch-induced loads on the life of joint gear-teeth shall be minimal in order to have the full fatigue-life available primarily for on-orbit operations.

4/mcs490/3

(d) The deflections of the system under dynamic inputs shall be such as not to violate the available dynamic envelope.

(e) The retention system support locations should interface on the metallic structural components of the arm.

Two different approaches were investigated during this study:

(a) Cradled-joint design, in which a "cradle" supports the structure on two sides of a joint. A typical arrangement, for the elbow joint, is shown in Figure 4. The cradles would have stiffness, in the Z-X plane, much higher than the arm, in order to provide an alternate load path and thus reduce the loads in the gear train. Cradles for the wrist region could be selectively gimballed in order to reduce yaw-moments (moments about the Z-axis, M_Z).

(b) A free-joint design, in which the gear train of the joint is "decoupled" or "declutched".

The effective inertia of a motor rotor (and other inertia elements on the input shaft) at the output of the gearbox varies as the square of the gear-ratio. As discussed further in a later section, the effective inertias of the joints are very high; this has the result of a joint being "inertia-controlled" i.e., it does not rotate at high frequencies at which the arm structure vibrates under random inputs. Providing a slipping clutch or another load path which would by-pass the gear-train in the joint, would isolate the gear-train. Such an arrangement would have to be operational only during launch.

The studies also indicated that:

(a) The three support structures (in addition to that at the shoulder) could be moved along the longeron somewhat, to better locations.

(b) Lower Z direction stiffness of the support structure would provide relief to joint loads, since it would have the effect of lowering Z-direction natural frequencies and cutting off high-frequency inputs.

(c) Addition of damping could be considered to reduce response. A modal magnification factor (Q) of 15 has been used in the analysis. Response levels would be reduced with additional damping (lower Q).

BASELINE CONFIGURATION

The results of these studies led to a number of trade-offs and also a review of the vibration environment. As a result, a baseline configuration for launch was arrived at, with the following features:

(a) A brace at the shoulder joint was introduced to protect the shoulder pitch joint. The brace is shown in Figures 1 and 2.

(b) The elbow joint was moved toward its support and the first Wrist Support (fwd) was moved aft.

(c) A review of launch environment resulted in lower vibration levels due to the effects of water-spray at lift-off and inclusion of arm inertia effects in orbiter dynamics. The environment is shown in Table 2.

(d) The cradled-joint designs and free-joint designs were not considered feasible on the grounds of weight-penalty, reliability, program delays due to development efforts required, etc.

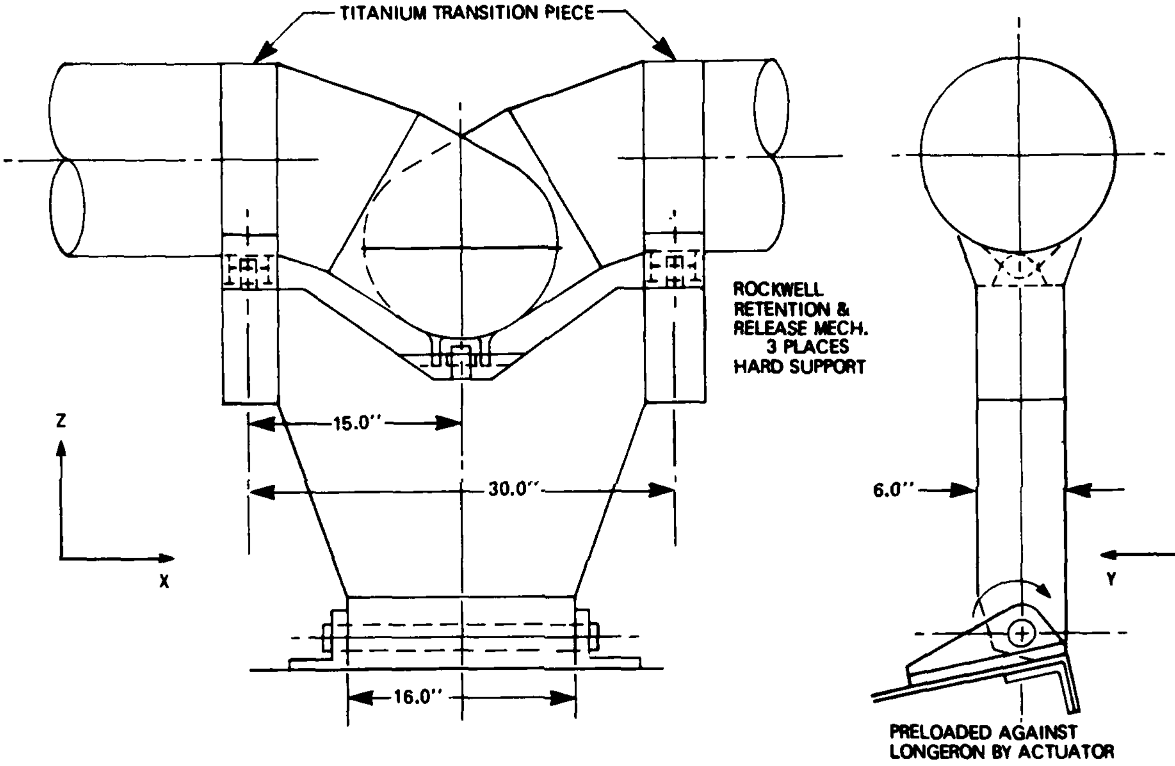
TITANIUM TRANSITION PIECE
ROCKWELL RETENTION & RELEASE MECH. 3 PLACES HARD SUPPORT
Z
X
15.0"
30.0"
16.0"
6.0"
Z
Y
PRELOADED AGAINST LONGERON BY ACTUATOR

FIG. 4 ELBOW RETENTION; CRADLE TYPE

(e) Additional damping or isolation pads at the retention system support points, to be used if found necessary.

(f) A weight reduction and stiffness-optimization study had shown that wrist joint structures could be reduced in diametral dimensions without significant reduction in required stiffness, because of their proximity to the arm tip. Reduction in stiffness in this region would reduce the wrist-joint loads under vibration. The diametral envelope for the region was reduced from 34.29 cm (13.5") to 24.13 cm (9.5") as a result of this study.

ANALYSIS

With the development of the baseline configuration, the dynamic analysis entered the phase of generating loads that would be used for detailed design of the structural components of the arm and the retention system. The approach taken for analysis was to develop a mathematical model and a set of assumptions to be used in the analysis, e.g. load paths, load transfer characteristics of the geartrains, modal damping, etc. The basic assumptions were separately investigated, by further analysis and/or tests, for their validity. This led to a "baseline model" which was used to generate loads and to support the iterative design process. Since the effects of various simplifying assumptions had been studied separately, the baseline model remained relatively simple and could be used in a cost-effective manner.

4/mcs490/4

A finite-element model of the Manipulator Arm and the retention system has been used. The model is shown in Figure 5. The theory of finite-element techniques is fairly well known and discussed extensively in references such as (5). The whole structure has been idealized as an assemblage of beam elements, to which stiffness properties are assigned. "Lumped" masses are assigned to nodes. The number of "mass" nodes have been selected to obtain the low order vibration nodes (up to 100 Hz) with sufficient accuracy.

The dynamic response of the system to random input at the base is computed using the finite-element model. The basic theory is, again, well-known (Ref. 6, 7) and is not discussed here. Commercially available structural analysis programs, such as STARDYNE (Ref. 8) and NASTRAN (Ref. 9) are written to compute the structural response to dynamic inputs. STARDYNE has been used for most of the analysis; some supplementary analysis has been done using NASTRAN.

Mathematical modelling involves use of judgement and assumptions about the system to be analysed. Some of the assumptions made for the base-line model, in addition to the assumption of linearity, are discussed below. The validity of these assumptions and their implications have been investigated further and are discussed in a later section.

(a) The joint gear-trains are assumed to have the capacity to transmit moments through the gear teeth in the launch dynamic environment. The gear-trains are, thus, assumed to provide structural continuity for transfer of bending moments.

Stiffness characteristics of the gear-trains, are included in the appropriate beam elements for the joint structures in the model.

(b) The damping in the system acts as "modal" damping i.e. each mode of the structure has a certain amount of damping associated with it. In the baseine model, a magnification factor, $Q = 15$ (damping ratio = 0.033) has been used for all the modes.

(c) Random input to the system, applied at the longeron, is assumed to be spatially correlated.

RESULTS

Two locations on the arm are provided for the attachment of TV cameras and lights: one at the elbow joint (optional) and the other at the wrist joint.

(a) Mode Shapes and Frequencies

The first sixteen frequencies and mode shapes of the system (camera at wrist) are:

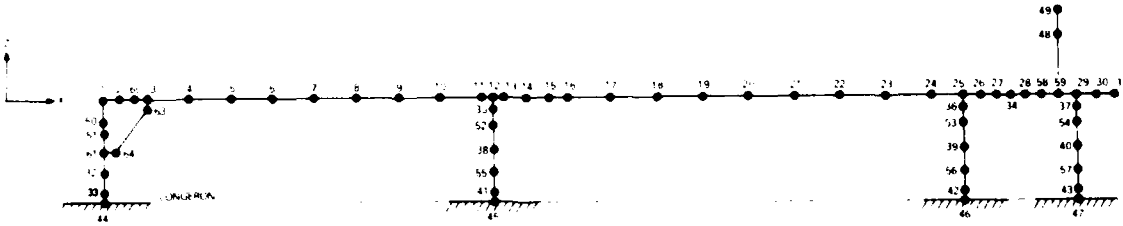

49
48
4
5
6
7
8
9
12
14
15
16
17
18
19
22
23
24
25
26
27
28
58
59
29
30
31
34
63
60
64
33
LONGERON
44
52
38
55
41
36
53
39
56
42
46
37
54
40
57
43
47

FIG. 5 MATH MODEL STOWED ARM (RMS)
(Camera at Wrist)

NO.	f(Hz)	MODE SHAPE
1	9.1	Y-mode (displacement in the X-Y plane)
2	10.1	Y-mode
3	11.5	Y-mode
4	15.6	Y-mode
5	17.9	Z-X mode (displacements in the Z-X plane)
6	26.2	Y-mode (camera)
7	26.9	Z-mode
8	30.2	Y-mode
9	34.2	Z-mode
10	43.8	Y-Z mixed mode
11	44.9	Z-Y mixed mode
12	50.5	Z-mode
13	57.4	Z-mode
14	71.8	Y-mode
15	77.8	Z-mode
16	91.3	Z-mode

Some of the mode shapes are shown in Figure 6a through 6c.

4/mcs490/5

(b) Loads

The bending moments at the arm joints (gear-trains) in response to the random input are:

DIRECTION OF JOINT	BENDING MOMENT (3-SIGMA) (N-m)	DIRECTION OF BASE INPUT
Shoulder-Yaw	107.6 (79 lbf-ft)	Z
Shoulder-Pitch	282.4 (208 lbf-ft)	X
Elbow-Pitch	885.8 (653 lbf-ft)	Z
Wrist-Yaw	186.0 (137 lbf-ft)	Z
Wrist-Pitch	907.0 (669 lbf-ft)	Z

The shoulder joints are now well protected by the brace. The Z-direction input produces the largest pitch bending-moments. The low frequency modes of the system are in the Y-direction (lateral) providing good isolation for Y-direction random input which starts at 20 Hz. The Z-direction modes start at around 20 Hz and are excited by the random input. The modes generally have low participation factors for X-direction input (the primary Z-X mode is at 17.9 Hz), so the response to X-direction inputs is also quite low. The My bending moments along the arm, for Z-direction input are shown in Figure 7.

Fatigue damage to the gear teeth has been estimated using the Miner-Palmgren hypothesis for cumulative fatigue damage, which defines fatigue damage D as:

$$D = \sum \frac{n_i}{N_i}$$

where:

n_i = Number of cycles at a stress level

N_i = Number of cycles necessary to cause failure at that stress level

The damage index D is a dimensionless number between 0 and 1, and failure is considered to occur when D = 1. The hypothesis is not generally collaborated by experimental data; however, it is commonly used because of its simplicity and for the lack of anything better at the design stage. Conservatism lies in using a low number for D as a failure criterion. The random response loads can be converted to "equivalent" sinusoidal loads using the approach discussed in Ref. 7. In using this approach, the damage index for the gear teeth has been calculated to be very small (<0.01), thus providing confidence that no significant fatigue damage would occur due to the random launch loads. (The effect of quasi-static loads is included by using a Soderberg-diagram for fatigue life).

INVESTIGATION OF ASSUMPTIONS

The simplifying assumptions used in the baseline model have been investigated further for their validity, and are discussed below:

(a) Gear-Train Load Transfer

The baseline model assumes that the gear-trains provide structural continuity. This assumption eliminates the need for an explicit modelling of the gear-train in studying the dynamics of the system.

The apparent inertia, I_o, at the output of a gear-train is:

$$I_o = I_m \times N^2$$

where I_m = inertia on the motor shaft

N = gear ratio

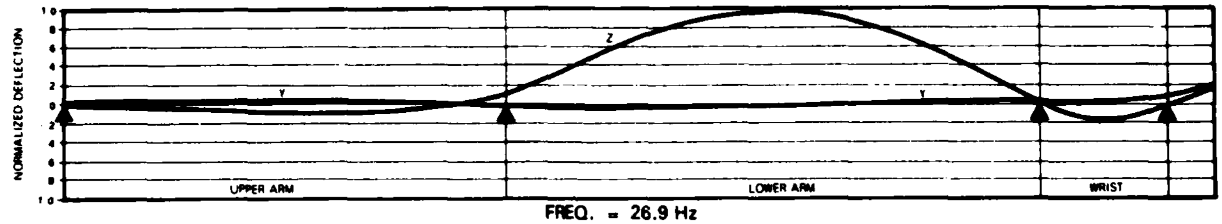

FREQ. = 26.9 Hz

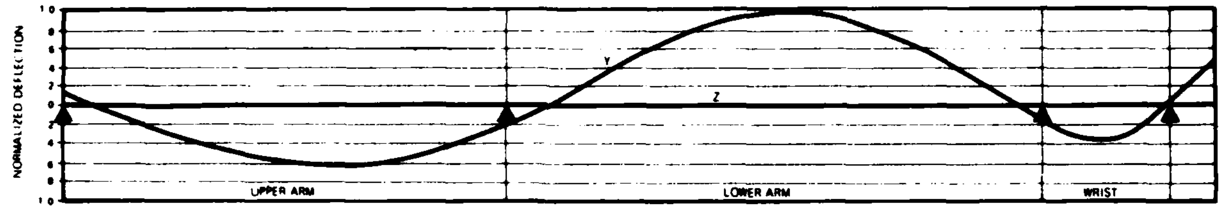

FREQ. = 30.2 Hz

FIG. 6a. RMS ARM NORMAL MODES (Camera at Wrist)

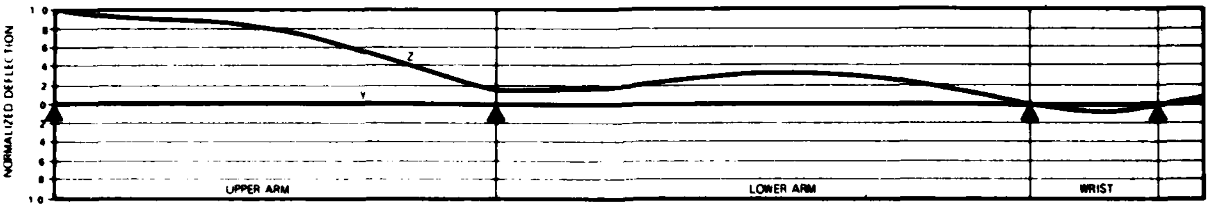

FREQ. = 34.2 Hz

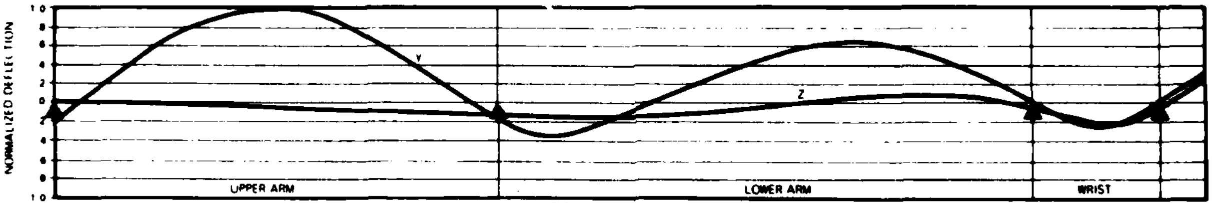

FREQ. = 43.8 Hz

FIG. 6b RMS ARM NORMAL MODES (Camera at Wrist)

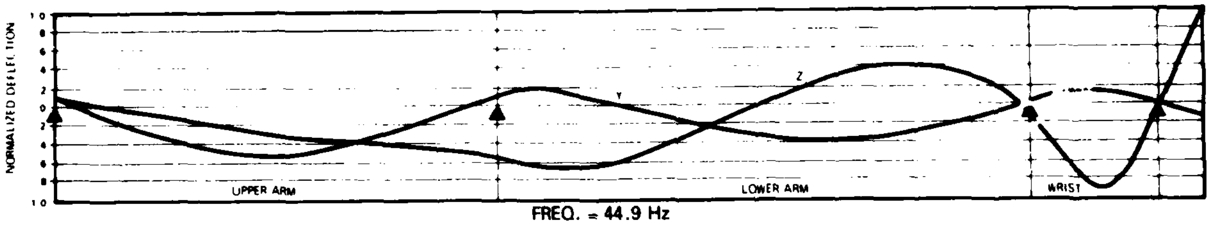

FREQ. = 44.9 Hz

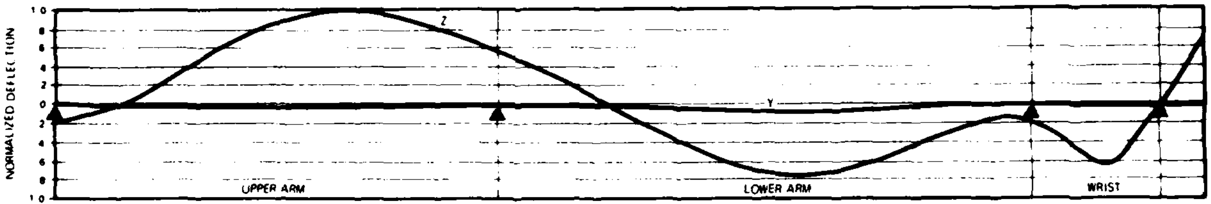

FREQ. = 50.5 Hz

FIG. 6c RMS ARM NORMAL MODES (Camera at Wrist)

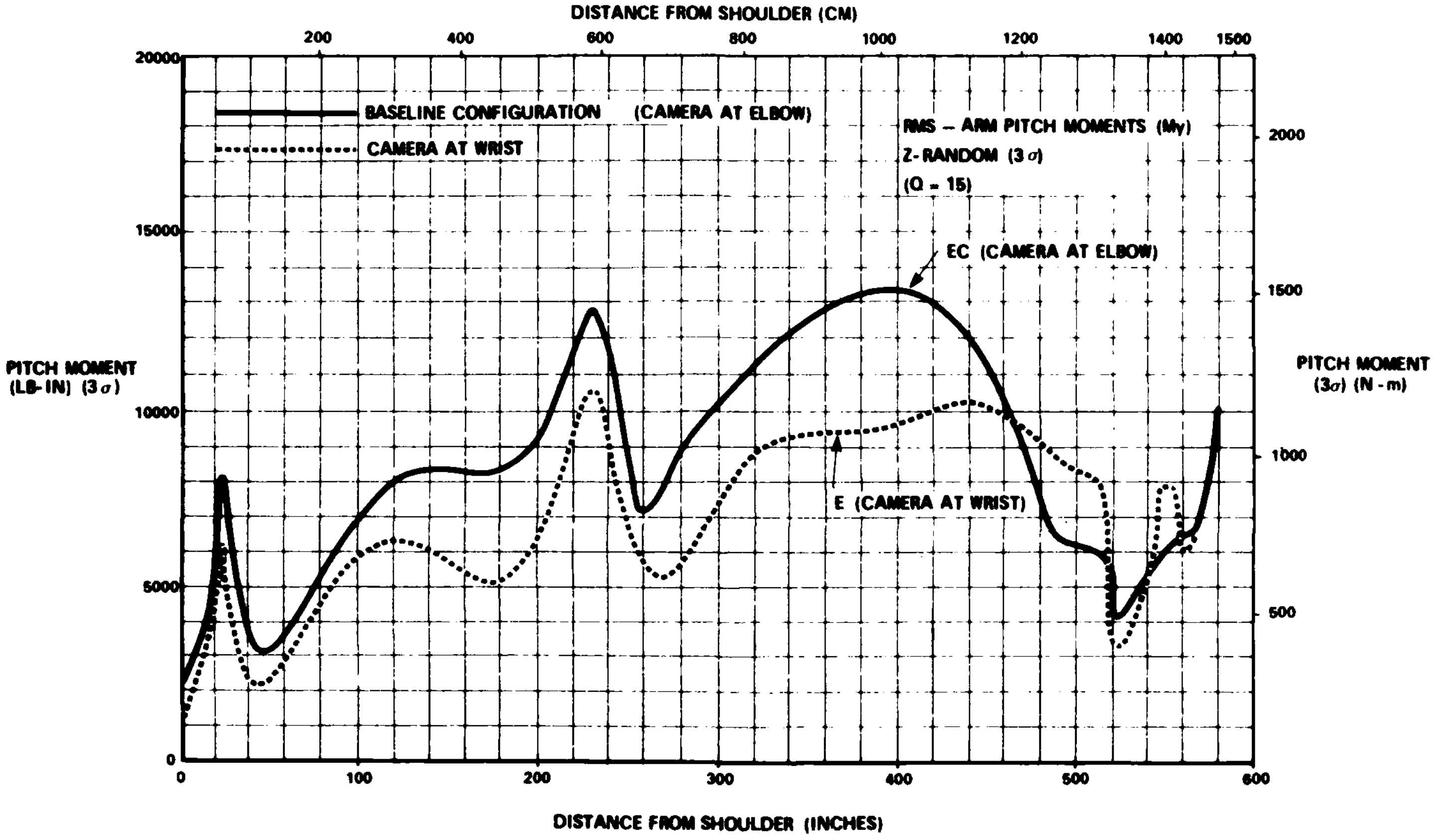

FIG. 7 BENDING MOMENTS ALONG THE ARM

The apparent-inertias for the arm joints are:

Shoulder Joints = 1196.5 Kg-m^2
(882.5 lb-ft-sec^2)

Elbow Joint = 559.3 Kg-m^2
(412.5 lb-ft-sec^2)

Wrist Joints = 193.9 Kg-m^2
(143.0 lb-ft-sec^2)

A finite-element model of a joint gearbox has been developed; the model for the shoulder-pitch gearbox is shown in Figure 8, as an example. (Another method of modelling the effects of a gear-train is described in Ref. 10 and will not be discussed here.)

A symmetric "tree" of beam-elements is attached to Node 1 of the baseline model. Pin connections at nodes 103 and 113 produce a mechanical ratio of 40:1 for each branch. A small mass (0.5 Kg or 1.1 lb) is lumped at each of the nodes 106, 107, 116 and 117 so that the apparent inertia at node 1 of beam 1-2 equals the apparent inertia of the gearbox. The "ground" of the "tree" is attached at node 110, a short distance below node 1 in the baseline model. The "tree" now has the desired feature that a moment applied at node 1 of beam 1-2 produces a reaction at node 110 of beam 1-110 equal to the applied moment within engineering accuracy; the reaction is 41/40 times the applied moment, (instead of 1841/1840, the actual ratio) an error of 2.5%. A higher mechanical ratio in the "tree" would reduce the error at the risk of introducing numerical computational problems. The choice of 40:1 has been made as an acceptable compromise and it also represents the gear-ratio of the differential planetary drive. The beam 104-108 at node 104, and beam 114-118 at node 114, are pinned about Y-axis. The connections 100-105 and 115-120 are very low stiffness torsional springs. These are necessary to prevent rigid-body singularities and do not affect the basic structural characteristics of the model.

The results for the base-line model, enlarged to include gear-train models at shoulder-pitch, elbow-pitch and wrist-pitch joints are presented below.

4/mcs490/6

The frequencies and mode shapes of the system are:

FREQUENCY (Hz.)	MODE
4.8	Wrist-Joint (Gear-Train)
5.7	Elbow Joint (Gear-Train) Rotational Mode
7.2	Shoulder Joint (Gear-Train) Rotational Mode
8.6	Y-mode
10.0	Y-mode
11.2	Y-mode
17.3	Y-mode
18.1	Z-X mode
25.9	Z-mode
30.7	Y-mode
34.1	Z mode
43.5	Y-Z mode
45.4	Z-Y mode
52.1	Z mode
54.8	Y-Z mode
59.9	Z-mode
74.8	Y-mode
82.8	X-Y mode
93.0	Z-mode

The first three modes are the local rotational modes of the shoulder, elbow and wrist joints in which the gear-train elements undergo large rotations. The frequencies for these modes are well below the lowest frequency of the random input. Other frequencies (and mode-shapes) are very close to those for the baseline model.

The response moments, My, at some selected locations are compared with those of the baseline model in Table 3. A plot of My moments along the arm is shown in Figure 9.

There is good agreement between the two sets of results. The elbow and wrist joints loads are within 5%. In some regions the percentage difference of loads is large; however, the loads there are small to begin with. Also, the differences between the results of the two models generally increase along the arm towards the wrist region. This may be explained by the fact that the effective inertias of wrist joints are much lower than those of other joints; the assumption of structural continuity for these joints introduces larger errors.

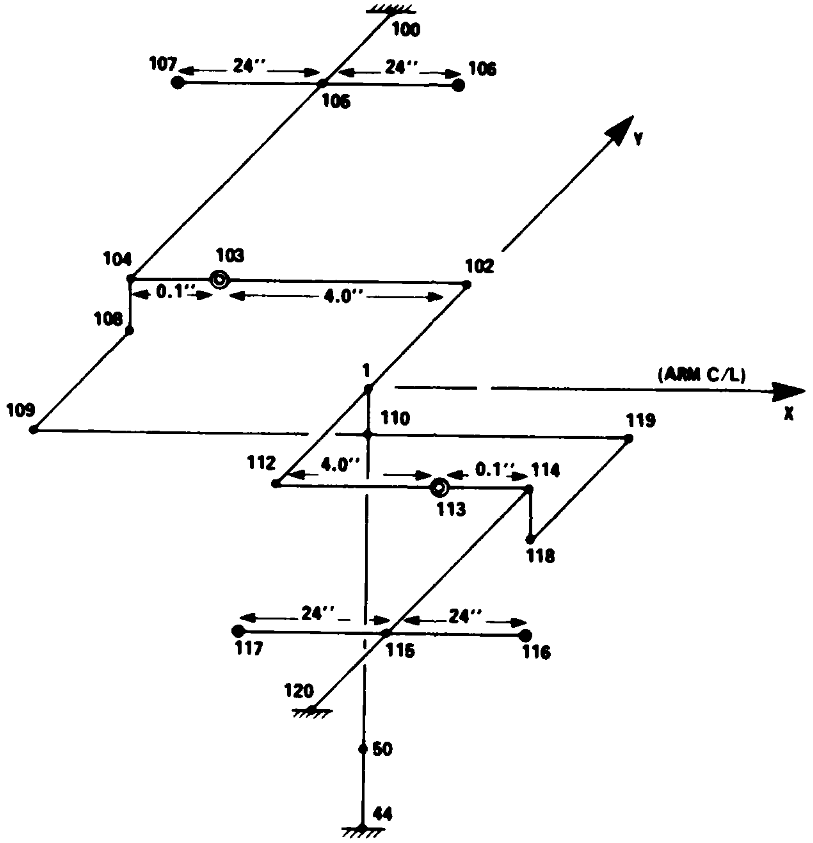
100
107
24"
24"
106
105
Y
104
103
102
0.1"
4.0"
108
1
(ARM C/L)
X
109
110
119
112
4.0"
0.1"
114
113
118
24"
24"
117
115
116
120
50
44

WEIGHT ON NODES 106, 107, 116, & 117 = 1.1 LBS.

FIG. 8 GEARBOX MODEL (SHOULDER PITCH)

TABLE 3

PITCH, My, MOMENTS (N-m) FOR Z-INPUT

(3-SIGMA VALUES)

JOINT	BASELINE MODEL	WITH GEARTRAIN MODELS	% CHANGE
Shoulder (Node 1)	234 (2068)	257 (2272)	9.8
Mid-Section - Upper Boom (Node 7)	950 (8410)	917 (8113)	-3.5
Elbow (Node 14)	886 (7839)	922 (8162)	4.1
Mid-Section - Lower Boom (Node 20)	1496 (13245)	1378 (12200)	-7.9
Wrist (Pitch) (Node 34)	588 (5207)	606 (5363)	3.0
Wrist (Yaw) (Node 28)	702 (6216)	663 (5866)	-5.6
Wrist (Roll) (Node 29)	1155 (10223)	1179 (10435)	-2.1

Note: The numbers in parenthesis are in lbf-in.

4/mcs490/11

TABLE 4

MODAL Q's FOR SET A AND SET B

FREQUENCY	MODAL Q FOR SET A	MODAL Q FOR SET B
25.0	18.5	25.0
34.2	8.3	10.4
41.2	22.2	32.3
44.6	12.0	15.9
51.9	11.9	24.4
57.8	16.1	22.7
92.8	8.7	11.4
97.1	16.7	22.4

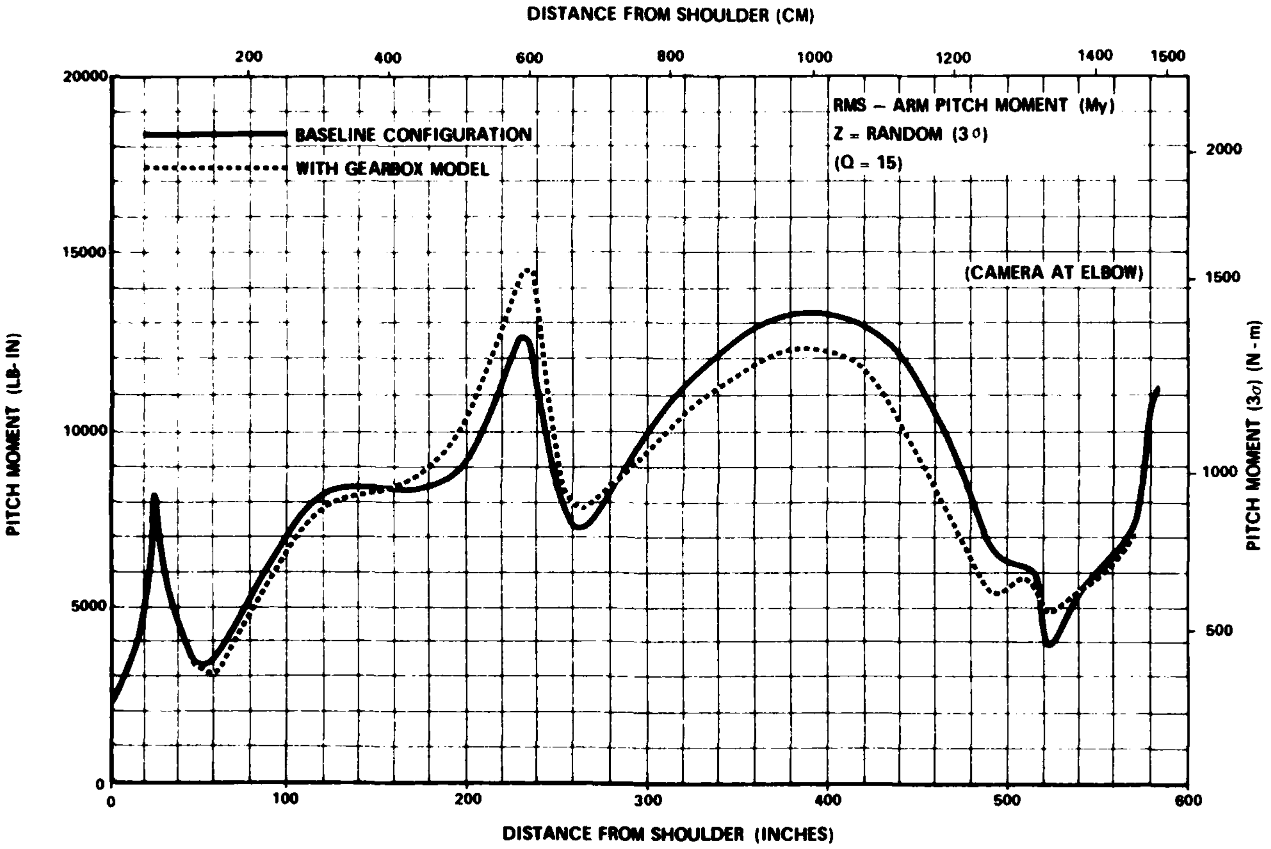

FIG. 9 BENDING MOMENTS ALONG THE ARM, WITH & WITHOUT GEARBOX MODEL

A test has also been conducted to determine the dynamic response characteristics of a joint. The shoulder pitch joint was selected for this test. The test results indicated that no resonant frequencies of the gearbox or the joint could be identified in the frequency range of 5-100 Hz. The tests also confirmed that the gearbox transmitted loads as a "continuous" structure above 5 Hz.

(b) Damping

The stowed arm system has three regions (sub-structures) where damping characteristics can be separately identified. The damping characteristic for each substructure can be defined in terms of a "loss-factor" which is related to viscous-damping by the relationship: loss factor = 1/Q.

4/mcs490/7

i) The retention system which is provided by the Orbiter contractor. The loss-factor for this structure is estimated to be between 0.1 (Q = 10) and 0.125 (Q = 8).

ii) The Arm joint structures which consist of metallic components, bolted together. Some friction losses can be expected at the bearings and the geartrains. However, the structural elements are stiffness-designed and stress-levels are generally small under the expected vibratory loads. A loss-factor of 0.067 (Q = 15) to 0.1 (Q = 10) is estimated for these components.

iii) The arm booms are expected to have very low energy dissipation characteristics. A loss factor of 0.0067 (Q = 150) to 0.01 (Q = 100) is estimated for these components.

The damping matrix can be added to the equations of motion as an imaginary quantity.

The solution can be obtained again in terms of normal modes. However, the eigenvalues and eigenvectors are now complex (Ref. 6).

The Q for each mode can be computed from the complex eigenvalue. NASTRAN has been used to compute the eigenvalues and damping Q's of each mode. These modal Q's have then been used for the baseline model.

Results for two sets of values of Q's for substructures are presented here. The two sets are:

Set A (nominal expected Q's of substructures):

Arm booms, $Q_A = 100$

Retention fittings, $Q_R = 8$

Joint structures, $Q_j = 10$

Set B (highest expected Q's of substructures):

Arm booms, $Q_A = 150$

Retention fittings, $Q_R = 10$

Joint structures, $Q_j = 15$

The frequencies and modes shapes significant for Z-inputs, and the modal Q's are given in Table 4.

The response moments, My, along the arm for Set A and Set B data are compared with those of the baseline model in Table 5.

The results show that the Set A data, which correspond to nominal expected damping, produce loads which are very close to the baseline results where Q = 15 was assumed for all modes.

(c) Effect of Uncorrelated Input

The random input to the system is applied at four discrete locations. The input has been assumed to be spatially correlated for the baseline model. This is equivalent to assuming that the system is mounted on a rigid platform which is providing the acceleration input.

However, since the attachment points are far apart along the longeron and the orbiter structure is flexible, it is reasonable to question the assumption of spatial correlation of input. A study has been made to evaluate the effect of uncorrelated inputs.

TABLE 5

PITCH, My, MOMENTS (N-m) AT DIFFERENT POINTS ON THE ARM (Z-INPUT, 3-SIGMA VALUES)

LOCATION	BASELINE (Q = 15, ALL MODES) My	SET A My	SET A % VARIATION FROM BASELINE	SET B My	SET B % VARIATION FROM BASELINE
1. Shoulder-pitch joint (node 1)	886 (7840)	824 (7295)	-6.9	952 (8429)	7.5
2. Mid-section upper arm boom (node 7)	1497 (13250)	1583 (14014)	5.8	1845 (16333)	23.3
3. Elbow joint (node 14)	886 (7840)	823 (7285)	-7.0	952 (8427)	+7.5
4. Mid-section lower arm (node 20)	1497 (13250)	1583 (14014)	+5.8	1845 (16333)	+23.3
5. Wrist-pitch joint (node 34)	588 (5208)	563 (4985)	-4.3	671 (5940)	+14.0

Note: The numbers parentheses are in lbf-in.

TABLE 6

PITCH, My, MOMENTS (N-m) DUE TO CORRELATED/UNCORRELATED Z-INPUTS, (Q = 15 ALL MODES) RMS VALUES

CASE	A	B		C		D		E		F	
	CORRELATED (1111)	(1-1-1-1)		(1-1-1-1)		(1-1-1-1)		(1-1-1-1)		(1-1-1-1)	
NODES	My	My	%	My	%	My	%	My	%	My	%
1	80 (708)	95 (838)	18	95 (840)	18	98 (863)	21	98 (871)	33	96 (851)	20
7	324 (2866)	369 (3270)	14	393 (3480)	21	387 (3424)	19	389 (3440)	20	398 (3524)	23
14	297 (2628)	323 (2857)	9	287 (2537)	-4	287 (2537)	-5	281 (2488)	-1	276 (2439)	-1
20	519 (4594)	706 (6253)	36	446 (3945)	-15	485 (4291)	-7	535 (4736)	3	420 (3714)	-20
34	199 (1763)	230 (2037)	16	184 (1625)	-8	205 (1818)	3	212 (1878)	7	181 (1598)	-10
28	235 (2084)	256 (2269)	9	233 (2058)	-1	263 (2329)	12	265 (2345)	13	234 (2067)	-1
29	380 (3366)	336 (2977)	-11	389 (3443)	2	334 (2958)	-12	390 (3454)	3	332 (2943)	-11

Note: The numbers in parentheses are in lbf-in.

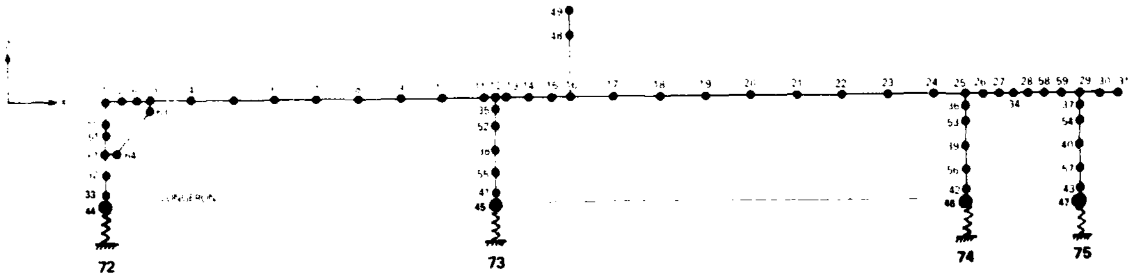
49
48
3
14
15
16
17
18
19
20
21
22
23
24
25
26
27
28
58
59
29
30
31
34
35
52
55
45
36
53
39
56
42
46
37
54
40
57
43
47
64
33
44
72
73
74
75

FIG. 10 MATH MODEL STOWED ARM (RMS) FOR UNCORRELATED INPUTS
(Camera at Elbow)

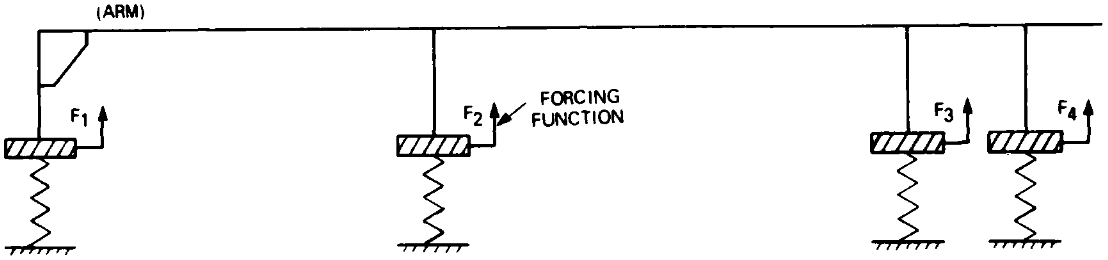
(ARM)
F1
F2
FORCING FUNCTION
F3
F4

(NEGATIVE FACTOR INDICATES 180° OUT-OF-PHASE RELATIONSHIP)

	F_1	F_2	F_3	F_4	
CASE A:	1	1	1	1	(CORRELATED)
CASE B:	1	−1	−1	1	
CASE C:	1	1	−1	−1	
CASE D:	1	−1	1	−1	
CASE E:	1	−1	1	1	
CASE F:	1	1	−1	1	

FIG. 11 COMBINATIONS OF FORCING FUNCTIONS CONSIDERED

(d) The Model for Uncorrelated Inputs

The input is specified in terms of acceleration p.s.d. The uncorrelated inputs can be handled more easily if the problem is reformulated and the input applied as a force p.s.d. This has been done by modifying the baseline model to the one shown in Figure 10.

The baseline model is attached to ground at nodes 72, 73, 74 and 75 (instead of nodes 44, 45, 46 and 47). Very large masses are lumped at node 44, 45, 46 and 47 (9072 Kg or 20,000 lbs. each). Low stiffness springs are introduced between the nodes 44 and 72, 45 and 73, 46, 74, 47 and 75. The additional masses and springs introduce new-order low frequency modes of the system (between 0.3 Hz and 1 Hz), leaving the modes and frequency of the main structure (above the nodes 44, 45, 46 and 47) practically unchanged. The input force p.s.d. is applied to the nodes 44, 45, 46 and 47. Only the masses lumped at nodes 44, 45, 46 and 47 need be considered to calculate the force p.s.d. from the acceleration p.s.d. Because of large masses at nodes where the forces are applied, the dynamic effects of the relatively small mass of the Arm structure can be neglected.

4/mcs490/8

(e) Loads with Uncorrelated Inputs

The system is now driven by independent forcing functions applied at nodes 44, 45, 46 and 47. For this study a 180° out-of-phase relationship between forcing functions has been assumed. Figure 11 shows the different combinations of forcing functions studied. Case A is the correlated input condition (baseline).

The response moments, My, produced in the structure for uncorrelated inputs (Case A to F, Figure 11) are shown in Table 6. The results show that there is a general increase of loads for Case B of uncorrelated inputs. For Cases C to F some loads go up and some go down. The effect of uncorrelated inputs is to excite a different set of modes from that of "correlated" inputs.

No data from the Orbiter are available yet as to which case of uncorrelated inputs is more realistic. In absence of this information, the baseline model with correlated inputs has been used.

CONCLUSIONS

The dynamic behaviour of Mechanical Arm of the Shuttle Remote Manipulator System in stowed configuration in the Orbiter, posed some special problems. An overview of the design-process and analysis undertaken to arrive at a satisfactory solution has been presented here. The objective of keeping the on-orbit performance as the primary design-driver for the structure has been met.

ACKNOWLEDGEMENTS

The Remote-Manipulator System for the U.S. Space Shuttle is being designed and developed by Spar Aerospace under contract (number 15SR.31053-7-3839) to National Research Council of Canada (NRCC) as a NASA/NRCC Cooperative Program. The authors would like to thank these organizations for permission to publish this paper.

REFERENCES

1. Kumar, P., Truss, P., Wagner-Bartak, C.G., "System Design Features of the Space Shuttle Remote Manipulator" Proceedings, Fifth World Congress on Machines and Mechanisms, July, 1979, Montreal, Canada.

2. Faget, M.A., Cohen, A., "Concept Design of the Payload Handling Manipulator System" JSC-09709, June 1975, NASA Johnson Space Centre, Houston, Texas.

3. "Contract End-Item Specification: Remote Manipulator System for the Space Shuttle Orbiter Vehicle-Part I", SPAR-SG.392, Spar Aerospace Limited, Toronto, Canada.

4. Doetch, K., "The Remote Manipulator System for the Space Shuttle Orbiter", September, 1977, Jahrestagung 1977 of the Deutsche Gasellschaft fur luft-und Raumfart eV, Berlin, W. Germany.

5. Przemieniecki, J.S., "Theory of Matrix Structural Analysis", McGraw-Hill Book Co., 1968.

6. Hurty, W., Rubenstein, M., "Dynamics of Structures" Prentice-Hall Inc., 1964.

7. Crede, C.E., "Failure Resulting from Vibration" in "Random Vibration - Vol. II", (Ed. Crandall S.H.) M.I.T. Press, 1963.

8. MRI/STARDYNE for Scope 3.4 Operating System, User Information Manual, Control Data Corporation.

9. MSC/NASTRAN User's Manual, 1976, The MacNeal - Schwendler Corporation.

10. Gossain, D.M., "Effect of a High Gear-Ratio Joint on Dynamics of an Articulated Structure". Canadian Aeronautics and Space Journal, Vol.25, No.3, Third Quarter, 1979.

STRUCTURAL DYNAMIC CHARACTERISTICS
OF THE
SPACE SHUTTLE REACTION CONTROL THRUSTERS

Gersten L. Schachne and Jeffrey H. Schmidt
The Marquardt Company
Van Nuys, California

Several configurations of the reaction control thrusters for the Space Shuttle Orbiter were structurally analyzed using finite element models. Acceleration responses and frequencies from these analyses were compared with those recorded during random vibration tests. Various methods for determining structural damping were considered from which one, comparison of test and analytic g_{rms}, was selected.

The resulting analytical dynamic characterization of the structure led to successfully designed and qualified thrusters.

INTRODUCTION

Space Shuttle Mission

The primary design and operations goal for the Space Shuttle Program is to provide routine access to space. The Shuttle flight system is composed of the Orbiter, an external tank that contains the ascent propellant to be used by the Orbiter main engines, and two solid rocket boosters. The Orbiter and solid rocket boosters are reusable; the external tank is expended in each launch (Figure 1). The nominal duration of each mission is seven (7) days. This can be increased to 30 days if the necessary consumables are added. A typical mission is shown in Figure 2.

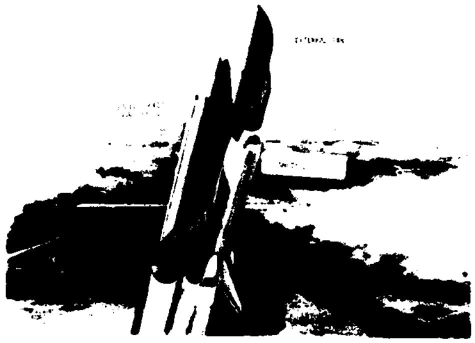

Figure 1. Space Shuttle Launch Configuration

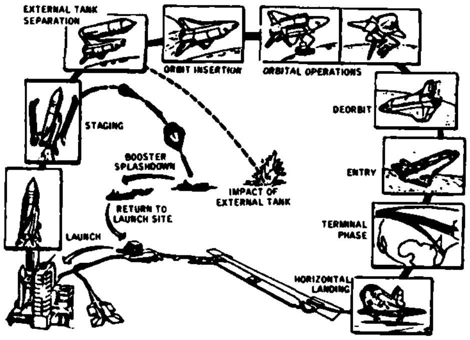

Figure 2. Typical Space Shuttle Mission Profile

Reaction Control System

The method of controlling the Orbiter (pitch, yaw, roll) and providing its 3-axis translational velocity at orbit insertion, during its flight phase and upon reentry is performed by the Reaction Control System (RCS). This system is used for external tank separation and also serves as a backup for the Orbital Maneuvering System (OMS) for the de-orbit burn.

The RCS contains 38 primary thrusters and 6 smaller vernier thrusters (Figure 3). The forward fuselage of the shuttle contains the forward propulsion modules which have 14 primary and 2 vernier thrusters. The two aft propulsion pods of the shuttle each contain 12 primary and 2 vernier thrusters. These two pods are located on either side of the aft section under the vertical stabilizer. The thruster

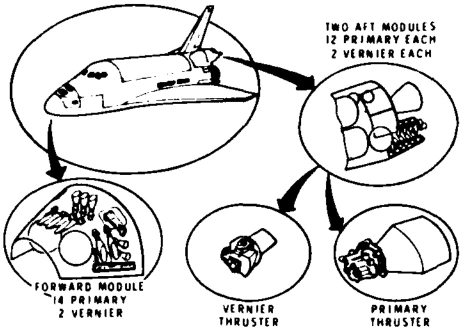
TWO AFT MODULES
12 PRIMARY EACH
2 VERNIER EACH
FORWARD MODULE
14 PRIMARY
2 VERNIER
VERNIER THRUSTER
PRIMARY THRUSTER

Figure 3. Reaction Control System

propellants are monomethylhydrazine as the fuel and nitrogen tetroxide as the oxidizer. The propellants are earth storable and are hypergolic (ignite upon contact with each other).

There are several different thruster configurations, depending upon where they are located in the fuselage. These configurations are categorized as non-scarfed, short-scarfed, and long-scarfed thrusters depending upon the contour of the exit nozzle.

Thruster Structural Loads

The RCS thrusters are subjected to a variety of structural loads during each Space Shuttle mission. The mission profile necessitated an investigation of the following external conditions:

A. Aerodynamic Loads
B. Shock Loads

1. Transportation (packaged)
2. Ground Handling (unpackaged)
   a. Bench Handling
   b. Basic Design
   c. Hoisting
3. Ferry Flight (nonoperating)
   a. Maneuvering
   b. Landing
4. Orbital Flight (operating)
   a. Acceleration
   b. Transient Loading

C. Vibration

1. Transportation (packaged)
2. Orbital Flight (Nonoperating)
   a. Aero-Acoustics
   b. Random Vibration

STRUCTURAL ANALYSIS

Analytical Dynamic Characterization

The initial goal of the analysis was to completely describe the structural dynamic characteristics of a typical space shuttle reaction control thruster.

The task was initiated with the following steps:

1. Construct a finite element model of a prototype thruster that would be based strictly on prototype drawings.

2. Construct the mathematical model in sufficient detail to

   a. Duplicate all relevant load paths,

   b. Duplicate all structural thicknesses and dimensions.

3. Accurately represent the weight, C.G. and stiffness of the engine and major engine structural components.

The above steps were deemed necessary to predict actual hardware modes and frequencies. Once an adequate model was created, all dynamic load environments were considered with the result that the random vibration environment was far more severe than all others.

Non-Scarf Primary Engine Details

Several different engine configurations were analyzed.

The engine selected for further detailed discussion is a non-scarf primary engine. It is this type of engine that uncovered the most design deficiencies, and provided the most difficult analysis task. A schematic of a non-scarf engine is shown in Figure 4 and illustrates all major structural components that were included in the dynamic model. Of noteworthy importance are the following items:

1. Chamber, nozzle
2. Injector, mounting flange
3. Oxidizer and fuel valves
4. Junction Box
5. P-C Transducer

The random vibration environment for this engine is shown in Figure 5.

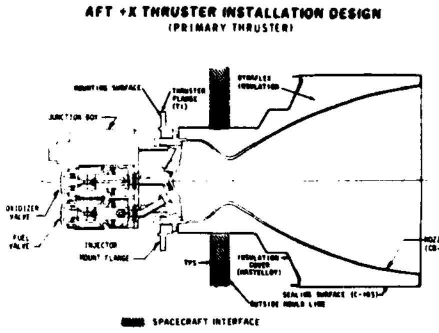
AFT +X THRUSTER INSTALLATION DESIGN
(PRIMARY THRUSTER)
MOUNTING SURFACE
THRUSTER FLANGE (T1)
DYNAFLEX INSULATION
JUNCTION BOX
OXIDIZER VALVE
FUEL VALVE
INJECTOR MOUNT FLANGE
TPS
INSULATION COVER (HASTELLOY)
NOZZLE (CB-103)
SEALING SURFACE (C-103)
OUTSIDE MOULD LINE
SPACECRAFT INTERFACE

Figure 4. Non-Scarf Primary Engine

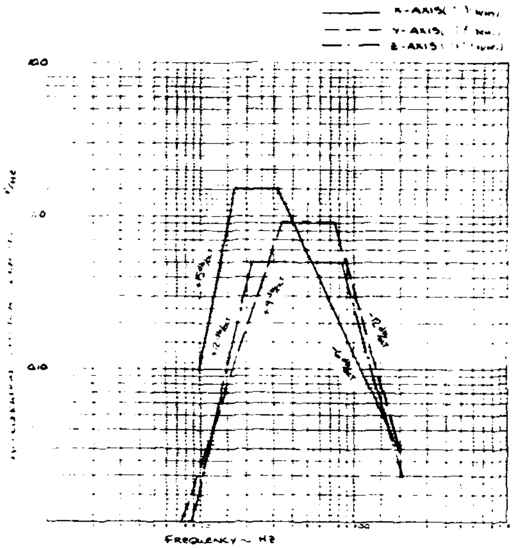

Figure 5. Random Vibration Environment

Structural Model Description

The structural dynamic model (using the Stardyne finite element computer program) attempted, as outlined previously, to duplicate the actual hardware--a typical non-scarf aft primary engine. The model was composed of the following elements, etc:

1. Total number of model node points = 135
2. Total number of degrees of freedom =810
3. Number of general beams with 6 D.O.F. at each end = 26
4. Number of rigid beams, or extensions = 30
5. Number of triangular plate elements =30
6. Number of rectangular plate elements = 78
7. Number of stiffness matrix additions =1
8. Number of nodal points with mass (weight) = 103

No weight inertias were included.

Item 7, a stiffness matrix addition, represents the entire injector to chamber, injector to valve standoff and injector to mount bolt interfaces. This assemblance of stiffness coefficients was derived from a detailed axisymmetric finite element model of the aforementioned structural components. See Figure 6.

Computer plots from two different axis directions of the modeled primary non-scarf engine are shown in Figures 7 and 8. Superimposed on these plots (shown by dashed lines) is the first frequency and mode shape of the engine.

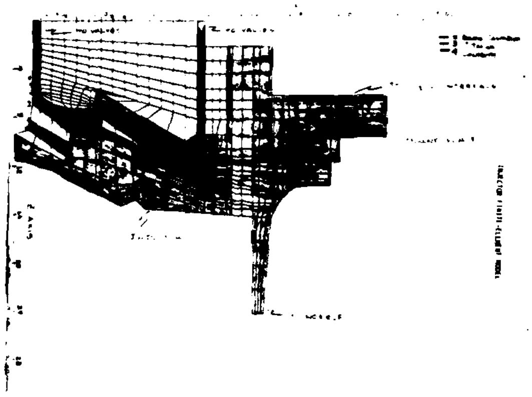

Figure 6. Injector Finite-Element Model

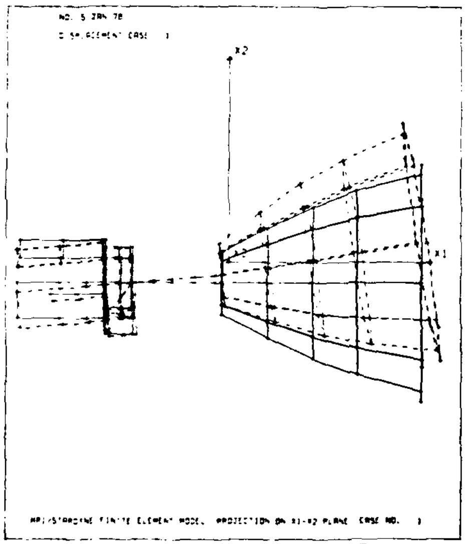

Figure 7. Computer Plot, X1-X2 Plane

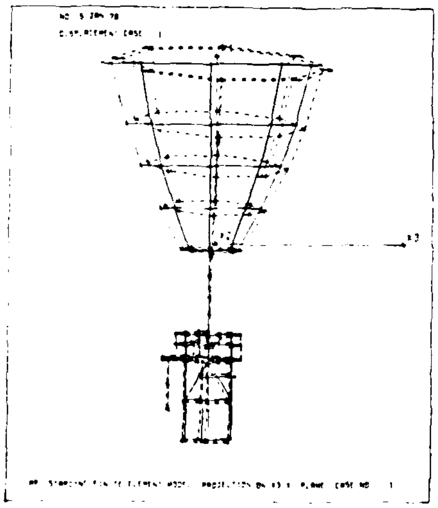

Figure 8. Computer Plot, X1-X3 Plane

TABLE 1

Mode and Frequency Summary of Non-Scarf, Aft Primary Engine

Mode Number	Frequency (Hz)	Mode Description
1	216.3	1st Nozzle, Y Bending
2	216.5	1st Nozzle, Z Bending
3	378.5	Local Nozzle Bending
4	486.5	Local Nozzle Bending
5	612.2	Z Valve, Components Mode
6	624.0	Y Valve, Components Mode
7	678.3	J-Box, Y Mode
8	699.8	J-Box, Z Mode
9	868.6	Higher Order Mode, Valves, etc.
10	949.2	Local Nozzle Bending
11	956.0	Local Nozzle Bending
12	1120.1	Local Nozzle Bending
13	1121.5	Local Nozzle Bending
14	1197.8	Axial Mode of Engine
15	1214.9	Local Nozzle Bending
16	1266.7	Higher Order Mode, Valves, etc.
17	1355.5	Local Nozzle Bending
18	1432.0	Local Nozzle Bending
19	1506.3	Local Nozzle Bending
20	1622.5	Local Nozzle Bending
21	1854.0	Local Nozzle Bending
22	1951.7	Higher Order Mode, Valves, etc.

Modal Analysis Results

Results obtained from the dynamic model consisted of 22 natural frequencies and mode shapes contained within the input power spectral density frequency range of 20-20,000 Hz. These are listed in Table 1 with a brief mode shape description.

Random and Sine Analyses

At this point, both random and sine testing and analysis were considered for a clearer test to analytic comparison. Though sine was not a critical environment, sine testing was considered to be the more effective means of determining natural frequencies and giving indications of modal damping used subsequently for the more critical random environment.

Analytically, sine was chosen as the first dynamic environment to be investigated for the following reasons:

1. It was hypothesized that "close" natural frequencies could be distinguished by a sweep type of analysis. A random type of analysis, on the other hand, tends to lose frequencies because of modal overlap.
2. Sine response peaks could easily be distinguished and thus damping would be proportional to the peak response at a resonant frequency.

However, once random analysis reports were obtained via PSD response plots, identical response peaks were observed. The random package used via Stardyne included cross product terms [1]. The same random analysis was then run but with the added simplification that all cross product terms in the random analysis were discarded [2]. All overall g_{rms} values from both sine and random analysis were unchanged, which led to the conclusion that modal overlap did not occur. All further random analyses used the latter simplified and more cost effective approach.

Random Results

Analytical effort culminated in the production of PSD plots at nodes having the highest g_{rms} responses, since these locations would be the most suited for test comparison. At the same time, damping was relatively unknown, therefore all analyses were performed at a constant, arbitrary 5% damping for all natural frequencies and modes. From the twenty-two natural frequencies within the environment spectrum only five frequencies dominated the total responses of various structural components, and were later verified by testing.

Typical analytical PSD plots at maximum g_{rms} response locations are compared with their comparable test PSD plots at two nodes in Figures 9 to 12 and illustrate that essentially single degree of freedom systems exist and simulate the entire non-scarf engine. The structural response at these 5 frequencies dominated the thruster design loads. These one degree of freedom systems are as follows:

1. Axial (1300 Hz)
2. Lateral (Y) for valves,etc. (600 Hz)
3. Lateral (Z) for valves, etc.(600 Hz)
4. Lateral (Y) for nozzle (220 Hz)
5. Lateral (Z) for nozzle (220 Hz)

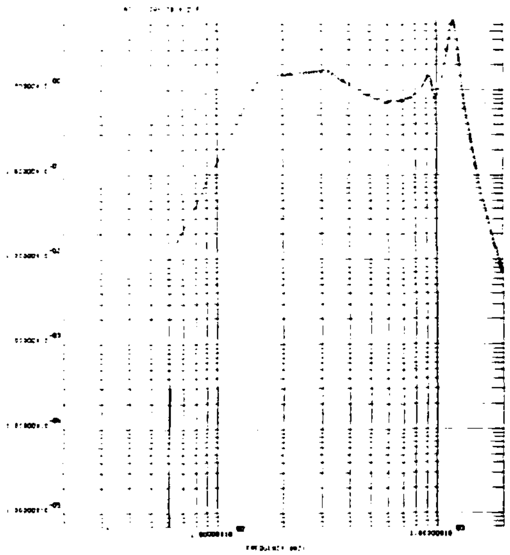

Figure 9. Analytic Response Plot (Node 228)

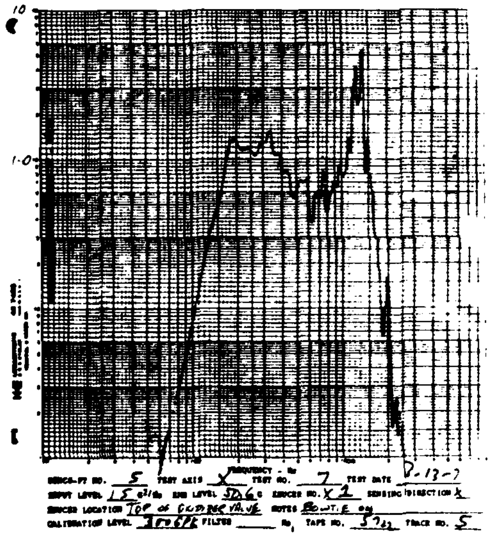

Figure 10. Test Response Plot (Node 228)

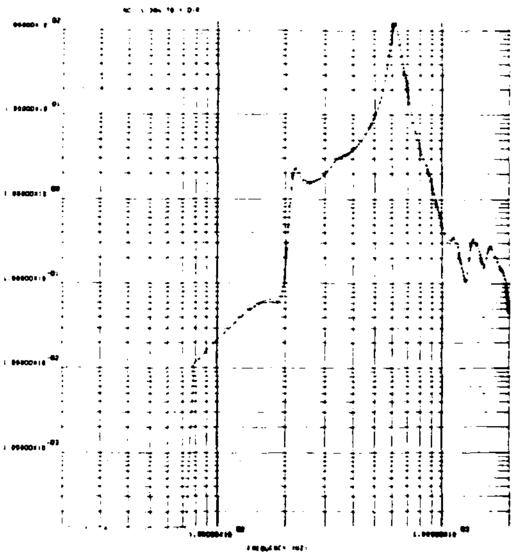

Figure 11. Analytic Response Plot (Node 35)

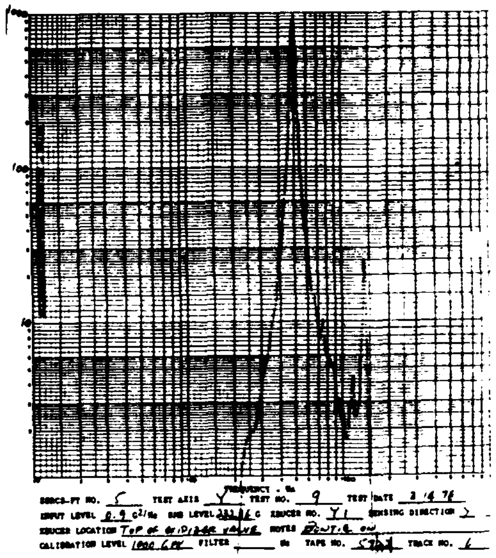

Figure 12. Test Response Plot (Node 35)

Effort was now directed to confirm that model predictions were indeed accurate by accurate by actual hardware testing. Testing would not only confirm model validity by mode and frequency comparison but would allow a means to evaluate thruster damping characteristics that were required for an accurate displacement, acceleration and internal load assessment for further design development.

VIBRATION TESTS

Fixturing

The three different configurations of the primary thruster (non-scarfed, short-scarfed and long-scarfed) and the long-scarfed vernier thruster were vibration tested during the development phases of the program.

Two vibration fixtures were used for each configuration to test the engine along its lateral and thrust axes. Figures 13 and 14 show examples of the long-scarfed thruster in its fixtures. Two fixtures were used so that the engine need only be vibrated on the head of the shaker. This did away with the high frequency problem associated with trying to control the input to a test item attached to a massive slip table.

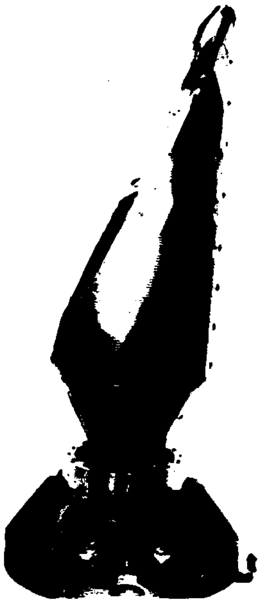

Figure 13. Engine in Thrust Axis Test Fixture

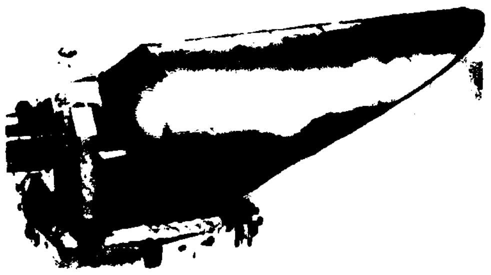

Figure 14. Engine in Lateral Axis Test Fixture

The engines were attached to the fixture with four bolts through a mounting flange. Torques on these bolts were determined by the amount of fixity needed to simulate the end conditions used in the structural analysis.

Vibration tests for all thruster configurations were conducted "hard-mounted" to the shaker head. However, the spectra for the forward thrusters were re-derived to simulate the impedance match between a "hard-mounted" and an "as-mounted" thruster in the Space Shuttle.

Control and Response Instrumentation

The input was controlled from the average of four accelerometers. These were located at points determined by a fixture survey to be best suited for minimizing fixture responses.

Response accelerometers were attached to the engine at a number of discrete points, which were chosen to match the same node points used in the structural model. Figures 15 and 16 show the locations of these accelerometers.

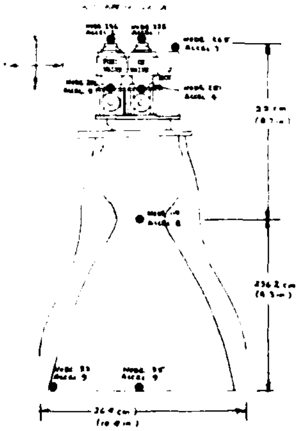

Figure 15. Accelerometer Locations

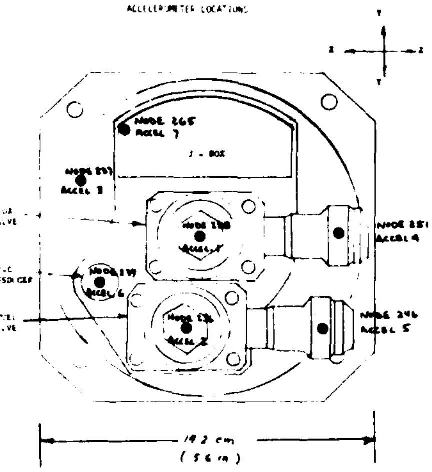

Figure 16. Accelerometer Locations

Strain gages had also been used in early tests to match experimental data with predicted data, but were soon dropped because they were hard to mount in areas of interest and were easily broken.

Resonant frequencies of components were determined in the early stages by running low level (2g and 5g) sine sweeps. A maximum response at a node would indicate presence of a resonance. Mode shapes were approximated by plotting acceleration vs. distance from a fixed support at a given frequency.

Test Tolerances

It was necessary during the testing phases to ensure that data reduction be consistent since a number of different outside test labs were used to test the thrusters. The tolerances on acceleration spectral density were as shown in Table 2:

TABLE 2

Test Tolerances

Spectrum Freq. Bandwidth	Nominal Filter Bandwidth	Tolerances
20-100 Hz	10 Hz or less	Plus 3 dB Minus 1.5 dB
100-350 Hz	25 Hz or less	Plus 3 dB Minus 1.5 dB
350-2000 Hz	50 Hz or less	Plus 3 dB Minus 1.5 db

Test Results

Acceleration spectral densities were plotted versus frequency from data recorded from the response accelerometers. RMS acceleration was also recorded.

Results of this data reduction are compared with the predicted responses in the next section to obtain modal damping.

Modal analysis using the Hewlett Packard 5451B Fourier Analyzer was also performed on the data to obtain damping. Results of using this technique and comparison with the method used in this paper are presented in the next section.

TEST TO ANALYTIC COMPARISONS - DAMPING

General Philosophy

The final result for any structural dynamic analyses is to accurately predict accelerations, displacements and internal loads. However, all analytical results depend directly upon structural damping which, without test results, can only be assumed. Loads, accelerations, etc., for a random environment are proportional to the square root of damping and vary directly with damping for a sine environment.

The general criteria used for interpretation of the resulting random laods were as follows:

1. All margin of safety based on yield shall use 3σ RMS loads.
2. All fatigue margins shall use 2.2σ RMS loads for the total number of vibration cycles and shall be compared directly to sine generated fatigue allowables.

The structural design repercussions of incorrect damping values were obivous; that is:

1. Using damping values that were too low led to an overweight design, but one with high positive margins.
2. Using damping values that were too high resulted in negative margins and possible structural failure.

All damping evaluations for this particular engine configuration made the following general assumptions:

For each engine type, i.e.,
1. long scarf primary engine,
2. short scarf primary engine,
3. nonscarf primary engine,
4. vernier engine,
damping values depended primarily on overall geometry, bolted joints and the insulation.

Within an engine type, any geometric variations would not change damping and, therefore, the design loads.

Methods of Damping Determination

Once it was established that a good comparison existed between analyses and test results for the primary frequencies and modes, several different schemes were evaluated to acquire damping for detail load generation. (See typical response plots illustrating the correlation between test and analytics, Figure 9 to 12). The methods considered were as follows:

1. Comparison of sine results
2. Comparison of peaks in the PSD plots
3. Comparison of g_{rms}
4. Using damping estimates directly from a Hewlett Packard technique of modal analysis.

Method 1 was discarded for the following reasons:

1. It was established early in testing that the amount of apparent damping was not linear to input level.
2. The sine requirement was not critical, thus overtesting for sine was ruled out.
3. Random was critical for yield and fatigue and would produce designing loads. Therefore, emphasis had to be placed upon matching random test results.

Method 1 was discarded because of the problem introduced by different bandwidth filters during data reduction. That is, the smaller the bandwidth filter, the higher the peak. Thus, comparison was difficult and rather meaningless.

Since g_{rms} will not vary with the filter bandwidths, but varies as the normal dispersion of random output, Method 3 was chosen. Method 4, which was relatively unknown, was also chosen for further evaluation.

Paramount to implementing Method 3, was matching test and analytic locations and choosing locations at which high g_{rms} values were expected. The locations for accelerometers were guided by preliminary random analyses that assumed 5% damping for all modes. The locations chosen were as shown in Figures 15 and 16.

Results of Selected Methods

The results of Method 3 are shown in Tables 3 to 5. These damping values were arrived at by a direct comparison of test to analytic PSD plots for g_{rms}. The following assumptions and/or corrections were made to the data:

1. Any frequency difference noted between test and analysis was taken into account by altering the analytically predicted g_{rms} as follows:

$$(g_A)_{new} = (g_A)_{old} \times \left[\frac{f_T}{f_A}\right]^{\frac{1}{2}}$$

g_A = g_{rms}, analytic

f_T = test frequency, Hz

f_A = analytic frequency, Hz

2. The major contribution to overall g_{rms} occurred at the fundamental frequency of that structural component. This assumption was met by placing the accelerometers at maximum response predicted locations.
3. Damping was then calculated by:

$$\zeta_T = \zeta_A \left[\frac{(g_A)_{new}}{g_T}\right]^2$$

TABLE 3

Determination of Damping, X-Input Direction

Structural Item	Model Node No.	Test Accel. No.	Frequency at Major Response (Hz)		G^*_{rms} (Absolute)		G_{rms} (Relative)		Damping
			Anal.	Test	Anal.	Test	Anal.	Test	(%)
Oxidizer Valve	228	1	1260	1350	45.9	50.6	20.0	24.7	3.5
Fuel Valve	236	2	1260	1350	47.8	55.0	21.9	29.1	3.0
Mount Plate	237	3	1260	1200	41.6	29.0	15.7	3.1	-
Oxidizer Inlet	251	4	1260	1000	46.0	37.0	20.1	11.1	-
Fuel Inlet	246	5	1260	1200	48.0	86.0	22.1	60.1	-
Top of P-C	239	6	900	900	43.4	53.0	17.5	27.1	2.1
Top of J-Box	265	7	1260	1350	44.7	38.0	18.8	12.1	13.0
Nozzle Throat	119	8	1260	1300	44.2	28.0	18.3	2.1	-
Nozzle End	33,35	9	1260	1300	63.8	74.0	37.9	48.1	3.2

* Read directly from PSD plots.

Average (Components) = 5.7%
Nozzle = 3.2%

TABLE 4

Determination of Damping - Y-Input Direction

Structural Item	Model Node No.	Test Accel. No.	Frequency at Major Response (Hz)		G^*_{rms} (Absolute)		G_{rms} (Relative)		Damping
			Anal.	Test	Anal.	Test	Anal.	Test	(%)
Oxizider Valve	228	1	620	500	114.0	233.0	86.2	205.2	0.71
Fuel Valve	236	2	620	500	115.8	216.0	88.0	188.2	0.88
Mount Plate	237	3	610	490	46.0	57.0	18.2	29.2	-
Oxidizer Inlet	251	4	610	500	55.4	85.0	27.6	57.2	-
Fuel Inlet	246	5	620	480	55.8	75.0	28.0	47.2	-
Top of P-C	239	6	620	500	83.4	109.0	55.6	81.2	1.90
Top of J-Box	265	7	660	500	170.2	158.0	142.4	130.2	4.53
Nozzle Throat	119	8	220	220	40.4	58.0	12.6	30.2	-
Nozzle End	33,35	9	220	220	42.3	41.0	14.5	13.2	6.03

Average (Components) = 2.01%
Nozzle = 6.03%

TABLE 5

Determination of Damping - Z-Input Direction

Structural Item	Model Node No.	Test Accel. No.	Frequency at Major Response (Hz)		G^*_{rms} (Absolute)		G_{rms} (Relative)		Damping
			Anal.	Test	Anal.	Test	Anal.	Test	(%)
Oxidizer Valve	228	1	610	500	88.0	163.7	66.5	142.2	0.90
Fuel Valve	236	2	610	520	99.2	181.6	77.7	160.1	1.00
Mount Plate	237	3	600	480	32.9	43.0	11.4	21.5	-
Oxidizer Inlet	251	4	600	480	36.8	70.0	15.3	48.5	-
Fuel Inlet	246	5	600	500	42.6	32.0	21.1	10.5	-
Top of P-C	239	6	610	490	60.9	98.0	39.4	76.5	1.07
Top of J-Box	265	7	600	480	63.2	83.0	41.7	61.5	1.84
Nozzle Throat	119	8	220	220	33.6	41.0	12.1	19.5	-
Nozzle End	33,35	9	220	220	46.1	43.0	24.4	21.5	6.44

* Read directly from PSD plots.

Average (Components) = 1.21%
Nozzle = 6.44%

TABLE 6

Hewlett Packard Technique of Modal Analysis Results

X-Axis Excitation		Y-Axis Excitation		Z-Axis Excitation	
Freq. (Hz)	Damping (%)	Freq. (Hz)	Damping (%)	Freq. (Hz)	Damping (%)
1180.0	0.96	228.1	1.68	234.7	1.86
1336.0	2.64	392.9	3.36	474.5	2.30
1396.9	3.03	520.7	3.98	780.6	2.70
		900.9	0.33	819.2	2.96

where:

ζ_T = test damping, %

ζ_A = assumed analytical damping, (5% for all frequencies)

g_T = test g_{rms}

Typical test and analytic plots used to compute average damping at each basic component frequency are shown in Figures 9 to 12. Damping values derived via application of Method 3 are shown in Tables 3-5, for each axis of excitation.

Method 4 results are as shown in Table 6. The results shown were obtained by using the same accelerometers and by exciting the engine at the engine mount with a low-level broad band spectrum of 1.0 g_{rms}. The modal frequencies, damping coefficients, and mode shapes were then extracted from the measured broad band transfer functions via an analytical curve fitting algorithm.

Method Comparison

The main objective for any test and analytic structural effort is to develop as good as correlation as posible such that various unknowns can be readily determined and used for further design iterations and/or changes.

In this particular application, Space Shuttle Reaction Control engines, it was imperative to develop an analytical dynamic characterization of a typical development engine and verify via testing. Only with good correlation can damping, an analytical unknown, be determined with any confidence. Having this parameter provides the means to a successfully designed qualification hardware.

Method 3 was chosen as the only viable approach and did allow a matching of analytical values to test. Method 4 may become extremely useful if predicted damping values can duplicate tested results via analytics. This could not be done for this application. The primary reason that this method was not as successful as the one used was because data could only be obtained at low input levels and not at levels of interest.

Comparison of damping results between Methods 3 and 4 is shown in Table 6 and illustrates the magnitude of error that could have been incorporated by using the results of Method 4.

CONCLUSIONS

1. Comparisons of frequencies and responses can be accurately made between test and analysis using only a random environment (as opposed to sine).
2. The reduction of structural characteristics of a complicated structure to a few major frequencies allowed for a simplified procedure to determine modal damping such that test to analytic comparison could be accomplished. Use of accurate mode, frequency and damping values thus led to a design that ensured structural integrity.
3. The value of any method used to predict damping for a dynamic environment is based on the ability to match actual test results. Therefore, it is concluded that the approach taken here was found to be the most useful one.

REFERENCES

1. W. C. Hurty and M. F. Rubenstein, "Dynamics of Structures", page 404, Eq. 11.78, Prentice Hall, Inc. Englewood Cliffs, N.J., 1965.
2. IBID, page 405, Eq. 11.79.

DISCUSSION

Voice: I am rather curious about that random vibration test spectrum. These thrusters are designed for multiple launches, what is the duration of the random vibration test?

Mr. Schachne: We qualify our thrusters for a total mission time of 34 minutes in each axis. We qualify them for 10 missions and then for another 25 missions so that when they are fully qualified they will have been exposed to 34 minutes of vibration along each of the three axes. That will represent a 100 missions which is a full qualification for a Space Shuttle mission.

Mr. Hosford (MBIS): Did you compare the peaks with $(g_{rms})^2$ for control?

Mr. Schachne: Yes we did because we gave quite a bit of thought to putting in the different peaks and rms values.

Mr. Schmidt: We found out that if we tried to compare peaks that it was very sensitive to the way that the test data were reduced, and it depended a lot on filter bandwidth. So the tighter the filter bandwidth, the larger the peaks and knowing that it was very hard to make a comparison. We found that g_{rms} was very insensitive to filter bandwidth so that's why we chose it.

Mr. Bingman (Air Force Flight Dynamics Laboratory): Were your values of 25 or above g_{rms} generated by the thrusters themselves?

Mr. Schmidt: No. The environments in the aft compartment were due to the main engine firing. Actually both the aft and forward compartment environments were due to the main engine firing. But the forward compartment was not near the main engines so all of its vibration input was along the longerons of the Space Shuttle. The aft engines were near the main engines so their inputs were mostly from acoustics.

Mr. Bingman: Was the acoustic environment from the launch environment or was it from the main engine firing?

Mr. Schmidt: The environments were from the main engine firing.

MODIFICATION OF FLIGHT VEHICLE VIBRATION MODES
TO ACCOUNT FOR DESIGN CHANGES

C. W. Coale and M. R. White
Lockheed Missiles and Space Company
Sunnyvale, California

A method of incorporating spacecraft structural changes by modifying existing flight vehicle modes is presented. The method is applicable for arbitrary changes of mass, stiffness, and structural configuration in a limited area of the vehicle.

INTRODUCTION

The determination of detailed dynamic load distributions in flight vehicles during critical flight events is a major task in any present-day aerospace vehicle program. A typical analysis may involve the following steps: (1) Formulation of a finite element model of the basic spacecraft, (2) Determination of cantilevered normal modes and interface constraint modes of the spacecraft, (3) Modal synthesis of additional subsystems onto the spacecraft, (4) Modal synthesis of the complete spacecraft to the booster to determine free modes of the flight vehicle, (5) Transient response calculations in modal generalized coordinates, (6) Back transformation to determine vehicle structural accelerations, (7) Calculation, using a loads model, of vehicle deflections and internal loads.

The process is both costly and time consuming; and it may involve several aerospace companies. There is thus a continuing need for streamlining and improving the efficiency of this "load cycle analysis". Quite commonly, subsequent to the completion of a load cycle analysis, design modifications are made to the spacecraft. A new load cycle is then required to assess the effects of these design changes on vehicle response and loads.

It is possible, however, to bypass a portion of the new analysis cycle. The present paper describes a method of incorporating spacecraft changes by directly modifying existing flight vehicle modes. This has more significance than might be supposed. The original modes of the spacecraft are determined from the finite element model using a large-scale, iterative eigensolver – a relatively costly process. Also, as pointed out above, transfer of data between several companies may be involved in the load cycle. The present method can be used by the spacecraft contractor to directly determine new flight vehicle modes, bypassing both of these bottlenecks, with savings of both time and computer costs.

MODE MODIFICATION

The mode modification method consists of expressing the new vehicle modes in terms of the set of previous vehicle modes plus a set of constraint functions associated with the area of the vehicle which is to be modified. An eigenvalue problem for the new modes is formulated. In this eigenvalue problem the finite element mass and stiffness matrices in the area of modification are explicitly displayed and may be modified in any arbitrary manner – the method is not a perturbation method. Solution of the eigenvalue problem yields directly a set of new system modes of the modified flight vehicle.

Consider now the procedure in more detail. The complete flight vehicle of Fig. 1 consists of a spacecraft and booster combination. For this vehicle, discrete finite-element models of both the spacecraft and booster have been formulated. The structural dynamic behavior of the vehicle therefore can be expressed mathematically by a displacement vector u and mass and stiffness matrices K and M. For purposes of the present analysis these arrays are expressed as

$$\begin{array}{ccc} u & M & K \\ \left\{\begin{array}{c} u^{(1)} \\ \hline u^{(2)} \end{array}\right\} & \left[\begin{array}{c|c} M^{(1)} & 0 \\ \hline 0 & M^{(2)} \end{array}\right] & \left[\begin{array}{c|c} K^{(1)} & 0 \\ \hline 0 & K^{(2)} \end{array}\right] \end{array} \tag{1}$$

---

*This paper was presented at the 49th Symposium.

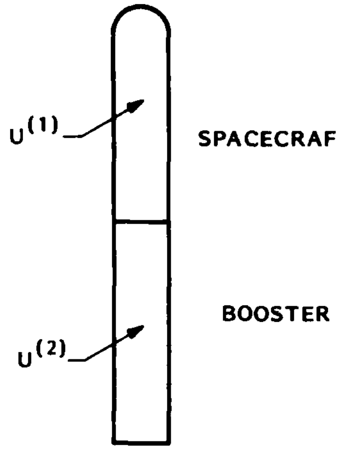

ORIGINAL FLIGHT VEHICLE

FIGURE 1

Here $u^{(1)}$, $M^{(1)}$, $K^{(1)}$ represent the spacecraft and $u^{(2)}$, $M^{(2)}$, $K^{(2)}$ the booster. In Eq (1) the spacecraft and booster are assembled but not connected; in addition, connection conditions are required. These are expressed in the form

$$u_I^{(1)} = u_I^{(2)} \tag{2}$$

If the two substructures are defined in different coordinate systems the connection conditions must take this fact into account. The equations of motion of the vehicle are

$$\begin{aligned} M\ddot{u} + K u &= f \quad \text{with} \quad u_I^{(1)} = u_I^{(2)} \\ u(0) &= u_0 \\ \dot{u}(0) &= \dot{u}_0 \end{aligned} \tag{3}$$

Assume now that an eigenvalue analysis of the vehicle model has been performed and that vehicle modes ψ_N of the free vehicle are available. Associated with modes ψ_N are modal frequencies ω_N and generalized masses μ_N.

With this information available the equations of motion may be transformed to modal generalized coordinates. Thus using the transformation

$$\left\{ \begin{array}{c} u^{(1)} \\ \hline u^{(2)} \end{array} \right\} = \left[\begin{array}{c} \psi_N^{(1)} \\ \hline \psi_N^{(2)} \end{array} \right] \left\{ q_N \right\} \tag{4}$$

the equations of motion in generalized coordinates are found to be

$$\begin{aligned} \bar{M}\ddot{q}_N + \bar{K} q_N &= \bar{f}_N \\ q_N(0) &= q_{N0} \\ \dot{q}_N(0) &= \dot{q}_{N0} \end{aligned} \tag{5}$$

where

$$\bar{M} = \psi_N^T M \psi_N = \mu_N \qquad \bar{K} = \psi_N^T K \psi_N = \mu_N \omega_N^2$$

$$\bar{f}_N = \psi_N^T f$$

$$q_{N0} = \mu_N^{-1} \psi_N^T M u_0$$

$$\dot{q}_{N0} = \mu_N^{-1} \psi_N^T M \dot{u}_0$$

In these equations the connection conditions have been satisfied during the determination of the modal functions ψ_N, for which

$$\psi_{NI}^{(1)} = \psi_{NI}^{(2)}$$

holds.

A change in the spacecraft structure is now proposed and it is necessary to evaluate the behavior of the modified flight vehicle. It is of course possible to repeat the process used to determine the original system modes of the vehicle, but this can be a costly, time-consuming process for a large scale vehicle model. Mode modification provides an alternative procedure.

A change area of the spacecraft is specified, encompassing all degrees of freedom affected by changes in mass and/or stiffness (Fig. 2). The arrays of Eq (1) can be rewritten to make the change area explicit as shown in Eq (6)

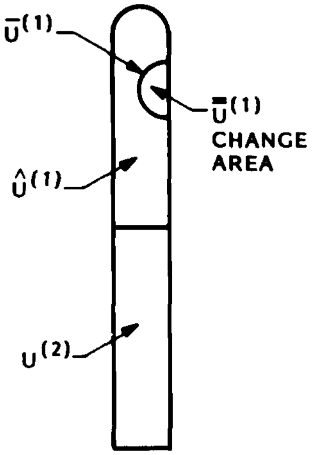

MODIFICATION OF VEHICLE

FIGURE 2

$$\begin{array}{cccc}
u_0 & M_0 & K_0 & \\
\left\{\begin{array}{c} \bar{u}^{(1)} \\ \hline \bar{\bar{u}}^{(1)} \\ \hline \hat{u}^{(1)} \\ \hline u^{(2)} \end{array}\right\}
&
\left[\begin{array}{c|c|c|c} \underline{M}_{11}^{(1)} & M_{12}^{(1)} & M_{13}^{(1)} & 0 \\ \hline {M_{12}^{(1)}}^T & M_{22}^{(1)} & 0 & 0 \\ \hline {M_{13}^{(1)}}^T & 0 & M_{33}^{(1)} & 0 \\ \hline 0 & 0 & 0 & M^{(2)} \end{array}\right]
&
\left[\begin{array}{c|c|c|c} \underline{K}_{11}^{(1)} & K_{12}^{(1)} & K_{13}^{(1)} & 0 \\ \hline {K_{12}^{(1)}}^T & K_{22}^{(1)} & 0 & 0 \\ \hline {K_{13}^{(1)}}^T & 0 & K_{33}^{(1)} & 0 \\ \hline 0 & 0 & 0 & K^{(2)} \end{array}\right]
& (6)
\end{array}$$

As shown in Fig. 2, displacements of the boundary of the change area are denoted by $\bar{u}^{(1)}$, those interior to the change area by $\bar{\bar{u}}^{(1)}$ and the displacements of the unchanged portion of the spacecraft by $\hat{u}^{(1)}$. Note in Eq (6) that by definition the displacements $\bar{\bar{u}}^{(1)}$ of the interior of the change area have no direct mass or stiffness coupling to the unchanged spacecraft displacements $\hat{u}^{(1)}$. Note also that the matrices $\underline{M}_{11}^{(1)}$ and $\underline{K}_{11}^{(1)}$ are marked specially. This is for convenience later in the analysis where the mass and stiffness of the change area is separated from that of the unchanged portion of the spacecraft. In general, the original modes ψ_N are not adequate to describe the desired modes ψ_L of the modified vehicle. This defect can be remedied by adding a set of constraint functions φ_D to the modal set ψ_N. The constraint functions are determined by constraining to zero every degree of freedom in the modification area and calculating, for an imposed unit displacement at each constrained degree of freedom in turn, displacements at all other degrees of freedom of the vehicle. By this means, if there are N_D degrees of freedom in the change area, N_D functions φ_D can be determined. The constraint functions φ_D can be divided into two subsets, φ_A and φ_{B1}. Functions φ_A are those functions associated with the boundary displacements $\bar{u}^{(1)}$ which cause displacements in the unchanged vehicle. Functions φ_{B1} are associated with the interior displacements $\bar{\bar{u}}^{(1)}$ and are trivial in that each consists of a single non-zero displacement (equal to 1.0), with all other displacements zero. Functions φ_A may be calculated from the finite element model of the flight vehicle. We have then for the transformation to generalized coordinates

$$\begin{array}{cccc}
 & \Psi_0 & & \\
u_0 & \begin{array}{ccc} \psi_N & \varphi_A & \varphi_{B1} \end{array} & q_0 & \\
\left\{\begin{array}{c} \bar{u}^{(1)} \\ \hline \bar{\bar{u}}^{(1)} \\ \hline \hat{u}^{(1)} \\ \hline u^{(2)} \end{array}\right\}
=
&
\left[\begin{array}{ccc} \bar{\psi}_N^{(1)} & I & 0 \\ \hline \bar{\bar{\psi}}_N^{(1)} & 0 & I \\ \hline \hat{\psi}_N^{(1)} & \hat{\varphi}_A^{(1)} & 0 \\ \hline \psi_N^{(2)} & \varphi_A^{(2)} & 0 \end{array}\right]
&
\left\{\begin{array}{c} q_N \\ \hline q_A \\ \hline q_{B1} \end{array}\right\}
& (7)
\end{array}$$

or

$$u_0 = \Psi_0 \, q_0 \qquad (8)$$

As discussed above, the functions φ_A are obtained by constraining the change area in the complete vehicle stiffness matrix and determining the static response to successive unit displacements of the change area boundary. If the booster stiffness matrix is not available, it would be sufficient to use a statically reduced interface stiffness package to represent the booster during this calculation.

It may be noted that the vehicle modes ψ_N and the set of constraint functions $(\varphi_A \mid \varphi_{B1})$ each contain separately a representation of rigid body motion of the vehicle. It is necessary to remove this redundancy by one of the following:

(1) eliminate the rigid body modes ψ_R from the set of free body modes ψ_N,

(2) eliminate a sufficient number of properly chosen functions from $(\varphi_A \mid \varphi_{B1})$ to eliminate rigid body motion from this set,

(3) During calculation of $(\varphi_A \mid \varphi_{B1})$, apply arbitrarily-chosen statically-determinate constraints to the vehicle.

Application of the transformation of Eq (7) to the arrays of Eq (6) yields

$$q_0 \qquad \bar{M}_0 = \Psi_0^T M_0 \Psi_0 \qquad \bar{K}_0 = \Psi_0^T K_0 \Psi_0 \qquad (9)$$

or, in more detail, Eq (10)

The arrays of Eq (10) still represent the original vehicle, and if the eigenvalue problem

$$-\omega^2 \bar{M}_0 \, q_0 + \bar{K}_0 \, q_0 = 0$$

were solved and back transformed to structural coordinates the original modes would be obtained. (Additional to the original modes may be modes of the change area with the unchanged structure behaving quasistatically.)

$$\begin{array}{ccc} q_0 & \bar{M}_0 & \bar{K}_0 \\ \left\{\begin{array}{c} q_N \\ \hline q_A \\ \hline q_{B1} \end{array}\right\} & \left[\begin{array}{c|c|c} \diagdown\,\psi_N^T M \psi_N\,\diagdown & \psi_N^T M \varphi_A & \bar{\psi}_N^{(1)T} M_{12}^{(1)} + \bar{\bar{\psi}}_N^{(1)T} M_{22}^{(1)} \\ \hline \varphi_A^T M \psi_N & \varphi_A^T M \varphi_A & M_{12}^{(1)} \\ \hline M_{12}^{(1)T} \bar{\psi}_N^{(1)} + M_{22}^{(1)} \bar{\bar{\psi}}_N^{(1)} & M_{12}^{(1)T} & M_{22}^{(1)} \end{array}\right] & \left[\begin{array}{c|c|c} \diagdown\,\psi_N^T K \psi_N\,\diagdown & \psi_N^T K \varphi_A & \bar{\psi}_N^{(1)T} K_{12}^{(1)} + \bar{\bar{\psi}}_N^{(1)T} K_{22}^{(1)} \\ \hline \varphi_A^T K \psi_N & \varphi_A^T K \varphi_A & K_{12}^{(1)} \\ \hline K_{12}^{(1)T} \bar{\psi}_N^{(1)} + K_{22}^{(1)} \bar{\bar{\psi}}_N^{(1)} & K_{12}^{(1)T} & K_{22}^{(1)} \end{array}\right] \end{array} \tag{10}$$

$$\begin{array}{ccccc} u_0 & & \begin{array}{ccc} & \Psi_0 & \\ \psi_N & \varphi_A & \varphi_{B1} \end{array} & S_0 & q_0^* \\ \left\{\begin{array}{c} \bar{u}^{(1)} \\ \hline \bar{\bar{u}}^{(1)} \\ \hline \hat{u}^{(1)} \\ \hline u^{(2)} \end{array}\right\} & = & \left[\begin{array}{c|c|c} \bar{\psi}_N^{(1)} & I & 0 \\ \hline \bar{\bar{\psi}}_N^{(1)} & 0 & I \\ \hline \hat{\psi}_N^{(1)} & \hat{\varphi}_A^{(1)} & 0 \\ \hline \psi_N^{(2)} & \varphi_A^{(2)} & 0 \end{array}\right] & \left[\begin{array}{c|c|c} I & 0 & 0 \\ \hline -\bar{\psi}_N^{(1)} & I & 0 \\ \hline -\bar{\bar{\psi}}_N^{(1)} & 0 & I \end{array}\right] & \left\{\begin{array}{c} q_S \\ \hline q_A \\ \hline q_{B1} \end{array}\right\} \end{array} \tag{11}$$

$$\begin{array}{cccc} u_0 & & \begin{array}{ccc} & \Psi_0^* & \\ \psi_S & \varphi_A & \varphi_{B1} \end{array} & q_0^* \\ \left\{\begin{array}{c} \bar{u}^{(1)} \\ \hline \bar{\bar{u}}^{(1)} \\ \hline \hat{u}^{(1)} \\ \hline u^{(2)} \end{array}\right\} & = & \left[\begin{array}{c|c|c} 0 & I & 0 \\ \hline 0 & 0 & I \\ \hline \hat{\psi}_S^{(1)} & \hat{\varphi}_A^{(1)} & 0 \\ \hline \psi_S^{(2)} & \varphi_A^{(2)} & 0 \end{array}\right] & \left\{\begin{array}{c} q_S \\ \hline q_A \\ \hline q_{B1} \end{array}\right\} \end{array} \tag{12}$$

It is convenient for application of the mode-modification method to further transform the problem to replace the system modes ψ_N in Eq (7) by new functions ψ_S. The motivation for this second transformation will be explained below. The transformation is shown in Eqs (11) and (12)

Note that only the functions ψ_N have been altered, while φ_A and φ_{B1} remain unchanged. The new functions ψ_S are linear combinations of the original functions.

The mass and stiffness matrices associated with the new generalized coordinates are obtained from the arrays of Eq (10) as shown in Eq (13) and the expanded form of Eq (14).

$$q_0^* \qquad \bar{M}_0^* = S_0^T \bar{M}_0 S_0 \qquad \bar{K}_0^* = S_0^T \bar{K}_0 S_0 \tag{13}$$

$$\overset{q_0^*}{\left\{\begin{array}{c} q_S \\ \hline q_A \\ \hline q_{B1} \end{array}\right\}} \qquad \overset{\overline{M}_0^*}{\left[\begin{array}{c|c|c} \psi_S^T M \psi_S & \psi_S^T M \varphi_A & 0 \\ \hline \varphi_A^T M \psi_S & \varphi_A^T M \varphi_A & M_{12}^{(1)} \\ \hline 0 & M_{12}^{(1)^T} & M_{22}^{(1)} \end{array}\right]} \qquad \overset{\overline{K}_0^*}{\left[\begin{array}{c|c|c} \psi_S^T K \psi_S & \psi_S^T K \varphi_A & 0 \\ \hline \varphi_A^T K \psi_S & \varphi_A^T K \varphi_A & K_{12}^{(1)} \\ \hline 0 & K_{12}^{(1)^T} & K_{22}^{(1)} \end{array}\right]} \qquad (14)$$

$$\overset{\tilde{u}_0}{\left\{\begin{array}{c} \bar{u}^{(1)} \\ \hline \bar{\bar{u}}^{(1)} \end{array}\right\}} \qquad \overset{\tilde{M}_0}{\left[\begin{array}{c|c} M_{11}^{(1)} & M_{12}^{(1)} \\ \hline M_{12}^{(1)^T} & M_{22}^{(1)} \end{array}\right]} \qquad \overset{\tilde{K}_0}{\left[\begin{array}{c|c} K_{11}^{(1)} & K_{12}^{(1)} \\ \hline K_{12}^{(1)^T} & K_{22}^{(1)} \end{array}\right]} \qquad (15)$$

The motivation for utilizing this transformation is as follows. The transformation to generalized coordinates of Eq (7) describes displacements $\bar{u}^{(1)}$ and $\bar{\bar{u}}^{(1)}$ in the change area in terms of all three sets of functions. Thus when a change is made in the mass or stiffness of the change area, triple products are required to calculate the changes to $\overline{M}_0$ and $\overline{K}_0$ of Eq (10) and these changes affect all parts of these arrays. The transformation of Eq (12) on the other hand represents change area displacements in terms of functions φ_A and φ_{B1} only and furthermore the displacements $\bar{u}^{(1)}$ and $\bar{\bar{u}}^{(1)}$ are one-to-one with coordinates q_A and q_{B1}. Thus only portions of arrays $\overline{M}_0^*$ and $\overline{K}_0^*$ of Eq (14) are altered by modifications in the change area and the changes can be made by direct overlays of mass and stiffness matrices in structural coordinates.

It is now possible to account for, in an accurate manner, arbitrary changes in this area including the following possibilities:

(1) Alter the mass and stiffness in the change area leaving the topology unchanged.

(2) Remove the change area structure entirely leaving a "hole" in the vehicle.

(3) Remove the change area structure and replace it with completely new structure.

First consider removal of the structure in the change area. Denote the displacements, mass, and stiffness of this area, considered as a separate structure, as $\tilde{u}_0$, $\tilde{M}_0$, and $\tilde{K}_0$. Details of these matrices are shown in Eq (15) above.

The submatices $M_{11}^{(1)}$ and $K_{11}^{(1)}$ in these arrays must be distinguished from $\underline{M}_{11}^{(1)}$ and $\underline{K}_{11}^{(1)}$ of Eq (6) because the latter quantities include effects from both the change area and the unchanged vehicle.

The transformation of the quantities of Eq (15) to generalized coordinates q_0^* is, from Eq (12)

$$\overset{\tilde{u}_0}{\left\{\begin{array}{c} \bar{u}^{(1)} \\ \hline \bar{\bar{u}}^{(1)} \end{array}\right\}} = \overset{\tilde{\Psi}_0}{\left[\begin{array}{c|c|c} \tilde{\psi}_S & \tilde{\varphi}_A & \tilde{\varphi}_{B1} \\ 0 & I & 0 \\ \hline 0 & 0 & I \end{array}\right]} \overset{q_0^*}{\left\{\begin{array}{c} q_S \\ \hline q_A \\ \hline q_{B1} \end{array}\right\}} \qquad (16)$$

and the result of the transformation is

$$\begin{array}{ccc} q_0^* & \Delta\bar{M}_0^* & \Delta\bar{K}_0^* \\ \left\{\begin{array}{c} q_S \\ \hline q_A \\ \hline q_{B1} \end{array}\right\} & \left[\begin{array}{c|c|c} 0 & 0 & 0 \\ \hline 0 & M_{11}^{(1)} & M_{12}^{(1)} \\ \hline 0 & M_{12}^{(1)^T} & M_{22}^{(1)} \end{array}\right] & \left[\begin{array}{c|c|c} 0 & 0 & 0 \\ \hline 0 & K_{11}^{(1)} & K_{12}^{(1)} \\ \hline 0 & K_{12}^{(1)^T} & K_{22}^{(1)} \end{array}\right] \end{array} \qquad (17)$$

Removal of the change-area structure from the vehicle consists of subtraction of the mass and stiffness matrices of Eq (17) from those of Eq (14). This subtraction yields

$$\begin{array}{ccc} q_1^* & \bar{M}_1^* & \bar{K}_1^* \\ \left\{\begin{array}{c} q_S \\ \hline q_A \\ \hline q_{B1} \end{array}\right\} & \left[\begin{array}{c|c|c} \psi_S^T M \psi_S & \psi_S^T M \varphi_A & 0 \\ \hline \varphi_A^T M \psi_S & \begin{array}{c} \varphi_A^T M \varphi_A \\ -M_{11}^{(1)} \end{array} & 0 \\ \hline 0 & 0 & 0 \end{array}\right] & \left[\begin{array}{c|c|c} \psi_S^T K \psi_S & \psi_S^T K \varphi_A & 0 \\ \hline \varphi_A^T K \psi_S & \begin{array}{c} \varphi_A^T K \varphi_A \\ -K_{11}^{(1)} \end{array} & 0 \\ \hline 0 & 0 & 0 \end{array}\right] \end{array} \qquad (18)$$

Since q_{B1} in Eq (18) and $\bar{\bar{u}}^{(1)}$ and φ_{B1} of Eq (12) are associated with structure which is no longer present they can be eliminated and the problem expressed more concisely as shown in Eqs (19) and (20) below.

$$\begin{array}{ccccc} \tilde{u}_1 & & \begin{array}{cc} \multicolumn{2}{c}{\tilde{\Psi}_1^*} \\ \tilde{\psi}_S & \tilde{\psi}_A \end{array} & q_1^* \\ \left\{\begin{array}{c} \bar{\bar{u}}^{(1)} \\ \hline \hat{u}^{(1)} \\ \hline u^{(2)} \end{array}\right\} & = & \left[\begin{array}{c|c} 0 & I \\ \hline \hat{\psi}_S^{(1)} & \hat{\varphi}_A^{(1)} \\ \hline \psi_S^{(2)} & \varphi_A^{(2)} \end{array}\right] & \left\{\begin{array}{c} q_S \\ \hline q_A \end{array}\right\} \end{array} \qquad (19)$$

$$\begin{array}{ccc} q_1^* & \bar{M}_1^* & \bar{K}_1^* \\ \left\{\begin{array}{c} q_S \\ \hline q_A \end{array}\right\} & \left[\begin{array}{c|c} \psi_S^T M \psi_S & \psi_S^T M \varphi_A \\ \hline \varphi_A^T M \psi_S & \begin{array}{c} \varphi_A^T M \varphi_A \\ -M_{11}^{(1)} \end{array} \end{array}\right] & \left[\begin{array}{c|c} \psi_S^T K \psi_S & \psi_S^T K \varphi_A \\ \hline \varphi_A^T K \psi_S & \begin{array}{c} \varphi_A^T K \varphi_A \\ -K_{11}^{(1)} \end{array} \end{array}\right] \end{array} \qquad (20)$$

These arrays represent the vehicle of Fig. 3 which has a "hole" in it. Solution of an eigenvalue problem using $\bar{M}_1^*$ and $\bar{K}_1^*$ would yield modes of this vehicle.

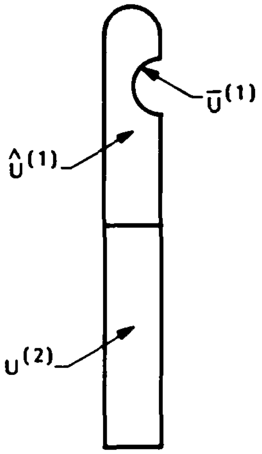

VEHICLE WITH
STRUCTURE REMOVED
FIGURE 3

Consider next the addition of new structure to the change area. This new structure need bear no resemblance to the original change-area structure. However, $\bar{u}^{(1)}$, the boundary of the unchanged portion of the vehicle, must have been properly defined such that the boundary $\bar{u}^{(3)}$ of the new structure is compatible with part or all of $\bar{u}^{(1)}$.

As shown in Fig. 4, we denote the new structure as substructure 3 with the representation of Eq (21)

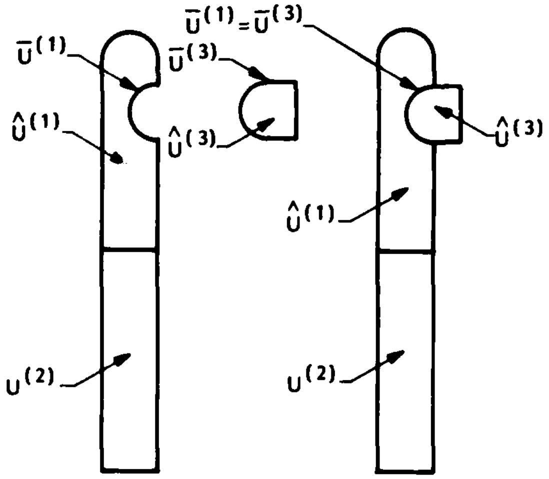

MODIFIED FLIGHT VEHICLE
FIGURE 4

$$\begin{array}{ccc} \tilde{u} & \tilde{M}_2 & \tilde{K}_2 \\ \left\{\begin{array}{c} \bar{u}^{(3)} \\ \hline \hat{u}^{(3)} \end{array}\right\} & \left[\begin{array}{c|c} M_{11}^{(3)} & M_{12}^{(3)} \\ \hline {M_{12}^{(3)}}^T & M_{22}^{(3)} \end{array}\right] & \left[\begin{array}{c|c} K_{11}^{(3)} & K_{12}^{(3)} \\ \hline {K_{12}^{(3)}}^T & K_{22}^{(3)} \end{array}\right] \end{array} \qquad (21)$$

The process of attaching the new structure is completely analogous to that used previously to remove structure.

A transformation to generalized coordinates similar to Eq (16) is used

$$\begin{array}{ccc} \tilde{u}_2 & & \tilde{\Psi}^* & q_2^* \\ \left\{\begin{array}{c} \bar{u}^{(3)} \\ \hline \hat{u}^{(3)} \end{array}\right\} & = & \left[\begin{array}{c|c|c} \tilde{\psi}_S & \tilde{\varphi}_A & \tilde{\varphi}_{B3} \\ 0 & I & 0 \\ \hline 0 & 0 & I \end{array}\right] & \left\{\begin{array}{c} q_S \\ \hline q_A \\ \hline q_{B3} \end{array}\right\} \end{array} \qquad (22)$$

This transformation is used to obtain an equation corresponding to Eq (17)

$$
\begin{array}{c}q_2^*\\ \left\{\begin{array}{c}q_S\\ \hline q_A\\ \hline q_{B3}\end{array}\right\}\end{array}
\qquad
\begin{array}{c}\Delta\overline{M}_2^*\\ \left[\begin{array}{c|c|c}0&0&0\\ \hline 0&M_{11}^{(3)}&M_{12}^{(3)}\\ \hline 0&M_{12}^{(3)T}&M_{22}^{(3)}\end{array}\right]\end{array}
\qquad
\begin{array}{c}\Delta\overline{K}_2^*\\ \left[\begin{array}{c|c|c}0&0&0\\ \hline 0&K_{11}^{(3)}&K_{12}^{(3)}\\ \hline 0&K_{12}^{(3)T}&K_{22}^{(3)}\end{array}\right]\end{array}
\tag{23}
$$

Finally, combination of the arrays of Eqs (20) and (23), with q_S and q_A overlaid yields a representation of the vehicle with the new structure attached.

$$
\begin{array}{c}q_2^*\\ \left\{\begin{array}{c}q_S\\ \hline q_A\\ \hline q_{B3}\end{array}\right\}\end{array}
\qquad
\begin{array}{c}\overline{M}_2^*\\ \left[\begin{array}{c|c|c}\psi_S^T M \psi_S&\psi_S^T M \varphi_A&0\\ \hline \varphi_A^T M \psi_S&\begin{array}{c}\varphi_A^T M \varphi_A\\ -M_{11}^{(1)}+M_{11}^{(3)}\end{array}&M_{12}^{(3)}\\ \hline 0&M_{12}^{(3)T}&M_{22}^{(3)}\end{array}\right]\end{array}
\qquad
\begin{array}{c}\overline{K}_2^*\\ \left[\begin{array}{c|c|c}\psi_S^T K \psi_S&\psi_S^T K \varphi_A&0\\ \hline \varphi_A^T K \psi_S&\begin{array}{c}\varphi_A^T K \varphi_A\\ -K_{11}^{(1)}+K_{11}^{(3)}\end{array}&K_{12}^{(3)}\\ \hline 0&K_{12}^{(3)T}&K_{22}^{(3)}\end{array}\right]\end{array}
\tag{24}
$$

The implied transformation from structural to generalized coordinates which would produce the arrays of Eq (24) is (analogous to Eqs (11) and (12))

$$
\begin{array}{c}u_2\\ \left\{\begin{array}{c}\bar{u}^{(1)}\\ \hline \hat{u}^{(3)}\\ \hline \hat{u}^{(1)}\\ \hline u^{(2)}\end{array}\right\}\end{array}
=
\begin{array}{c}\Psi_2\\ \begin{array}{ccc}\psi_N&\varphi_A&\varphi_{B3}\end{array}\\ \left[\begin{array}{c|c|c}\bar{\psi}_N^{(1)}&I&0\\ \hline 0&0&I\\ \hline \hat{\psi}_N^{(1)}&\hat{\varphi}_A^{(1)}&0\\ \hline \psi_N^{(2)}&\varphi_A^{(2)}&0\end{array}\right]\end{array}
\begin{array}{c}S_2\\ \left[\begin{array}{c|c|c}I&0&0\\ \hline -\bar{\psi}_N^{(1)}&I&0\\ \hline 0&0&I\end{array}\right]\end{array}
\begin{array}{c}q_2^*\\ \left\{\begin{array}{c}q_S\\ \hline q_A\\ \hline q_{B3}\end{array}\right\}\end{array}
\tag{25}
$$

$$\begin{array}{c} u_2 \\ \left\{\begin{array}{c} \bar{u}^{(1)} \\ \hline \hat{u}^{(3)} \\ \hline \hat{u}^{(1)} \\ \hline u^{(2)} \end{array}\right\} \end{array} = \begin{array}{c} \Psi_2^* \\ \begin{array}{ccc} \varphi_S & \varphi_A & \varphi_{B3} \end{array} \\ \left[\begin{array}{c|c|c} 0 & I & 0 \\ \hline 0 & 0 & I \\ \hline \hat{\varphi}_S^{(1)} & \hat{\varphi}_A^{(1)} & 0 \\ \hline \varphi_S^{(2)} & \varphi_A^{(2)} & 0 \end{array}\right] \end{array} \begin{array}{c} q_2^* \\ \left\{\begin{array}{c} q_S \\ \hline q_A \\ \hline q_{B3} \end{array}\right\} \end{array} \qquad (26)$$

The eigenvalue problem using $\bar{M}_2^*$ and $\bar{K}_2^*$ of Eq (24) yields normal modes of the vehicle of Fig. 4c. The eigenvectors η_L^* are in generalized coordinates, accompanied by eigenvalues ω_L^2

$$\begin{array}{c} \eta_L^* \\ \left[\begin{array}{c} \eta_S \\ \hline \eta_A \\ \hline \eta_{B3} \end{array}\right] \end{array} \qquad \left\{ \omega_L^2 \right\} \qquad (27)$$

The structural mode vectors are obtained from Eq (25) as

$$\begin{array}{c} \psi_L \\ \left[\begin{array}{c} \bar{\psi}_L^{(1)} \\ \hline \hat{\psi}_L^{(3)} \\ \hline \hat{\psi}_L^{(1)} \\ \hline \psi_L^{(2)} \end{array}\right] \end{array} = \begin{array}{c} \begin{array}{ccc} \psi_N & \varphi_A & \varphi_{B3} \end{array} \\ \left[\begin{array}{c|c|c} \bar{\psi}_N^{(1)} & I & 0 \\ \hline 0 & 0 & I \\ \hline \hat{\psi}_N^{(1)} & \hat{\varphi}_A^{(1)} & 0 \\ \hline \psi_N^{(2)} & \varphi_A^{(2)} & 0 \end{array}\right] \end{array} \begin{array}{c} S_2 \\ \left[\begin{array}{c|c|c} I & 0 & 0 \\ \hline -\bar{\psi}_N^{(1)} & I & 0 \\ \hline 0 & 0 & I \end{array}\right] \end{array} \begin{array}{c} \eta_L^* \\ \left[\begin{array}{c} \eta_S \\ \hline \eta_A \\ \hline \eta_{B3} \end{array}\right] \end{array} \qquad (28)$$

The foregoing provides a basic description of the mode modification method. However, for application of the method it is useful to discuss further several procedural considerations. First there is the determination of the generalized arrays $\bar{M}_0^*$ and $\bar{K}_0^*$ of Eq (14), which represent the original vehicle. In the analysis these are obtained from M_0 and K_0 of Eq (6) by setting up Ψ_0 (in terms of ψ_N) and calculating $\bar{M}_0$ and $\bar{K}_0$, as in Eq (9). Subsequently, these arrays are transformed to $\bar{M}_{(0)}^*$ and $\bar{K}_0^*$ in Eq (13) using transformation S_0. It is evident that an alternate, more direct approach, would be to form Ψ_0^* as shown in Eq (12) (in terms of ψ_S) and directly determine $\bar{M}_0^*$ and $\bar{K}_0^*$ as

$$q_0^* \qquad \bar{M}_0^* = \Psi_0^{*T} M_0 \Psi_0^* \qquad \bar{K}_0^* = \Psi_0^{*T} K_0 \Psi_0^* \qquad (29)$$

This latter approach is possible and perhaps preferable in some cases. However in flight vehicles involving several separate substructures as in Fig. 1 the finite element mass and stiffness matrices of the entire vehicle are not always available. This occurs commonly when different companies are involved and data in terms of generalized functions is transferred. In such cases portions of the matrices $\bar{M}_0$ and $\bar{K}_0$ of Eq (10) can be set up using the system modal parameters, rather than directly with triple products. Thus

$$\begin{aligned} \left[\bar{M}_0\right]_{11} &= \psi_N^T M \psi_N = \left[\mu_N\right] \quad \text{Diagonal} \\ \left[\bar{K}_0\right]_{11} &= \psi_N^T K \psi_N = \left[\mu_N \omega_N^2\right] \text{Diagonal} \end{aligned} \qquad (30)$$

Thus the choice of alternate means of determining $\bar{M}_0^*$ and $\bar{K}_0^*$ of Eq (14) depends on the particular problem and the data available to the analyst.

A second procedure to be considered is that of the determination of the change area mass and stiffness matrices, both for the original configuration and for the configuration with design changes.

There are two ways to obtain these matrices. One method is to set up finite element models of both the original and design-modified change areas as separate, stand-alone structures. This method was implied in the previous discussion and yields the matrices of Eq (15) and (21).

A second method can alternatively be used. From the original spacecraft mass and stiffness matrices $M_0^{(1)}$ and $K_0^{(1)}$ of Eq (6) the smaller mass and stiffness matrices $\tilde{M}_0$ and $\tilde{K}_0$ can be abstracted

$$\begin{array}{ccc} \tilde{u} & \underline{\tilde{M}}_0 & \underline{\tilde{K}}_0 \\ \left\{\begin{array}{c} \bar{u}^{(1)} \\ \hline \bar{u}^{(2)} \end{array}\right\} & \left[\begin{array}{c|c} \underline{M}_{11}^{(1)} & M_{12}^{(1)} \\ \hline {M_{12}^{(1)}}^T & M_{22}^{(1)} \end{array}\right] & \left[\begin{array}{c|c} \underline{K}_{11}^{(1)} & K_{12}^{(1)} \\ \hline {K_{12}^{(1)}}^T & K_{22}^{(1)} \end{array}\right] \end{array} \qquad (31)$$

These matrices are not exactly what is desired because they contain unwanted mass and stiffness (in $\underline{M}_{11}^{(1)}$ and $\underline{K}_{11}^{(1)}$) from the unchanged portion of the spacecraft. It is difficult to remove this unwanted behavior. It is possible, nevertheless, to use these matrices in place of those of Eq (15) to remove the change area. The resulting arrays represent the vehicle elastically constrained to ground at the boundary $\bar{u}^{(1)}$ and with the change area removed.

Next the spacecraft model is modified to incorporate the design changes in the change area. From the new spacecraft mass and stiffness matrices we can abstract out matrices $\underline{\tilde{M}}_2$ and $\underline{\tilde{K}}_2$ corresponding to Eq (21), but also containing unwanted behavior from the unchanged spacecraft. Indeed the unwanted behavior is exactly the same as in the original matrices $\underline{M}_0$ and $\underline{K}_0$. When we add in the new matrices $\underline{\tilde{M}}_2$ and $\underline{\tilde{K}}_2$, as described after Eq (21), the unwanted behavior disappears by cancellation and we have the desired final arrays of Eq (24). This method has the advantage of dealing directly with the spacecraft model and does not require separate change-area models.

A third procedural consideration is that of ill conditioning. If the original modes ψ_N are nearly a complete set of normal modes then the additional functions φ_A and φ_{B1} may be linear combinations of the normal modes. Any attempt to solve an eigenvalue problem utilizing the data of Eq (10), (20) or (24) would then experience difficulty. One obvious solution to this problem, if it should arise, is to identify the dependent functions of the set represented in Eq (7), (12) or (26) and eliminate them.

In most engineering problems, however, the original modes ψ_N are a small subset of the complete set of modes for the structure and problems associated with linear dependency are unlikely.

BEAM-TRUSS EXAMPLE

The planar beam-truss model of Fig. 5 will be used for a first demonstration of the mode modification method. This application is not intended to be typical but is used to illustrate the procedures applicable to larger, more complex configurations and as a verification of the method. For the model of Fig. 5 each of the eleven nodes has three displacements u_x, u_y, and θ_z. Thus the model has a total of 33 degrees of freedom. Since this example consists of only one structure, the substructure (2) of Figure 1 is not present.

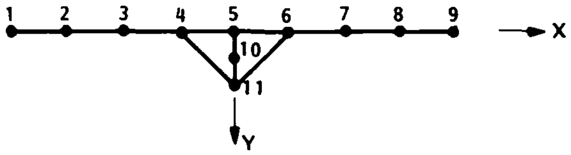

BEAM-TRUSS MODEL – ORIGINAL CONFIGURATION

FIGURE 5

Free body modes ψ_N of the structure have been calculated previously and are initially available. They consist of three rigid body modes and eight elastic modes below 150 Hz.

Two separate design changes to the model are considered:

(1) Non symmetric mass and stiffness changes to the change area structure with no change in configuration.

(2) Modification of the center structure of the model to that of Figure 6, with an increase in the total number of degrees of freedom to 39.

Each of these changes destroys the original symmetry of the model and significantly alters the modal behavior of the structure.

A change area is chosen in the original model, covering both of the design changes described above. It consists of the structure between nodes 4 and 6, including nodes 5, 10, and 11; that is, the central triangular truss. Thus $\bar{u}^{(1)}$ the boundary of the change area, will have 6 DOF (nodes 4 and 6) while $\bar{u}^{(1)}$, the interior, comprises 9 DOF (nodes 5, 10 and 11).

Using the finite element model of the original structure, six constraint functions $\varphi_A^{(1)}$ are determined, corresponding to $\bar{u}^{(1)}$. In this example each of these functions represents rigid motion of one of the "wing beams" with the remainder of the structure stationary.

With ψ_N and $\varphi_A^{(1)}$ as well as M_0 and K_0 of the original structure available it is now possible to form the arrays $\bar{M}_0$ and $\bar{K}_0$ of Eq (10), the transformation S_0 of Eq (11) and the arrays $\bar{M}_0^*$ and $\bar{K}_0^*$ of Eq (14). Because of the redundancy of the rigid body modes in the function set of Eq (7) the three rigid modes are eliminated from the modal set ψ_N in the calculation.

Before proceeding with the design change it is advisable to solve an eigenvalue problem formed from $\bar{M}_0^*$ and $\bar{K}_0^*$. These matrices represent the original structure in generalized coordinates, and the back transformed eigensolutions, should yield the original modes and frequencies ψ_N, ω_N. In the present simple example exact agreement was obtained. This is not a trivial calculation because it checks the processing through Eq (14) of the analysis.

Consider now the first design modification where mass and stiffness changes are made in the central truss area of the structure of Fig. 5. For this example, the set of free body modes ψ_N was limited to the first five elastic modes. The change area matrices $\tilde{M}$ and $\tilde{K}$ (15 DOF) for both the original and modified structures are determined by abstracting them from the corresponding matrices of the complete structures (the alternate method discussed previously).

With this data the arrays $\bar{M}_2^*$ and $\bar{K}_2^*$ are obtained. These arrays represent the structure of Fig. 5 with modified mass and stiffness. Solution of the eigenvalue problem formed from them yields the frequencies and generalized modal vectors for this structure. Structural modes of the modified structure, ψ_L, are calculated from Eq (28). To verify the modes obtained in the above manner by mode modification, a direct calculation of these modes is made from the modified finite element model. A comparison of the results obtained is presented in Table 1 and shows excellent frequency agreement. The triple products of the two sets of modes with respect to the mass and stiffness matrices of the modified structure are also presented. Maximum off-diagonal term, as a percent of the diagonal value is less than 0.02 percent, indicating very good agreement between the sets of mode shapes.

Application of mode modification for the second design change proceeds in a similar manner. For this case, ψ_N was arbitrarily expanded to include the first eight elastic modes (to 150 Hz). The matrices $\tilde{M}_2$ and $\tilde{K}_2$ (21 DOF in this case) are abstracted from the full matrices of the structure shown in Fig. 6. Arrays $\bar{M}_2^*$ and $\bar{K}_2^*$ are constructed, enabling formulation of the eigenvalue problem. Solution of this problem yields frequencies and generalized modal vectors for the modified structure. Again, structural modes are calculated from Eq (28). Comparison of results of mode modification and direct solution is shown in Table 2. Note that because of the additional information contained in functions φ_A and φ_{B3}, the mode modification method is able to find modes higher in frequency than the highest original mode (but still below the frequency cutoff of 150 Hz for the original modes). Maximum off diagonal term in the triple products is 0.046 percent of the diagonal value.

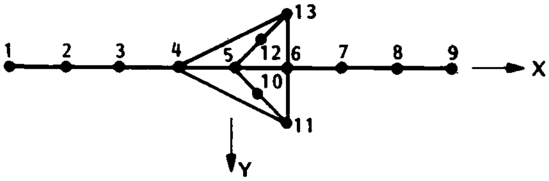

BEAM-TRUSS MODEL – MODIFIED CONFIGURATION

FIGURE 6

FLIGHT VEHICLE ADAPTOR CHANGE

For further demonstration and verification of the mode modification method, calculations are made on a flight vehicle consisting of a spacecraft and an upper stage booster (Fig. 7a). The spacecraft is represented by a finite element model having 1752 degrees of freedom, whereas the booster model has only 113 degrees of freedom. The interface between the spacecraft and booster is rigid and therefore consists of 6 degrees of freedom only. At the base of the spacecraft there is a truss-type adaptor. For purposes of illustration, a design change is made to this adaptor, consisting of changing both its mass and stiffness.

Figure 7b shows a sketch of the adaptor which is the modification area for this problem consisting of 138 DOF with $\bar{u}^{(1)}$ having 42 DOF and $\bar{\bar{u}}^{(1)}$, 96 DOF. Some features of this problem are: (1) the modification area completely separates the unchanged portions of the original vehicle into two separate parts, (2) the boundary area $\bar{u}^{(1)}$ itself consists of two parts $\bar{u}_1^{(1)}$, 36 DOF at the upper end of the adaptor and $\bar{u}_2^{(1)}$, 6 DOF, at the lower end. A set of system modes of the original flight vehicle are initially available. These modes were determined by modal synthesis of the two substructures wherein the spacecraft was represented by rigid body modes and 50 cantilevered normal modes while the booster because of its small number of degrees of freedom was left in structural coordinates. The resulting flight vehicle modes are:

$$\psi_N = \left[\begin{array}{c}\psi_N^{(1)}\\ \hline \psi_N^{(2)}\end{array}\right], \quad \mu_N, \quad \omega_N^2$$

The mode modification method is now applied to determine a new set of flight vehicle modes ψ_L representing the adaptor-modified vehicle. For this purpose a set of 42 constraint functions φ_A is determined. The first 36 of these functions, φ_{A1} are found by constraining the spacecraft at all 138 DOF of the modification area and calculating constraint functions for the 36 DOF of $\bar{u}_1^{(1)}$. The displacements of the booster corresponding to these functions are zero. The products $M^{(1)} \varphi_{A1}^{(1)}$ and $K^{(1)} \varphi_{A1}^{(1)}$ are also calculated at this time. The remaining 6 constraint functions φ_{A2} correspond to the boundary displacements $\bar{u}_2^{(1)}$. When these degrees of freedom are released and moved they produce rigid body motion of the booster only. Therefore, the remaining 6 constraint functions consist of rigid body functions of the booster with all spacecraft displacements zero.

To remove the rigid body redundancy discussed previously, the six rigid body modes of the modal set ψ_N are removed. Then matrices $\overline{M}_0$ and $\overline{K}_0$ are formed, and transformed using S_0 to $\overline{M}_0^*$ and $\overline{K}_0^*$ The check solution obtained by reproducing the original modal frequencies by solution of the eigenvalue problem formed by $\overline{M}_0^*$ and $\overline{K}_0^*$ yields the results shown in Table 3. The change area matrices $\widetilde{M}_0$ and $\widetilde{K}_0$ as well as $\widetilde{M}_2$ and $\widetilde{K}_2$ are formed by abstracting them from the corresponding spacecraft matrices. Finally the arrays of Eq (24) are formed and solved for η_L and ω_L^2 ; from Eq (28), the structural modes ψ_L of the modified structure are obtained.

For comparison and validation of these mode-modification results a set of modes of the modified vehicle were also obtained by the conventional method of reanalyzing the modified spacecraft, and subsequent modal synthesis with the booster. The comparison of modal frequencies of the modified vehicle obtained directly and with mode modification are shown in Table 4.

The results again show that the mode modification method produces modal information which compares very favorably with direct calculation.

CONCLUSIONS

The method of this paper appears to have usefulness as an analysis tool of considerable benefit to the structural dynamicist. It certainly will be useful for approximate parameter-studies and other design-change investigations. It may have potential for direct use in final analysis of a modified structure. Further development and application of the method should establish more clearly its true scope.

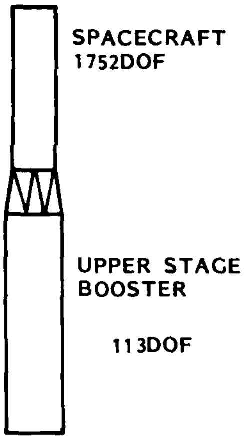

FLIGHT VEHICLE
(a)

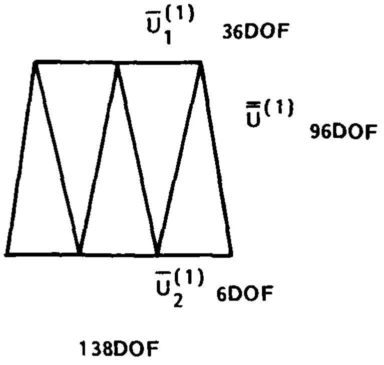

ADAPTOR (CHANGE AREA)
(b)

FLIGHT VEHICLE – ADAPTOR MODIFICATION
FIGURE 7

Table 1

BEAM-TRUSS MODEL MODIFICATION 1
COMPARISON OF MODAL RESULTS
MODE-MOD VS DIRECT CALCULATION

Elastic Mode No.	Modal Frequency (Hz)			Max Off Diagonal Term (Percent of Diagonal) $\psi_L^T M \psi_D$ * $\psi_L^T K \psi_D$
	Orig Structure	Modified Structure Mode Mod	Modified Structure Direct Calc	
1	3.937	3.907	3.907	0.0005
2	8.657	8.463	8.463	0.0017
3	20.864	17.167	17.167	0.0078
4	21.672	21.781	21.780	0.0170
5	27.341	27.468	27.464	0.0186

* ψ_D : Modal Vectors/Direct Calculation

ψ_L : Modal Vectors/Mode Modification

Table 2

BEAM-TRUSS MODEL MODIFICATION 2
COMPARISON OF MODAL RESULTS
MODE-MOD VS DIRECT CALCULATION

Elastic Mode No.	Modal Frequency (Hz)			Max Off Diagonal Term (Percent of Diagonal) $\psi_L^T M \psi_D$ * $\psi_L^T K \psi_D$
	Orig Structure	Modified Structure Mode Mod	Modified Structure Direct Calc	
1	3.937	3.524	3.524	0.00003
2	8.657	6.242	6.242	0.00002
3	20.865	9.269	9.269	0.00002
4	21.672	9.735	9.735	0.00002
5	27.341	20.959	20.959	0.00003
6	54.073	22.321	22.321	0.0002
7	56.597	53.561	53.561	0.0006
8	114.461	54.237	54.237	0.0006
9		95.414	95.411	0.0318
10		108.384	108.384	0.0001
11		121.722	121.721	0.0225
12		143.640	143.518	0.0460

* ψ_D : Modal Vectors/Direct Calculation

ψ_L : Modal Vectors/Mode Modification

Table 3

FLIGHT VEHICLE ADAPTOR MODIFICATION
COMPARISON OF STRUCTURAL FREQUENCIES
ORIGINAL MODAL FREQ VS MODE-MOD CHECK SOLUTION

Elastic Mode No	Original Modal Freq (HZ)	Mode Mod Modal Freq (HZ)
1	5.385	5.383
2	5.693	5.691
3	12.999	12.999
4	14.771	14.764
5	15.324	15.323
6	16.774	16.771
7	17.313	17.313
8	17.491	17.491
9	19.604	19.598
10	21.507	21.507
11	21.673	21.665
12	22.014	22.014
13	22.233	22.229
14	23.084	23.083
15	23.763	23.763
16	26.386	26.383
17	28.077	28.048
18	29.468	29.468
19	29.607	29.606
20	30.591	30.591
21	31.888	31.882
22	32.347	32.347
23	33.171	33.170
24	34.402	34.380
25	35.742	35.740
26	35.973	35.791
27	36.331	36.315
28	36.628	36.613
29	37.335	37.335
30	37.495	37.495

Table 4

FLIGHT VEHICLE ADAPTOR MODIFICATION
COMPARISON OF MODAL RESULTS
MODE-MOD VERSUS DIRECT CALCULATION

	FREQUENCY (Hz)		MAX OFF DIAGONAL TERM (PERCENT OF DIAGONAL)
	MODE MOD	DIRECT CALC	$\psi_L^T K \psi_D$ OR $\psi_L^T M \psi_D$ *
1	5.330	5.332	.16
2	5.649	5.650	.60
3	12.964	12.965	.24
4	14.602	14.609	.91
5	15.231	15.229	.68
6	16.632	16.636	.30
7	17.309	17.309	.33
8	17.489	17.489	.27
9	19.527	19.532	.29
10	21.435	21.449	1.92
11	21.503	21.503	.55
12	22.007	22.007	.88
13	22.174	22.182	1.82
14	23.043	23.043	.19
15	23.756	23.758	.44
16	26.244	26.250	.15
17	27.817	27.841	.30
18	29.453	29.453	.33
19	29.524	29.524	.26
20	30.585	30.585	.15
21	31.777	31.785	.18
22	32.303	32.303	.36
23	33.164	33.165	2.37
24	33.308	33.329	2.34
25	33.691	33.710	.55
26	34.152	34.198	.59
27	35.543	35.544	.52
28	35.880	35.882	.26
29	37.331	37.332	2.05
30	37.487	37.483	.26

*ψ_D: MODAL VECTORS/DIRECT CALCULATION

ψ_L: MODAL VECTORS/MODE MODIFICATION

EVALUATION OF AIRBORNE LASER BEAM JITTER USING STRUCTURAL DYNAMICS COMPUTER CODES AND CONTROL SYSTEM SIMULATIONS

C. L. Budde and P. H. Merritt
Air Force Weapons Laboratory
Kirtland AFB, New Mexico

and

C. D. Johnson
Anamet Laboratories Inc.
San Carlos, California

Beam stabilization for the Airborne Laser Laboratory (ALL) is accomplished by inertially stabilizing an annular reference mirror attached to the beam expanding telescope on the Airborne Pointing and Tracking System (APT). The analysis reported here documents the calculation of the residual beam jitter due to vibrations of the ALL and required the use of the NASTRAN finite element computer code to determine the motion of the various optical elements in the beam expanding telescope. These motions were then combined in an analytical expression to calculate the optical path motion for both the high energy laser and autoalignment beams. The final step was the incorporation in the frequency domain of the effects of the two servo mechanisms that stabilize the telescope to an inertial reference and drive the beam steering mirror to align the autoalignment beam and the high energy laser beam to the annular reference mirror.

INTRODUCTION

Beam stabilization for the Airborne Laser Laboratory (ALL) is accomplished by inertially stabilizing an annular reference mirror which is attached to the beam expanding telescope of the Airborne Pointer Tracker (APT) [1]. An autoalignment system sends out an annular beam which surrounds the high energy laser (HEL) beam and follows the same beam path. The annular beam reflects off the annular reference mirror and returns to an autocollimator, which then steers a two axis servo controlled mirror to slave the HEL beam to the stabilized annular reference mirror. Since the present annular reference beam uses only the outer annular region of the telescope primary mirror and since the autoalignment system operates near visible wavelengths, the figure of the primary mirror must be held to visible tolerances at the outer edges. Thermal distortions make this requirement difficult to meet, causing the autoalignment beam to defocus at the autoalignment autocollimator and thus degrading the performance of the autoalignment system. In order to investigate a possible solution to this problem, a study was conducted to see if an annular reference mirror around the small secondary mirror prior to the primary mirror would provide an acceptable reference for the autoalignment system. If the primary mirror was not included in the autoalignment system, the issue was, "How much beam jitter would not be sensed and corrected for by the modified autoalignment system?" The analysis reported here documents the calculation of the residual beam jitter due to the vibrations of the ALL aircraft.

The Analysis Flow Diagram, Figure 1, outlines the computational procedures used to determine the residual output beam jitter for the two competing optical systems. Finite element models were developed for the APT inner gimbal assembly including the telescope. Using measured vibration data from previous flight tests as forcing functions, the NASTRAN structural analysis computer code [4] was used to conduct random frequency response analyses. By using optical sensitivity equations which relate beam motion to the combined effect of the rigid body motion of the individual mirrors, the analyses yielded resultant beam motion uncorrected by the control systems. The PSDs of the uncorrected beam jitter of the HEL beam as well as the uncorrected beam jitter detected by the two competing autoalignment systems were obtained from NASTRAN. The effect of the APT inertial stabilization control system was incorporated by applying the stabilization error rejection function to the three jitter PSDs. This intermediate result produced the stabilization corrected output beam jitter plus the error signals to be used to drive the competing autoalignment systems. By using the autoalignment closed loop transfer function with the stabilization corrected optical error signal, the autoalignment correction to the HEL

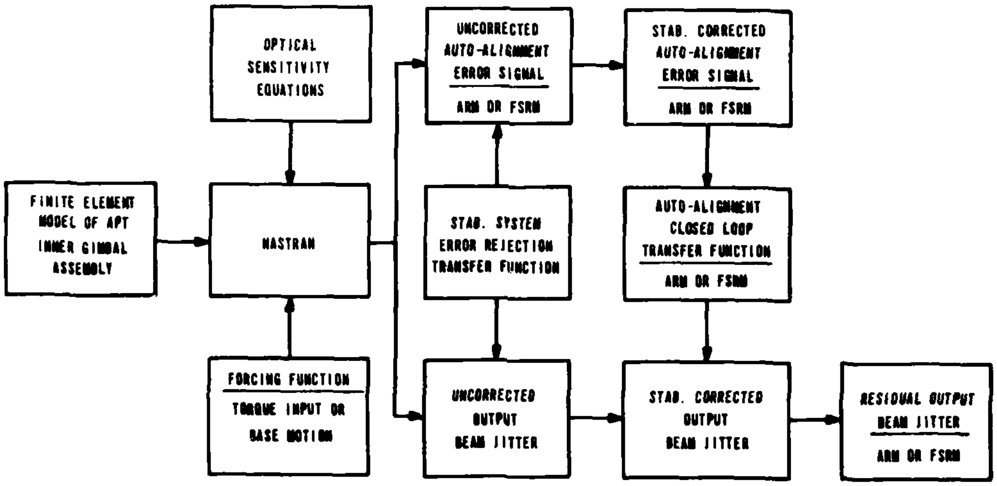
OPTICAL SENSITIVITY EQUATIONS
UNCORRECTED AUTO-ALIGNMENT ERROR SIGNAL
ARM OR FSRM
STAB. CORRECTED AUTO-ALIGNMENT ERROR SIGNAL
ARM OR FSRM
FINITE ELEMENT MODEL OF APT INNER GIMBAL ASSEMBLY
NASTRAN
STAB. SYSTEM ERROR REJECTION TRANSFER FUNCTION
AUTO-ALIGNMENT CLOSED LOOP TRANSFER FUNCTION
ARM OR FSRM
FORCING FUNCTION
TORQUE INPUT OR BASE MOTION
UNCORRECTED OUTPUT BEAM JITTER
STAB. CORRECTED OUTPUT BEAM JITTER
RESIDUAL OUTPUT BEAM JITTER
ARM OR FSRM

Figure 1.
Analysis Flow Diagram

beam jitter was calculated. By then coherently combining the HEL beam jitter and the auto-alignment correction, the PSD of the residual output beam jitter was obtained.

NASTRAN MODELS

Figure 2 shows an exploded view of the Airborne Laser Laboratory (ALL) Airborne Pointer Tracker (APT). Further details of the APT are given in Reference 1. For this study, only the inner gimbal assembly was of interest. The analysis of the APT was performed using the finite element code NASTRAN [4]. The mathematical model of the inner gimbal assembly was broken up into four smaller components: the gimbal ring; the beam expander, which contains a number of smaller subassemblies; the primary mirror; and the annular reference mirror. A detailed description of each of the models is given in Reference 2 along with information on the modes of vibration for each component. Plots of the finite element models are shown in Figures 3 through 6.

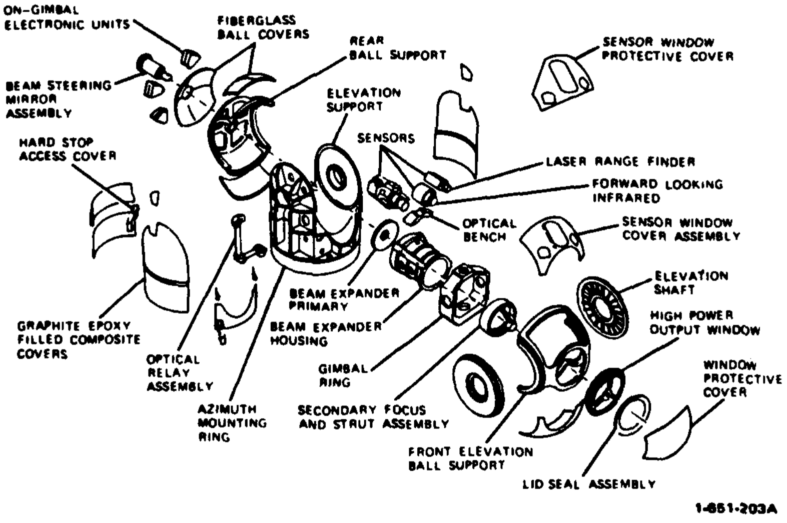
ON-GIMBAL ELECTRONIC UNITS
FIBERGLASS BALL COVERS
REAR BALL SUPPORT
SENSOR WINDOW PROTECTIVE COVER
BEAM STEERING MIRROR ASSEMBLY
ELEVATION SUPPORT
HARD STOP ACCESS COVER
SENSORS
LASER RANGE FINDER
FORWARD LOOKING INFRARED
OPTICAL BENCH
SENSOR WINDOW COVER ASSEMBLY
ELEVATION SHAFT
BEAM EXPANDER PRIMARY
HIGH POWER OUTPUT WINDOW
GRAPHITE EPOXY FILLED COMPOSITE COVERS
BEAM EXPANDER HOUSING
OPTICAL RELAY ASSEMBLY
GIMBAL RING
WINDOW PROTECTIVE COVER
AZIMUTH MOUNTING RING
SECONDARY FOCUS AND STRUT ASSEMBLY
FRONT ELEVATION BALL SUPPORT
LID SEAL ASSEMBLY
1-651-203A

Figure 2.
Exploded View of APT

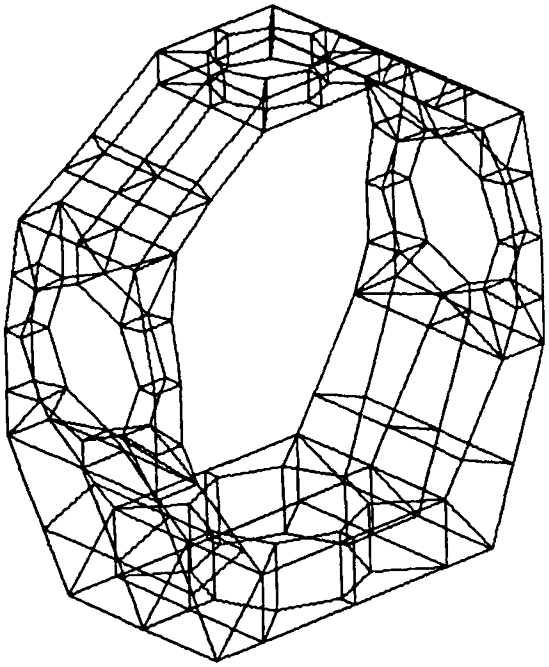

Figure 3.
Finite Element Model of the Gimbal Ring

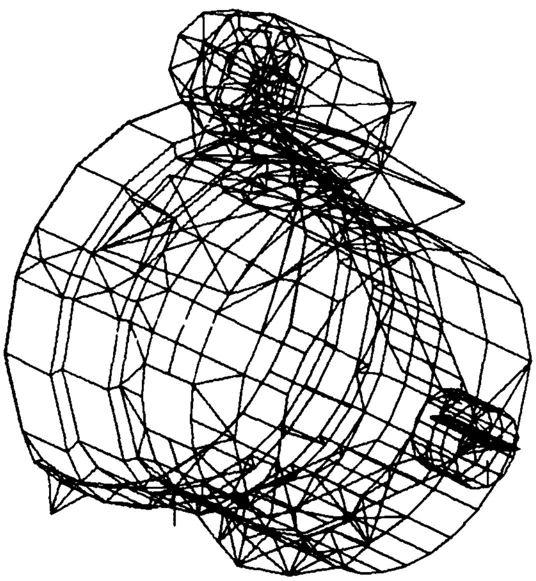

Figure 4.
Finite Element Model of the Beam Expander
with Saddle and Sensors

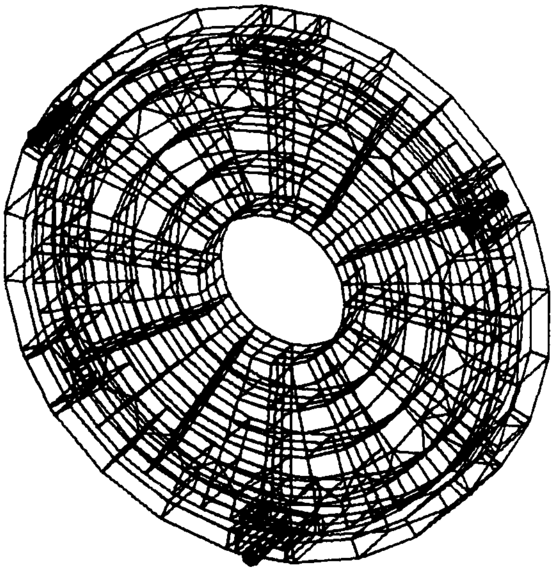

Figure 5.
Finite Element Model of the Graphite-Epoxy
Primary Mirror

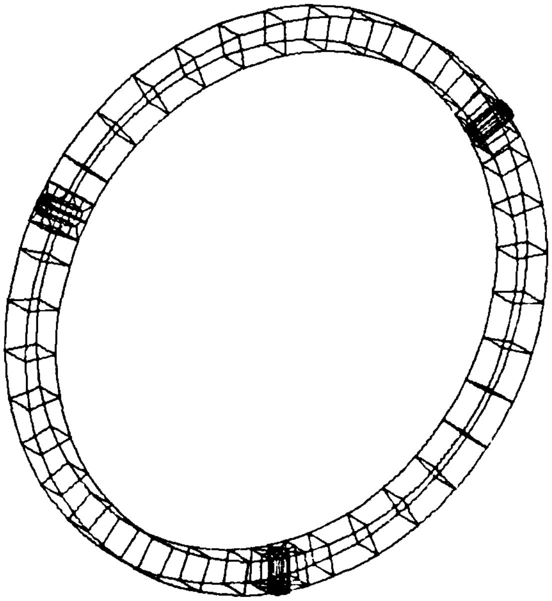

Figure 6.
Finite Element Model of the Beryllium
Annular Reference Mirror

If the four component models were combined into a large single model, the resulting model would contain 16,242 degrees of freedom. Attempting to execute such a large model in a single pass on the computer is impractical because of the tremendous cost and because the run time would exceed the mean-time-to-failure of the computer. Therefore, the approach taken was to break the structure into a number of components, execute those components individually, and combine the results from the component analyses into a system analysis. The procedure used to perform this analysis is known as component modal synthesis. Both References 2 and 3 contain further details on this technique.

OPTICAL SENSITIVITY EQUATIONS

In order to study the effects of structural vibrations upon the beam pointing accuracy of the APT, optical sensitivity equations must be derived which relate beam motion to the linear and angular perturbations of the optical elements in the system. These equations are based on the linear geometric trace of a single optical ray. Only rigid body perturbations of the optical elements were considered. For the primary mirror and the annular reference mirror, which were modeled in great detail, the rigid body motion was defined as the average motion of a number of points around the circumference of the mirror.

Figure 7 shows the optical layout of the APT beam expanding telescope. With Figure 7 as reference, equation (1) gives the tilt error of the high energy laser beam leaving the APT.

$$\Delta\Theta_0 \approx \frac{2}{R_P}(\Delta X_S - \Delta X_P) - \frac{2R_S}{R_P}\Delta\Theta_S + 2\Delta\Theta_P \qquad (1)$$

R_P and R_S are the radii of curvature of the primary and secondary mirror respectively. The ΔXs are translational perturbations and the $\Delta\Theta$s are rotational perturbations. Subscript S refers to the secondary mirror and subscript P refers to the primary mirror. For azimuth tilt error, azimuth rotations and lateral displacements of the mirrors are used. For elevation tilt error, elevation rotations and vertical displacements are used.

Equation (2) gives the tilt error of the autoalignment beam received at the autoalignment sensor for the system using the annular reference mirror.

$$\Delta\Theta_{AA} \approx \frac{4}{R_S}(\Delta X_{SA} - \Delta X_P) - 4\Delta\Theta_{SA} + \frac{4R_P}{R_S}\Delta\Theta_P - \frac{2R_P}{R_S}\Delta\Theta_R \qquad (2)$$

Note the substitution of the secondary annulus mirror for the secondary mirror in equation (2). For this system, the secondary annulus has the same radius of curvature as the secondary mirror. Subscript SA refers to the secondary annulus mirror and subscript R refers to the annular reference mirror.

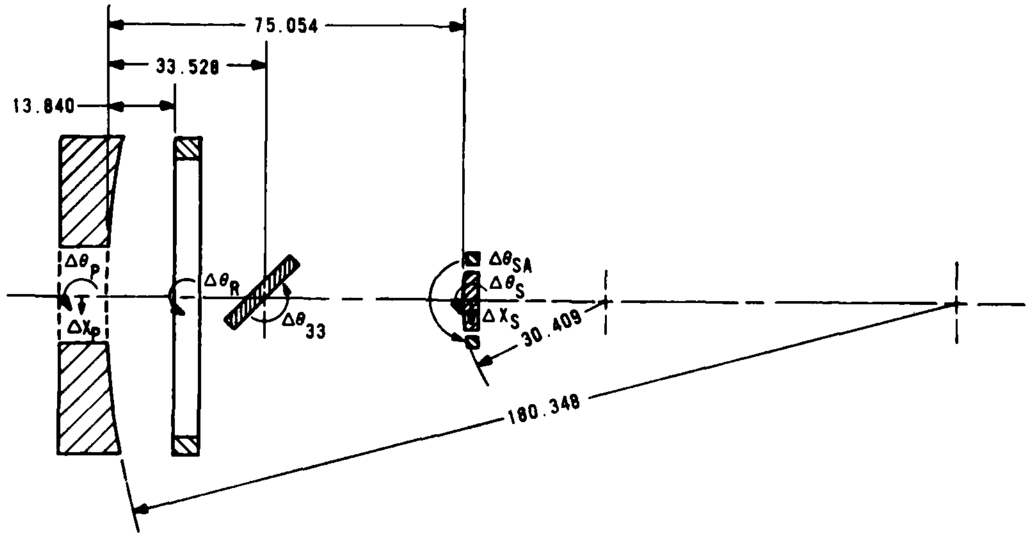

Figure 7.
APT Telescope Optical Layout

Equation (3) gives the tilt error of the autoalignment beam at the autoalignment sensor for the system using the flat secondary reference mirror.

$$\Delta\theta_{AAFS} \approx -2\Delta\theta_{SA} \qquad (3)$$

These optical sensitivity equations were incorporated directly into the NASTRAN model using the multi-point constraint feature.

LOADING CONDITIONS

The loading on the inner gimbal assembly can be characterized by a combination of torques and base accelerations in three orthogonal directions. Actual flight data was used to define these loading conditions in PSD form over the frequency range 5 to 500 Hz. Shown in Table 1 are the RMS values of the five loading conditions over this same frequency range.

Table 1.
RMS Loading Conditions

Azimuth Torque	353.3 in-lbs
Elevation Torque	594.4 in-lbs
X-Acceleration	69.34 in/sec^2
Y-Acceleration	106.90 in/sec^2
Z-Acceleration	64.14 in/sec^2

X is the line-of-sight direction, Y is the horizontal direction, and Z is the vertical direction. Figure 8 shows the PSD of the azimuth driving torque, while Figure 9 shows the PSD of the Y base acceleration. In addition to the loading conditions listed above, white PSD torques were applied to the drives in order to study the structural response unperturbed by peaks in the loading. Each loading case was analyzed separately.

RANDOM FREQUENCY RESPONSE ANALYSIS

Given the finite element models, optical sensitivity equations, and loading conditions described above; the NASTRAN structural analysis computer code [4] was used to perform random frequency response analyses. Each loading condition was analyzed as a separate case. The loading was applied in PSD form and all of the responses were obtained in PSD form. The PSD of the uncorrected beam jitter of the high energy laser beam, PSDs of the uncorrected beam jitter of the autoalignment beam for the two competing autoalignment systems, PSDs of the relative motion between optical components and/or mounting planes, and PSDs of the motion

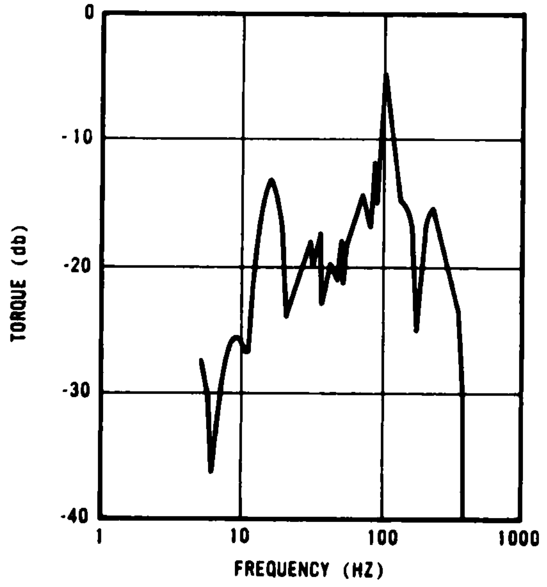

Figure 8.
Input PSD Torque at the Fine Azimuth Drive

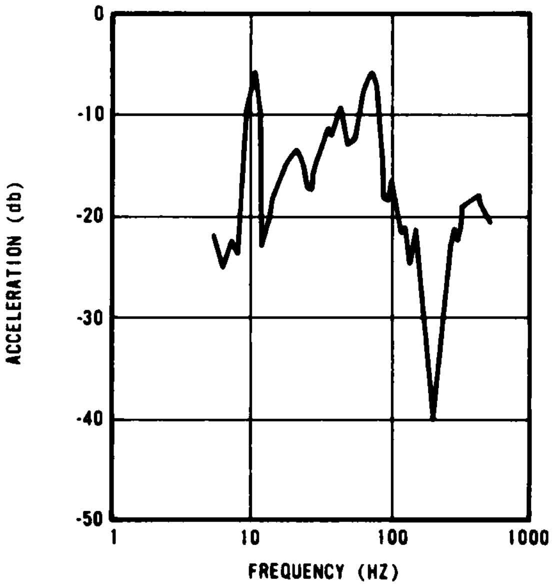

Figure 9.
Base Acceleration PSD in the Horizontal (Y) Direction

of selected optical components were obtained. All analyses were performed for the frequency range 5 to 500 Hz. As a typical example, Figure 10 shows the uncorrected azimuth PSD tilt error of the high energy laser beam due to the input azimuth PSD torque. By studying the response of the system to the different types of loading conditions, it was determined that the gimbal torques have a greater effect on beam jitter below 100 Hz, while the base accelerations have a greater effect on beam jitter above 100 Hz.

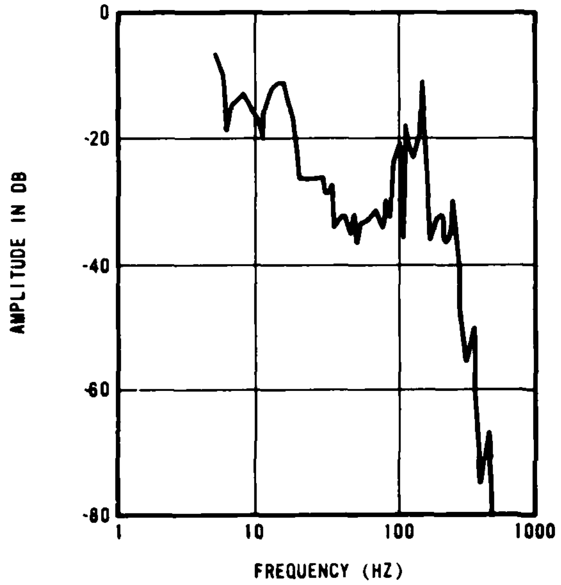

Figure 10.
Uncorrected Azimuth PSD Tilt Error of High Energy Laser Beam Leaving APT Resulting from Input Azimuth PSD Torque

CONTROL SYSTEM CALCULATIONS

As explained, the NASTRAN model provided the jitter of the autoalignment beam as seen by the autoalignment autocollimator and the jitter of the HEL beam as it exits the telescope. However, the NASTRAN output was based completely on structural models and assumed the telescope to be a free gimbal with no restraints. This is not the true system operation. The telescope is an actively controlled stable platform using two rate integrating gyroscopes to sense inertial motion.

Referring to Figure 1, the Analysis Flow Diagram, it is seen that the control systems interact with the NASTRAN output at several locations. First, consider the autoalignment reference beam, top center block of Figure 1. The optical reference beam is projected by relay mirrors off the autoalignment steering mirror, through the telescope, and is then reflected by the Annular Reference Mirror which is mounted on the telescope. The response calculated by NASTRAN indicated a larger amount of motion than would actually occur in all of the angular terms in equation (2). The translation terms, however, would not be affected by the angular motion of the telescope. In addition, the significant translation motions occurred at high frequencies and hence were not influenced by the control system. The active control system which functions to reject the low frequency motions and inertially stabilize the telescope is referred to as the stabilization system. The transfer function that describes the operation of this control system is classically called the "error rejection function." This is a ratio of the error (inertial motion after the control system operation) to the input motion (the motion calculated by NASTRAN). By multiplying the squared stabilization error rejection function times the PSD of the autoalignment sensed error, the low frequency beam motion seen by the autoalignment sensor is greatly reduced. This is, of course, exactly how the hardware systems perform.

Secondly, consider how the stabilization system affects the HEL beam leaving the telescope. Referring to equation (1), since the secondary and primary mirrors are both rigidly attached to the telescope, it is seen that $\Delta\Theta_S$ and $\Delta\Theta_P$ would incorporate the telescope motion into the output beam. Again, the translation is a higher frequency term that would effect the outgoing beam at frequencies above the operating region of the control system. Therefore, just as with the autoalignment reference beam, the calculated PSD of the output beam motion was multiplied by the squared error rejection function of the stabilization system.

The above descriptions account for two major corrections to the NASTRAN calculations. However, there is a third effect which still had to be accounted for. The purpose of the autoalignment system is to sense any optical errors up to the telescope and correct for them by driving a high frequency two axis steering mirror. This mirror, Θ_{33} in Figure 7, sits just prior to the secondary mirror. Both the autoalignment and the output beams sense $\Delta\Theta_P$ in equations (1) and (2). Also, if $\Delta\Theta_S$ is truly measured by $\Delta\Theta_{SA}$, this term is common to both equations. The translation term is again similar if the secondary annulus measures the secondary mirror translation. Therefore, for the system using the on gimbal annular reference mirror, the autoalignment system corrects for several errors. For the proposed flat secondary reference, equation (3) does not contain the beam expander terms. However, also notice that equation (2) contains a term, $\Delta\Theta_R$, angular motion of the annular reference mirror, not in the output beam equation (1). If this mirror resonated, it could put false signals back into the autoalignment system. Therefore, the computer simulation needed to accurately include the autoalignment effects.

This posed two calculation requirements. First, the autoalignment system only corrects the output beam over the frequency bandwidth of the autoalignment system. Therefore, a "closed loop" transfer function was calculated for the autoalignment system. This function describes how well the steerable mirror follows an optical error sensed by the autocollimator. The closed loop transfer function was squared and multiplied by the PSD of the stabilization corrected autoalignment error signal, as shown in Figure 1. The second problem was that the two PSDs of the autoalignment correction and the output beam error could not be directly combined to estimate output jitter. The reason was that the steerable mirror obviously had to be driven with the correct phase to cancel the output jitter, and PSDs don't contain phase by definition. However, the NASTRAN models and the control system models both calculate phase. Therefore, the output beam jitter phase and the autoalignment phase were calculated and stored by NASTRAN. Then the autoalignment control system phase was calculated and applied to the NASTRAN autoalignment values. Then the two PSDs were combined coherently by using the following equation:

$$\Phi_{RR} = \Phi_{00} + \Phi_{33} - 2\sqrt{\Phi_{00}\Phi_{33}}\cos\alpha \qquad (4)$$

where

Φ_{RR} = residual output beam PSD

Φ_{00} = output beam PSD uncorrected by autoalignment

Φ_{33} = PSD for the steering mirror controlled by the autoalignment system

α = phase of autoalignment mirror with respect to the output beam.

This coherent addition scheme is shown schematically in Figure 11. Note that all quantities in equation (4) are functions of frequency. Also note that the last term on the right side is equal to twice the real part of the cross power spectrum.

The final result was an evaluation of output beam jitter utilizing the complex NASTRAN model and the complex control system models. By using NASTRAN outputs, it was possible to use the control system simulations to evaluate different disturbance inputs and different autoalignment reference mirrors. The control system simulation is described in Reference 5.

VERIFICATION OF MODEL

It was obviously necessary to compare the computer predictions to real data to "anchor" the results. It was not possible to obtain any real data for the performance with the flat secondary, since this configuration had not been built. However, a large amount of test data was available from previous flight testing for the on gimbal annular reference mirror configuration. Given all of the loading conditions that were analyzed, the best forcing function input to NASTRAN was considered to be the measured flight torque which should include all of the disturbance effects. Data was also available from a target board carried on another airplane. This data showed the effects

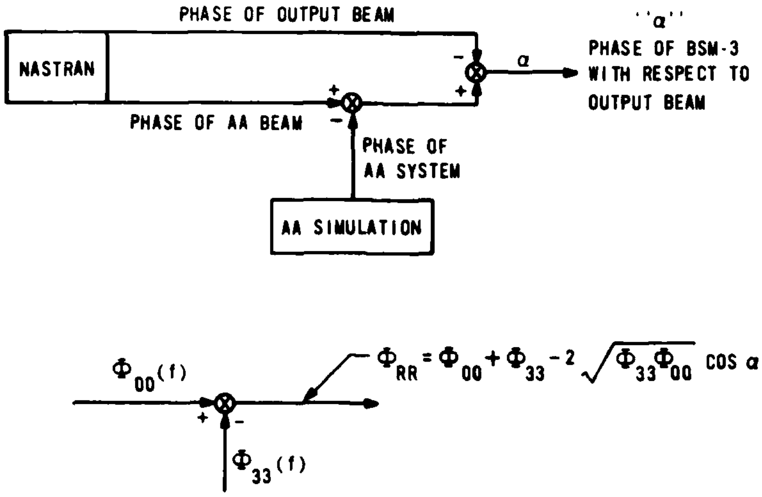
PHASE OF OUTPUT BEAM
NASTRAN
-
+
α
"α"
PHASE OF BSM-3 WITH RESPECT TO OUTPUT BEAM
+
-
PHASE OF AA BEAM
PHASE OF AA SYSTEM
AA SIMULATION
$\Phi_{00}(f)$
+
-
$\Phi_{33}(f)$
$\Phi_{RR} = \Phi_{00} + \Phi_{33} - 2\sqrt{\Phi_{33}\Phi_{00}}\cos\alpha$

Figure 11.
Coherent Beam Addition

of the total output beam motion including input beam motion to the pointing system. The input beam motion was not modeled during this computer effort. The overlay of two typical PSDs is shown in Figure 12. This figure compares the analytical prediction of residual beam jitter with target board data for the azimuth axis under flight torque loading.

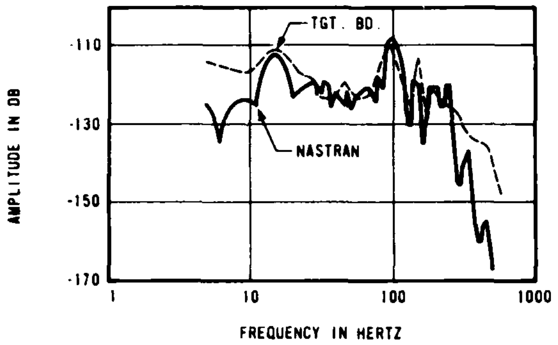

Figure 12.
Azimuth PSD Comparison of NASTRAN Prediction to Target Board Data

Notice that there is some disagreement at low frequency and at high frequency, but most of the significant effects between 10 Hz and 200 Hz seem to be modeled. The forward sum of the PSDs also supports the validity of the models. Notice in Figure 13 that the forward sums compare very well except at the starting point and above 200 Hz. The disagreement at low frequency is not completely understood, but it may be aircraft to aircraft motion, or possibly a low frequency asymptote in the data due to data analysis using fast fourier transform techniques. The disagreement at high frequency is probably due to some mirror resonances or input laser motion not modeled by NASTRAN. However, since this analysis effort was to obtain a comparison of the two system designs, not a comparison of system model to real data, the authors felt that the comparison was adequate to permit completion of the project.

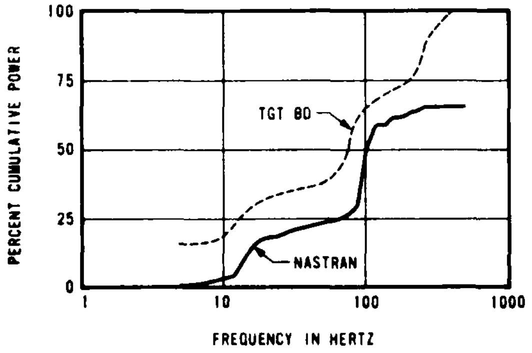

Figure 13.
Azimuth Forward Sum Comparison of NASTRAN Prediction to Target Board Data

SYSTEM RESULTS

It was possible to compare PSDs and RMS levels for the two competing system designs.

The PSD comparison for the azimuth axis is shown in Figures 14 and 15. It is seen that the flat secondary change did not have a major effect on the output PSD. Most of the major peaks are similar in both PSDs. The most noticeable change is a shift in the relative magnitudes of the peaks. Notice that the 15 Hz resonance is more dominant in Figure 14 than in Figure 15. The high frequency fall off is slightly different also. On these two particular figures, the RMS level decreased by 20% by going to the flat secondary configuration.

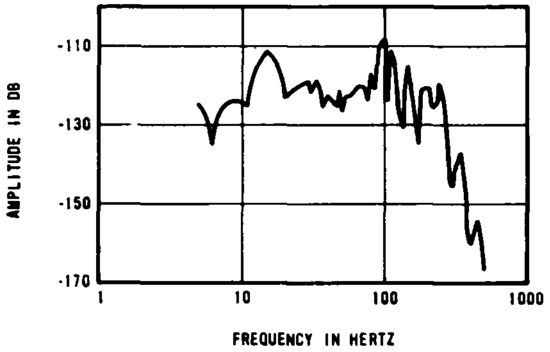

Figure 14.
Azimuth PSD Resultant Beam Jitter for ARM Reference System Due to Input Azimuth PSD Torque

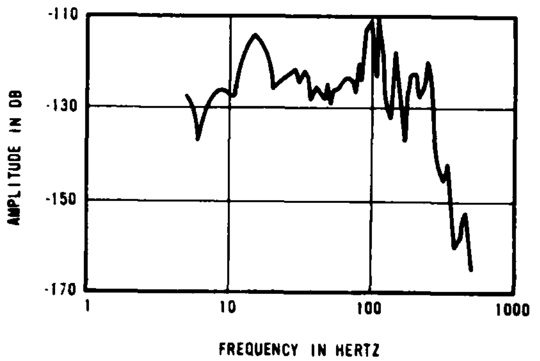

Figure 15.
Azimuth PSD Resultant Beam Jitter for Flat Secondary System Due to Input Azimuth PSD Torque

The RMS levels of the two systems for the different loading conditions are normalized and listed in Tables 2 and 3. Note that all values are normalized to airborne performance with flight torque loading for the ARM reference system. The results show good performance of the flat secondary configuration in comparison to the annular reference mirror system. Notice that the flat secondary RMS level is smaller than the Annular Reference Mirror (ARM) level in four of eight cases. In the other four cases the flat secondary never drastically increased the jitter. The rather large values predicted for the linear vibration loading may be caused by the quality of the input vibration data. The instrumentation scaling on the collected linear vibration data was such that a high proportion of the recorded signal levels may have been caused by instrumentation noise.

Table 2.
Comparison of System Models for Azimuth Axis

INPUT DISTURBANCE	ARM REFERENCE	FLAT SECONDARY
Flight Torque	1.00	0.78
Z Linear Vibration	0.76	0.64
X Linear Vibration	0.57	0.52
Y Linear Vibration	4.45	4.92

Table 3.
Comparison of System Models for Elevation Axis

INPUT DISTURBANCE	ARM REFERENCE	FLAT SECONDARY
Flight Torque	1.00	1.04
Z Linear Vibration	2.46	2.68
X Linear Vibration	1.06	1.01
Y Linear Vibration	1.29	1.54

CONCLUSIONS

This paper has described a sophisticated and comprehensive, yet practical and straightforward method of simulating the behavior of a complex servo-mechanical-optical-control system. The predicted residual output beam jitter for the unmodified system was compared to measured flight data and good agreement was obtained. By comparing the predicted residual output beam jitter for the two competing autoalignment systems, the main conclusion of the study was derived. The analysis showed that the modified system using an annular reference mirror around the telescope secondary mirror gave equivalent residual output beam jitter. Since the new autoalignment system would provide reduction of the autoalignment beam focus problem, easier optical alignment, relaxation of the optical figure requirement for the primary mirror, and a decrease in system complexity; it was determined that the new system was superior. Therefore, the new reference mirror was incorporated into the flight hardware. The result of this study proved the value of a systems analysis which combined optical sensitivity equations, structural models, and control system simulations.

REFERENCES

1. Hughes Aircraft Company, "Airborne Pointing and Tracking System: Operation and Maintenance Handbook (Third Edition)," HAC Report No. P73-1R/J79-366, January 1979.

2. Johnson, C. D., "Structural-Optical Sensitivity Study of the APT Inner Gimbal Assembly," ASIAC Report No. 179.1A, Anamet Laboratories, July 1979.

3. Klosterman, A. L. and Lemon, J. R., "Building Block Approach to Structural Dynamics," VIBR-30, ASME Publication, 1969.

4. McCormick, C. W. (Editor), "MSC/NASTRAN User's Manual," MSR-39, MacNeal-Schwendler Corporation, May 1979.

5. Sebesta, H. R., Ebbesen, L. R. and Perrault, J. E., "Modeling and Simulation of Pointing and Alignment Systems," AFWL-TR-77-264, March 1978.

DISCUSSION

Mr. Vitaliano (Harris Corporation): How many degrees of freedom did the model have, how many modes were extracted and what was the approximate cost to get through one iteration?

Mr. Johnson: The model has approximately 23,000 degrees of freedom and 40 to 50 modes were extracted from the system model.

FATIGUE LIFE PREDICTION FOR MULTILEVEL
STEP-STRESS APPLICATIONS

Ronald G. Lambert
General Electric Company
Aircraft Equipment Division
Utica, New York 13503

A cumulative fatigue damage procedure is developed which uses linear elastic fracture mechanics theory as its basis in order to predict the fatigue life of structures subjected to multilevels of sequentially applied stress. The applied stress can be sinusoidal or random. The material's fatigue curve is treated as a scatterband of failure points.

INTRODUCTION

Closed form equations have been developed that calculate the fatigue life of structures subjected to multilevels of sequentially applied sinusoidal or random stress. Fatigue life is expressed in terms of median cycles to failure, probability of failure at N applied stress cycles and cycles to first failure. The deterministic damage law proposed in this paper applies to all initial crack (i.e., flaw) lengths that either exist in the structural material as dislocations or metallurgical inclusions, were introduced during manufacturing fabrication and assembly operations, or were created during temporary overload conditions. The sequence effects on fatigue life are accounted for which are consistent with empirical data.

APPROACH SUMMARY

The analytical approach taken to develop the fatigue life prediction equations is as follows: Paris' crack growth equation is applied to sinusoidal step-stress levels [1]. Linear elastic fracture mechanics equations that relate a structural element's crack length, applied stress and stress cycles are used to calculate crack half-length "a" throughout the various sequential stress levels [2]. Crack growth is traced from an initial crack length value of a_i to the final value where fracture of the structural element occurs. The condition imposed between stress levels is that the final crack length of the previous stress level becomes the initial crack length of the present stress level. That is, the crack size does not change between stress levels. All of these equations are algebraically arranged into a more convenient form which then represents a cumulative damage law referenced to the nth stress level of n stress levels. The median cycles to failure at the nth stress level are then determined. This is described in Appendix A.

The median values of the damage functions at all stress levels up to and including that for the nth stress level are developed as an extension of Appendix A. The resulting damage functions are in terms of cycle ratio damage functions D_j and correction factors $X_{j,\ell}$ which account for the dependency upon the initial crack size, the sequence and values of the applied stress levels, a geometrical parameter and the material's fracture toughness. This part of the analysis is deterministic in nature (i.e., no random variables are considered).

A material's fatigue curve is treated as a scatterband of failure points, not a single line, by letting the fatigue curve parameter A become a random variable with average value $\overline{A}$ and standard deviation Δ [3]. The resulting expression for probability of failure at N cycles F(N) is in terms of the previously derived cumulative damage median values and the material's fatigue curve parameters $\overline{A}$, Δ and β.

All derived equations are extended to cover the sequentially applied random step-stress level case by using previously developed relationships between a material's sinusoidal and random fatigue curves [2,4]. For a given average number of stress cycles, there exists a random rms stress level that will propagate a crack of the same size as that of a calculable corresponding sinusoidal stress.

LIMITATIONS

Application of the proposed expressions is limited to cases where the material is stressed elastically in the linear region of the crack growth rate curve and where the fracture mechanics geometrical parameter remains relatively constant. These limitations are not considered to be serious practical limitations.

PROPOSED DAMAGE LAW

Appendix A describes the derivation of the proposed damage law. Define:

ΔS_j = jth applied sine stress range level

N_j = actual number of stress cycles applied at the jth stress level

N_{f_j} = number of stress cycles to failure at the jth stress level

ΔK_c = material's fracture toughness

Y = geometrical parameter $\simeq$ constant

a_i = initial crack half-length

a_{c_j} = critical crack half-length at the jth stress level

C_o = crack growth rate curve constant

θ = crack growth rate curve constant

$\phi = \dfrac{\theta - 2}{2}$

$$k = C_o \phi Y^{\theta} \tag{1}$$

$$a_{c_j} = \left[\frac{\Delta K_c}{Y \Delta S_j}\right]^2 \tag{2}$$

$$N_{f_j} = \frac{1}{k \Delta S_j^{\theta}} \left[\left(\frac{1}{a_i}\right)^{\phi} - \left(\frac{1}{a_{c_j}}\right)^{\phi}\right] \tag{3}$$

$$D_j = \frac{N_j}{N_{f_j}} \tag{4}$$

n = number of step-stress levels

$$X_{j,n} = \left[\frac{1 - \left(\dfrac{a_i Y^2 \Delta S_j^{\,2}}{\Delta K_c^{\,2}}\right)^{\phi}}{1 - \left(\dfrac{a_i Y^2 \Delta S_n^{\,2}}{\Delta K_c^{\,2}}\right)^{\phi}}\right] \tag{5}$$

Failure occurs when

$$\sum_{j=1}^{n-1} (D_j X_{j,n}) + D_n = 1 \tag{6}$$

This assumes that failure has not already occurred at one of the jth stress levels ($j < n$).

N_{m_n} = fatigue life = median cycles to failure at the nth stress level

$$N_{m_n} = N_{f_n} \times D_n \tag{7}$$

where

$$D_n = 1 - \sum_{j=1}^{n-1} (D_j X_{j,n}) \tag{8}$$

It will be noted that the product $D_j X_{j,n}$ represents the equivalent cumulative damage at the nth stress level done by actual damage D_j at the jth stress level. That is, it is the "damage at the jth level reflected" to the nth level.

DAMAGE FUNCTION MEDIAN VALUES

It is possible for failure to occur at one of the jth stress levels prior to reaching the nth stress level ($j < n$). Therefore, the damage function median values stress levels prior to the nth level must be calculated. Note: It will later be shown that the damage function is a random variable. However, the significant value for this analysis is the damage median value.

Define

n = total number of step-stress levels

L = Roman numeral designation of one of the n stress levels

ℓ = English numerical designation of stress level L

n = 2, 3, 4, ...

L, ℓ = 1, 2, 3, ..., n

D_ℓ = damage accumulated during stress level L; $D_\ell = N_\ell / N_{f_\ell}$

D_L = total cumulative damage at stress level L; equivalent damage of all previous stress levels relative to level L plus D_ℓ

As an extension of Appendix A;

$$D_I = \frac{N_1}{N_{f_1}} = D_1 \tag{9}$$

$$D_{II} = \frac{N_1}{N_{f_1}} \left[\frac{1 - \left(\frac{a_i Y^2 \Delta S_1{}^2}{\Delta K_c{}^2} \right)^{\phi}}{1 - \left(\frac{a_i Y^2 \Delta S_2{}^2}{\Delta K_c{}^2} \right)^{\phi}} \right] + \frac{N_2}{N_{f_2}} \qquad (10)$$

or

$$D_{II} = D_1 X_{1,2} + D_2 \qquad (11)$$

$$D_{III} = D_1 X_{1,3} + D_2 X_{2,3} + D_3 \qquad (12)$$

$$D_{IV} = D_1 X_{1,4} + D_2 X_{2,4} + D_3 X_{3,4} + D_4 \qquad (13)$$

$$D_L = \sum_{j=1}^{\ell-1} D_j X_{j,\ell} + D_\ell \qquad (14)$$

Failure will occur when $D_L = 1$.

MEDIAN TOTAL CYCLES-TO-FAILURE

The median total cycles to failure N_{m_T} is equal to all of the cycles at the $n-1$ various stress levels plus N_{m_n}:

$$N_{m_T} = \sum_{j=1}^{n-1} N_j + N_{m_n} \qquad (15)$$

FAILURE PROBABILITIES

Reference [3] describes in detail the derivation of the probability of failure at N stress cycles equation F(N). The material's fatigue curve is treated as a scatterband of failure points by letting the term A in the following fatigue curve expression become a random variable of average value $\bar{A}$ and standard deviation Δ.

$$\frac{\Delta S}{2} = A\, N^{-1/\beta} \qquad (16)$$

$\frac{\Delta S}{2}$ = cyclic stress amplitude (MPa)(ksi)

A = fatigue curve constant (MPa)(ksi)

N = cycles to failure

β = fatigue curve slope parameter

$\bar{A}$ = average value of A (MPa)(ksi)

Δ = standard deviation of A (MPa)(ksi)

NOTE: $\frac{\bar{A}}{\Delta} \approx 13$ for many structural materials

$\beta \approx 9$ for ductile materials

$\beta \approx 20$ for brittle materials

As previously defined,

D_L = median value of damage function at stress level L

From reference [3],

$$F(N_1)_I = 0.5 + \mathrm{erf}\left[\frac{\bar{A}}{\Delta}\,\{D_I{}^{1/\beta} - 1\}\right]$$

$$\vdots$$

$$F(N_\ell)_L = 0.5 + \mathrm{erf}\left[\frac{\bar{A}}{\Delta}\,\{D_L{}^{1/\beta} - 1\}\right] \qquad (17)$$

where

$$\mathrm{erf}(\alpha) = \frac{1}{2\pi} \int_0^{\alpha} e^{-y^2/2}\, dt \qquad (18)$$

$$\mathrm{erf}(0) = 0 \quad ; \quad \mathrm{erf}\,(\infty) = 0.5$$

$$\mathrm{erf}(-\alpha) = -\mathrm{erf}\,(\alpha)$$

See Reference [4].

SCATTERBAND WIDTH EFFECT

The effect of increasing the width of the scatterband (i.e., of increasing the value of Δ in equation (17)) is to increase the failure probability in the early stress cycles. Stated differently increasing Δ lowers the cycles to first failure, which is perhaps the most significant fatigue life characterization.

CYCLES TO FIRST FAILURE

If there are b independent opportunities for failure, the first failure will occur on the average when F(N) = 1/b. Thus, the value of N that makes F(N) = 1/b is the fatigue life of cycles to first failure.

SINE-RANDOM STRESS EQUIVALENCY

For a given average number of stress cycles, there exists a random rms stress level that will propagate a crack of the same size as that of a calculable corresponding sinusoidal stress. From Reference [2] the equivalency is quantitatively expressed as

$$\Delta S = \left(\frac{2\bar{A}}{\bar{C}}\right) \sigma \qquad (19)$$

where

ΔS = sine stress range (MPa)(ksi)

$\bar{A}$ = average sine fatigue curve constant (MPa)(ksi)

$\overline{C}$ = average random fatigue curve constant (MPa)(ksi)

σ = random rms stress (MPa)(ksi)

From Reference [4]:

$$\Delta S = 2^{1.5}\left[\Gamma\left(\frac{2+\beta}{2}\right)\right]^{1/\beta}\sigma \qquad (20)$$

As before, β = fatigue curve slope parameter.

All of the previously developed damage and fatigue life equations can be used for random stress cases by substituting $(2\overline{A}/\overline{C})\sigma$ in place of ΔS.

EXAMPLES (GENERAL)

Two examples of single stress level and six examples of step-stress cases will be worked out. Figure 1 will be used as the stressed specimen for all examples.

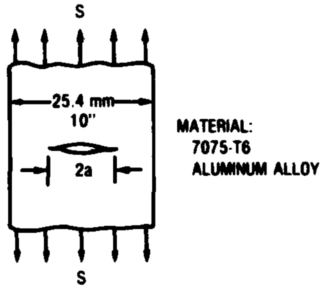

Fig. 1 - Center cracked strip loaded in tension

C_o = 1.5×10^{-10} m/cycle

(6.0×10^{-9} in./cycle)

Y = 1.77

θ = 4 ; ϕ = 1 ; β = 9.65

ΔK_c = 2.2 MPa $\sqrt{m}$ (20 ksi $\sqrt{in.}$)

$\overline{A}$ = 1240 MPa (180 ksi)

$\overline{C}$ = 552 MPa (80 ksi)

Δ = 124 MPa (18 ksi)

The examples will use various combinations of the stress levels 69, 103, 138, 172 MPa (10, 15, 20, 25 ksi) and initial crack half-lengths a_i of 1.27 and 2.54 mm (0.050 and 0.100 inch).

Table 1 shows the applied stresses that will be used in different sequences. Each sine ΔS value and its equivalent random σ value is consistent with equation (20).

TABLE 1
Applied Stress Levels

ΔS		σ (rms)	
(MPa)	(ksi)	(MPa)	(ksi)
69	10	15.3	2.22
103	15	22.9	3.33
138	20	30.7	4.44
172	25	38.2	6.67

EXAMPLES (SPECIFIC)

Table 2 shows the given conditions of initial crack half-length a_i, stress levels and sequences and number of applied stress cycles at each stress level.

TABLE 2. GIVEN CONDITIONS

Example	a_i		j	ΔS_j		N_j
	(mm)	(in.)		(MPa)	(ksi)	(cycles)
1	2.54	0.100	1	69	10	N_1
2	2.54	0.100	1	172	25	N_1
3	2.54	0.100	1	69	10	7825
			2	172	25	N_2
4	2.54	0.100	1	172	25	110
			2	69	10	N_2
5	1.27	0.050	1	69	10	8160
			2	103	15	1530
			3	138	20	448
			4	172	25	N_4
6	1.27	0.050	1	172	25	164
			2	138	20	448
			3	103	15	1530
			4	69	10	N_4
7	2.54	0.100	1	69	10	3913
			2	103	15	690
			3	138	20	182
			4	172	25	N_4
8	2.54	0.100	1	172	25	55
			2	138	20	182
			3	103	15	729
			4	69	10	N_4

Find:

(a) The critical crack half-length values

(b) The damage function values

(c) The median cycles to failure at the nth stress level, N_{m_n}

(d) The total median cycles to failure, N_{m_T}

(e) F(N) versus N

Solution:

(a) Table 3 shows the critical crack half-length values. Refer to equation (2). Note that a_i is inversely related to ΔS.

TABLE 3. CRITICAL CRACK HALF-LENGTH VALUES

ΔS		a_c	
(MPa)	(ksi)	(mm)	(in.)
69	10	32.5	1.28
103	15	14.4	0.567
138	20	8.1	0.319
172	25	5.2	0.204

(b) Table 4 shows the damage function expressions using equations (3), (4), (5) and (9) - (14). Note that the "reflected" damage values are different from the actual damage values. For example 3, ($\Delta S_2 > \Delta S_1$) the actual damage value N_1/N_{f_1} = 0.5 which "reflects" to a value of 0.904 at the second stress level due to the correction term X = 1.81.

(c) Table 5 shows the N_{mn} values using equations (7) and (8) and the data from Table 4. For example 3, failure occurs for $D_{II} = 1$; $N_2/221 = 1 - 0.904 = 0.096$. Therefore, $N_2 = 21$ cycles.

TABLE 4. DAMAGE FUNCTION EXPRESSIONS

Example	j	N_j (cycles)	N_{f_j} (cycles)	N_j/N_{f_j}	X	D
1	1	N_1	15,650	$N_1/15650$	-	$D_I = N_1/15650$
2	1	N_1	221	$N_1/221$	-	$D_I = N_1/221$
3	1	7825	15,650	0.5	-	$D_I = N_1/15650$
	2	N_2	221	$N_2/221$	$X_{1,2} = 1.81$	$D_{II} = 0.904 + N_2/221$
4	1	110	221	0.5	-	$D_I = N_1/221$
	2	N_2	15,650	$N_2/15650$	$X_{1,2} = 0.533$	$D_{II} = 0.277 + N_2/15650$
5	1	8160	32,640	0.25	-	$D_I = N_1/32640$
	2	1530	6,120	0.25	$X_{1,2} = 1.05$	$D_{II} = 0.263 + N_2/6120$
	3	448	1,790	0.25	$X_{1,3} = 1.14$ $X_{2,3} = 1.08$	$D_{III} = 0.555 + N_3/1790$
	4	N_4	656	$N_4/656$	$X_{1,4} = 1.27$ $X_{2,4} = 1.21$ $X_{3,4} = 1.12$	$D_{IV} = 0.900 + N_4/656$
6	1	164	656	0.25	-	$D_I = N_1/656$
	2	448	1,790	0.25	$X_{1,2} = 0.895$	$D_{II} = 0.224 + N_2/1790$
	3	1530	6,120	0.25	$X_{1,3} = 0.828$ $X_{2,3} = 0.887$	$D_{III} = 0.405 + N_3/6120$
	4	N_4	32,640	$N_4/32640$	$X_{1,4} = 0.786$ $X_{2,4} = 0.877$ $X_{3,4} = 0.949$	$D_{IV} = 0.653 + N_4/32640$
7	1	3913	15,650	0.25	-	$D_I = N_1/15650$
	2	690	2,760	0.25	$X_{1,2} = 1.12$	$D_{II} = 0.280 + N_2/2760$
	3	182	729	0.25	$X_{1,3} = 1.34$ $X_{2,3} = 1.20$	$D_{III} = 0.636 + N_3/729$
	4	N_4	221	$N_4/221$	$X_{1,4} = 1.81$ $X_{2,4} = 1.62$ $X_{3,4} = 1.35$	$D_{IV} = 1.19 + N_4/221$

TABLE 4. DAMAGE FUNCTION EXPRESSIONS (Continued)

Example	j	N_j (cycles)	N_{f_j} (cycles)	N_j/N_{f_j}	X	D
8	1	55	221	0.25	-	$D_I = N_1/221$
	2	182	729	0.25	$X_{1,2} = 0.743$	$D_{II} = 0.186 + N_2/729$
	3	729	2,760	0.25	$X_{1,3} = 0.619$ $X_{2,3} = 0.834$	$D_{III} = 0.363 + N_3/2760$
	4	N_4	15,650	$N_4/15650$	$X_{1,4} = 0.553$ $X_{2,4} = 0.745$ $X_{3,4} = 0.893$	$D_{IV} = 0.542 + N_4/15650$

TABLE 5. MEDIAN CYCLES TO FAILURE AT THE nth STRESS LEVEL

Example	N_{m_n} (cycles)
1	15,650
2	221
3	21
4	11,315
5	66
6	11,326
7	0*
8	7,168

*From Table 4 failure will occur during the application of the first stress cycle at the fourth stress level (i.e., $N_4 = 0$).

(d) Table 6 shows the values of the total median cycles to failure using equation (15) and data from Tables 4 and 5.

Table 7 arranges the data from Tables 4 and 6 to show the effect of stress sequence.

TABLE 6. TOTAL MEDIAN CYCLES TO FAILURE

Example	N_{m_T} (cycles)
1	15,650
2	221
3	7,846
4	11,425
5	10,204
6	13,468
7	4,785
8	8,134

TABLE 7. STRESS SEQUENCE DATA

Example	Stress Level Sequence	$\sum N_j/N_{f_j}$	N_{m_T} (cycles)	Compares with Example
3	Increasing	0.596	7,846	4
5	Increasing	0.850	10,204	6
7	Increasing	0.750	4,785	8
4	Decreasing	1.22	11,425	3
6	Decreasing	1.10	13,468	5
8	Decreasing	1.21	8,134	7

(e) Table 8 gives the parameters to be used for the calculations of probability of failing at N cycles F(N) versus N. Refer to equations (17) and (18). $F(N) = 0.5 + \text{erf}(\alpha)$. Plots of F(N) versus N_{TOTAL} are shown in Figures 2 through 7.

DISCUSSION OF EXAMPLE RESULTS

Stress Sequence Effects

Table 7 shows the effects of stress sequence. Those sequences of increasing stress level have uncorrected (i.e., linear) cycle ratio damage value summations of less than unity and, hence, shorter total fatigue lives. Those with decreasing levels have linear damage summations greater than unity and longer total fatigue lives.

The above stress sequence effect results are in agreement with limited test data on 24S-T and 7075-T6 aluminum alloys presented in Ref. [5].

Data were presented for sequences of two to ten stress levels. Those sequences with increasing stress levels had damage summations less than unity while those of decreasing stress level sequences were greater than unity. These data tend to confirm the derived equations.

TABLE 8. FAILURE PROBABILITY PARAMETERS

Example	Stress Level	N_{TOTAL}	$\alpha = \left[\frac{\bar{A}}{\Delta}\{D_L^{1/\beta} - 1\}\right]$	Cycle Limits
1	I	N_1	$10\left\{\left(\frac{N_1}{15650}\right)^{0.1036} - 1\right\}$	$0 \leq N_1 \leq \infty$
2	I	N_1	$10\left\{\left(\frac{N_1}{221}\right)^{0.1036} - 1\right\}$	$0 \leq N_1 \leq \infty$
3	I	N_1	$10\left\{\left(\frac{N_1}{15650}\right)^{0.1036} - 1\right\}$	$0 \leq N_1 \leq 7825$
	II	$7825 + N_2$	$10\left\{\left(0.904 + \frac{N_2}{221}\right)^{0.1036} - 1\right\}$	$0 \leq N_2 \leq \infty$
4	I	N_1	$10\left\{\left(\frac{N_1}{221}\right)^{0.1036} - 1\right\}$	$0 \leq N_1 \leq 110$
	II	$110 + N_2$	$10\left\{\left(0.277 + \frac{N_2}{15650}\right)^{0.1036} - 1\right\}$	$0 \leq N_2 \leq \infty$
5	I	N_1	$10\left\{\left(\frac{N_1}{32640}\right)^{0.1036} - 1\right\}$	$0 \leq N_1 \leq 8160$
	II	$8160 + N_2$	$10\left\{\left(0.263 + \frac{N_2}{6120}\right)^{0.1036} - 1\right\}$	$0 \leq N_2 \leq 1530$
	III	$9690 + N_3$	$10\left\{\left(0.555 + \frac{N_3}{1790}\right)^{0.1036} - 1\right\}$	$0 \leq N_3 \leq 448$
	IV	$10138 + N_4$	$10\left\{\left(0.900 + \frac{N_4}{656}\right)^{0.1036} - 1\right\}$	$0 \leq N_4 \leq \infty$
6	I	N_1	$10\left\{\left(\frac{N_1}{656}\right)^{0.1036} - 1\right\}$	$0 \leq N_1 \leq 164$
	II	$164 + N_2$	$10\left\{\left(0.224 + \frac{N_2}{1790}\right)^{0.1036} - 1\right\}$	$0 \leq N_2 \leq 448$
	III	$612 + N_3$	$10\left\{\left(0.405 + \frac{N_3}{6120}\right)^{0.1036} - 1\right\}$	$0 \leq N_3 \leq 1530$
	IV	$2142 + N_4$	$10\left\{\left(0.653 + \frac{N_4}{32640}\right)^{0.1036} - 1\right\}$	$0 \leq N_4 \leq \infty$
7	I	N_1	$10\left\{\left(\frac{N_1}{15650}\right)^{0.1036} - 1\right\}$	$0 \leq N_1 \leq 3913$
	II	$3913 + N_2$	$10\left\{\left(0.280 + \frac{N_2}{2760}\right)^{0.1036} - 1\right\}$	$0 \leq N_2 \leq 690$
	III	$4603 + N_3$	$10\left\{\left(0.636 + \frac{N_3}{729}\right)^{0.1036} - 1\right\}$	$0 \leq N_3 \leq 182$
	IV	$4785 + N_4$	$10\left\{\left(1.19 + \frac{N_4}{221}\right)^{0.1036} - 1\right\}$	$0 \leq N_4 \leq \infty$
8	I	N_1	$10\left\{\left(\frac{N_1}{221}\right)^{0.1036} - 1\right\}$	$0 \leq N_1 \leq 55$
	II	$55 + N_2$	$10\left\{\left(0.186 + \frac{N_2}{729}\right)^{0.1036} - 1\right\}$	$0 \leq N_2 \leq 182$
	III	$237 + N_3$	$10\left\{\left(0.363 + \frac{N_3}{2760}\right)^{0.1036} - 1\right\}$	$0 \leq N_3 \leq 729$
	IV	$966 + N_4$	$10\left\{\left(0.542 + \frac{N_4}{15650}\right)^{0.1036} - 1\right\}$	$0 \leq N_4 \leq \infty$

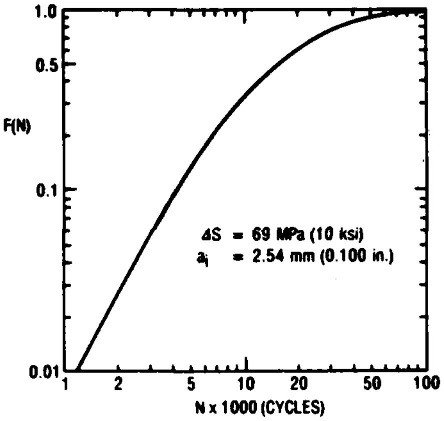

Fig. 2 - Plot of F(N) for Example 1

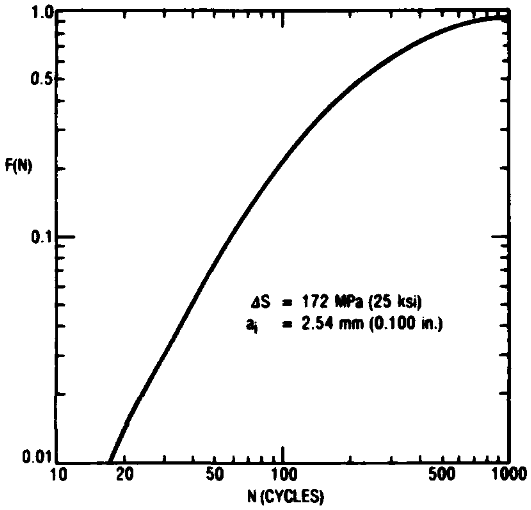

Fig. 3 - Plot of F(N) for Example 2

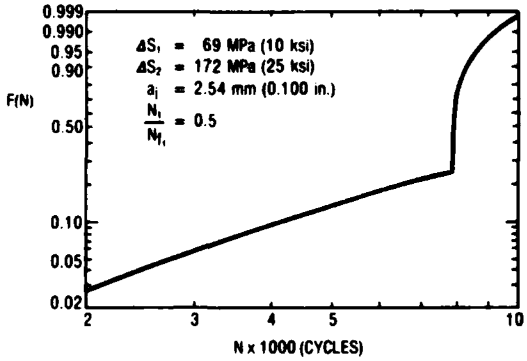

Fig. 4 - Plot of F(N) for Example 3

Initial Flaw Size Effects

Table 9 shows the effect of a_i on fatigue life. Examples 5 and 7 as well as 6 and 8 have the same stress level sequences. They differ only in a_i values. Large a_i values reduce fatigue life.

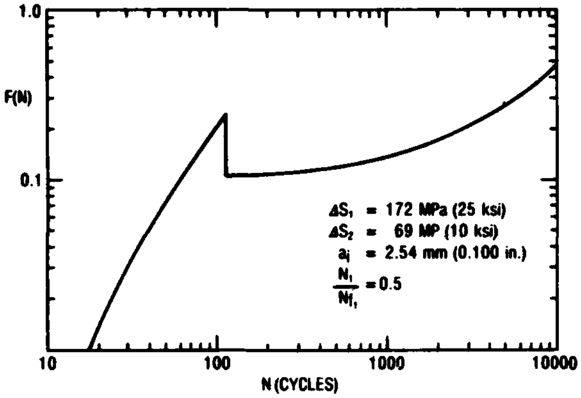

Fig. 5 - Plot of F(N) for Example 4

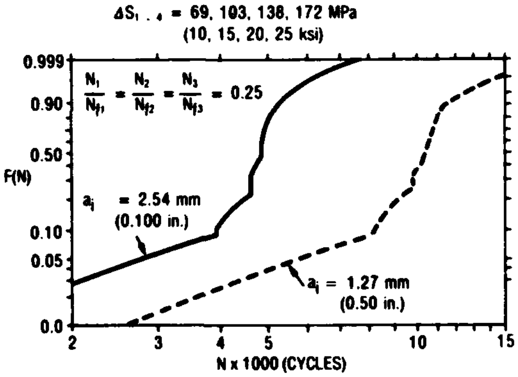

Fig. 6 - Plots of F(N) for Examples 5 and 7

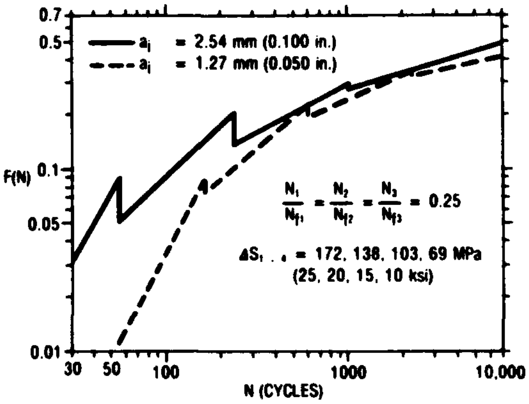

Fig. 7 - Plots of F(N) for Examples 6 and 8

TABLE 9. INITIAL FLAW SIZE EFFECTS DATA

Example	a_i		N_{m_T}
	(mm)	(in.)	(cycles)
5	1.27	0.050	10,204
7	2.54	0.100	4,785
6	1.27	0.050	13,468
8	2.54	0.100	8,134

Failure Probabilities

Figures 2 and 3 show the general shape of single stress level failure probability curves. Note that $F(N_m) = 0.5$. Figures 4 and 5 show the stress level sequence effects previously discussed occurring in the region of early failures. The entire shapes of the curves are different for the two sequences.

Figures 6 and 7 show the initial flaw size effects. A large initial crack length significantly reduces fatigue life. The discontinuities between stress levels are due to a change in the critical crack length value. See equation (2).

CONCLUDING REMARKS

It is believed that the derived fatigue life equations are simple, accurate and practical. These expressions indicate that a large fatigue curve scatterband, a large initial crack (flaw) and the applied stress level sequence have a significant effect on fatigue life which tend to be confirmed by empirical test data.

REFERENCES

1. S.T. Rolfe and J.M. Barsom, Fracture and Fatigue Control in Structures - Applications of Fracture Mechanics, Prentice-Hall, Inc., 1977.

2. R.G. Lambert, "Fracture Mechanics Applied to Step-Stress Fatigue under Sine/Random Vibration," The Shock and Vibration Bulletin 48, Naval Research Laboratory, Washington, DC, September 1978.

3. R.G. Lambert, "Probability of Failure Prediction for Step-Stress Fatigue under Sine or Random Stress," Presented at 49th Shock and Vibration Symposium, Washington, DC, October 1978.

4. R.G. Lambert, "Analysis of Fatigue under Random Vibration," The Shock and Vibration Bulletin 46, Naval Research Laboratory, Washington, DC, August 1976.

5. Fatigue of Aircraft Structures, NAVAIR 01-1A-13, Revised 1960, Naval Air Systems Command, p 98.

SYMBOLS

a	crack half-length
a_c	critical value of crack half-length at stress level ΔS or σ
a_{c_j}	critical value of crack half-length at stress level ΔS_j or σ_j
a_i	initial crack half-length
A	material fatigue curve constant
$\bar{A}$	average value of A
b	number of independent opportunities for failure
$\overline{C}$	constant of random fatigue curve
$\overline{C}$	average random fatigue curve constant
c_o	constant of crack growth rate curve
D	cycle ratio damage function
D_j	damage function at the jth stress level ΔS_j or σ_j
$\frac{da}{dN}$	crack growth rate
erf	error function
$F(N)$	probability of failure in N cycles
in.	inches
j	index
σ_j	j^{th} applied random rms stress
k	constant
ΔK_c	fracture toughness
ksi	thousands of pounds per square inch
ℓ	English numeral equivalent of L
L	Roman numeral designation of one of n stress levels
ΔS_j	j^{th} applied sine stress range level
n	total number of step-stress levels
N	number of stress cycles
N_j	number of stress cycles applied at the jth stress level ΔS_j or σ_j
N_{f_j}	number of stress cycles to failure at the jth stress level ΔS_j or σ_j
N_m	
N_{m_n}	median cycles to failure
N_{m_T}	

rms	root-mean-square
X	damage law correction factor
$X_{j,\ell}$	correction factor
y	dummy variable
Y	geometrical parameter
α	dummy variable
β	fatigue curve slope parameter
Δ	standard deviation of A
σ	random rms stress value
θ	constant of crack growth rate curve
ϕ	crack growth rate constant
$\Gamma(\alpha)$	gamma function with argument α
m	metre
mm	millimeter
MPa	mega Pascals
1.0988	$\frac{\text{MPa}\ \sqrt{\text{metre}}}{\text{ksi}\ \sqrt{\text{in.}}}$
6.895	$\frac{\text{MPa}}{\text{ksi}}$
25.4	$\frac{\text{mm}}{\text{in.}}$

APPENDIX A

DERIVATION OF FATIGUE LIFE EXPRESSIONS FOR n STEP-STRESS LEVELS

LINEAR ELASTIC FRACTURE MECHANIC'S CRACK GROWTH EQUATIONS:

a = crack half-length = crack size

a_i = initial crack size

N = number of applied stress cycles

ΔS = sinusoidal stress range = twice stress amplitude

Y = geometrical parameter ≈ constant

C_o, θ = crack growth curve constants

$\frac{da}{dN}$ = crack growth rate

Paris' equation:

$$\frac{da}{dN} = C_o(Y\,\Delta S\, a^{1/2})^{\theta} \text{ metre/cycle (in./cycle)} \qquad (21)$$

Define: $\phi = \frac{\theta - 2}{2}$

$$k = C_o \phi Y^{\theta}$$

Integrating equation (21)

$$a = \frac{1}{\left[\left(\frac{1}{a_i}\right)^{\phi} - k\,\Delta S^{\theta} N\right]^{1/\phi}} \qquad (22)$$

For $a = a_c$ at $N = N_f$ = cycles to failure where a_c = critical crack half-length

$$N_f = \frac{1}{k\,\Delta S^{\theta}}\left[\left(\frac{1}{a_i}\right)^{\phi} - \left(\frac{1}{a_c}\right)^{\phi}\right] \qquad (23)$$

$$a_c = \left[\frac{\Delta K_c}{Y\,\Delta S}\right]^2 \text{ metre (inches)} \qquad (24)$$

where ΔK_c = material's fracture toughness

Consider the four step-stress level case: (ΔS_1, ΔS_2, ΔS_3, ΔS_4)

Define:

a_{c_j} = critical crack size corresponding to the jth stress level; see equation (24)

N_{f_j} = cycles to failure for ΔS_j acting independently; see equation (23)

a_j = cumulative crack size at the end of the jth stress level

a_{i_j} = initial crack size at the beginning of the jth stress level

N_j = actual stress cycles applied during the jth stress level

$D_j = \frac{N_j}{N_{f_j}}$ = cycle ratio damage done during the jth stress level

The condition imposed between stress levels is

$$a_{i_{j+1}} = a_j \qquad (25)$$

Equations (23), (24) and (25) will be used repeatedly.

$$N_{f_1} = \frac{1}{k\,\Delta S_1^{\theta}}\left[\left(\frac{1}{a_i}\right)^{\phi} - \left(\frac{1}{a_{c_1}}\right)^{\phi}\right]$$

$$a_1 = \frac{1}{\left[\left(\frac{1}{a_i}\right)^{\phi} - k\,\Delta S_1^{\theta} N_1\right]^{1/\phi}}$$

critical crack half-length

$$N_{f_2} = \frac{1}{k\ \Delta S_2{}^{\theta}}\left[\left(\frac{1}{a_i}\right)^{\phi} - \left(\frac{1}{a_{c2}}\right)^{\phi}\right]$$

$$a_{i_2} = a_1$$

$$a_2 = \frac{1}{\left[\left(\frac{1}{a_1}\right)^{\phi} - k\ \Delta S_2{}^{\theta} N_2\right]^{1/\phi}}$$

$$N_{f_3} = \frac{1}{k\ \Delta S_3{}^{\theta}}\left[\left(\frac{1}{a_i}\right)^{\phi} - \left(\frac{1}{a_{c3}}\right)^{\phi}\right]$$

$$a_{i_3} = a_2$$

$$a_3 = \frac{1}{\left[\left(\frac{1}{a_2}\right)^{\phi} - k\ \Delta S_3{}^{\theta} N_3\right]^{1/\phi}}$$

$$N_{f_4} = \frac{1}{k\ \Delta S_4{}^{\theta}}\left[\left(\frac{1}{a_3}\right)^{\phi} - \left(\frac{1}{a_{c4}}\right)^{\phi}\right]$$

From previous expressions

$$N_1 = \frac{1}{k\ \Delta S_1{}^{\theta}}\left[\left(\frac{1}{a_i}\right)^{\phi} - \left(\frac{1}{a_1}\right)^{\phi}\right]$$

$$N_2 = \frac{1}{k\ \Delta S_2{}^{\theta}}\left[\left(\frac{1}{a_1}\right)^{\phi} - \left(\frac{1}{a_2}\right)^{\phi}\right]$$

$$N_3 = \frac{1}{k\ \Delta S_3{}^{\theta}}\left[\left(\frac{1}{a_2}\right)^{\phi} - \left(\frac{1}{a_3}\right)^{\phi}\right]$$

crack half-length

Failure occurs when $a_4 = a_{c4}$

$$N_4 = \frac{1}{k\ \Delta S_4{}^{\theta}}\left[\left(\frac{1}{a_i}\right)^{\phi} - \left(\frac{1}{a_{c4}}\right)^{\phi}\right]$$

$$D_4 = \frac{N_4}{N_{f_4}} = \frac{\left(\frac{1}{a_3}\right)^{\phi} - \left(\frac{1}{a_{c4}}\right)^{\phi}}{\left(\frac{1}{a_i}\right)^{\phi} - \left(\frac{1}{a_{c4}}\right)^{\phi}}$$

$$D_4 = \frac{\left(\frac{1}{a_2}\right)^{\phi} - k\Delta S_3{}^{\theta} N_3 - \left(\frac{1}{a_{c4}}\right)^{\phi}}{\left(\frac{1}{a_i}\right)^{\phi} - \left(\frac{1}{a_{c4}}\right)^{\phi}}$$

$$D_4 = 1 - \frac{\left[k\Delta S_1{}^{\theta} N_1 + k\Delta S_2{}^{\theta} N_2 + k\Delta S_3{}^{\theta} N_3\right]}{\left(\frac{1}{a_i}\right)^{\phi} - \left(\frac{1}{a_{c4}}\right)^{\phi}}$$

$$D_1 = \frac{N_1}{N_{f_1}} = \frac{k\Delta S_1{}^{\theta} N_1}{\left(\frac{1}{a_i}\right)^{\phi} - \left(\frac{1}{a_{c1}}\right)^{\phi}}$$

$$D_2 = \frac{N_2}{N_{f_2}} = \frac{k\Delta S_2{}^{\theta} N_2}{\left(\frac{1}{a_i}\right)^{\phi} - \left(\frac{1}{a_{c2}}\right)^{\phi}}$$

$$D_3 = \frac{N_3}{N_{f_3}} = \frac{k\Delta S_3{}^{\theta} N_3}{\left(\frac{1}{a_i}\right)^{\phi} - \left(\frac{1}{a_{c3}}\right)^{\phi}}$$

$$D_4 = 1 - D_1\left[\frac{\left(\frac{1}{a_i}\right)^{\phi} - \left(\frac{1}{a_{c1}}\right)^{\phi}}{\left(\frac{1}{a_i}\right)^{\phi} - \left(\frac{1}{a_{c4}}\right)^{\phi}}\right] - D_2\left[\frac{\left(\frac{1}{a_i}\right)^{\phi} - \left(\frac{1}{a_{c2}}\right)^{\phi}}{\left(\frac{1}{a_i}\right)^{\phi} \quad \left(\frac{1}{a_{c4}}\right)^{\phi}}\right] - D_3\left[\frac{\left(\frac{1}{a_i}\right)^{\phi} - \left(\frac{1}{a_{c3}}\right)^{\phi}}{\left(\frac{1}{a_i}\right)^{\phi} - \left(\frac{1}{a_{c4}}\right)^{\phi}}\right]$$

$$D_4 = 1 - D_1\left[\frac{1 - \left(\frac{a_i}{a_{c1}}\right)^{\phi}}{1 - \left(\frac{a_i}{a_{c4}}\right)^{\phi}}\right] - D_2\left[\frac{1 - \left(\frac{a_i}{a_{c2}}\right)^{\phi}}{1 - \left(\frac{a_i}{a_{c4}}\right)^{\phi}}\right] - D_3\left[\frac{1 - \left(\frac{a_i}{a_{c3}}\right)^{\phi}}{1 - \left(\frac{1}{a_{c4}}\right)^{\phi}}\right]$$

Define

$$X_{j,n} = \frac{1 - \left(\frac{a_i}{a_{cj}}\right)^{\phi}}{1 - \left(\frac{a_i}{a_{cn}}\right)^{\phi}} = \frac{1 - \left(\frac{a_i Y^2\ \Delta S_j{}^2}{\Delta K_c{}^2}\right)^{\phi}}{1 - \left(\frac{a_i Y^2\ \Delta S_n{}^2}{\Delta K_c{}^2}\right)^{\phi}} \qquad (26)$$

$$D_4 = 1 - D_1X_{1,4} - D_2X_{2,4} - D_3X_{3,4} \qquad (27)$$

N_4 = fatigue life; median cycles to failure

$$N_4 = N_{f_4} \times D_4 \qquad (28)$$

Failure occurs when

$$D_1X_{1,4} + D_2X_{2,4} + D_3X_{3,4} + D_4 = 1 \qquad (29)$$

For n step-stress levels, failure occurs when

$$\sum_{j=1}^{n-1} (D_jX_{j,n}) + D_n = 1 \qquad (30)$$

DISCUSSION

Mr. Salive (David Taylor Naval Ship Research & Development Center): Did you get reproducibility in your cummulative number of unity? When you used an ascending series of cycles you said you got a value of .75. Was that a consistent number or was it a rather large scatter associated with that value of .75 as the failure criterion?

Mr. Lambert: That is a deterministic analysis result. So that will come out the same every time from that standpoint.

Mr. Salive: If you ran it experimentally would that number have a distribution function associated with it?

Mr. Lambert: Yes. In fact, this was part of the derivation of the probability of failure curves in a paper that I presented last year. I treat this damage function as a random variable. You can describe the probability of failure in several ways. One way is that it is the probability that your number of applied cycles exceeds the number of cycles to failure and that is also equal to the probability that your accumulated damage exceeds unity. It is the integeral of the probability density function of your damage function times the differential. It is a random variable and it has a funny look because it tends to peak before you get to unity. It is a basis for the derivation of the probability of failure of the curves that I presented here.

Mr. Salive: Is the standard error that you would expect with respect to that sort of function small enough so that you can discriminate between the difference of .75 and 1.21 that was shown?

Mr. Lambert: If you are dealing with structures that don't have a lot of scatter band as a result of either fabrication or assembly procedures, or some environmental effects I would say yes you could distinguish between these. In fact, in some of the Navair data they get some cycle ratios that are quite wild. There is no way I can explain why they get such wild numbers. For example, if you had four stress levels you shouldn't really expect to find a summation of the cycle ratio damage functions greater than four because by definition, each one would fail on its own when it reaches unity and yet they get sixteen. Now there is something I don't understand maybe there is something non linear going on. I would expect this to be accurate if indeed your stress situation is linear elastic fracture mechanics. Whenever that would apply these would apply and I think you could distinguish between them.

Mr. Salive: Would the Air Force like scatter associated with material tests or structural tests?

Mr. Lambert: These equations now apply to structural elements.

Mr. Salive: I have similar results using Miner's law with large scatter in material tests. You can still use these equations. You can put any value of delta in that you really want. The question you have asked is can you use the cycles ratio damage function as a discriminant for telling if this equation is accurate or not and I have never really gone through that exercise to put in large numbers of delta. I have used numbers like 10% of the average value which is representative of basic materials. I am sure you can and I have seen situations where the true scatter band due to fabrication can be much larger than that. That doesn't mean that these can't work out it depends on your sample size. You flip a coin and heads or tails comes up 50% of the time but if you only flip it twice I don't know that it will come out exactly the way you think. I don't know if cycles ratio damage function on an experimental basis is a good discriminant to distinguish whether this theory is correct or not.

LATERAL INSTABILITY DURING SPIN TESTS OF A PENDULOUSLY SUPPORTED DISC

F. H. Wolff, A. J. Molnar, G. O. Sankey, J. H. Bitzer
Westinghouse R&D Center
Pittsburgh, Pennsylvania

The spin test facility experienced two shaft failures while studying crack growth properties in a low cycle fatigue disc specimen. The failures were attributed to lateral vibrations of a low frequency whirl instability occurring because of shaft hysteresis, looseness of bolts connecting mating components of the rotor, and insufficient external damping. Theory and experimental verification are presented which permit lateral instabilities of pendulously supported disc systems to be calculated.

INTRODUCTION

During a spin test, in the facility shown in Figure 1, to determine crack growth properties in a low cycle fatigue disc specimen, two flexible shaft failures were encountered. After considerable study these failures were attributed to excessive lateral vibrations caused by a low frequency whirl instability. The purpose of this investigation was to verify the cause of shaft failures, and provide guidelines that would avoid future problems of this nature.

Three probable factors combined to cause a whirl instability:

(1) shaft hysteresis - instability from shaft hysteresis forces exciting a whirl mode.

(2) looseness of bolts connecting mating components of the rotor especially at either end of the smallest diameter shaft connecting the test specimen.

(3) insufficient external (rotor support) damping.

The contribution of the second factor is difficult to determine but recent work by W. T. Thomson [1] on a similar configuration has made it possible to analyze the hysteretic whirl effects. This type of analysis is presented along with some resulting changes to the spin-test facility.

A series of tests were then conducted on the original and modified configuration of the spin-test facility. These tests verified the theory and confirmed the presence of the previously mentioned whirl exciting factors, as well as the degree each contributed to the whirl instability.

The spin tests were completed in the modified facility and the whirl amplitudes were very small.

SHAFT HYSTERETIC WHIRL

For a vertically oriented system whirl is defined as the rotation of the deflected shaft about the vertical axis while spin is the rotation of the disc with respect to the inertial coordinates. Both forward and backward whirl may occur. Instabilities (during forward whirl) can take place when the spin is greater than the whirl where shaft hysteresis energy is fed into the system. If this hysteresis energy is greater than the energy being dissipated through bearings, supports, etc., the system becomes unstable. There are several kinds of whirl [2] which, in general, result from a tangential force, normal to the radial shaft deflection, whose magnitude is proportional to (or varies monotonically with) that deflection. At some "onset" rotational speed such a force system will overcome the stabilizing external damping forces to induce a whirling motion of ever increasing amplitude until failure occurs. Although the shaft deflection may reach a limit cycle (stable whirl), when the whirl frequency is different than the spin frequency alternating stresses are introduced to the shaft fibers which can lead to fatigue failure.

With some radial shaft deflection, the flexure of the shaft would

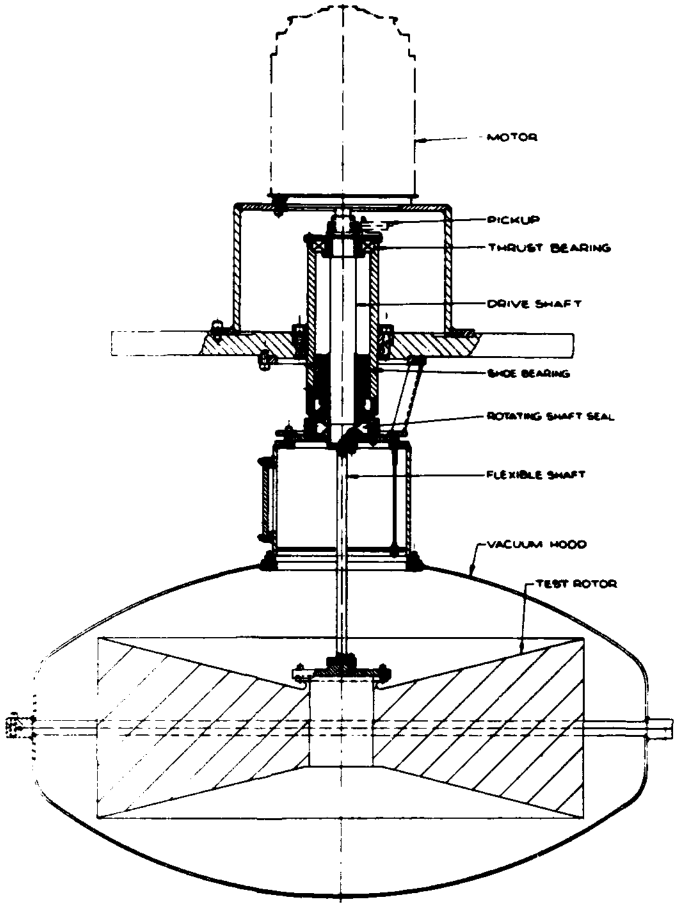
MOTOR
PICKUP
THRUST BEARING
DRIVE SHAFT
SHOE BEARING
ROTATING SHAFT SEAL
FLEXIBLE SHAFT
VACUUM HOOD
TEST ROTOR

Fig. 1 - Spin test machine

induce a neutral strain axis normal to the deflection direction. From first order considerations of elastic beam theory, the neutral axes of stress and strain would be coincident; accordingly, the net elastic restoring force would be parallel to and opposing the deflection. Hence, any deflection would be the normal running speed vibration which is a steady stress. In actual fact, hysteresis, or internal friction in the rotating shaft causes a phase shift between the neutral axes (Figure 2). The net effect in the restoring force is not parallel to the deflection and has a tangential component normal to the deflection which is in the direction of rotation causing a forward whirl motion when the spin frequency is greater than the whirl frequency.

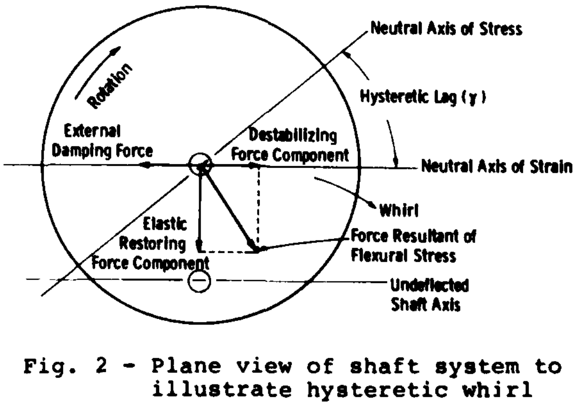
Rotation
Neutral Axis of Stress
Hysteretic Lag (γ)
External Damping Force
Destabilizing Force Component
Neutral Axis of Strain
Whirl
Elastic Restoring Force Component
Force Resultant of Flexural Stress
Undeflected Shaft Axis

Fig. 2 - Plane view of shaft system to illustrate hysteretic whirl

DEVELOPMENT OF SPIN, WHIRL, AND STABILITY RELATIONSHIPS

Thomson's comprehensive treatment of a pendulously supported flywheel system has been applied to the spin test rotor in Figure 3 to determine why the .75 inch shaft failed and what could be done to correct the problem. Based on an energy balance between hysteresis-viscous damping, the stable and unstable operations of the system are theoretically derived.

From Figure 4 the beam deflection (η) and slope (θ) at the rotor in terms of unbalance force (P) and moment (M) are

$$\eta = \alpha_{11}P + \alpha_{12}M$$
$$\theta = \alpha_{12}P + \alpha_{22}M \qquad (1)$$

where the flexibility influence coefficients of a beam of length (L), with infinitely stiff end (λ) for $\ell = L - \lambda$, and rigidity EI are

$$\alpha_{11} = \frac{\ell^3}{3EI} + \frac{\ell^2\lambda}{EI} + \frac{\ell\lambda^2}{EI}$$

$$\alpha_{12} = \frac{\ell^2}{2EI} + \frac{\ell\lambda}{EI}$$

$$\alpha_{22} = \frac{\ell}{EI}$$

The total deflection (r) and slope at the rotor center are

$$r = \zeta + \eta = \left(\frac{1}{k} + \alpha_{11}\right) P + \alpha_{12}M$$
$$= \bar{\alpha}_{11}P + \alpha_{12}M \qquad (2)$$
$$\theta = \alpha_{12}P + \alpha_{22}M$$

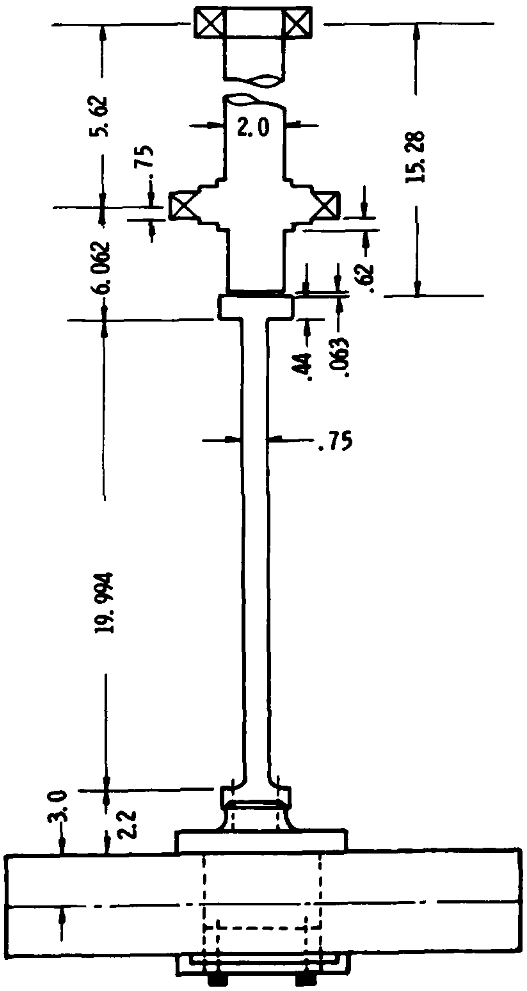

Fig. 3 - Schematic of spin test system showing dimensions (inches) for analysis

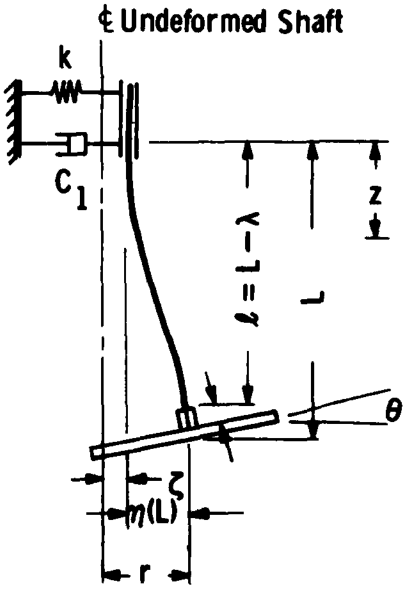

Fig. 4 - Model of spin test system with bearing translation

where k is the bearing stiffness coefficient and

$$\bar{\alpha}_{11} = (\frac{1}{k} + \alpha_{11}).$$

Defining the unbalance force and moment for a disc of mass (m), diameter (J_d) and polar (J_p) moments of inertia as

$$\begin{aligned} P &= mr\omega^2 \\ M &= -J_d\omega^2 \left(a\,\frac{\Omega}{\omega} - 1\right)\theta \end{aligned} \qquad (4)$$

where

$a = J_p/J_d$

ω = whirl speed

Ω = running speed

gives

$$\begin{aligned} r &= \bar{\alpha}_{11} mr\omega^2 - \alpha_{12} J_d \omega^2 \left(a\,\frac{\Omega}{\omega} - 1\right)\theta \\ \theta &= \alpha_{12} mr\omega^2 - \alpha_{22} J_d \omega^2 \left(a\,\frac{\Omega}{\omega} - 1\right)\theta \end{aligned} \qquad (5)$$

By introducing the following nondimensional quantities

$$\begin{aligned} F &= \omega\sqrt{\bar{\alpha}_{11} m} \;, \quad D = \frac{\alpha_{22} J_d}{\bar{\alpha}_{11} m} \\ S &= \Omega\sqrt{\bar{\alpha}_{11} m} \;, \quad E = \frac{\alpha_{12}^2}{\bar{\alpha}_{11}\alpha_{22}} \end{aligned} \qquad (6)$$

equation (5) becomes

$$\begin{aligned} &\left\{F^2 - 1\right\} r - \left\{\frac{\bar{\alpha}_{11}}{\alpha_{12}} EDF^2 \left(a\,\frac{S}{F} - 1\right)\right\}\theta = 0 \\ &\left\{\frac{\alpha_{12}}{\bar{\alpha}_{11}} F\right\} r - \left\{DF^2 \left(a\,\frac{S}{F} - 1\right) + 1\right\}\theta = 0 \end{aligned} \qquad (7)$$

Solving the determinant of equation (7) gives the frequencies and mode shapes

$$\begin{aligned} S &= \frac{F^4 + \frac{(D + 1)}{D(E - 1)} F^2 + \frac{1}{D(E - 1)}}{aF\left(F^2 + \frac{1}{E - 1}\right)} \\ \frac{r}{\theta} &= \frac{\alpha_{12}}{\alpha_{22}} \, \frac{DF^2\left(a\,\frac{S}{F} - 1\right)}{F^2 - 1} \end{aligned} \qquad (8)$$

Figure 5 shows a plot of whirl speeds vs. running speed for the spin test configuration that failed. Only the lower forward whirl mode which is close to the 1st critical speed leads to hysteresis instability.

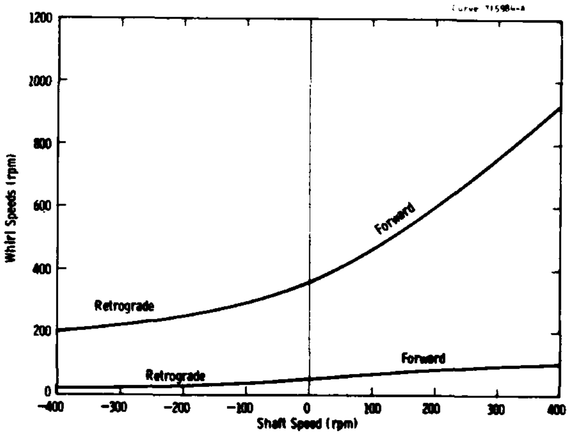

Fig. 5 - Spin-whirl relationship for original rotor

Using the complex modulus of elasticity the stress (σ) - strain (ε) relationship can be written as

$$\sigma = (1 + i\gamma)\varepsilon E \qquad (9)$$

where γ is the shaft hysteresis damping constant. The hysteresis work (U') is given by the area under the hysteresis curve (ellipse for sinusoidal loading)

$$U' = \pi\gamma E\varepsilon^2 \qquad (10)$$

The ratio of hysteresis work to elastic strain energy (U) is

$$\frac{U'}{U} = 2\pi\gamma \qquad (11)$$

In order to evaluate the hysteresis and strain energies, the deflection shape of the shaft under whirl is needed. The bending moment (M) at z is

$$M(z) = M + P(\ell + \lambda - z) \qquad (12)$$

The deflection then becomes

$$\eta(z) = \frac{P}{EI}\left\{-\frac{J_d}{m}\left(a\,\frac{\Omega}{\omega}-1\right)\frac{\theta z^2}{r2} + (\ell+\lambda)\,\frac{z^2}{2} - \frac{z^3}{6}\right\} \qquad (13)$$

Since Ω/ω and r/θ are known from the steady state solution at any spin speed Ω, the shaft deflection and hysteresis work are also known at any Ω.

$$U' = 2\pi\gamma\,\frac{1}{2}\,EI\int_0^{\ell}\left(\frac{d^2\eta}{dz^2}\right)^2 dz = \frac{\pi\gamma K_2^2\,F(\Omega)\,\eta^2(L)}{EI} \qquad (14)$$

where K_2 is the translational stiffness of shaft

$$P = K_2\eta(L) \qquad (15)$$

and

$$F(\Omega) = \left\{\left[\ell+\lambda-\frac{J_d}{m}\left(a\,\frac{\Omega}{\omega}-1\right)\frac{\theta}{r}\right]^2\ell - \left[\ell+\lambda-\frac{J_d}{m}\left(a\,\frac{\Omega}{\omega}-1\right)\frac{\theta}{r}\right]\ell^2+\frac{\ell^3}{3}\right\} \qquad (16)$$

The average rate of work per cycle done by hysteresis is

$$\frac{dU'}{dt} = \frac{U'\,(\Omega-\omega)}{2\pi} \qquad (17)$$

The force due to the bearing damper with coefficient C_1 is

$$F_{C_1} = C_1\omega\zeta \qquad (18)$$

therefore, the work done by the bearing damping is

$$U_{C_1} = F_{C_1}\,2\pi\zeta = C_1\,2\pi\omega\zeta^2 \qquad (19)$$

The rate of work done by the bearing damper is

$$\frac{dU_{C_1}}{dt} = \frac{U_{C_1}}{2\pi/\omega} = C_1(\omega\zeta)^2 \qquad (20)$$

The stability of the system can be found by equating the rate of work done by hysteresis (eq. (17)) to that of bearing damper (eq. (20))

$$C_1\omega^2\zeta^2 = \gamma K_2^2\,\frac{F(\Omega)}{2EI}\,\eta^2(L)\,(\Omega-\omega) \qquad (21)$$

If the right hand side of equation (21) becomes larger than the left side then instability occurs. Hence, letting

$$C_2 = \frac{K_2^2\,F(\Omega)}{2EI} \qquad (22)$$

and

$$\zeta = \frac{P}{k}, \qquad \eta(L) = \frac{P}{K_2}$$

the criteria for stability becomes

$$\frac{C_1}{\gamma}\,\frac{1}{C_2}\left(\frac{K_2}{k}\right)^2\omega \geq \frac{\Omega}{\omega} - 1 \qquad (23)$$

Since all quantities are known for any Ω, the value of C_1 needed to stabilize the system at any $\Omega > \omega$ can be found.

A study of equation (23) indicates that all systems of this type are inherently unstable; i.e., for constant values of C_1, C_2, K_2, k and ω there exists some onset running speed Ω for which the stability criteria is no longer satisfied. Therefore, if the running speed of pendulously supported rotor is increased indefinitely it will become unstable. Hence, an important design consideration is to ensure that the bearing can supply sufficient damping for the entire speed range. Furthermore, the bearing stiffness is a very important factor; the softer the bearing the lesser the amount of bearing damping needed for stability (Figure 6). Figure 6 shows the stable regions (amount of damping C_1/γ needed to satisfy equation (23)) for spin test configuration using two values of bearing stiffness (1800, 4500 lb/in). Note, as the running speed increases the damping required increases.

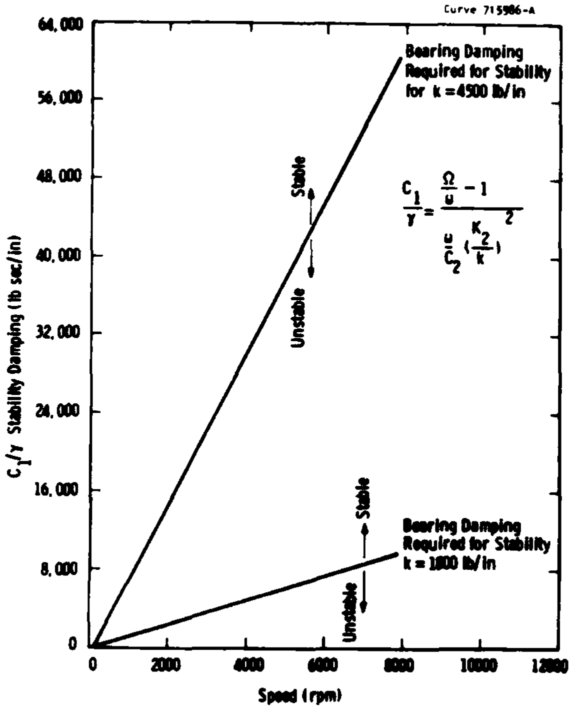

Fig. 6 - Stability curve for original rotor system

DISCUSSION OF SPIN TEST CONFIGURATION

To quantify the whirl-instability characteristics of the MARD spin test, an estimate of γ (structural damping constant) is needed. Unfortunately, there is a wide scatter in data available for shaft material 4340 steel. The literature [3], [4] indicates a factor in the range [0.00025, 0.001] might be valid. If the original design failed due to shaft hysteresis and the failure was witnessed between 3600-4000 rpm, the value of γ can be backed out from a stability plot. The damping devices (C_1/γ) provided by the bearing for the original design are plotted on Figure 7 using $C_1 \Omega$ = 7500 lb/in (Table 1). The intersection of the stability curve (damping needed to maintain stability) for k = 4500 lb/in and the actual damping provided curves is where the unstable onset rpm occurs. From Figure 7 the C_1/γ curve for γ = 0.0007 intersects the stability curve near 4000 rpm; accordingly, a shaft damping constant of γ = 0.0007 was assumed for further analysis. On that basis to maintain stability over the desired speed range (0 to 8000 rpm), bearing stiffness $\leq$ 1800 lb/in is needed.

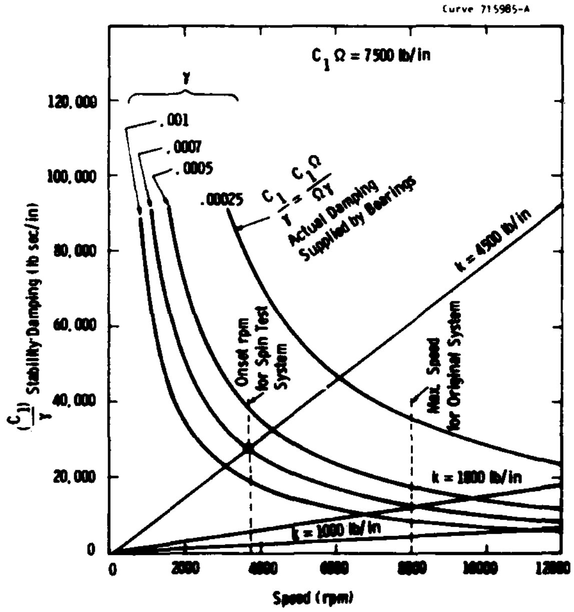

Fig. 7 - Stability curves with bearing damping for original rotor system

The bearing was redesigned to give more flexibility and damping. If the redesign has a bearing stiffness of 1000 lb/in (at high speeds) and damping constant around 7500 lb/in, then the new system should be stable up to at least 12,000 rpm when considering only hysteretic effects.

Although the redesign system has been running successfully, there had been incidents where large deflections had been observed. Deflections and whirl orbits of the flexible shaft were measured using linear proximity probes 90° apart. Upon examining the system, working on the shaft adapter was noticed. It appeared that the bolts were working loose causing a whirl; the redesigned bearing is providing sufficient damping to limit the deflections. When the bolts are tightened as a precaution, the large deflections disappear. It is possible that the synchronous motor during transient conditions is creating large enough shaft torques to loosen the bolts. Body bound bolts with set screws along with smaller transient driving torques have essentially eliminated this problem.

CERAMIC BLADED ROTOR TESTS

Upon completion of the original rotor tests, a slightly smaller rotor, which was used to spin test ceramic blades, was set up to check the theory and to determine the cause of the earlier failures.

With the improved bearing design (larger clearance, $k \cong 1800$ lb/in), the ceramic bladed rotor was brought up to 8000 rpm while the whirl amplitude was monitored with two probes. Very small whirls were noticed at each multiple of the lower forward whirl mode (165 rpm).

The bearing clearance was reduced to that of the original design ($k = 4500$ lb/in). Once again the ceramic bladed rotor was brought up to 8000 rpm. Although stability was maintained, the whirl amplitudes were noticeably larger. In addition, frequency response data was recorded with a Hewlett Packard Digital Spectrum Analyzer (Table 1). Both the measured response data and calculated lower forward whirl mode for this rotor are shown in Figure 8. The comparisons are nearly exact showing the accuracy of the model. The calculated lower forward whirl mode for the original rotor is also shown in Figure 8.

A dissipative material was painted on the shaft to enhance the hysteretic whirl condition. This rotor was brought up to 5000 rpm with stability being maintained. However, the whirl amplitudes were large indicating the negative damping aspects of the dissipative material.

To complete the tests, the bolts which hold the rotor to the shaft

TABLE 1

Test and Calculated Lower Forward Whirl Mode

Shaft Speed (rpm)	Lower Forward Whirl Mode (rpm)		
	Ceramic Bladed Rotor Test	Ceramic Bladed Rotor Calculated	Original Rotor Calculated
0		62.4	50.1
20		65.3	53.0
50		69.8	57.3
70		72.8	60.2
100		77.4	64.6
120		80.3	67.5
150		84.7	71.1
170		87.5	74.3
200		91.6	78.2
260	100.7	99.1	85.1
300	105.1	103.7	89.2
400	115.0	113.4	97.7
500	122.2	121.0	
600	128.8	127.0	109.1
700	133.5	131.9	
800	137.2	135.8	116.2
900	140.4	139.0	
1000	141.6	141.7	120.8
1200	147.8	146.0	124.2
1500	151.6	150.4	
2000	155.0	155.0	131.2
3000	160.8	160.0	135.0
4000	162.6	162.4	136.8
5000	164.6	164.0	138.0
6000	171.2	165.0	138.8

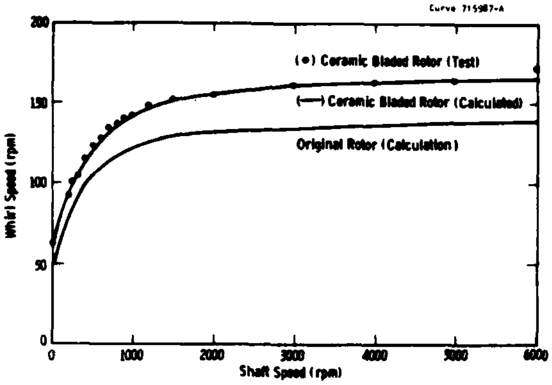

Fig. 8 - Low forward whirl mode for test and calculated rotors

were slightly loosened. The failure occurred at 2000 rpm showing, conclusively, that any amount of looseness cannot be tolerated. A slight loosening of the bolts introduced an *effective loss factor using Figure 7 of*

$$C_1 = \frac{7500}{2000 \times 2\pi} = 0.597 \ \frac{\text{lb-sec}}{\text{in.}}$$

$$\frac{C_1}{\gamma} = 14.3$$

$$\gamma = \frac{0.597}{14.3} \approx 0.042 \text{ (effective loss factor)}$$

This effective loss factor is more than 40 times larger than the highest expected loss factor for the type of steel used in the shaft.

CONCLUSIONS

Lateral instabilities caused the two shaft failures that occurred during spin testing a low cycle fatigue disc specimen. The exact cause was a combination of shaft hysteresis and loose mating bolts at the ends of the smallest diameter shaft. Loose mating bolts were the major factor in causing the subsynchronous whirl instability. When tests were conducted with no looseness in rotor bolts (set screws kept bolt-tight), the original system was stable throughout the desired speed range (0-8000 rpm). Although the whirl was stable the amplitude was considerably larger than the whirl amplitude in the redesigned system. The redesigned system has an oil film damper at the lower bearing. It limits the whirl of a tight rotor system to amplitudes which are so small they are difficult to detect over most of the operating speed range.

REFERENCES

1. W.T. Thomson, F.C. Younger and H.S. Gordon, "Whirl Stability of the Pendulously Supported Flywheel System", J. of Applied Mechanics, Paper No. 77-APM-20, 1977.

2. C.M. Harris and C.E. Crede, "Shock and Vibration Handbook", 2nd Edition, Chapter 5, McGraw-Hill Book Co., 1976.

3. C.M. Harris and C.E. Crede, "Shock and Vibration Handbook", 2nd Edition, Chapter 36, McGraw-Hill Book Co., 1976.

4. R.D. Holm, "Vibrational Method for Measuring the Damping of Materials Under Uniaxial Stress", Research Report No. 79-1E7-MEDAM-R1, 1979.